

AD-766 406

A CENTER OF COMPETENCE IN SOLID STATE MATERIALS AND  
DEVICES

FLORIDA UNIVERSITY

PREPARED FOR  
AIR FORCE CAMBRIDGE RESEARCH LABORATORIES

OCTOBER 1972

DISTRIBUTED BY:

**NTIS**

**National Technical Information Service  
U. S. DEPARTMENT OF COMMERCE**

# A CENTER OF COMPETENCE IN SOLID STATE MATERIALS AND DEVICES

by

Fredrik A. Lindholm, Arthur J. Brodersen, Eugene R. Chenette,  
Larry L. Hench, Sheng S. Li, Aldert van der Ziel

Electrical Engineering Department  
College of Engineering  
University of Florida  
Gainesville, Florida 32601

Contract No. F 19628-68-C-0058

Project No. 8687

**FINAL REPORT**

1 September 1967-1 September 1972  
10 October 1972

Contract Monitor  
Andrew C. Yang  
Solid State Sciences Laboratory

Approved for public release; distribution unlimited.

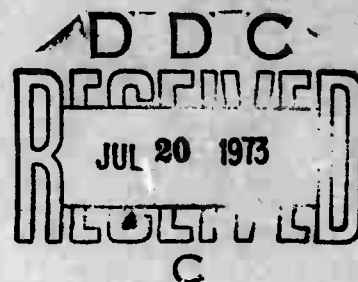
Reproduced by  
**NATIONAL TECHNICAL  
INFORMATION SERVICE**  
US Department of Commerce  
Springfield, VA. 22151

Sponsored by

Advanced Research Projects Agency  
ARPA Order No. 1060

Monitored by

**AIR FORCE CAMBRIDGE RESEARCH LABORATORIES  
AIR FORCE SYSTEMS COMMAND  
UNITED STATES AIR FORCE  
BEDFORD, MASSACHUSETTS 01730**



AD 766406

AS NOTED IN THE NTIS ANNOUNCEMENT,  
PORTIONS OF THIS REPORT ARE NOT  
LEGIBLE. HOWEVER, IT IS THE BEST  
REPRODUCTION AVAILABLE FROM THE  
COPY FURNISHED NTIS BY THE CONTRIB-  
UTOR.

DOCUMENT CONTROL DATA - R&D

(Security classification of title, body of abstract and indexing annotation must be entered when the overall report is classified)

1. ORIGINATING ACTIVITY (Corporate author) University of Florida Engineering and Industrial Experiment Station Gainesville, Florida 32601	2a. REPORT SECURITY CLASSIFICATION Unclassified 2b. GROUP
--	---

3. REPORT TITLE A CENTER OF COMPETENCE IN SOLID STATE MATERIALS AND DEVICES
--

4. DESCRIPTIVE NOTES (Type of report and inclusive dates) Scientific final, 1 September 1967-1 September 1972	Approved 30 Mar. 73
--	------------------------

5. AUTHOR(S) (First name, middle initial, last name) Fredrik A. Lindholm Arthur J. Brodersen Eugene R. Chenette	Larry L. Hench Sheng S. Li Aldert van der Ziel
--	--

6. REPORT DATE 10 October 1972	7a. TOTAL NO. OF PAGES 208	7b. NO. OF REFS 160
-----------------------------------	-------------------------------	------------------------

8a. CONTRACT OR GRANT NO. F 19682-68-C-0058 ARPA Order No. 1010 19629 b. PROJECT, TASK, WORK UNIT NOS. 8687 n/a/ n/a c. DOD ELEMENT 61101D d. DOD SUBELEMENT n/a	9a. ORIGINATOR'S REPORT NUMBER(S)  9b. OTHER REPORT NO(S) (Any other numbers that may be assigned this report)  AFCRL- TR-73-0164
--	---

10. DISTRIBUTION STATEMENT A - Approved for public release; distribution unlimited
---

11. SUPPLEMENTARY NOTES This research was supported by Advanced Research Projects Agency	12. SPONSORING MILITARY ACTIVITY Air Force Cambridge Research Laboratories (LQ) L. G. Hanscom Field Bedford, Massachusetts 01730
--	--

13. ABSTRACT The five-year research program sponsored by this contract has produced technical findings in several areas: characterization of semiconductor devices and integrated circuits; electronic ceramics; noise within solids and semiconductor devices; quantum and electronic properties of elemental and compound semiconductors; and magnetic films. This report begins with a summary of these findings. It then describes our most recent results, as follows. It is shown how the falloff of transistor gain and cutoff frequency at high currents depends on the device operating conditions; this description enabled a new interpretation to be given to experimental results previously reported. The decline observed in the response of p-i-n photodiodes for short wavelength excitation is explained by accounting for carrier transport and recombination in the p-type region. We describe a method for the numerical calculation of the energy structure and charge distribution resulting from various defects in the solid state including clustering and amorphous disorder. A recombination and trapping model is developed to interpret photoconductivity data observed on high resistivity $3As_2Se_3-2Sb_2Se_3$ amorphous films. A study of the influence of crystalline microstructure on the electrical characteristics of $Li_2O-2SiO_2$ crystals shows that for volume fractions of crystals exceeding twenty percent the dc conductivity and ac dielectric losses are markedly reduced.
---

14.	KEY WORDS	LINK A		LINK B		LINK C	
		ROLE	WT	ROLE	WT	ROLE	WT
	silicon						
	photodetectors						
	transistors						
	amorphous semiconductors						
	defects in silicon						

**TR-73-0164**  
**AFCRL** ~~████████~~

## **A CENTER OF COMPETENCE IN SOLID STATE MATERIALS AND DEVICES**

by  
Fredrik A. Lindholm, Arthur J. Bradersen, Eugene R. Chenette,  
Larry L. Hench, Sheng S. Li, Aldert van der Ziel

Electrical Engineering Department  
College of Engineering  
University of Florida  
Gainesville, Florida 32601

Contract Na. F 19628-68-C-0058  
Project Na. 8687

**FINAL REPORT**  
1 September 1967-1 September 1972  
10 October 1972

Contract Monitor  
Andrew C. Yang  
Solid State Sciences Laboratory

Approved for public release; distribution unlimited.

Sponsored by  
Advanced Research Projects Agency  
ARPA Order No. 1060

Monitored by  
**AIR FORCE CAMBRIDGE RESEARCH LABORATORIES**  
**AIR FORCE SYSTEMS COMMAND**  
**UNITED STATES AIR FORCE**  
**BEDFORD, MASSACHUSETTS 01730**

*ib*

ARPA Order No. 1060

Program Code No. 1D10

Contractor: University of Florida

Effective Date of Contract: 11 September 1967

Contract No. F19628-68-C-0058

Principal Investigator and Phone No.

Dr. Fredrik A. Lindholm/904 392-0904

AFCRL Project Scientist and Phone No.

Dr. Andrew C. Yong/617 861-2225

Contract Expiration Date: 31 August 1972

Qualified requestors may obtain additional copies from the  
Defense Documentation Center. All others should apply to the  
National Technical Information Service.

jc

## ABSTRACT

The five-year research program sponsored by this contract has produced technical findings in several areas: characterization of semiconductor devices and integrated circuits; electronic ceramics; noise within solids and semiconductor devices; quantum and electronic properties of elemental and compound semiconductors; and magnetic films. This report begins with a summary of these findings. It then describes our most recent results, as follows. It is shown how the falloff of transistor gain and cutoff frequency at high currents depends on the device operating conditions; this description enables a new interpretation to be given to experimental results previously reported. The decline observed in the response of p-i-n photodiodes for short wavelength excitation is explained by accounting for carrier transport and recombination in the p-type region. We describe a method for the numerical calculation of the energy structure and charge distribution resulting from various defects in the solid state including clustering and amorphous disorder. A recombination and trapping model is developed to interpret photoconductivity data observed on high resistivity  $3\text{As}_2\text{Se}_3\text{-}2\text{Sb}_2\text{Se}_3$  amorphous films. A study of the influence of crystalline microstructure on the electrical characteristics of  $\text{Li}_2\text{O-}2\text{SiO}_2$  crystals shows that for volume fractions of crystals exceeding twenty percent the dc conductivity and ac dielectric losses are markedly reduced.



## SUMMARY

The five-year research program sponsored by this contract has produced technical findings in several areas: characterization of semiconductor devices and integrated circuits; electronic ceramics; noise within solids and semiconductor devices; quantum and electronic properties of elemental and compound semiconductors; and magnetic films. This report begins with a summary of these findings. It then describes our most recent results, as follows.

For transistors having epitaxial collectors, the falloff of transistor gain and cutoff frequency at high current may depend predominantly on phenomena occurring in the collector region. We show in detail how the mechanism responsible for falloff depends on device operating conditions and the structural and material parameters of the device make-up. We illustrate the usefulness of this description in understanding observed device behavior and show how it enables a new interpretation to be given to experimental results previously reported. Important implications for transistor modeling are also discussed.

An expression for the quantum yield of p-i-n photodiodes is formulated that takes into account the effects of carrier transport and recombination in the p-type region and consequently describes the decline in the response observed for short wavelength excitation. Applied to a silicon p-i-n photodiode, this expression yields theoretical predictions in excellent agreement with experimental data over the entire spectral range.

Many of the properties that make semiconductor devices useful in both electronic and optical applications arise from the defect structure in the solid state. Previous methods available for calculating the details of the energy levels and charge distribution resulting from defects apply only to such simple defect centers as shallow-level donors and acceptor impurities. We describe here a method enabling calculations for various other kinds of defects including vacancies, vacancy-impurity clustering and amorphous disorder. Using this method we have done calculations for certain specific defects in silicon: boron and phosphorous impurities, the vacancy and boron and phosphorous complexes, and impurity clusters. The pertinence to radiation-damaged silicon is discussed.

We report the results of photoconductivity experiments done on high-resistivity  $3\text{As}_2\text{Se}_3\text{-}2\text{Sb}_2\text{Se}_3$  amorphous films in a temperature range from  $278^\circ\text{K}$  to  $308^\circ\text{K}$  as functions of the light intensity. At intermediate light levels the photocurrent varies as the light intensity to the 0.7 power and at high light intensities it varies in direct proportion to the light intensity. To explain the observed data a recombination trapping model is suggested.

Previous studies in this program have shown that it is possible to control the volume fraction of crystals in pure  $\text{Li}_2\text{O-}2\text{SiO}_2$  glasses by nucleation and growth heat treatments. The resulting glass-ceramics exhibit improved mechanical and thermo properties. The present study shows the influence of the crystal in microstructure on the electrical characteristics of the glass-ceramics. If the volume fraction of crystals exceeds twenty percent the dc conductivity and ac dielectric losses of the material decline markedly. The temperature dependence of the electrical processes increases with the volume fraction of crystals. Interpretation of these results is given based on an application of heterogeneous dielectric mixing laws to glass-ceramic materials.

## TABLE OF CONTENTS

	<u>Page</u>
I. <u>Introduction</u>	1
II. <u>Summary of Research Program</u>	3
A. CHARACTERIZATION OF SEMICONDUCTOR DEVICES AND INTEGRATED CIRCUITS	3
A-1 Introduction	3
A-2 Relating Device Make-up to Internal Device Variables	5
A-2.1 The effects of high doping in semiconductor devices	5
A-2.2 Transport in semiconductors with low scattering rate and at high frequencies	8
A-2.3 The effect of a buried layer on the collector breakdown voltages of bipolar junction transistors	9
A-2.4 High current regimes in transistor collector regions	9
A-3 Generation and Unification of Device Circuit Models	10
A-3.1 Device modeling for computer-aided design and analysis of integrated circuits	10
A-3.2 Integrated-circuit transistor and diode models for network-analysis programs	11
A-3.3 Incorporation of the Early effect in the Ebers-Moll model	12
A-3.4 Unified modeling of field-effect devices	12
A-4 Selection of Circuit Models	15
B. ELECTRONIC CERAMICS	18
B-1 Introduction	18
B-2 Semiconducting Glasses	19
B-2.1 Microstructural effects	19
B-2.2 Irradiation effects	19
B-2.3 Theory	20
B-3 Glass Ceramics	20
B-3.1 Nucleation and crystallization kinetics	21
B-3.2 Microstructural effects on properties	22
B-3.3 Irradiation effects	22
B-4 Characterization Methods	23
B-4.1 X-ray methods	23
B-4.2 Microscopy	23
B-4.3 Surface properties	24
B-4.4 Dielectrics	24
B-5 Silicon Defect and Irradiation Damage Calculations	24
B-6 Conferences and Books	25
C. QUANTUM AND ELECTRONIC PROPERTIES OF SEMICONDUCTORS AND RELATED DEVICES	29
C-1 Introduction	29

	<u>Page</u>
C-2 Studies of Diffusivity-Mobility Ratio and Density of States Function for Degenerate Semiconductors	30
C-2.1 Generalized Einstein Relation	30
C-2.2 Density of states function for degenerate semiconductors	30
C-3 Studies of Recombination and Trapping Mechanisms in Semiconductors by Using Photomagnetolectric (PME) and Photoconductive (PC) Methods	30
C-3.1 Photomagnetolectric and photoconductive effects in phosphorous-doped silicon at low temperatures	30
C-3.2 Recombination and trapping processes of the injected carriers in gold-doped silicon	31
C-3.3 Low-temperature photomagnetolectric properties of gold-doped n-type silicon	31
C-3.4 Photomagnetolectric and photoconductive effects in n-type InAs	31
C-3.5 Investigation of the recombination and trapping processes of photoinjected carriers in semi-insulating Cr-doped GaAs using PME and PC methods	32
C-3.6 Determination of electron and hole capture rates in nickel-doped germanium using photomagnetolectric and photoconductive methods	32
C-3.7 Electron mobility and shallow impurity levels in In-doped and Cu-doped cadmium-sulfide	33
C-3.8 Investigation of recombination and trapping processes in $3\text{As}_2\text{Se}_3$ - $2\text{Sb}_2\text{Se}_3$ amorphous films by photoconductivity method	33
C-3.9 Radiative recombination in $\text{O}_2$ -doped n-type GaAs at low temperatures	34
C-4 Theoretical and Experimental Studies of Metal-Semiconductor Schottky-Barrier and PME Photodetectors	34
C-4.1 A new grating type gold-n type silicon Schottky barrier photodiode	34
C-4.2 Photodetection using photomagnetolectric and Demer effects in gold-doped silicon	34
C-4.3 Quantum yield of metal-semiconductor photodiodes	34
C-4.4 Quantum yield of p-i-n photodiodes	35
C-4.5 Analysis of Transient Capacitance Experiments for Au-GaAs Schottky Barrier Diodes in the Presence of Deep Impurities	35
D. NOISE IN SOLIDS AND IN SOLID-STATE DEVICES	37
D-1 Low Frequency Noise in Bipolar Junction Transistors	37
D-2 Noise in Phototransistors	38
D-3 Noise in Bipolar Transistors as a Function of Temperature	39
D-4 Noise in Junction Field-Effect Transistors and in MOS Field-Effect Transistors	39

	<u>Page</u>
D-5 Noise in Zener and Avalanche Breakdown	40
D-6 Effect of Radiation on Noise in Junction Field- Effect Transistors	40
D-7 Noise in Amorphous Semiconductors	40
E. MAGNETIC FILMS	41
E-1 Thin Films	41
III. <u>High Current Regimes in Transistor Collector Regions</u> (D. L. Bowler and F. A. Lindholm)	43
1. Introduction	43
2. Theoretical Development	44
A. Collector not fully depleted	44
B. Collector fully depleted	45
C. Operation at low collector voltage	45
D. Operation at high collector voltages	48
3. Discussion	49
A. Interpretation of device performance data	49
B. Implications for device modeling	50
Appendix: Behavior of the Depletion Region Edge	52
A. Saturated velocity case	52
B. Constant mobility case	53
References	55
IV. <u>Quantum Yield of p-i-n Photodiodes</u> (S. S. Li and F. A. Lindholm)	57
1. Introduction	57
2. Derivation of Quantum Yield for a p-i-n Photodiode	59
i. P-type region ( $0 < x < x_0$ )	61
ii. Intrinsic region ( $x_0 < x < W$ )	62
iii. N-type region ( $x > W$ )	62
3. Results and Discussions	63
Appendix: Spectral Response in p-type Surface Region	65
References	68
V. <u>Cluster Model Calculations of Silicon Defects</u> (H. F. Schaafe and L. L. Hench)	73
Introduction	73
Molecular Cluster Method	74
A. Closed-shell systems	75
1. Open-shell systems	80
2. Further comments on excited states	81
3. Semiempirical approximations	82
4. Cluster boundary conditions	85
5. Parameterization for energy level diagrams	88
6. Population analysis	89
7. Results on crystalline clusters	90
a. diamond and carbon structures	90
b. silicon	95

	<u>Page</u>
c. $\beta$ -silicon carbide	96
d. $\text{SiO}_2$ clusters	96
e. summary	98
B. Impurity and vacancy complexes	98
1. Vacancy in silicon	102
2. Vacancy-impurity complexes	105
3. Multi-impurity clusters	108
References	113
VI. <u>Investigation of Recombination and Trapping Processes in <math>3\text{As}_2\text{Se}_3</math>-<math>2\text{Sb}_2\text{Se}_3</math> Amorphous Films by Photoconductivity Method</u> (S. S. Li and P. K. Chaudhari)	175
1. Introduction	175
2. Theory	175
3. Experimental Details	177
4. Results and Discussions	178
a. Intermediate light level	179
b. The high light levels	180
References	182
VII. <u>Dielectric Properties of Lithium-Disilicate Glass-Ceramics</u> (W. D. Tuohig and L. L. Hench)	186
Introduction	186
Experimental Procedure	188
Results	188
Discussion	189
VIII. <u>Discussion</u>	200

## I. Introduction

The original general objective of this research program was to establish at the University of Florida a "Center of Competence in Solid State Materials and Devices" capable of doing research of benefit to the Department of Defense. At this stage, five years following initiation of contract support, ample evidence exists that the University of Florida has indeed become such a center of competence. Among the evidence supporting this conclusion are the technical findings fostered by this contract. These are documented in the nine previous reports in this series<sup>1-9</sup> and in 118 related papers published in research journals.

During the past year the objectives of the research program have shifted decisively. In accordance with an agreement made with the contract monitor in January 1971, we have focussed the objectives to give greatest emphasis to the following problem areas:

1. The development of new types of detectors with stress given to utilizing the Demer and photomagnetolectric effects in semiconductors and to utilizing new mask geometries for Schottky barrier detectors compatible with conventional silicon technology.
2. The incorporation of the effects of irradiation into the characterization of device behavior; junction field-effect devices are to receive special attention. Emphasis is placed on the development of characterizations enabling computer simulation and design of circuits.
3. Full static and dynamic characterization of bipolar and field-effect devices aiming both toward improved device design and toward improved circuit implementation. The characterization is to deal with operation over a wide range of temperatures, with emphasis on the range between ordinary room temperature and cryogenic temperatures.
4. Noise studies proceeding collaterally with each of the efforts listed above.
5. Radiation studies of amorphous semiconductors.

The content of the present report reflects this change in emphasis. The report begins with a summary of major technical findings produced during the five years of this contract, and then describes our most recent results.

## REFERENCES

1. F. A. Lindholm et al, Scientific Report No. 1, Contract #F 19628-68-C-0058, College of Engineering, University of Florida, 10 April 1968.
2. F. A. Lindholm et al, Scientific Report No. 2, Contract #F 19628-68-C-0058, College of Engineering, University of Florida, 10 October 1968.
3. F. A. Lindholm et al, Scientific Report No. 3, Contract #F 19628-68-C-0058, College of Engineering, University of Florida, 10 April 1969.
4. F. A. Lindholm et al, Scientific Report No. 4, Contract #F 19628-68-C-0058, College of Engineering, University of Florida, 10 October 1969.
5. F. A. Lindholm et al, Scientific Report No. 5, Contract #F 19628-68-C-0058, College of Engineering, University of Florida, 10 April 1970.
6. F. A. Lindholm et al, Scientific Report No. 6, Contract #F 19628-68-C-0058, College of Engineering, University of Florida, 10 October 1970.
7. F. A. Lindholm et al, Scientific Report No. 7, Contract #F 19628-68-C-0058, College of Engineering, University of Florida, 10 March 1971.
8. F. A. Lindholm et al, Scientific Report No. 8, Contract #F 19628-68-C-0058, College of Engineering, University of Florida, 10 October 1971.
9. F. A. Lindholm et al, Scientific Report No. 9, Contract #F 19682-68-C-0058, College of Engineering, University of Florida, 10 April 1972.



## II. Summary of Research Program (September 1967 to September 1972)

The five-year research program sponsored by this contract has produced technical findings in several areas: characterization of semiconductor devices and integrated circuits; electronic ceramics; noise within solids and semiconductor devices; quantum and electronic properties of elemental and compound semiconductors; and magnetic films. These findings appear documented in over one hundred technical papers published in research journals and in a comparable number of papers presented orally at national and international research meetings. Here, following, we describe the major results.

### A. CHARACTERIZATION OF SEMICONDUCTOR DEVICES AND INTEGRATED CIRCUITS

#### A-1 Introduction

Semiconductor devices and circuits form the core of the great majority of electronic systems. At present, a substantial part of the design of these devices and circuits is based on laboratory experimentation and iterative cut-and-try procedures. To reduce the cost and time of such procedures and to secure superior system performance, much effort in this nation now aims toward the development of computer techniques to aid design. Essential to the success of such techniques is the proper characterization of semiconductor devices and integrated circuits. As its main objective, this portion of our research program has focussed attention upon fundamental problems related to securing these characterizations.

One can view the starting point in semiconductor circuit and system design as the processing steps used in fabrication: mask generation, diffusion or implantation of impurities, etc. The end point is a circuit that meets specifications in system performance and cost. In between are four modeling problems, as Fig. II-1 illustrates.

The first of these problems seeks to describe for each device in the circuit the relationship between the processing and the resulting physical make-up: the spatial distribution of impurities and defects, the corresponding distribution of the pertinent material parameters, etc.

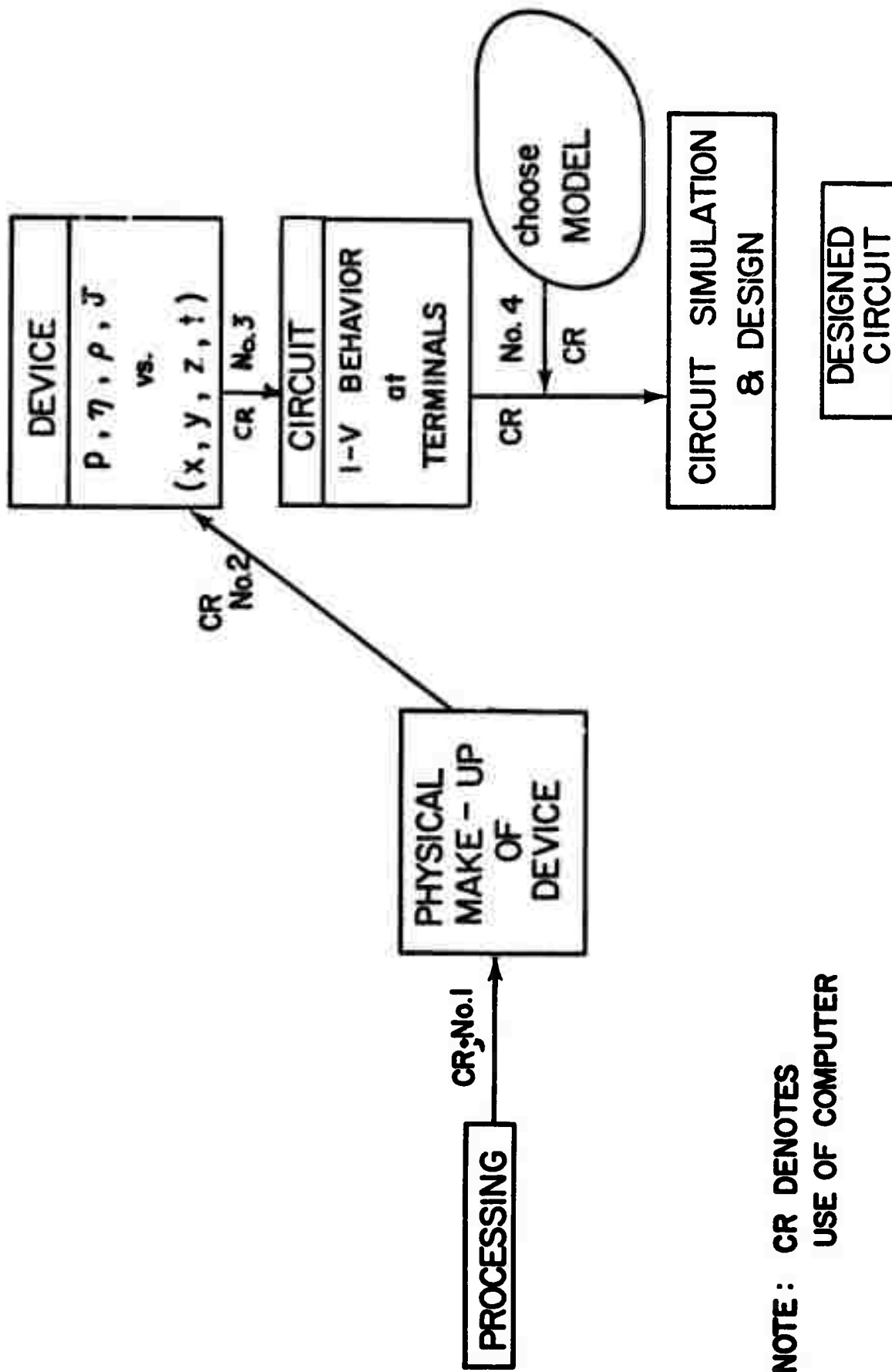


Fig. II-1 Four modeling problems involved in modern circuit design.

In the second problem one deals with the relevant partial differential equations, often by numerical methods, to relate the physical make-up to the spatial and temporal dependence of such internal variables as free carrier densities, charge densities, current density, and electric field. Response is sought for excitation pertinent to the proposed system application. The understanding thus gained directly guides the design of the devices comprising the circuit.

Moreover, it supplies insight vital in the third modeling problem, in which one links the physical make-up and the current-voltage behavior at the terminals of each device. The vehicle describing this behavior is usually called a circuit model or an equivalent circuit. The availability of adequate circuit models is essential in the design of any circuit.

The fourth modeling problem involves selection from the reservoir of available models of a circuit model to represent each device in the circuit being designed.

This research program has made contributions mainly in the last three of these modeling problems, as is described below.

## A-2 Relating Device Make-up to Internal Device Variables

In this second modeling problem we have contributed in several areas.

A-2.1 THE EFFECTS OF HIGH DOPING IN SEMICONDUCTOR DEVICES: Although the fabrication techniques used for two decades have produced regions of semiconductor devices such as bipolar and field-effect transistors in which high concentrations of impurities (exceeding  $5 \times 10^{17}$  per cubic centimeter) are present, traditional semiconductor device theory and design practice largely ignore the consequent effects on device operation. Aside from the first-order phenomenological treatment by Kauffman and Bergh<sup>1</sup> and by Buhanan,<sup>2</sup> and the early similar work by Kroemer,<sup>3</sup> transistor theory took no account of the presence of heavy doping. Under the sponsorship of this contract Kleppinger and Lindholm<sup>4,5</sup> pioneered an effort to describe the effects of high doping in a way useful to the semiconductor device designer. Based on this contract-supported work, which is described below, Van Overstraeten et al.,<sup>6</sup> DeMan and Mertens<sup>7</sup> (of the University of Louvain in Belgium) and Mock<sup>8</sup> (of the IBM Corporation) have demonstrated that heavy doping takes a dominant role in determining the current gain and frequency response of bipolar

transistors. Before the availability of these results, efforts toward optimizing transistor design were frustrated by the poor capability of existing theory to predict these two parameters from knowledge of the physical make-up yielded by the fabrication processing. The new results, based on contract-supported research, enabled greatly improved prediction, thus providing a basis for improving the design of bipolar transistors and the electronic systems in which they are used. Recently DeMan and Mertens<sup>7</sup> report the incorporation of the effects of heavy doping into their computer program for the computer-determined design of semiconductor circuits.

The main objective of the research by Kleppinger and Lindholm,<sup>4,5</sup> supported by this contract, was to combine and phrase existing theories available in the physics literature in a form amenable to the semiconductor device theorist and designer. In the first<sup>4</sup> of the two papers published from this research, Kleppinger and Lindholm developed and justified an approach to the problem of describing the dependence on impurity concentration of the density of quantum states in a semiconductor. The approach applies generally to any semiconductor, including those widely used in device fabrication: silicon, germanium and gallium arsenide. The approach combined previously separate theories concerning the various contributors to the dependence of the quantum-state density, utilizing an approximation that enabled application of the superposed theory over the range of impurity concentrations of technological interest. To demonstrate the practical utility of the approach, the prediction yielded by its application to gallium arsenide was compared to an experimentally determined density of states. Agreement was satisfactory. Throughout, the paper stressed the implications to semiconductor device design.

In their second paper,<sup>5</sup> Kleppinger and Lindholm applied the approach explicitly to silicon, which is the semiconductor of greatest importance in the technology of integrated circuits. They calculated the density of states and the Fermi level, and showed the calculated density states to agree with pertinent experimental results.

As a consequence of this research, collaboration began between Dr. Lindholm and Dr. Roger Van Overstraeten, Professor and Head of the Solid State Electronic Laboratory, University of Louvain, Belgium. In May of 1972 Dr. Van Overstraeten began a month-long visit in Gainesville, Florida to do

research with Dr. Lindholm. This visit produced a research paper<sup>9</sup> which places on firmer ground the description of current within heavily doped material. The paper includes the derivation of an expression describing current in a semiconductor with an arbitrary quantum density states, enabling, as a special case, a description of the effects of the warping of the quantum density of states which accompanies heavy doping. Special attention is given to the Einstein ratio of diffusivity to mobility. In semiconductor device theory, this ratio has gained importance for two reasons. First, it appears whenever carrier drift and diffusion coexist, which in device materials frequently occurs. Second, mobility is much more easily measured than is diffusivity, and knowledge of the Einstein ratio thus yields a value for diffusivity without need for direct measurement. For nondegenerate semiconductors in thermal equilibrium, the Einstein ratio equals the thermal voltage. However, rigorous analysis of device behavior requires understanding of the Einstein ratio in semiconductors that are both highly-doped and in nonequilibrium. Early efforts supported by this contract<sup>10,11</sup> contributed to this understanding, but ignored the distortion of the quantum density of states that occurs with high doping. The computations done in our more recent study<sup>9</sup> show a dependence of the Einstein ratio on impurity concentration that contrasts markedly with earlier predictions.

REFERENCES (\*indicates research sponsored by  
this contract)

1. W. L. Kauffman and A. A. Bergh, "The Temperature Dependence of Ideal Gain in Double Diffused Silicon Transistors," IEEE Transactions on Electron Devices, ED-15, 732 (1968).
2. D. Buhanan, "Investigation of Current-Gain Temperature Dependence in Silicon Transistors," IEEE Transactions on Electron Devices, ED-16, 117 (1969).
3. H. Kroemer, "Theory of a Wide-Gap Emitter in Transistors," Proceedings I.R.E., 45, 1535 (1957).
- \* 4. D. D. Kleppinger and F. A. Lindholm, "Impurity Concentration Dependence of the Density of States in Semiconductors," Solid State Electronics, 14, 199 (1971).
- \* 5. D. D. Kleppinger and F. A. Lindholm, "Impurity Concentration Dependent Density of States and Resulting Fermi Level for Silicon," Solid State Electronics, 14, 407 (1971).

6. R. Van Overstraeten, H. De Man, and R. Mertens, "Transport Equations in Heavy Doped Silicon," IEEE Transactions on Electron Devices (March 1973).
- R. Van Overstraeten, H. DeMan, and R. Mertens, "Calculation of the Emitter Efficiency of a Bipolar Transistor," IEEE Transactions on Electron Devices (to appear).
7. H. DeMan and R. Mertens, "SITCAP--A Simulator of Bipolar Transistors for Computer-Aided Circuit Analysis Program," Digest of Technical Papers: 1973, IEEE International Solid-State Circuits Conference, 16, 104 (1973).
8. M. S. Mock, "Transport Equations in Heavily Doped Silicon, and the Current-Gain of a Bipolar Transistor," Solid State Electronics (to appear).
- \* 9. R. Van Overstraeten and F. A. Lindholm, "Generalized Non-Equilibrium Transport Equations and Einstein Ratio for a Semiconductor with an Arbitrary Density of States," Solid State Electronics (to appear).
- \*10 F. A. Lindholm and R. W. Ayers, "Generalized Einstein Relation for Degenerate Semiconductors," Proceedings of the IEEE, 56, 371 (1968).
- \*11 S. S. Li and F. A. Lindholm, "Alternative Formulation of Generalized Einstein Relation for Degenerate Semiconductors," Proceedings of the IEEE, 56, 1256 (1968).

A-2.2 TRANSPORT IN SEMICONDUCTORS WITH LOW SCATTERING RATE AND AT HIGH FREQUENCIES:<sup>1</sup> The conventional hydrodynamic transport equations used in the analysis of the electrical characteristics of semiconductor devices require modification when the number of recombination-generation-trapping-tunneling events become comparable to the number of scattering events. These modifications may become important in describing the transport of minority carriers across the thin base region of a microwave transistor and in devices made of compound semiconductors with high mobilities and low lifetimes. If the signal frequency becomes comparable to the collision frequency, additional modifications may be needed.

This study gives a rigorous derivation of the hydrodynamic carrier transport equations by extending the moment method to include the moment equation of the collision-free path, which is generalized to contain both the scattering and the generation-recombination-trapping-tunneling events. This leads to a description of the flow of electrons or holes that contains an inductive term neglected in previous characterizations in semiconductor

device physics. If the signal frequency becomes comparable to the reciprocal of the average collision relaxation time, this inductive term can take an important role.

#### REFERENCES

1. C. T. Sah and F. A. Lindholm, "Transport in Semiconductors with Low Scattering Rate and at High Frequencies," Solid State Electronics (to appear).

#### A-2.3 THE EFFECT OF A BURIED LAYER ON THE COLLECTOR BREAKDOWN VOLTAGES OF BIPOLAR JUNCTION TRANSISTORS:<sup>1</sup>

Bipolar transistors designed for high-frequency or high-speed applications are very shallow structures. For example, devices used for small-signal microwave amplification may have emitter and collector junctions that lie within 5000 Å units from the surface; typically, the devices are fabricated by successive diffusions into  $N/N^+$  epitaxially grown silicon. The N-type epitaxial material is made thin, less than 10 microns, to reduce collector series resistance. Similar devices are used commonly in high-speed digital integrated circuits. The standard buried collector technology presently employed by the Bell System uses epitaxial layers which are 7 to 9 microns thick.

In this study, we describe a premature punch-through effect occurring in this type of transistor that can lower the collector breakdown voltages below the values predicted by existing theory. We express the premature punch-through voltage,  $BV_{PPT}$ , which characterizes the effect, in terms of parameters of the fabrication processing, and from this derive an expression for the thickness of the epitaxial collector that maximizes  $BV_{PPT}$  and, hence, the usable region of device operation. Measurements are presented that support the theoretical predictions.

#### REFERENCES

1. F. W. Hewlett, Jr., F. A. Lindholm, and A. J. Brodersen, "The Effect of a Buried Layer on the Collector Breakdown Voltages of Bipolar Junction Transistors," Solid State Electronics (to appear).

#### A-2.4 HIGH CURRENT REGIMES IN TRANSISTOR COLLECTOR REGIONS:<sup>1</sup> This work is described in Section III of this report.

#### REFERENCES

1. D. L. Bowler and F. A. Lindholm, "High Current Regimes in Transistor Collector Regions," IEEE Transactions on Electron Devices (March 1973).

### A-3 Generation and Unification of Device Circuit Models

This phase of our work deals with the third modeling problem defined in Figure II-1. The emergence in recent years of the computer as a tool for the analysis and design of semiconductor devices and circuits has focussed renewed attention on the models that characterized the terminal behavior of devices. In particular, because the computer has afforded for the first time a general means of accomplishing the detailed analysis of large-signal transient behavior, it has awakened special interest in large-signal (nonlinear) dynamic models. Our work has focussed mainly on the large-signal dynamic circuit models for the bipolar transistor and for various types of field effect transistors: insulated-gate (IGFET or MOSFET), junction-gate (JFET), and metal-gate (MESFET).

In the historical perspective of the research done under the sponsorship of this contract, there were two main issues that needed initial study:

- (a) generation of new and more completely adequate circuit models using advances made in the second modeling problem defined in Fig. II-1, concerning semiconductor device physics; and
- (b) evaluation of existing circuit programs for accuracy and suitability in circuit analysis codes, making modifications where needed.

Concerning the first of these issues, each of our advances outlined above in Section A-2 potentially enables the generation of new and superior circuit models. To the present, our studies concerning highly-doped semiconductors, summarized above, have had the most impact. The effects of the warping of the quantum density of states that accompanies high doping has recently been included in a new and comprehensive circuit-analysis program developed by DeMan and Mertens (reference 7, Section A-2).

For the second of these issues our work toward evaluating the existing circuit models for semiconductor devices began with an invited research paper<sup>1</sup> at the 1968 International Symposium on Circuit Theory. This paper tried to assess where the technical community stood in 1968 in relation to device models for computer-aided design. Subsequently, it led to the following more comprehensive statement of the considerations involved.

A-3.1 DEVICE MODELING FOR COMPUTER-AIDED DESIGN AND ANALYSIS OF INTEGRATED CIRCUITS:<sup>2</sup> A list is proposed of properties considered to be desirable for



models for integrated devices. These properties serve as a guide in modeling per se and as vehicle for assessing the adequacy of any given model. In illustration, the adequacy is examined of a generalized Ebers-Moll Model for the large-signal, dynamic behavior of the integrated bipolar transistor. This examination discloses two related unsolved problem areas: the accounting for high-level behavior while retaining an accuracy-simplicity compromise, and the determination of model parameter values for device operation over a wide range of currents. Three approaches for attacking these problems are suggested and compared.

Attention then turned to the need for modifying conventional transistor models to adapt them for use in existing network-analysis programs, which led to:

#### A-3.2 INTEGRATED-CIRCUIT TRANSISTOR AND DIODE MODELS FOR NETWORK-ANALYSIS

PROGRAMS:<sup>3</sup> A set of new models of varying complexity and accuracy is derived for the large-signal transient behavior of bipolar transistor and diode structures found in integrated circuits. The derivation starts with the defining equations of the so-called nonlinear model for the four-layer integrated-circuit transistor and proceeds by reformulating several terms in these equations to remove, in effect, current sources in the symbolic model dependent on the complex frequency variable  $s$ . The removal of this dependence yields models containing resistors, capacitors, and nonfrequency-dependent sources. With the availability of these models, network-analysis programs unable to accommodate frequency-dependent sources become directly applicable to the computation of the large-signal transient behavior of bipolar integrated circuits. Considerations pertaining to practical application guide the choice of approximations used in the derivation. The limits of validity of these approximations and of others that set the range of validity of the resulting models receive careful attention.

Related to this general problem of tailoring transistor circuit models to the needs of computer-aided circuit analysis programs, we reported a simple, pragmatic method of describing an aspect of device physics neglected in previous circuit models:

#### A-3.3 INCORPORATION OF THE EARLY EFFECT IN THE EBERS-MOLL MODEL:<sup>4,5</sup>

The addition of a single parameter, termed the Early voltage, enables incorporation of the Early effect in the Ebers-Moll model for the large-signal static behavior of transistors. The consequent voltage dependences of collector current, common-emitter current gain, and small-signal output conductance are set forth.

To this point, attention had focussed mainly on the bipolar transistor. Advances in fabrication technology had made it plain, however, that the insulated-gate field-effect transistor (IGFET) would soon challenge the bipolar transistor as the active device most widely used in electronic systems. For the IGFET and related devices, a clear need existed to demonstrate the relations among the available circuit models. This motivated the following study.

#### A-3.4 UNIFIED MODELING OF FIELD-EFFECT DEVICES:<sup>6</sup>

A unifying approach is described to the derivation of models for field-effect devices. The most general model yielded by this approach contains, as special cases, models for the small- and large-signal behavior of the two major types of field-effect transistor and of other related devices such as the semiconductor current limiter and the pinch resistor. From this most general model emerge, by application of particular approximations and constraints, several models proposed earlier for use in computer-aided circuit analysis. The unifying approach thus demonstrates the relationships borne among various of the existing models for field-effect devices. In addition, it provides a wide diversity of new models of different complexities and degrees of accuracy.

Full utilization of the computer for the design of semiconductor circuits requires that the parameters of circuit models for devices be rapidly, accurately, and economically determined. During the last year of this contract and continuing to the present, a portion of our research effort has yielded considerations pertinent to the design of a facility for automating the determination of the parameters of bipolar and field-effect transistor circuit models. The results achieved to date <sup>7,8</sup> bear however, not only on this problem but also on the broader problem of the systematic design of electronic circuits.

The automation facility desired must supply parameters enabling computer simulation of circuit behavior by any of the major TREE analysis codes. Of central concern is the effect on device and circuit performance of neutron dosage, gamma rate and pulse power. The simulations of interest must include the capability of predicting response to large-signal and time-varying excitation.

In planning a system capable of achieving these objectives, one must first define the model whose parameters are to be measured. Upon this requirement, in a surprisingly subtle way, hinges to a large degree the success or failure of the desired measurement system. The approach taken in our effort can be understood only in appropriate perspective, which we now briefly try to supply.

Two decades of effort have made available many different transistor models, which provide different compromises between accuracy and mathematical complexity and which contact to different degrees with the processing used in device fabrication. The existence of this vast reservoir of available models helps yet also hinders the designer of a system for parameter measurement.

Two approaches are apparent. Either one can select from the reservoir the single existing model that at present appears to be best suited to the needs of the radiation-effects community, and design a facility capable of automatically yielding its parameters. Or, alternatively, one can try to design a facility able to measure the parameters of any of the existing models and, if possible, of any model likely to be developed in the future.

History argues in favor of this second approach. The past two decades have seen continual development of new and increasingly more adequate models, and no reason exists to suppose that this development will soon cease. Indeed, the smaller and more sharply defined geometries promised by emerging technologies such as electron beam techniques and ion implantation create a pressing need for new and better models. Thus a parameter measuring system tailored to any single existing transistor model is likely doomed to early obsolescence. It is by far the wiser approach to design the system to be compatible with all of the existing models and, insofar as possible, with all models of the future.

In the way of this approach stands the chaos of the existing large-signal transistor models. Discussions concerning the many alternative models available are widely scattered in the literature; and, for the most part, the treatments leave unclear the relationships among the different models. To the circuit designer and analyst, an understanding of these relationships and of the range of model complexity and accuracy available to his use is highly desirable. To the designer of an effective and sufficiently general facility for automatic parameter measurement, such an understanding is essential.

The main thrust of our effort, therefore, has been to simplify, reduce, and unify the results of previous studies to a form that clarifies the relationships among the models, the hierarchy of model complexities and accuracies, and the limits of model validity. We have demonstrated that all existing models are special cases of a general model, and have given reasons for the belief that future models will likewise be special cases. The general model is described by a matrix. The problem of designing a sufficiently general system for automated parameter measurement thus hinges on the problem of determining the parameters that define the elements of this matrix.

The origin of the chaos that persists in transistor modeling, despite decades of intense and well-financed effort, lies in the difficulty of the boundary-value problem describing transistor behavior. That is where our study has begun. We examine the approximations that have conventionally been made in dealing with this boundary-value problem and are thereby led to the general model and to the physical basis and approximations undergirding it. We then show that the general model contains as special cases all existing device circuit models.

The availability of the general model unifies the phenomenological inclusion of radiation effects; it proves to be as easy to include them in any one model as in any other.

#### REFERENCES

1. F. A. Lindholm, "Large-Signal Characterization of Integrated Circuits," 1968 IEEE International Symposium on Circuit Theory, 1, 101 (1968) (invited research paper).
2. F. A. Lindholm, "Device Modeling for Computer-Aided Analysis and Design of Integrated Circuits," Solid State Electronics, 12, 831 (1969).

3. F. A. Lindholm, "Integrated-Circuit Transistor and Diode Models for Network Analysis Program," IEEE Transactions on Circuit Theory, CT-18, 122 (1971).
4. F. A. Lindholm and D. J. Hamilton, "Incorporation of the Early Effect in the Ebers-Moll Model," Proceedings IEEE, 59, 1377 (1971).
5. F. A. Lindholm, P. Rohr, and D. J. Hamilton, "Modeling the Early Effect in Bipolar Transistors Using an Empirical but Effective Parameter," Proceedings IEEE, 60, 335 (1972).
6. F. A. Lindholm, "Unified Modeling of Field-Effect Devices," IEEE Journal of Solid State Circuits, SC-6, 250 (1971).
7. F. A. Lindholm, "Generation and Selection of Dynamic Large-Signal Models for Bipolar and Field-Effect Transistors," 1972 International IEEE Symposium on Circuit Theory, 4, 385 (1972) [invited research paper].
8. F. A. Lindholm and E. B. Dean, "Qualities Common to Existing Transistor Circuit Models," 1973 IEEE Conference on Nuclear and Space Radiation Effects (submitted).

#### A-4 Selection of Circuit Models

For many years, research in semiconductor device characterization focussed nearly exclusively on the first three of the modeling problems indicated in Fig. II-1. In 1971, under the sponsorship of this contract, we pioneered research concerning the fourth problem which deals with selection of models.

Success in the simulation and automated design of integrated circuits depends critically on the models chosen to represent the behavior of active devices. The basic consideration involved in the choice is to obtain required accuracy from a model of minimum complexity. Basing calculations on a model of insufficient accuracy will normally lead to meaningless results. On the other hand, use of a model more complex than needed threatens the capability of computer memory, increases CPU time, increases the chance of numerical errors, and limits the size of circuits that the simulation program can accommodate. Moreover, the more complex the model the more time and effort must be spent determining the model parameters. A design using optimization techniques compounds the need for model simplicity because such a design requires many circuit analyses.

To counter these problems we described a method<sup>1,2</sup> that selects, for each transistor in a circuit, the model of least complexity that will

give acceptable accuracy. At the heart of the method is the capability to assess model adequacy. This capability derives from a self-consistency test in which the values of currents and voltages computed in a simulation of the circuit behavior are compared with onset parameters. By this comparison one determines whether these computer values are consistent with the approximations underlying the device models used in the simulation. The onset parameters for a model are the terminal currents and voltages above or below which the model fails to give a satisfactory representation of device behavior. We set forth the onset parameters for the Ebers-Moll model and discuss their determination by terminal measurement and by calculation based on the transistor makeup. To illustrate the method of model assessment, we simulated the performance of an operational amplifier; the effectiveness of the method in selecting model complexity was demonstrated.

Two invited research papers followed concerning this same subject. The first<sup>3</sup> revised the specification of one of the onset parameters described earlier and assessed the applicability of the method to the simulation of circuit behavior in a radiation environment. The second paper<sup>4</sup> made additional extensions of the method: to accommodate the field-effect transistor, rather than solely the bipolar transistor; and to accommodate the selection of models representing time-varying response, rather than solely static behavior.

The core idea of our method for model selection has been incorporated into one of the most comprehensive computer-aided programs for circuit analysis presently available.<sup>5</sup>

#### REFERENCES (\*indicates support by this contract)

- \*1. F. A. Lindholm and S. W. Director, "Assessing Model Adequacy in Integration Circuits Simulation," 1971 IEEE International Solid State Circuits Conference: Technical Digest, 17 (1971).
  - \*2. F. A. Lindholm, S. W. Director and D. L. Bowler, "Assessing Model Adequacy in Selecting Model Complexity in Integrated-Circuit Simulation," IEEE Journ. Solid State Circuits, SC-6, 213-222 (1971) [invited research paper].
  - \*3. F. A. Lindholm, "Device Characterization for Computer Analysis of Large Circuits," 1971 IEEE Annual Conference on Space and Radiation Effects: Digest, 106 (1971) [invited research paper].
- F. A. Lindholm, "Devices Characterization for Computer Analysis of Large Circuits," IEEE Transactions on Nuclear Science, 18, 206-210 (1971) (invited research paper).

- \*4. F. A. Lindholm, "Generation and Selection of Dynamic Large-Signal Models for Bipolar and Field-Effect Transistors," 1972 International IEEE Symposium on Circuit Theory, 4, 385 (1972) [invited paper].
- 5. H. J. DeMan and R. Mertens, "SITCAP--A Simulator of Bipolar Transistors for Computer-Aided Circuit Analysis Programs," 1973 IEEE Int. Solid State Circuits Conference: Digest, 16, 104 (1973).

## B. ELECTRONIC CERAMICS

### B-1 Introduction

The general objective of the electronic ceramics program sponsored in this research contract was to establish the relative importance of microstructure on the electronic behavior of a potential new generation of electronic materials and to determine the influence of radiation environments on the properties and microstructure of the materials. Two major classes of new electronic materials were selected for investigation; semiconducting glasses and glass-ceramic insulators. Both types of materials had received little systematic investigation of microstructural-properties-irradiation relationships at the outset of our research program. In addition each type of material appeared to have considerable promise for highly radiation resistant components. Glass-ceramics were potentially radiation hard insulators or encapsulants. Semiconducting glasses were promising radiation insensitive resistor elements and showed some potential for active device replacement.

The aim of our research was to establish critical processing conditions and to understand the development of a controlled microstructure in these materials. Following identification of nucleation processes, we established the kinetics of crystallization and other aspects of microstructural evolution with thermal processing. The relationships between thermal processing and microstructure to the electrical conductivity, dielectric properties, mechanical strength and thermal properties was determined. And finally, the effect of fast neutron irradiation, and in some cases gamma irradiation, on the electrical properties of the materials was measured and related to changes in the microstructure of the material.

A total of 32 research publications and four edited books resulted from this research. In addition approximately sixty technical presentations were made at various international, national, and research laboratory meetings throughout this country and abroad. Seven advanced degrees were awarded for research of students involved in this program. Two summer consultantships for the U. S. Army amorphous semiconductor program at Picatinny Arsenal, Physical Sciences Branch were held by Professor L. L. Hench. This research project made it possible for him to introduce through



the summer program a materials processing and microstructural approach to the large amorphous semiconductor program in progress at Picatinny Arsenal.

A summary of the various aspects of the electronic ceramics research sponsored by this project follows with appropriate citations of papers published from the work included.

## B-2 SEMICONDUCTING GLASSES

### B-2.1 Microstructural Effects

The relative importance of thermal treatment and microstructure on the properties of amorphous semiconductors was first reported from research sponsored in this project.<sup>(1-5)</sup> Glasses in the  $V_2O_5-P_2O_5-R_2O$  systems, where  $R_2O$  is any alkali metal oxide, were studied. These papers establish that a cast semiconducting glass will possess electrical properties which are a function of the casting temperature, quench rate, and annealing time. The thermal variables alter a microphase separation in the glass which influences the electronic structure. Variations in electronic structure give rise to alterations in both the DC electrical conductivity and the AC dielectric spectra of the materials. Subsequent thermal treatments after casting result in both a coarsening of the phase separation and the onset of crystallization in the semiconducting glasses. These changes produce very large alterations in the dielectric properties of the semiconducting glasses as a result of the initiation of Maxwell-Wagners-Sillars heterogeneous dielectric losses due to the precipitation of high conductivity crystallites in the low conductivity glassy matrix.

### B-2.2 Irradiation Effects

The first studies of irradiation effects involving bulk amorphous semiconductors were performed in this project.<sup>(1,6-9)</sup> These studies were also of glasses in the  $V_2O_5-P_2O_5-R_2O$  system, where  $R_2O$  is any alkali metal oxide. The research has shown that the exposure of the semiconducting glasses to  $\gamma$ -irradiation increases the electrical conductivity by 10% when fluences in the range of  $2 \times 10^8$  rads are achieved. This effect is apparently due to ionization of the multivalence transition metal ions in the glass. Fast neutron exposures in the range of  $5 \times 10^{16}$  to  $5 \times 10^{17}$  nvt show that bulk semiconducting glasses in the as-cast state are relatively

little affected by fast neutron irradiation. However, semiconducting glasses that have been thermally treated to enhance, or modify, the electrical conductivity are strongly influenced by the fast neutron irradiation. Crystallites precipitated in the glass are disordered by the fast neutron irradiation exposure and the dielectric properties associated with the isolated high conductivity phase are destroyed. The general effect of the fast neutron irradiation is to make thermally treated semiconducting glasses appear more like bulk semiconducting glasses. Application of these results to predicting the radiation resistance of amorphous semiconductor switching devices led to the conclusion of a  $1 \times 10^{17}$  nvt damage threshold.

### B-2.3 Theory

Analysis of microstructural effects on the transport properties of amorphous semiconductors was also examined from a theoretical standpoint in the project. (1-3,10-14) The heterogeneous semiconductor theory evolved from this study has shown that many of the AC characteristics of semiconducting glasses are due to the presence of phase discontinuities in the materials.

A cluster calculation for amorphous solids was also developed. (10-14) The quantum mechanical calculation of the electronic band structure of amorphous solids was done with a CNDO semiempirical model. Clusters as large as 50 plus atoms were evaluated. This investigation has shown that there is only a very small tailing of band states in the forbidden gap even with large degrees of disorder in the solid. Consequently, there is little theoretical basis for the Cohen-Fritzsche-Ovskinsky band model proposed for amorphous semiconductors, which involves an overlap of band states in the middle of the forbidden energy band. The model proposed by Mott is much closer to being consistent with the calculation results obtained.

### B-3 GLASS-CERAMICS

The glass-ceramics research in this project was largely concerned with the  $\text{Li}_2\text{O-SiO}_2$  glass system. This binary glass system is basic to many of the commercial  $\text{Li}_2\text{O-Al}_2\text{O}_3\text{-SiO}_2$  glass-ceramic systems marketed by the glass industry. Consequently, understanding the mechanisms of

nucleation and crystallization, microstructural factors, and irradiation damage in the binary  $\text{Li}_2\text{O-SiO}_2$  system has led to a greater understanding of the behavior of the commercial glass-ceramics. Of even more importance is that the binary glass system is simple enough that it is possible to understand the fundamental mechanisms involved in the development and control of microstructure and the interpretation of the irradiation damage effects.

### B-3.1 Nucleation and Crystallization Kinetics

Identification of a metastable nucleation process in the  $\text{Li}_2\text{O-SiO}_2$  glasses was reported in a series of papers.<sup>(15-20)</sup> A metastable lithium metasilicate phase appears in the very early stages of heat treatment of the glasses. The phase appears as 200Å by 50Å needle-like precipitates in the glass. The metastable phase occurs in very small quantities, in a range of .01 volume percent or less. Identification of this phase required the use of a large number of investigative tools including hot stage transmission electron microscopy, x-ray small angle scattering, quantitative dielectric relaxation, and x-ray diffraction analysis using a Guinier-DeWolff camera. Applying the combination of these specific tools to this problem together in a concerted effort to identify the fundamental nucleation species was the first such effort in the glass literature. The results obtained have helped to clarify many of the more qualitative and less detailed investigations reported by a number of other authors. The results have also been applicable to understanding the mechanisms of nucleation in a number of multicomponent glasses reported.

By identifying the nucleation mechanism it was possible to apply this understanding to controlling the microstructure of crystallized glass-ceramics in the binary  $\text{Li}_2\text{O-SiO}_2$  system without resorting to the addition of heterogeneous nucleating agents. The kinetics of crystallization were measured using both quantitative x-ray diffraction and quantitative optical microscopy methods. Again the confirmation of the kinetics using a variety of tools was the first such effort in the glass-ceramics literature. The results obtained explain a number of the inconsistencies of the activation energies reported for crystallization in this system by other investigators.

### B-3.2 Microstructural Effects on Properties

Having determined the nucleation and crystallization kinetics of the  $\text{Li}_2\text{O-SiO}_2$  glass made it possible to produce a series of  $\text{Li}_2\text{O-SiO}_2$  glass-ceramics with controlled volume fractions and particle sizes of the  $\text{Li}_2\text{Si}_2\text{O}_5$  crystalline phase. The mechanical and dielectric properties of the controlled microstructure glass-ceramics were measured and the data analyzed using quantitative theories of mixing effects of second phases. (21-22) It was shown that a major factor in controlling the strength of glass-ceramics was the development of a dense glassy matrix prior to the crystallization of the bulk of the glass. If the matrix densification does not occur, large interfacial stresses were developed during the crystallization process and cracks resulting from the interfacial stresses markedly reduced the strength of the glass-ceramics. Quantitative microstructural effects on the dielectric properties showed that the properties were markedly changed when the crystallized phase became connected.

In both of these studies the systematic development of a controlled microstructure, the quantitative analysis of that microstructure, and the measurement of its effect on properties were the first such studies reported in the glass-ceramic literature.

### B-3.3 Irradiation Effects

The influence of fast neutron irradiation on nucleation processes in the glass-ceramics were investigated. (7,8,23) These studies showed that the metastable precipitates became disordered when exposed to a neutron fluence of  $1 \times 10^{17}$  nvt or greater. As a result, the relative effectiveness of the nucleation process was decreased. However, we also discovered during the course of this investigation that exposure of the glass to the neutron irradiation resulted in the formation of structural heterogeneities which increased the efficiency of subsequent thermal nucleation treatments.

A major finding in the irradiation investigation is that all crystallites of dielectric solids become progressively disordered as a result of the neutron irradiation. The progressive disordering decreases the electrical conductivity and eliminates progressively the AC dielectric

losses associated with the presence of an isolated second phase. To our knowledge these studies of neutron irradiation effects in glass-ceramics are still the only investigations in this field.

#### B-4 CHARACTERIZATION METHODS

In order to pursue the research topics discussed above it was necessary to develop or extend several analytical tools to serve as characterization methods for glasses and ceramic materials. A general review of a philosophy of characterization was published<sup>(24)</sup> and a book was edited on the subject of quantitative characterization of ceramics during a portion of this project.<sup>(25)</sup>

##### B-4.1 X-ray Methods

Limitations of sample preparation methods on the accuracy of x-ray spectrochemical analysis were examined in order to eliminate this troublesome source of efforts in the analysis of our experimental samples in the research program.<sup>(26)</sup> A major effort was expended in the application of a new type of x-ray powder camera, called the Guinier-DeWolff x-ray diffraction camera.<sup>(27)</sup> This camera was used to determine the volume fraction of very small quantities of second phases in the semiconducting glasses and the glass-ceramics being investigated. This study resulted in the quantitative use of the Guinier cameras which made possible the identification of the nucleation mechanisms and structural changes in the electronic materials being studied.

##### B-4.2 Microscopy

Sample preparation techniques were developed for obtaining measurements of nucleation and crystallization processes of glass-ceramics in the electron microscope. These measurements were done using the hot stage electron microscope which made it possible to see the sequence of the reaction mechanisms operating.<sup>(20)</sup> Possible errors in obtaining quantitative analyses of microstructures in the semiconducting glasses and glass-ceramics were delineated by a study of thickness error effects in optical microscopy.<sup>(28)</sup> This study made it possible to apply mathematical corrections to the quantitative microscopy measurements when needed.

#### B-4.3 Surface Properties

Many electronic materials are processed using powder ceramic techniques. Understanding the surface behavior of these powders is at a primitive stage of evolution at this time. Some of the characterization methods successfully used in other parts of this research project appear to be suitable for understanding surface powder characterization. The potential application of the dielectric and various x-ray techniques and electron microscopy techniques were explored and reported in this project. (29-30)

#### B-4.4 Dielectrics

Dielectric relaxation is especially sensitive to the presence of isolated heterogeneous phases. Consequently, the AC spectra of many of the materials being investigated is strongly influenced by the presence of nucleated and crystallized second phases. This development of quantitative dielectric relaxation as a microstructural analysis tool is one of the major outcomes of the characterization part of this research program. (17,29-32) This tool is now used by a number of investigators throughout the country to understand the early stages of second phase development in exploratory materials.

#### B-5 SILICON DEFECT AND IRRADIATION DAMAGE CALCULATIONS

The computer based cluster calculations developed for understanding the electronic structure and properties of an amorphous semiconductor are also suitable for analyzing the many complicated defect structures possible in crystalline silicon semiconductors. A series of progressively more complex defects were examined in this study, including impurity pairs, impurity-vacancy complexes, and multi-impurity complexes. (33-35) The energy levels associated with the impurities obtained from the cluster calculations correlated extremely well with the literature when literature values were available for comparison. Many defects calculated have been theorized in the literature without any calculational basis for the energy levels reported. Application of this method to understanding various processing problems and irradiation effects in low doped and degenerate silicon semiconductor devices are possible from this research.

## B-6 CONFERENCES AND BOOKS

The first conference on the Physics of Electronic Ceramics was organized and hosted at the University of Florida during the course of this project. The Conference brought together over 150 industrial, university, and government scientists to review the status of theory of electronic ceramics. Two books resulted from the Conference; "Physics of Ceramics," vol. A and "Physics of Ceramics," vol. B. Both were edited by L. L. Hench and D. B. Dove.

A timely book, "Characterization of Ceramics," was edited by L. L. Hench and R. W. Gould during the period of the contract. Many chapters in this book provide guidelines important to the characterization of all types of electronic materials.

Also, during the project an international symposium on nucleation and crystallization in glasses was organized by L. L. Hench for the American Ceramic Society. This led to Special Publication #5 by the ACS titled "Advances in Nucleation and Crystallization in Glasses," L. L. Hench and S. W. Freiman, editors. This volume provides a thorough summary of the major developments in the field of nucleation and crystallization of glasses in the 1960's and early 70's.

These four books constitute a significant library of up-to-date information on physical ceramics and glasses. This research project provided the impetus, motivation, and much of the intensive research climate within the University of Florida electronic materials group required to make the conferences a success and the publications a reality.

## REFERENCES

1. "Semiconducting Glass-Ceramics," L. L. Hench, Int. J. of Non-Crystalline Solids, 1 (1970). Proceedings from SEAS Conf., New York, May 1969, pp. 250-278.
2. "Polaronic Phenomena in Vandia-Phosphate Semiconducting Glass," H. F. Schaaake and L. L. Hench, Int. J. of Non-Crystalline Solids, 1 (1970). Proceedings from SEAS Conf., New York, May 1969, pp. 292-307.
3. "Heterogeneous Semiconducting Glasses," in Physics of Electronic Ceramics, L. L. Hench and D. B. Dove, editors, M. Dekker, Inc., 1971, pp. 197-223.
4. "Dielectric Breakdown of Ceramics," G. Walther and L. L. Hench, in Physics of Electronic Ceramics: Part A, L. L. Hench and D. B. Dove, editors, M. Dekker, Inc., 1971, pp. 539-562.
5. "Electric Properties of Glass," L. L. Hench and H. F. Schaaake, in Introduction to Glass Science, D. Pye and H. Simpson, editors, Plenum Press, New York, N. Y., pp. 583-661.
6. "Irradiation Effects in Semiconducting Glasses," L. L. Hench and G. A. Daughenbaugh, J. Nuclear Materials, 25 (1968) 58-63.
7. "Fast Neutron Effects in Glass-Ceramics and Amorphous Semiconductors," L. L. Hench, W. D. Tuohig and A. E. Clark, Ceramics in Severe Environments Conf., H. Palmour and W. Kreigel, editors, Plenum Press (1971) pp. 575-587.
8. "Irradiation Effects in Heterogeneous Amorphous Semiconductors," L. L. Hench, A. E. Clark and H. F. Schaaake, Int. J. of Non-Crystalline Solids (1972).
9. "Fast Neutron Irradiation Effects on Electrical Properties of  $KPO_3-V_2O_5$  Semiconducting Glass-Ceramics," H. F. Schaaake and L. L. Hench to be submitted to J. Non-Crystalline Solids.
10. "Existence of a Well Defined Band Gap in Amorphous Silicon and Diamond," Appl. Phys. Letters.
11. "Semiempirical Electronic Structure Calculations of Amorphous Diamond and Silicon," H. F. Schaaake and L. L. Hench, to be submitted to J. of Non-Crystalline Solids.
12. "Chemical Bonding in Amorphous Silica and the Effect of Disorder on the Band Gap," H. F. Schaaake and L. L. Hench, to be submitted to J. American Ceramic Society.
13. "Interatomic Force Model for Generating Equilibrium Atomic Positions in Amorphous Solids," J. of Non-Crystalline Solids.
14. "Structure-Property Relations in Amorphous and Defect Semiconductors and Dielectrics," H. F. Schaaake, Dissertation, University of Michigan Microfilms (1972).



15. "Crystallization Kinetics of a Lithia-Silica Glass," S. W. Freiman and L. L. Hench, J. American Ceramic Society, 51 (1968) 382-387.
16. "Further Analysis of Glass Crystallization Kinetics," S. W. Freiman and L. L. Hench, J. American Ceramic Society, 52 (1969) 111.
17. "Effects of a Metastable Precipitate on the Electrical Properties of a  $\text{Li}_2\text{O-SiO}_2$  Glass," D. L. Kinser and L. L. Hench, J. American Ceramic Society, 52 (1968) 445-449.
18. "Electrode Polarization in Alkali-Silicate Glasses," D. L. Kinser and L. L. Hench, J. American Ceramic Society, 52 (1969) 12, p. 638.
19. "The Early Stages of Crystallization of a  $\text{Li}_2\text{O-2SiO}_2$  Glass," L. L. Hench, D. L. Kinser and S. W. Freiman, Phys. Chem. of Glasses, 12 [2] (1971) 58-63.
20. "Hot-Stage Transmission Electron Microscopy of Crystallization of a Lithium Silica Glass," D. L. Kinser and L. L. Hench, J. Materials Sci., 5 (1970) 369.
21. "Mechanical Behavior of a Partially Crystallized  $\text{Li}_2\text{O-SiO}_2$  Glass," S. W. Freiman and L. L. Hench, J. American Ceramic Society, 55 [2] (1972) 86-90.
22. "Effects of Crystallization on  $\text{Li}_2\text{O-2SiO}_2$  Dielectric Properties," W. D. Tuohig and L. L. Hench, submitted to J. American Ceramic Society.
23. "Neutron Effects in Thermally Treated Glasses," W. D. Tuohig and L. L. Hench, J. Nuclear Materials, 31 (1969) 86-92.
24. "Introduction to Characterization of Ceramics," L. L. Hench, in Characterization of Ceramics, L. L. Hench and R. W. Gould, editors, M. Dekker, 1971, pp. 1-8 (NBS review).
25. "Characterization of Ceramics," L. L. Hench and R. W. Gould, editors, M. Dekker, Inc., 1971.
26. "Powder Sample Preparation Errors in X-ray Spectrochemical Analysis," D. E. Clark and L. L. Hench, Norelco Reporter, 17 (1970) 25-29.
27. "Application of Guinier X-ray Cameras in the Analysis of Solid State Reactions," G. J. Scott, D. E. Clark and L. L. Hench, presented 1970 American Ceramic Society Meeting, Philadelphia. Submitted to Bul. American Ceramic Society.
28. "Analysis of Thickness Error in Transmission Microscopy of Ceramics," C. V. Gokularathnam, S. W. Freiman and L. L. Hench, J. American Ceramic Society, 52 (1969) 6.
29. "Characterization of Powder Surfaces," L. L. Hench in Characterization of Ceramics, L. L. Hench and R. W. Gould, editors, M. Dekker, Inc. (1971) pp. 457-505.
30. "A Computer Program for Dielectric Humidity Effects," G. J. Scott and L. L. Hench, A Center for Unconventional Solid State Materials and Devices, Report #9.

31. "Humidity Effects on the Dielectric Properties of Electronic Substrates," L. L. Hench, Electronics Division Meeting of the American Ceramic Society, Boston, September 1969, invited paper. Submitted to J. American Ceramic Society.
32. "Dielectric Relaxation in Materials Analysis," L. L. Hench, Society of Aerospace Materials Process Engineers, 14th Annual Symposium and Exhibition, November 1968, pp. I-2-2 to I-2-18.
33. "Semiempirical Electric Structure Calculations of Clusters of Crystalline Diamond, Silicon, Silicon Carbide, and Silica," H. F. Schaake, L. L. Hench and M. J. Redman, Int. J. of Quantum Chemistry.
34. "Vacancy and Vacancy Complexes in Silicon: Semiempirical Electric Structure Calculations," H. F. Shaake and L. L. Hench.
35. "Semiempirical Electronic Structure Calculations of Boron and Phosphorous Impurities and Impurity Clusters in Silicon," H. F. Shaake and L. L. Hench.

## C. QUANTUM AND ELECTRONIC PROPERTIES OF SEMICONDUCTORS AND RELATED DEVICES

### C-1 Introduction

During the period of contract support, a substantial effort has focussed on the experimental and theoretical studies in semiconductor materials and devices that bear particular interest to DOD applications. These studies include:

- (a) calculation of the diffusivity-mobility ratio and the density of states function for degenerate and nondegenerate semiconductors;
- (b) experimental and theoretical investigation of the recombination and trapping mechanisms of the injected carriers in the defect centers of such semiconductors as silicon, gold-doped silicon, indium-arsenide, chromium-doped gallium arsenide, nickel-doped germanium and indium-doped cadmium-sulfide. Photomagnetoelectric and photoconductive methods have been used extensively to yield values of important parameters such as carrier lifetimes, capture rate and mobilities over a wide temperature range; and
- (c) experimental and theoretical studies of photodetectors. This study resulted in the development of a new grating type silicon Schottky barrier photodiode which shows superior performance characteristics over 0.4-1.06 $\mu$ m spectral range. In addition, it gave a new understanding of the quantum yield of metal-semiconductor photodiodes and p-i-n photodiodes.

As a result of this research effort, twenty-four papers have been published in national and international technical journals and six papers were presented at the national or international conferences.

A summary follows of the most important results.

## C-2 STUDIES OF DIFFUSIVITY-MOBILITY RATIO AND DENSITY OF STATES FUNCTION FOR DEGENERATE SEMICONDUCTORS

### C-2.1 Generalized Einstein Relation<sup>1</sup>

An expression has been derived, formulated in terms of tabulated functions, for a generalized Einstein relation valid for degenerate as well as nondegenerate semiconductors. To facilitate the use of this expression in device design, a graph has been constructed displaying the diffusivity-mobility ratio against carrier concentration; the graph holds for any temperature and for any materials whose density of quantum states varies, to a reasonable approximation, as the square root of energy. Separate curves have been plotted for the special cases of silicon and germanium. For any level of concentration, these curves afford a comparison with the constant value of the diffusivity-mobility ratio predicted by the conventional Einstein relation, and display the error deriving from its misuse.

### C-2.2 Density of States Function for Degenerate Semiconductors<sup>2</sup>

Theoretical calculation of density of quantum states as a function of impurity concentration has been made for silicon and germanium. The result indicates that deviation of the density of states function from conventional theory is negligible for electron energy greater than  $2kT$  above the conduction band edge. However, the tailing effect of density of states function in the forbidden gap becomes eminent for  $N_D \geq 5 \times 10^{19} \text{ cm}^{-3}$  for Si and  $N_D \geq 10^{19} \text{ cm}^{-3}$  for Ge.

## C-3 STUDIES OF RECOMBINATION AND TRAPPING MECHANISMS IN SEMICONDUCTORS BY USING PHOTOMAGNETOELECTRIC (PME) AND PHOTOCONDUCTIVE (PC) METHODS

### C-3.1 Photomagnetoelectric and Photoconductive Effects in Phosphorous-Doped Silicon at Low Temperatures<sup>3</sup>

The PME and the PC effects in phosphorus-doped silicon have been investigated as functions of illumination intensity and magnetic field at  $21.8^\circ\text{K}$  and  $4.2^\circ\text{K}$ . Concurrent measurements of the PME, PC and the Hall effects in this sample yield the ambipolar diffusion length, ambipolar diffusion constant and the carrier lifetimes. Theories for the PME and PC responses are developed for the case of high injection (strong illumination) and arbitrary magnetic field.

The experimental results are found in good agreement with the theoretical predictions. Study of the PME effective lifetime versus the excess carrier densities has been made for this sample. The results indicate that the Shockley-Read recombination model serves adequately for interpreting the observed data. The Quantity,  $\tau_{\infty}$ , as determined from S-R models, is found in excellent agreement with that obtained from PME theory. In addition, it is found that the effect of trapping can be neglected over the whole injection range for this sample.

#### C-3.2 Recombination and Trapping Processes of the Injected Carriers in Gold-Doped Silicon<sup>4</sup>

Steady-state recombination and trapping processes of the injected carriers in gold- and phosphorus-doped silicon have been studied for the case that the doping and temperature range are such that the equilibrium carrier densities are small compared with the impurity density. The fluctuation of the charge in the impurity centers as a result of injection is taken into account in the charge-neutrality condition. The relationship between the injected carriers (electrons and holes) for charge neutrality is established in the form of power laws (i.e.,  $\Delta p = \Gamma \Delta n^{\alpha}$ ) that hold in different ranges of injection. Numerical analyses of  $\Delta p$  versus  $\Delta n$  and  $\tau_n$  versus  $\Delta n$  are presented for the case of n-type silicon overcompensated and undercompensated by the gold impurities.

#### C-3.3 Low-Temperature Photomagnetoelectric Properties of Gold-Doped n-Type Silicon<sup>5</sup>

The photomagnetoelectric (PME) effect was observed between 21 and 84°K in silicon doped with gold and phosphorus. A generalized diffusion equation is formulated and solved with the impurity centers included in the charge-balance equation and arbitrary intensity of steady illumination. When the carrier densities are much smaller than the gold density, the charged impurities maintain charge neutrality, and this results in a range of injection where  $\Delta p = \Gamma_1 \Delta n + \Gamma_2 \Delta n^2$ . If the quadratic term dominates, the PME current is proportional to the  $\frac{4}{3}$  power of the photoconductance. This power law is observed in our measurements, from which we deduce values for effective carrier lifetimes between 36 nsec and 63  $\mu$ sec.

#### C-3.4 Photomagnetoelectric and Photoconductive Effects in n-Type InAs<sup>6</sup>

A study of the photomagnetoelectric (PME) and photoconductive (PC) effects in n-type InAs single crystals has been made between 4.2 and 300°K under small-signal conditions. It was found that for  $T > 77^\circ\text{K}$  the PME open-

circuit voltage is proportional to the magnetic induction, and for  $T > 21^\circ\text{K}$  the PME open-circuit voltage saturates at large magnetic induction, which is in accord with the large-Hall-angle PME theory. Carrier lifetimes were computed from the PME and PC data between 4.2 and  $300^\circ\text{K}$ , and the hole mobility was estimated from the PME data at 21 and  $4.2^\circ\text{K}$ . The observed linear relationship between the PME open-circuit voltage and photoconductance at low light levels manifests that the effect of trapping is essentially nil over the entire temperature range from 4.2 to  $300^\circ\text{K}$ .

### C-3.5 Investigation of the Recombination and Trapping Processes of Photoinjected Carriers in Semi-Insulating Cr-Doped GaAs Using PME and PC Methods<sup>7</sup>

Investigation of the recombination and trapping processes of photoinjected carriers in semi-insulating Cr-doped GaAs ( $\rho \sim 10^8 \Omega \text{ cm}$ ) has been made at 80 and  $300^\circ\text{K}$ , using the photomagnetoelectric (PME) and photoconductive (PC) effects under large-injection conditions. A generalized theory for the PME and PC effects is developed, taking into account the variation of carrier lifetimes with injected-carrier density (i.e.,  $\tau_n = \kappa \Delta n^\beta$ ) and of the trapping of holes in the Cr levels (i.e.,  $\Delta p = \Gamma \Delta n$ ,  $\Gamma < 1$ ), by using a simple recombination and trapping model. The result yields a power-law relationship between the PME short-circuit current and the photoconductance, in a form that  $I_{\text{PME}}$  varies as  $\Delta G^{2/(2+\beta)}$ , valid for different injection ranges. Two well-defined ranges of injection were observed from the present results: In region I (high injection),  $I_{\text{PME}}$  is directly proportional to  $\Delta G$  (i.e.,  $\beta=0$ ), and in region II (intermediate injection),  $I_{\text{PME}}$  varies with  $\Delta G^{1.2}$  (i.e.,  $\beta = -\frac{1}{3}$ ). Numerical values of  $\tau_n$ ,  $\tau_p$ , and  $I_{\text{PME}}$  as functions of  $\Delta G$  are given. The results are in good agreement with the theoretical predictions.

### C-3.6 Determination of Electron and Hole Capture Rates in Nickel-Doped Germanium Using Photomagnetoelectric and Photoconductive Methods<sup>8</sup>

Although room-temperature electron and hole capture rates for nickel atoms in germanium have been previously reported, no conclusive result has as yet been reached. This is due to the fact that carrier capture rates for nickel-doped germanium reported previously were determined mainly from the temperature dependence of lifetimes, which is further complicated and prone to obtain incorrect results when the capture rates become temperature dependent. In this report

we have demonstrated that by including the excess-carrier trapping effect in the theory of photomagnetoelectric (PME) and photoconductance (PC) effects and by elaborately controlling the compensation ratio of nickel and shallow-impurity densities in germanium, we are able to determine accurately three of the four capture rates for nickel atoms in germanium from room-temperature PME and PC measurements. In addition, with the present results, we are able to interpret the previous results consistently at room temperature. The present results are  $C_{n1} = 1.4 \times 10^{-9}$ ,  $C_{n2} = 8 \times 10^{-9}$ , and  $C_{p2} = 4 \times 10^{-8}$  in units of  $\text{cm}^3 \text{sec}^{-1}$  at  $T = 300^\circ\text{K}$ .

#### C-3.7 Electron Mobility and Shallow Impurity Levels in In-Doped and Cu-Doped Cadmium-Sulfide<sup>9</sup>

Electrical conductivity and Hall effect measurements were made between  $300^\circ\text{K}$  and  $4.2^\circ\text{K}$  on In-doped ( $\sim 6 \times 10^{17} \text{cm}^{-3}$ ) CdS single crystals. Normal band conduction was observed between  $300^\circ\text{K}$  and  $20^\circ\text{K}$ , while the impurity hopping conduction in the second shallow donor state ( $E_{D2}$ ), dominated the conduction mechanism for  $T < 20^\circ\text{K}$ . In the normal band conduction region, the best theoretical fit was obtained by using a two-shallow-impurity level model. The result yields  $E_{D1} = 0.033 \text{ eV}$  for In-level with  $N_{D1} = 6 \times 10^{17} \text{cm}^{-3}$  and  $E_{D2} = 0.007 \text{ eV}$  (which is unknown) with  $N_{D2} = 1.3 \times 10^{17} \text{cm}^{-3}$ , assuming  $N_A = 1 \times 10^{17} \text{cm}^{-3}$  and  $m_e = 0.2 m_0$ . The Hall mobility versus temperature was studied for both Cu-doped and In-doped CdS between  $4.2^\circ\text{K}$  and  $300^\circ\text{K}$ . It was found that the longitudinal optical phonons dominate the scattering of electrons for  $T > 200^\circ\text{K}$  and with  $\mu_L \approx 110 [\exp(300 \pm 10)/T - 1] \text{cm}^2/\text{V-sec}$ . A brief discussion of the scattering mechanism for  $T < 100^\circ\text{K}$  is given for both In-doped and Cu-doped CdS.

#### C-3.8 Investigation of Recombination and Trapping Processes in $3\text{As}_2\text{Se}_3-2\text{Sb}_2\text{Se}_3$ Amorphous Films by Photoconductivity Method<sup>10</sup>

Photoconductivity experiment has been performed on high resistivity ( $\rho \approx 10^9 \Omega\text{-cm}$ )  $3\text{As}_2\text{Se}_3-2\text{Sb}_2\text{Se}_3$  amorphous films in the temperature range from  $278^\circ\text{K}$  to  $308^\circ\text{K}$ , as a function of light intensity,  $I_0$ . The results are that at intermediate light levels the photocurrent varies as  $I_0^{0.7}$  and at high light levels the photocurrent is directly proportional to  $I_0$ . A simple recombination and trapping model is formulated to interpret the observed photoconductivity data. From the temperature dependence of the photocurrent, an effective trap level located  $0.3 \text{ eV}$  below the band edge is deduced.

### C-3.9 Radiative Recombination in $O_2$ -Doped N-Type GaAs at Low Temperatures<sup>11</sup>

Band to band radiative recombination in  $O_2$ -doped n-type GaAs has been investigated at 20.8°K and 4.2°K using photomagnetolectric (PME) and photoconductive (PC) methods. Capture rates  $B_r$  determined from the present experimental data are in excellent agreement with that computed from the Hall's direct radiative recombination formula.<sup>4</sup> The results are  $B_r = 1.15 \times 10^{-8} \text{ cm}^3/\text{sec}$  at 20.8°K and  $1.23 \times 10^{-7} \text{ cm}^3/\text{sec}$  at 4.2°K.

### C-4 THEORETICAL AND EXPERIMENTAL STUDIES OF METAL-SEMICONDUCTOR SCHOTTKY-BARRIER AND PME PHOTODETECTORS

#### C-4.1 A New Grating Type Gold-N Type Silicon Schottky Barrier Photodiode<sup>12</sup>

A new grating type Au-nSi Schottky-barrier photodiode has been fabricated and examined. The device is constructed with a new structure of contact mask. The mask forms a grating of gold film over the contacting silicon substrate. The resulting device shows features such as broad bandwidth, high responsivity, high quantum yield and low noise characteristics. Report is given here for the I-V characteristics, the spectral dependence of quantum yield, responsivity, noise performance and the technology used to fabricate such device. Without optimization, the present device shows a bandwidth of ~1GHz, a responsivity of 0.44 A/W at 0.63 $\mu\text{m}$  and 0.63 A/W at  $\lambda = 0.9\mu\text{m}$ .

#### C-4.2 Photodetection Using Photomagnetolectric and Demer Effects in Gold-Doped Silicon<sup>13</sup>

Photodetection in the visible and near IR wavelength region using photomagnetolectric and Demer effects in gold-doped silicon has been demonstrated. Response time  $t_r$  of 0.2  $\mu\text{s}$  and noise equivalent power (NEP) of  $6 \times 10^{-10}$  for a photomagnetolectric (PME) cell, and  $t_r < 0.03 \mu\text{s}$  and NEP =  $2.5 \times 10^{-10}$  for a Demer cell, were obtained from the present results.

#### C-4.3 Quantum Yield of Metal-Semiconductor Photodiodes<sup>14</sup>

A theoretical expression for the quantum yield of metal-semiconductor photodiodes is derived that takes into account the effects of the presence of an inversion region. This expression predicts a sharp decrease of the quantum yield in the short wavelength regime, in contrast with previous theoretical predictions. Applied to a Au-nSi Schottky-barrier photodiode, our theory displays the functional



dependence with which the quantum yield increases with increasing doping densities for short wavelengths and decreases with increasing doping densities for long wavelengths. Excellent agreement is demonstrated between theoretical predictions and experimental data in the short-wavelength regime (i.e., for  $0.4 < \lambda < 0.6 \mu\text{m}$ ).

#### C-4.4 Quantum Yield of P-I-N Photodiodes <sup>15</sup>

An expression for the quantum yield of p-i-n photodiodes is formulated that takes into account the effects of carrier transport and recombination in the p-type diffused layer and consequently describes the decline in the response observed for short wavelength excitation. Applied to a silicon p-i-n photodiode, this expression yields theoretical predictions in excellent agreement with experimental data over the entire spectral range.

#### C-4.5 Analyses of Transient Capacitance Experiments for Au-GaAs Schottky Barrier Diodes in the Presence of Deep Impurities <sup>16</sup>

Transient capacitance experiments have been performed for Au-n type GaAs Schottky barrier diodes between 285 and 316°K. The GaAs substrates are doped with oxygen and chromium respectively. From the transient dark-capacitance and photocapacitance measurements, the thermal emission rate, the doping densities and the thermal activation energies of oxygen and chromium impurities are obtained at  $T = 300^\circ\text{K}$ .

As a continuation of our past efforts our present research activities include: (1) study of the radiation damage in bulk GaAs single crystals by using the methods of photomagnetoelectric and photoconductive effects and the transient capacitance techniques, (2) study of electronic transport and optical properties in In AsP alloy systems, and (3) experimental and theoretical study of infrared photodetectors using InAsP alloys.

#### REFERENCES

1. S. S. Li and F. A. Lindholm, "Alternative Formulation of Generalized Einstein Relation for Degenerate Semiconductors," Proc. of IEEE Lett., Vol. 56, pp. 1256-57 (1968).
2. S. S. Li and J. Agraz, "Density of States in Degenerate Silicon and Germanium," Solid State Electronics, Vol. 12, pp. 505-509 (1969).
3. S. S. Li and C. T. Wang, "Photomagnetoelectric and Photoconductive Effects in n-type Silicon at Low Temperatures," Proc. of the 3rd International Photoconductivity Conference, edited by E. M. Pell, pp. 35-40, Pergamon Press (1971).

- S. S. Li, "Effects of Temperatures, Photoinjection and Magnetic Field on the Photomagnetolectric Response in Phys. Rev., Vol. 199, pp. 1246-51 (1969).
4. J. Agraz and S. S. Li, "Recombination and Trapping Processes of the Photoinjected Carriers in Gold-doped Silicon at Low Temperatures," Phys. Rev. B., Vol. 2, pp. 4966-4971 (1970).
  5. J. Agraz and S. S. Li, "Low Temperature Photomagnetolectric Effects in Gold-doped Silicon," Phys. Rev. B., Vol. 2, pp. 1847-1851 (1970).
  6. S. S. Li and C. I. Huang, "Low Temperature Photomagnetolectric Effects in InAs," Phys. Rev. B., Vol. 4, pp. 4633-4636 (1971).
  7. S. S. Li and C. I. Huang, "Investigation of Recombination and Trapping Processes of Photoinjected Carriers in Semi-insulating Cr-doped GaAs," J. Appl. Phys., 43, pp. 1757-1761 (1972).
  8. H. F. Tseng and S. S. Li, "Determination of Electron and Hole Capture Rates in Ni-doped Germanium Using Photoconductive and Photomagneto-electric Methods," Phys. Rev. B. 15, Vol. 6, pp. 3066-3072 (1972).
  9. S. S. Li and C. I. Huang, "Electron Mobility and Shallow Impurity Levels in In-doped and Cu-doped CdS," Phys. Rev. B., Vol. 3, pp. 3266-3270 (1971).
  10. S. S. Li and P. K. Chaudhari, "Photoconductivity in  $3\text{As}_2\text{Se}_3\text{-}2\text{Sb}_2\text{Se}_3$  Amorphous Films," J. Noncrystalline Solids, Vol. 11(4), pp. 285-292 (1973).
  11. C. I. Huang and S. S. Li, "Study of Radiative Recombination in Oxygen-doped GaAs at Low Temperatures," Physica Status Solidi, accepted (1973).
  12. S. S. Li and C. T. Wang, "A New Grating-type Au-n Si Schottky Barrier Photodiode," Proc. of the 22nd Electronic Components Conference (Washington, D. C.) pp. 105-109 (1972).
- C. T. Wang and S. S. Li, "A New Grating Type Au-nSi Schottky Barrier Photodiode," IEEE Trans. on Electron Devices, accepted (1973).
13. S. S. Li and H. F. Tseng, "A New Fast Solid-State PME Photodetector Using Gold-doped Silicon," Proc. of the 15th Annual Tech. Symp. on S.P.I.E., Anaheim, pp. 517-523 (1970).
  14. S. S. Li, C. T. Wang and F. A. Lindholm, "Quantum Yield of Metal-Semiconductor Photodiodes," J. Appl. Phys., Vol. 43, pp. 4123-4129 (1972).
  15. S. S. Li and F. A. Lindholm, "Quantum Yield of p-i-n Silicon Photodiodes," Physica Status Solidi, Vol. 15, pp. 237-242 (1973).
  16. C. I. Huang and S. S. Li, "Study of Transient Capacitance Measurements in Au-n GaAs Schottky Diodes in the Presence of Deep Impurity Levels," Solid State Electronics, accepted (1973).

#### D. NOISE IN SOLIDS AND IN SOLID-STATE DEVICES

During the five years of contract support, our comprehensive laboratory facilities for the measurement of noise, impedance and complete static and small-signal frequencies characteristics have enabled research that has produced many useful technical findings. As an integral part of our overall efforts here in solid-state electronics, the noise research program has contributed in the following ways:

- (a) As a tool for helping evaluate the quality of newly-developed devices. This capability proved valuable, for example, in the development of the new grating-type Schottky barrier photodiode by Li and Wang, described in Section C.
- (b) As a means to provide insight not obtainable in any other way. For example, study of noise in breakdown diodes leads to a detailed understanding of the conduction mechanisms predominating in reverse-biased silicon pn junctions.
- (c) As a means for corroborating data, reinforcing the results of other types of measurements and of theoretical predictions.
- (d) As a direct measure of the quality of a solid-state device acting as a switch and of its sensitivity as an amplifier or a detector.

Our research program has yielded results in each of these various areas; descriptions of the most important of these follow.

##### D-1 Low Frequency Noise in Bipolar Junction Transistors

D-1.1 This project involved the experimental study<sup>1</sup> of low frequency noise in bipolar junction transistors. In addition to the basic understanding provided by the research, it has, from a practical viewpoint, provided a characterization of the transistor that is useful in the design of integrated amplifiers.<sup>2,3</sup> The major results are: (a) the characterization of burst noise, demonstrating that the source of burst noise in bipolar junction transistors resides predominantly in the

emitter-base depletion region and in the depletion region at the surface of the base region near this junction; (b) the demonstration that the characterization of  $1/f$  noise requires two, rather than one, generators in the equivalent circuit -- one generator associated with the surface near the emitter-base junction and the second with the active base region; (c) the development of a complete equivalent circuit for the low-frequency noise; (d) the explanation of structuring of the low frequency noise spectra observed but previously unexplained.

A theoretical model that describes the burst noise was also developed. This model, based on assuming random occupancy of flaw centers associated with crystallographic defects, explains the characteristics of the burst noise seen in bipolar transistors. In contrast to previous explanations, this new model takes account of the influence of defects at the surface as well as those in the bulk. For many transistors the defects at the surface dominate in determining the observed burst noise. Experimental results on specially fabricated transistors, some of which were gold-doped, compare well with the predicted behavior. From the experimental data one can infer values of some of the material parameters that describe the defects.

#### REFERENCES

1. R. C. Jaeger and A. J. Brodersen, "Low Frequency Noise Sources in Bipolar Junction Transistors," IEEE Trans. Electron Devices, ED-17, 128 (1970).
2. R. C. Jaeger, A. J. Brodersen and E. R. Chenette, "A Superior Low Noise Amplifier," 1970 Int. Solid-State Circuits Conference: Digest, 13, 164 (1970).
3. R. C. Jaeger, A. J. Brodersen and E. R. Chenette, "Noise in Integrated Circuit Transistors," IEEE Journ. Solid State Circuits, SC-5, 63 (1970).
4. K. B. Cook, Jr. and A. J. Brodersen, "Physical Origin of Burst Noise in Transistors," Solid State Electronics, 14, 1237 (1971).

#### D-2 Noise in Phototransistors

This study<sup>1</sup> showed the utility of noise measurements in determining the parameters,  $\beta$  and  $f_T$ , which are crucial in characterizing a phototransistor. For transistors fabricated with only two leads, this capability proves of special value. Detectivity and noise equivalent power were

related, providing a rare example in which the noise characterization of the electrical engineer was joined to the sensitivity measures of the detector specialist.

#### REFERENCES

1. F. H. de la Moneda, E. R. Chenette and A. van der Ziel, "Noise in Phototransistors," IEEE Trans. Electron Devices, ED-18, 340 (1971).

#### D-3 Noise in Bipolar Transistors as a Function of Temperature<sup>1</sup>

We measured the noise in bipolar transistors at room temperature and at the temperature of liquid nitrogen (77°K). At room temperature excellent agreement between theory and experiment prevailed, which the literature abundantly suggests. At 77°K, however, many transistors show excess white noise. Our studies demonstrated that part of this noise arises from generation-recombination processes within the device materials; but the source of some of the excess noise remains unexplained. Research presently under way seeks an understanding of this source.

#### REFERENCES

1. G. A. Roig, E. R. Chenette and A. van der Ziel, "Transistor Noise at Extreme Temperatures," International Colloquium on Noise in Active Semiconductor Devices," Toulouse, France (1971).

#### D-4 Noise in Junction Field-Effect Transistors and in MOS Field-Effect Transistors<sup>1</sup>

This study revealed aspects of the limitations of these devices. From noise and static measurements we showed that leakage occurring in the substrate junction of an MOS field-effect transistor proved to be more degrading to device performance than the gate leakage current of junction field-effect transistors. These results held valid at high temperatures for all applications except those involving extremely low source resistance. The study gave a detailed understanding of the effect of substrate noise current upon device performance.

#### REFERENCES

1. R. S. Hijab and E. R. Chenette, "Field-Effect Transistor Noise at High Temperatures," Region III IEEE Convention (1972).

#### D-5 Noise in Zener and Avalanche Breakdown

In silicon MOS structures, avalanche breakdown occurs in the depletion region separating the electrical channel from the drain contact. Noise measurements demonstrated that only one type of current carrier predominates in causing multiplication.<sup>1</sup> Because secondary minority carriers are collected at the substrate terminal, they do not contribute to the multiplication process.<sup>1</sup>

Our present research concerning the noise properties of breakdown diodes is yielding insight concerning the conduction mechanisms in reverse-silicon pn junctions. Here both electrons and holes share the responsibility for the occurrence of multiplication. Noise measurements reveal the relative contributions of Zener and avalanche currents.

#### REFERENCES

1. C. S. Kim, E. R. Chenette and A. van der Ziel, "Noise in MOS Transistors," International Colloquium on Noise in Active Semiconductor Devices, Toulouse, France (1971).

#### D-6 Effect of Radiation on Noise in Junction Field-Effect Transistors

Damage produced by even moderate radiation tends to affect severely the low-frequency noise performance. Measurement of the noise spectra as a function of temperature yields information concerning energy levels associated with the various defect centers caused by the radiation damage. In our study now under way, we have measured the noise spectra of junction field-effect transistors before and after irradiation in the University of Florida nuclear reactor. Analysis of the data is proceeding, and the insight provided will be described in the next Scientific Report.

#### D-7 Noise in Amorphous Semiconductors<sup>1,2</sup>

The band structure and transport properties of chalcogenide semiconductor materials have attracted interest in recent years, especially, following the announcement of new electronic devices made of these materials. By comprehensive electrical and optical measurements, combined with measurements of noise spectra, we contributed to the understanding of transport in these materials. Data secured both from optical and electrical measurements were consistent with the prediction of a theoretical

model containing a reasonably well-defined energy gap. Noise measurements showed a strong  $1/f$  characteristic, which is expected: lack of structure gives rise to a wide distribution of time constants.

#### REFERENCES

1. P. K. Chaudhari, E. R. Chenette and A. van der Ziel, "Amorphous Semiconducting Films: I. Optical Properties," Journ. Applied Physics, 43, 3145 (1972).
2. P. K. Chaudhari, E. R. Chenette and A. van der Ziel, "Amorphous Semiconducting Films: II. Electrical Properties," Journ. Applied Physics, 43, 3149 (1971).

#### E. MAGNETIC FILMS

Part of the research under this contract was directed at digital memory applications of magnetism, a subject directly relevant to military applications. During the tenure of the contract, the emphasis shifted from an investigation of properties relevant to random-access memory with thin films to topics related to sequentially-accessed memory with circular magnetic domains. There follows a synopsis of the main results.

##### E-1 Thin Films

We were interested in fast switching (reverse) processes, as particularly relevant to memory systems under development elsewhere. At the initiation of the study the physical process was unclear by which fast reversal takes place, due to confusion because of the anomalously high threshold at which the fast performance began. We identified<sup>1</sup> threshold conditions in a consistent way and related them to measurements of dispersion.

An improved technique<sup>2</sup> was developed for the analysis of eddy-current interactions: particularly those interactions between film and stripline arising from a transient trapped-flux torque. By a simple R-C circuit approximation to the magnetic diffusion equation, we took geometrical factors into account.

#### REFERENCES

1. J. K. Watson, "Effect on Magnetic Film Switching of Crystallite Interactions," IEEE Trans. Magnetics, 4, 722 (1968).
2. J. K. Watson and C. T. Leis, "Analog Approximations of Transient Flux Diffusion," INTERMAG Conference paper 21.5, Washington, D. C. (1970); IEEE Trans. Magnetics, 6, 655 (1970); IEEE Trans. Magnetics, 7, 304 (1971).



### III. High Current Regimes in Transistor Collector Regions (D. L. Bowler and F. A. Lindholm)

#### 1. INTRODUCTION

A number of authors have investigated the falloff of transistor  $f_T$  and  $\beta$  arising from high current in the epitaxial collector region. The possibility that these effects are due to base-widening was first suggested by Messenger<sup>1</sup> and first published by Kirk<sup>2</sup>. Beale and Slatter<sup>3</sup> have studied devices which are biased in such a way that they appear, at the terminals, to be in the active region but in which, at high collector currents, the large internal voltage drops lead to saturation of the intrinsic transistor. Clark<sup>4</sup>, and also Hahn<sup>5, 6</sup>, have discussed the dc characteristics of transistors operating in this same mode.

In contrast, van der Ziel and Agouridis<sup>7</sup> have suggested the possibility that multi-dimensional effects are important and have proposed a model incorporating lateral injection. Whittier and Tremere<sup>8</sup> adopted the idea that above some critical current space-charge-limited flow would set in and then, in an extensive experimental study, attempted to determine whether the falloff above that critical current behaved more like the van der Ziel and Agouridis model or more like the Kirk model.

It is difficult to reconcile these various suggestions of the internal phenomena responsible for observed transistor behavior for they appear to be alternative explanations of the same thing. It is the purpose of this paper to demonstrate that they are not, and to suggest a framework within which the factors governing the dominance of one phenomenon relative to another and the consequent implications on the functional dependences of transistor gain and frequency response are revealed.

In particular, we will show that the high current behavior of devices having long, low conductivity epitaxial collectors, depends on the applied collector-to-base voltage. For voltages lower than some critical value the depletion region will collapse as the collector current is increased and at some critical current the device will enter either the saturation or quasi-saturation mode of operation. For voltages higher than the critical value, increasing collector current will cause the depletion region to expand until

the collector is fully depleted (if it was not already so depleted at zero current by the applied bias) after which further increase in the current to some critical value will result in a tendency for space-charge-limited flow to start. To explain currents higher than the critical, some mechanism involving multi-dimensional flow must be invoked. We illustrate the usefulness of these conclusions to the understanding of measured device performance by several examples and consider their implications in device modeling for computer-aided circuit analysis and design.

## 2 . THEORETICAL DEVELOPMENT

We consider a one-dimensional npn transistor in which the uniform collector doping ( $N_{dc}$ ) is much less than the base doping. This assures that the depletion region is essentially all on the collector side of the collector-base junction. We assume that conduction in the undepleted portion of the collector is ohmic and that hole current in the collector is negligible. We begin the discussion by noting that there are two situations of interest. In one, the device voltages and currents are such that the collector is not fully depleted. In the other, the voltages and currents are such that full depletion takes place.

### A. COLLECTOR NOT FULLY DEPLETED

In Figure 1 we show the situation when the collector is not fully depleted. The base-to-collector metallurgical junction is at  $x=0$ , the collector width is  $W_c$ , and  $x_0$  indicates the edge of the depletion region when the collector current is zero. The plane  $x_2$ , which may be greater or smaller than  $x_0$ , indicates the depletion edge in the presence of collector current.

If the collector-to-base voltage,  $V_{cb}$ , is held constant and the collector current is increased, two tendencies will develop. One will tend to cause the edge of the depletion region to expand toward  $W_c$ , the other will tend to cause it to collapse toward  $x=0$ . In the first case, as the collector current increases, the electrons which comprise the current cause a reduction in the net charge in the depletion region and therefore, in order to maintain the applied potential, the depletion region will tend to expand; i.e.  $x_2$  will move toward  $W_c$ . On the other hand, an increasing collector current gives rise to an increasing voltage which the charge in the depletion region must maintain and tends to cause the collapse of the depletion region; i.e.  $x_2$  moves toward  $x=0$ . We wish to determine under what conditions each of

these tendencies will prevail<sup>9</sup>.

#### B. COLLECTOR FULLY DEPLETED

If the tendency of the depletion region to expand dominates, the situation ultimately becomes that shown in Figure 2(a.). Here we show the case in which the collector region is fully depleted, either by the applied  $V_{cb}$  in the absence of current or by some appropriate combination of collector voltage and collector current. Again we assume that  $V_{cb}$  is held constant. As the collector current is increased, the electrons will again cause a reduction in the net charge density in the collector region and this means that in order to support the applied potential the electric field distribution in the collector must change.

We show qualitatively in Figure 2(b) how the electric field behaves under these conditions. The field distribution marked (a) corresponds to the collector current at which the depletion region just extends to  $W_c$ . As the collector current increases above this value, the field distribution changes in such a way as to keep the area under the curve constant since  $V_{cb}$  is assumed constant. This is illustrated by curves (b)-(d). At a sufficiently high value of collector current the electric field at the collector-base junction will become zero as indicated by curve (e). We call the current at which this occurs  $I_{c-hcc}$ , the onset current for phenomena associated with high collector currents. Normally, for the transistor to carry currents larger than this, it would be necessary for space-charge-limited flow to begin. However, in the usual circuit environment where there are resistive loads in the collector, and also in the situation presently under consideration where  $V_{cb}$  is constrained to remain constant, space-charge-limited flow cannot occur<sup>11</sup> so other mechanisms must account for increased currents. We will refer to operation at currents greater than  $I_{c-hcc}$  as operation in the mode associated with space-charge-limited flow.

#### C. OPERATION AT LOW COLLECTOR VOLTAGE

In Figure 3 we illustrate qualitatively common emitter characteristics typical of high voltage epitaxial transistors which have a collector doping substantially lower than the base doping. These characteristics show what has been described as two-region saturation<sup>4</sup>. At the lowest values of  $V_{ce}$  the conductivity of the collector is fully modulated by the injection of minority carriers from the base and the device displays typically low saturation resistance. At somewhat higher values of  $V_{ce}$  the collector conductivity

is not fully modulated and the device is in partial or quasi-saturation.

Hahn<sup>6</sup> has shown that a line drawn through the points on common emitter characteristics at which operation changes from quasi-saturation to active region will be straight and that its slope corresponds to the equilibrium resistance of the undepleted collector. This line is shown as  $I_2$  in Figure 3. When  $V_{cb}$  is greater than  $V_{be}$  we have  $V_{cb} \approx V_{ce}$  and  $I_2$  can be described by

$$I_2 = q N_{dc} \mu_n V_{cb} A_c / W_c \quad (1)$$

where the symbols have their usual meanings. Below this line the transistor is operating in the active region while above it it is operating in full or partial saturation.

Also shown on Figure 3 is the current  $I_1$ . This current is defined as the current that would flow if all the carriers in the epitaxial region moved with saturated velocity. Thus

$$I_1 = q N_{dc} v_s A_c \quad (2)$$

where  $v_s$  is the saturated velocity of the electrons in the collector.

We define a voltage  $V_1$  as the collector-to-base voltage at which  $I_1 = I_2$ . Thus, from (1) and (2) we find

$$V_1 = W_c \frac{v_s}{\mu_n} \quad (3)$$

The ratio of  $v_s$  to  $\mu_n$  is of the order of  $10^4$  volts/cm so the order of magnitude of  $V_1$  is about one volt per micron of epitaxial layer thickness.

Consider operation of the transistor at constant  $V_{cb}$  ( $V_{ce}$ ) less than  $V_1$  along an operating path such as that labeled A in Figure 3. When the collector current is zero, the collector-base junction is reverse biased and a depletion region extends into the epitaxial layer. As the collector current is increased, the reverse bias at the intrinsic junction must decrease until, when the operation crosses  $I_2$ , the intrinsic junction becomes forward biased. Thus as the collector current is increased along A, the depletion region must collapse and give way to injection of minority carriers into the collector at currents greater than  $I_2$ .

An analytic treatment of the dependence of depletion region width on collector current is given in the Appendix. A simple, general result cannot be obtained because of the dependence on electric field of the velocity of electrons moving through the depletion region. We can, however, obtain

analytical results which apply to the limiting cases of constant (saturated) velocity and constant mobility.

In the constant velocity case we find

$$\frac{x_2}{x_0} = \left[ \frac{1 - I_c/I_2}{1 - I_c/I_1} \right]^{1/2} \quad (4)$$

Here,  $x_2$  and  $x_0$  were defined in Figure 1,  $I_1$  and  $I_2$  were defined in (1) and (2), and  $I_c$  is the collector current. We note that (4) is in the same form as Kirk's result.

$I_2$  may be more or less than  $I_1$  depending on the device makeup and applied voltage. If  $I_2$  is less than  $I_1$ ,  $V_{cb}$  will be less than  $V_1$  (c.f. Figure 3), and (4) shows that as the collector current is increased the depletion region will collapse,  $x_2$  finally reaching zero at the critical current  $I_2$ . This confirms the qualitative discussion above. In obtaining (4) we have neglected diffusion current near  $x_2$ ; therefore we do not expect it to be exact there, nor do we expect it to describe the final collapse of the depletion region in detail.

If  $I_2$  is greater than  $I_1$ ,  $V_{cb}$  will be greater than  $V_1$ , and (4) indicates that the depletion region width will increase with increasing collector current,  $x_2$  ultimately reaching  $W_c$ . We discuss this situation further in part D of this section.

In the constant mobility case we obtain in the Appendix the following approximate relationship between the edge of the depletion region and the collector current:

$$\frac{x_2}{x_0}^2 = \left[ 1 - \frac{I_c}{I_2} \right] \left[ 1 + B \frac{I_c}{I_2} \right] \quad (5)$$

for  $I_c < I_2$ .  $B$  is a constant of the order of 0.25 and, like (4), this result neglects diffusion current near  $x_2$ .

Equation (5) shows that as collector current is increased, the depletion region width will decrease, reaching zero when the critical current  $I_2$  is reached. Referring again to Figure 3 we have now shown that in the region of the characteristics to the left of  $V_1$ , increasing the collector current from zero results in the collapse of the depletion region whether constant velocity or constant mobility is assumed. There is no reason to suppose that the behavior would be otherwise when the velocity is between these two extremes and so we assume that collapse of the depletion region is to be

expected when the applied voltage is less than  $V_1$ , which we will hereafter refer to as  $V_{crit}$ .

#### D. OPERATION AT HIGH COLLECTOR VOLTAGES

In Figure 4 we turn our attention to operation at higher values of applied voltage than we have so far considered. We repeat the features shown on Figure 3 and, in addition, now, define the voltage  $V_2$ . This corresponds to the  $V_{cb}$  at which, in the absence of collector current, the epitaxial layer is fully depleted. The value of this voltage is:<sup>12</sup>

$$V_2 = q N_{dc} W_c^2 / 2 \epsilon \epsilon_0. \quad (6)$$

In order to make it possible to consider distinct regions of operation, we restrict our attention to devices for which  $V_2 > V_{crit}$ . This amounts to imposing the following relationship between collector doping and collector geometry:

$$N_{dc} > 1.02 \times 10^{15} / W_c \text{ (microns)} \quad (7)$$

for silicon devices. This is not a severe restriction.

In the preceding analysis we have shown that when the applied bias is greater than  $V_{crit}$  and electrons move through the depletion region at  $v_s$  the depletion region expands rather than collapses. Since  $V_{crit}$  is the applied bias which makes the average field across the collector large enough to cause the drift velocity to approach its saturated value it is reasonable to assume that for biases larger than  $V_{crit}$  this situation will occur. Thus if we consider operation along a path such as B in Figure 4, the depletion region will increase in width as the current is increased until it reaches the end of the epitaxial layer. There will be, then, a locus of currents at which the depletion region has expanded to  $W_c$ . Such a locus is qualitatively illustrated in Figure 4.

For currents higher than these values, the electric field distribution in the collector will change as discussed in part B of this section. We can calculate the current  $I_{c-hcc}$ , at which space-charge-limited flow will attempt to start, from equation (12) of the Appendix using the boundary condition that the electric field must be zero at the collector-base junction. Again, there is analytical difficulty due to the field dependence of the mobility. However, since we have taken the view that for biases above  $V_{crit}$  it is a reasonable assumption that the carrier velocity is  $v_s$ , we make that

assumption and find

$$I_{c-hcc} = qv_s \left[ 2\epsilon\epsilon_o V_{cb}/qW_c^2 + N_{dc} \right] A_c = I_1 + I_2 \left[ \frac{V_{crit}}{V_2} \right]. \quad (8)$$

Calculated values of  $I_{c-hcc}$  are shown on Figure 4 for the case  $V_{crit}/V_2 = 0.25$ .

In the region of the characteristics where the applied voltage is greater than  $V_2$ , the collector is fully depleted in the absence of collector current and, as the current is increased from zero, there is no expansion phase but the process described above sets in at once and (8) again gives  $I_{c-hcc}$ .

### 3. DISCUSSION

The results of the preceding section may be summarized as follows. If the applied potentials are such that operation is below  $V_{crit}$ , the depletion region will collapse with increasing collector current and at a critical current given by (1) will enter full or partial saturation. If the applied voltages put the operating point above  $V_{crit}$ , the depletion region will expand with increasing collector current until it reaches the end of the epitaxial layer, following which further increases in current will result in the onset of the mode associated with space-charge-limited flow.

#### A. INTERPRETATION OF DEVICE PERFORMANCE DATA

To illustrate the usefulness of this description in assessing the behavior of  $\beta$  and  $f_T$ , we show in Figure 5a,b,c results which are typical of measurements of those quantities made on a number of identically processed devices\*. In Figure 5d we show the calculated values of  $V_{crit}$ ,  $I_1$  and  $I_2$  for these devices, as well as the loci of the points at which the measurements were made. The  $\beta$  measurement of Figure 5a was made along path A of Figure 5d and since the collector current has been taken well above the critical current  $I_2$  we would expect to see the falloff that does, in fact, occur. The  $\beta$  measurement of Figure 5b was made along path B of Figure 5d. In this case, the collector current is always well below  $I_2$  and we do not expect any substantial falloff in  $\beta$ . This expectation is confirmed by the measurements. Hower<sup>13</sup> has developed an expression from which one may calculate the  $\beta$  falloff above the critical current. His development is based on a one-dimensional geometry. Points calculated using his approach are shown in Figure 5a and are seen to agree well with the measurements. Thus the  $\beta$  falloff for this device appears to be satisfactorily explained on the basis of one-dimensional effects due to high currents in the collector.

---

\* These devices and the measurements of  $f_T$  were supplied by M. Dickman, Tektronix, Inc., Beaverton, Oregon,

Further confirmation that a one-dimensional analysis suffices for this device is found in the fact that the value of the collector resistance calculated using the emitter mask area agree with the collector resistance determined by Hahn's method described in II,C. Thus emitter and collector areas are substantially the same and there is no suggestion of lateral carrier flow.

Turning now to the data shown in Figure 5c, we observe that  $f_T$  peaks at collector currents of about 50 ma, and has dropped appreciably at currents which are well below the critical current,  $I_2$  for the measurements on path B, and  $I_{c-hcc}$  (which will be greater than  $I_1$ ) for the measurements on path C. Thus we conclude that the  $f_T$  falloff for this device cannot be attributed to the effects of interest here, and other explanations must be sought.

As a second illustration, we refer to the paper by Whittier and Tremere<sup>8</sup>. They interpreted their results to mean that their measurements were made on devices which were operating in what we have called the mode associated with space-charge-limited flow. That is,  $V_{cb}$  was above  $V_{crit}$ , and collector current was above  $I_{c-hcc}$ . They concluded that the  $f_T$  falloff they observed was deminated by lateral injection of the type proposed by van der Ziel and Agouridis<sup>7</sup>.

In Table I we compare, for the devices used by Whittier and Tremere,  $V_{crit}$  as calculated by (3) and the  $V_{cb}$  actually used in their measurements. It will be seen that in almost all cases the voltage or voltages used are well below  $V_{crit}$ . This suggests an alternative interpretation of their data; namely, that their measurements were made almost entirely in the region of operation where falloff of  $f_T$  is due to the collector current exceeding  $I_2$ . One should then expect the falloff to be of the type characterized by Beale and Slatter's<sup>3</sup> one-dimensional analysis, rather than of a type which is to be expected when  $I_{c-hcc}$  is exceeded and multi-dimensional effects must surely be present.

## B. IMPLICATIONS FOR DEVICE MODELING

Emphasis has recently been given to the point that in selecting device models for computer-aided circuit simulation, one should choose from those available the simplest one that will give the required accuracy<sup>11,14</sup>. In the hierarchy of models which are now used, the one-dimensional Ebers-Moll<sup>15</sup> model is the least complex. Also one-dimensional, but incorporating considerably more detail, is the Gummel-Poon<sup>16</sup> model. In it, an approximation to one



multi-dimensional effect is possible through the value assigned to a parameter which is included to characterize emitter crowding. The fullest account of multi-dimensional effects can be taken by using one of the modified forms of the Ebers-Moll model which employ tabulated values of current gain and charge control time constants rather than single numbers<sup>17</sup>.

Our results suggest that if, in a circuit simulation, one determines that a particular device is operating in the quasi-saturation mode, then the one-dimensional Gummel-Poon model will probably give adequate results up to currents and gains typical of usual circuits. On the other hand, if the circuit simulation shows that the device is operating in the region where space-charge-limited flow may be important, then there are certainly multi-dimensional effects entering and it would be necessary to use one of the modified Ebers-Moll models.

## APPENDIX

### BEHAVIOR OF THE DEPLETION REGION EDGE

Referring to Figure 1, we assume that the collector is depleted for  $0 \leq x \leq x_2$  and that for  $x_2 \leq x \leq W_c$  there is ohmic conduction. We write Poisson's equation in the depletion region

$$\frac{d\epsilon}{dx} = \frac{1}{\epsilon\epsilon_0} (qN_{dc} - I_c/v_n A_c) \quad (9)$$

where  $v_n$  is the effective electron velocity, and integrating it obtain an expression for the voltage drop across the depletion region

$$V_{cb'} = - \int_0^{x_2} \epsilon \, dx . \quad (10)$$

The expression for the voltage drop across the undepleted part of the collector is

$$V_r = I_c(W_c - x_2)/qN_{dc}\mu_n A_c . \quad (11)$$

We then make use of the fact that the applied collector-to-base voltage

$$V_{cb} = V_{cb'} + V_r \quad (12)$$

to obtain a solution for  $x_2$ .

#### A. SATURATED VELOCITY CASE

Letting  $v_n = v_s$ , which implies that the diffusion current is everywhere negligible, (9) can be easily integrated subject to the boundary condition that the electric field at  $x_2$  must be the field required by the ohmic conduction in the undepleted region. That is

$$\epsilon_{x=x_2} = - I_c/qN_{dc}\mu_n A_c . \quad (13)$$

From (12) we then obtain

$$\frac{x_2}{x_o} = \left[ \frac{1 - I_c/I_2}{1 - I_c/I_1} \right]^{1/2} \quad (4)$$

which was given in the text.  $I_1$  and  $I_2$  are defined in (1) and (2).

#### B. CONSTANT MOBILITY CASE

Letting  $v_n = \mu_n E$  and proceeding as above, we find that it is not possible to obtain a meaningful solution by using the boundary condition (13). We attribute this problem to the neglect of the diffusion current which may, in this case, be appreciable in the vicinity of  $x_2$ . It is possible, however, to obtain an approximate result.

Instead of (13), we use a general form of boundary condition; namely,

$$\epsilon_{x=x'} = \epsilon' \quad (14)$$

where  $x'$  is an arbitrary point at which the field is  $\epsilon'$ . The result of integrating (9) under this condition and using (12) can be put in the form

$$(x - x')_N = \frac{\epsilon - \epsilon_o}{\epsilon_o} - \frac{I_c}{I_2} \ln \frac{\epsilon/\epsilon_o + I_c/I_2}{\epsilon'/\epsilon_o + I_c/I_2} \quad (15)$$

which relates normalized position to normalized electric field. Here

$$(x-x')_N = (x-x')/1/2 x_o^2/W_C \quad (16a)$$

$$\epsilon_o = V_{cb}/W_C \quad (16b)$$

The boundary condition we would like to match, given by (13), can be written

$$(\epsilon/\epsilon_o)_{x=x_2} = -I_c/I_2 \quad (17)$$

and we are interested in cases for which  $0 \leq I_c/I_2 \leq 1$  (cf. Figure 3). Note that for an npn device, the field in the collector will be negative and will have its maximum magnitude at the collector-base junction.

In Figure 6 we have used (15) to plot normalized electric field vs. normalized position with  $I_c/I_2$  as parameter. The boundary condition (14) chosen for this plot is  $\epsilon'/\epsilon_0 = -2$  at  $x'$ . Since from (17) the lowest possible value of  $\epsilon'/\epsilon_0$  at  $x_2$  is -1, this choice assures that  $x'$  is in the depletion region; i.e. to the left of  $x_2$  in Figure 1. We have also plotted in Figure 6 a line representing the value of the field in the undepleted portion of the collector (i.e. the boundary condition) for the choice  $I_c/I_2 = 0.5$ .

For this value of  $I_c$ , one would expect to get a straightforward graphical solution from the intersection of the line representing the boundary condition when  $I_c/I_2 = 0.5$  and the curve of position vs. electric field for the same value of  $I_c/I_2$  less than that corresponding to the boundary condition will make intersections, whereas those for values of  $I_c/I_2$  equal to or greater than that corresponding to the boundary condition will not. In order to get an approximate result, we make a linear approximation to the family of field-position curves. This assures us of an intersection and allows us to calculate a value of  $x_2$ . The approximation is illustrated by the dotted extension of the curve for  $I_c/I_2 = 0.5$  on the figure.

The form of the linear approximation to the field-position curves is

$$\epsilon/\epsilon_0 = -\epsilon'/\epsilon_0 + \frac{(x-x') N}{1 + B \frac{I_c}{I_2}} \quad (18)$$

where  $B \approx 0.25$ , and exact value depending on  $\epsilon'/\epsilon_0$ . This can be integrated and combined with (12) to obtain the result for  $x_2$

$$(x_2/x_0)^2 = (1 - I_c/I_2) (1 + B I_c/I_2) \quad (19)$$

which was given in the text.

## REFERENCES

1. G. Messenger, "An analysis of switching effects in high power diffused based silicon transistors," presented at the IEEE International Electron Devices Meeting, Washington, D. C., October 1959.
2. C. T. Kirk, Jr., "A theory of transistor cutoff frequency falloff at high current densities," IRE Trans. Electron Devices, vol. ED-9, pp. 164-174, March 1962.
3. J. R. A. Beale and J. A. G. Slatter, "The equivalent circuit of a transistor with a lightly-doped collector operating in saturation," Solid State Electronics, vol. 11, pp. 241-252, 1968.
4. L. E. Clark, "Characteristics of two-region saturation phenomena," IEEE Trans. Electron Devices, vol. ED-16, pp. 113-116, January 1969.
5. L. A. Hahn, "The saturation characteristics of high-voltage transistors," Proc. IEEE, vol. 55, pp. 1384-1388, August 1967.
6. L. A. Hahn, "The effect of collector resistance upon the high current capability of n-p-n transistors," IEEE Trans. Electron Devices, vol. ED-16, pp. 654-656, July 1969.
7. A. van der Ziel and D. Agouridis, "The cutoff frequency falloff in UHF transistors at high currents," Proc. IEEE (letters), vol. 54, pp. 411-412, March 1966.
8. R. J. Whittier and D. A. Tremere, "Current gain and cutoff frequency falloff at high currents," IEEE Trans. Electron Devices, vol. ED-16, pp. 39-57, January 1969.
9. D.L. Bowler and F. A. Lindholm, "High collector current in epitaxial transistors," 1971 IEE International Electron Devices Meeting, Washington, D. C., October 1971.
10. F. A. Lindholm, "Device characterization for computer analysis of large circuits," IEEE Trans, Nuclear Science, vol. NS-18, pp. 206-211, December 1971.
11. F. A. Lindholm, S. W. Director and D. L. Bowler, "Assessing model adequacy and selecting model complexity in integrated-circuit simulation," IEEE J. Solid-State Circuits, vol. SC-6, pp. 213-223, August 1971.
12. J. Lindmayer and C. Y. Wrigley, Fundamentals of Semiconductor Devices. Princeton: Van Nostrand, 1965, pp. 19-22.
13. P. Hower, private communication.
14. F. A. Lindholm and S. W. Director, "Assessing model adequacy in integrated-circuit simulation," 1971 IEEE International Solid-State Circuits Conference: Digest, vol. 17, pp. 42-42, February 1971.

15. J. J. Ebers and J. L. Moll, "Large signal behavior of junction transistors, "Proc. IRE, vol. 42, pp. 1773-1784, December 1954.
16. H. K. Gummel and H. C. Poon, "An integral charge-control model of bipolar transistors, "BSTJ, vol. 49, pp. 827-852, May-June 1970.
17. (a) A. F. Malmberg and F. N. Cornwell, "NET-1 Network Analysis Program LA-3119, "Los Alamos Scientific Laboratory, September 1964.  
  
     (b) L. D. Milliman, W. A. Massena, and R. H. Dickhaut, "CIRCUS, A Digital Computer Program Transient Analysis of Electronic Circuits - User's Guide, "Harry Diamond Laboratories, 346-1, January 1967.  
  
     (c) J. C. Bowers and S. R. Sedore, SCEPTRE: A Computer Program for Circuit and Systems Analysis. Englewood Cliffs: Prentice-Hall, 1971.

#### IV. Quantum Yield of P-I-N Photodiodes (Sheng S. Li and F. A. Lindholm)

##### 1. Introduction

Most previous studies of the spectral dependence of photocurrent and quantum efficiency of silicon photodiodes<sup>1-5</sup> were concerned with the photocurrent and the spectral response of the quantum efficiency for solar cells operating in the photovoltaic mode. The present paper will deal with p-i-n silicon diodes employed as photodetectors.

The operating principles of a p-n junction solar cell and a p-i-n photodetector are different in that the former uses a low resistivity substrate while the latter uses a high resistivity substrate. The maximum power requirement of the solar cell, dictates that the resistivity of silicon substrate be as low as possible<sup>6</sup> to minimize resistive power loss as current is drawn from the device. As a consequence of the low resistivity, the depletion layer is very thin, usually of the order of  $100^{\circ}\text{A}$ . For wavelengths of light of interest, the absorption of radiation takes place over distances large compared to the width of the depletion layer to be separated. The contribution of photocurrent in a solar cell thus comes mainly from both the surface diffused layer and the base region of the p-n diode. The contribution from the depletion layer region is usually neglected.

This contrasts with the behavior of reverse biased p-i-n photodiodes, which are the subject of this paper. Since a p-i-n photodiode operates in the depletion mode so that high speed and sensitivity can be achieved simultaneously, the depletion layer (i.e., the "i" region) for such device is usually very wide, and the contribution of photocurrent is mainly from the "i" region. Therefore, the existing theory for solar cells will not properly describe the spectral response of p-i-n photodetectors.

The analysis of the spectral response for a depletion mode p-n diode was first reported by Gärtner<sup>4</sup> and subsequently by Jordan and Milnes.<sup>5</sup> Gärtner's treatment ignored completely the diffused surface layer; and his result thus failed to predict correctly the shortwave spectral response. Jordan and Milnes focused their attention solely upon the transient photoeffect in diffused p-n junction diodes. Recently, McIntyre<sup>7</sup> and Spriggs et al.<sup>8</sup> calculated and measured the quantum efficiency of

the silicon p-i-n photodiode with special attention given to the behavior at long wavelengths. The magnitude and drop of the quantum efficiency at long wavelengths seems to be well explained by these papers.

Thus expressions for the quantum yield previously derived for a depletion mode photodiode fail to predict correctly the spectral dependence observed in metal-semiconductor and p-i-n photodiodes for short wavelength excitation. The short wavelength regime is defined as pertaining to frequencies of incident photons for which  $\alpha W \gg 1$ , where  $\alpha$  is the absorption coefficient of the semiconductor, and  $W$  is the depletion layer width. For the metal-semiconductor photodiode, Li et al.<sup>9</sup> have recently derived a general expression for the quantum yield that takes into account the effect of an inversion layer near the metal-semiconductor interface. Using this expression, they were able to explain quantitatively the sharp decrease of the quantum yield observed in the short wavelength regime (i.e. UV regime) for the Au-nSi Schottky barrier photodiodes. For the p-i-n photodiode, William<sup>10</sup> has recently reported experimental results taken on several silicon p-i-n photodiodes with different diffused layer widths. His measurements of the spectral dependence of the quantum yield suggest the quantum yield at the short wavelength side of the spectrum depends mainly on the diffused surface layer thickness. But no theory presently exists to explain this dependence.

In this paper, we shall derive a general expression for the quantum yield of a p-i-n photodiode that takes into account the effect of the diffused surface layer thickness. It is demonstrated that for short wavelength photons this component predominates in determining the photocurrent observed at the diode terminals.

The resulting expression is applied to silicon p-i-n photodiodes. Theoretical predictions and experimental data are then compared to demonstrate the accuracy of the predictions over the whole spectral range of interest.



## 2. Derivation of Quantum Yield for a p-i-n Photodiode

Fig. 1 (a) shows a schematic representation of a p-i-n photodiode under reverse bias conditions. The p-type region has thickness  $x_0$  and the intrinsic region has thickness  $W$ , with  $W \gg x_0$ . Let us assume that a monochromatic radiation impinges upon the surface at  $x = 0$ . The rate of generation of photocarriers is given by <sup>11</sup>

$$g(x) = \Phi_0 (1-R) \alpha e^{-\alpha x} \quad (1)$$

as is illustrated by Fig. 1(b). In Eq. (1),  $\Phi_0$  is the photon flux density,  $R$  is the reflection coefficient at the surface of p-region, and  $\alpha$  is the absorption coefficient.

Under steady state conditions, the total photocurrent density  $J_{ph}$  produced by the incident photons is the superposition of electron and hole current components:

$$J_{ph} = J_n + J_p \quad (2)$$

This applies at any plane  $x$  in the photodiode. Thus

$$\begin{aligned} J_{ph} &= J_n(x_0) + J_p(x_0) \\ &= J_n(x_0) + J_p(W) + J_i \end{aligned} \quad (3)$$

where

$$J_i = J_p(x_0) - J_p(W) \quad (4)$$

is the component of hole current density arising from carrier generation in the intrinsic region. To find the functional dependence of the quantum yield  $\eta$ , therefore, we need only express  $J_n(x_0)$ ,  $J_p(W)$ , and  $J_i$  as functions of  $\Phi_0, \alpha$ ,  $W$  and  $x_0$ .

The derivation of these expressions is based on the following assumptions: (1) photoinjection is small in both n-type and p-type regions (i.e.  $\Delta p \ll n_0$  and  $\Delta n \ll p_0$  in the n-type and p-type regions, respectively); (2) reverse-bias is small enough that no avalanche multiplication occurs in the intrinsic region; (3) excess carrier lifetime is extremely short at the illuminated surface so that  $\Delta n(0) = 0$  holds; (4) the excess carrier density at the border of the

intrinsic region is small enough that  $\Delta n(x_0) \approx 0$  holds; (5) the effect of electric field in the diffused layer (i.e., p-region) is neglected; (6) recombination in the depletion region is neglected.

Assumption (3) is valid for most silicon p-n junction photodiodes, since the carrier lifetime near the surface of the diffused layer is usually several orders of magnitude smaller than in the bulk.<sup>2,10</sup> This is due to the fact that the surface impurity concentration of the diffused layer is normally several orders of magnitude higher than that in the bulk. As a result of this high impurity concentration, the surface lifetime is expected to be much shorter than in the bulk. Thus carriers generated near the surface will recombine before they are able to diffuse toward the junction.

For completeness, a rigorous treatment which includes the effect of electric field and arbitrary surface recombination velocity in the diffused layer is given in the Appendix. However, the simplified model described above gives agreement within ten percent between the present theory and the experimental data reported for Si p-i-n photodiodes.

We shall consider separately the three regions that contribute to the photocurrent, as follows:

(1) p-type region ( $0 < x < x_0$ )

In this region the contribution to the photocurrent is mainly due to the electron diffusion current directed toward the intrinsic region near  $x = x_0$ . The component is obtained by solving the continuity equation

$$D_n \frac{\partial^2 \Delta n}{\partial x^2} - \frac{\Delta n}{\tau_n} = -\phi_0 (1-R) \alpha e^{-\alpha x} \quad (5)$$

The general solution of Eq. (5) can be written as

$$\Delta n = A \sinh\left(\frac{x_0 - x}{L_n}\right) + B \cosh\left(\frac{x_0 - x}{L_n}\right) - \frac{\phi_0 \alpha (1-R) \tau_n}{(\alpha^2 L_n^2 - 1)} e^{-\alpha x} \quad (6)$$

The constants A and B in Eq. (6) are determined from the boundary conditions that  $\Delta n = 0$  at  $x = 0$  and  $\Delta n \neq 0$  at  $x = x_0$ . Thus

$$A = \frac{\phi_0 \alpha (1-R) \tau_n}{(\alpha^2 L_n^2 - 1) \sinh\left(\frac{x_0}{L_n}\right)} [1 - \cosh\left(\frac{x_0}{L_n}\right) e^{-\alpha x_0}] \quad (7)$$

$$B = \frac{\phi_0 \alpha (1-R) \tau_n}{(\alpha^2 L_n^2 - 1)} e^{-\alpha x_0} \quad (8)$$

The electron diffusion current density at  $x = x_0$ , which consists of electrons directed toward the intrinsic region, is obtained by solving Eqs. (6) - (8) under the assumption  $\alpha L_n \gg 1$ . This procedure yields

$$\begin{aligned} J_n(x_0) &= q D_n \left. \frac{\partial \Delta n}{\partial x} \right|_{x=x_0} \\ &= q \phi_0 (1-R) \left[ e^{-\alpha x_0} - \frac{1}{\alpha L_n \sinh\left(\frac{x_0}{L_n}\right)} (1 - \cosh\left(\frac{x_0}{L_n}\right) e^{-\alpha x_0}) \right] \quad (9) \end{aligned}$$

which shows the functional dependence of  $J_n(x_0)$  on the absorption coefficient  $\alpha$  and thickness of p-type region  $x_0$ .

(ii) intrinsic region ( $x_0 < x < W$ )

The drift current density produced by carriers generated in this region is given by:<sup>1</sup>

$$J_i = q \int_{x_0}^{W+x_0} g(x) dx$$

$$= q\phi_0 (1-R) (e^{-\alpha W} - e^{-\alpha x_0}) \quad (10)$$

where we have assumed that  $W \gg x_0$ , so that  $W + x_0 \approx W$ .

(iii) n-type region, ( $x > W$ )

In this region, holes, the minority carriers, flow mainly by diffusion toward the reverse bias junction. Thus the pertinent continuity equation is

$$D_p \frac{\partial^2 \Delta p}{\partial x^2} - \frac{\Delta p}{\tau_p} = -\phi_0 (1-R) \alpha e^{-\alpha x} \quad (11)$$

where  $D_p$  and  $\tau_p$  denote the hole diffusion constant and lifetime, respectively. From the solution of this equation, one finds that<sup>1</sup>

$$J_p(W) = -(q\phi_0)(1-R) \frac{\alpha L_p}{(1+\alpha L_p)} e^{-\alpha W} \quad (12)$$

From Eqs. (9), (10) and (12), we obtain the total photo-current density

$$J_{ph} = q\phi_0 (1-R) \left[ -\left(\frac{1}{\alpha L_n}\right) (1 - \cosh\left(\frac{x_0}{L_n}\right) e^{-\alpha x_0}) \frac{1}{\sinh\left(\frac{x_0}{L_n}\right)} + \frac{e^{-\alpha W}}{(1+\alpha L_p)} \right] \quad (13)$$

and the quantum yield

$$\eta = \left| \frac{J_{ph}}{q\phi_0} \right| = (1-R) \left[ \left( \frac{1}{\alpha L_n \sinh\left(\frac{x_0}{L_n}\right)} \right) (1 - \cosh\left(\frac{x_0}{L_n}\right) e^{-\alpha x_0}) - \frac{e^{-\alpha W}}{(1+\alpha L_p)} \right] \quad (14)$$

which reduces to Gärtner's expression of  $\eta$  if  $x_0$  and  $R$  are set equal zero.

We shall now use Eq. (14) to compute the quantum yield of a silicon p-i-n photodiode, and compare the results with experimental data.

### 3. Results and Discussions

For a practical silicon p-i-n photodiode, the p-type region is usually very thin (of the order of one micron) and the intrinsic region (depletion region) is relatively wide. Thus, as Fig. 1(b) implies, the absorption of short wavelength photons gives rise to the generation of excess carriers confined mainly within the p-type material.

In calculating the quantum yield for silicon p-i-n photodiodes, we use the data for the absorption coefficient of silicon given by Dash and Newman<sup>12</sup> and the carrier diffusion length deduced from the lifetime data of silicon given by Ross and Madigan.<sup>13</sup> Fig. 2 shows the quantum yield versus photon wavelength for silicon p-i-n photodiodes with the depletion layer width  $W$  as a parameter and with  $x_0 = 1.5 \mu\text{m}$ . The solid lines are the results calculated from Eq. (14) with  $W = 0.32, 0.08, 0.04$  and  $0.01$  cm respectively, and the dash lines are the published data given by Melchior et.al.<sup>14</sup> The reflection coefficient,  $R$ , for silicon has been assumed constant and equal to 0.3 for the present calculation.<sup>15</sup>

The sharp decrease of the quantum yield on the short wavelength side of the spectrum can be explained as follows. The carriers generated by photons of short wavelength appear mainly in the p-type region, as implied by Eq. (5) and Fig. 1(b). Thus the photocurrent resulting from short wavelength excitation must come mainly from carriers generated in the p-type region. However, only near the plane  $x = x_0$  does diffusion direct electrons toward the intrinsic region. Thus only a small fraction of the carriers generated by short wavelength photons in the p-type region will contribute to the photocurrent  $J_n(x)_0$ . The resulting photoresponse contrasts with the predictions of Gärtner<sup>4</sup> that the quantum yield is unity in the short wavelength regime. The functional dependence of quantum yield is displayed by Eq. (9).

To test further the adequacy of the present theory, we measured the quantum yield of an HP 5082-4207 silicon p-i-n photodiode, and compared the result with our theoretical computation; the results are shown in Fig. 3. Again excellent agreement is obtained.

To see the relationship borne between thickness  $x_0$  of the p-type region and quantum yield, we computed the quantum yield versus photon wavelength for  $W = 0.01$  cm, and  $x_0 = 0.4, 0.8$  and  $1.2 \mu\text{m}$ , respectively, using material constants appropriate for silicon p-i-n photodiodes. The result, displayed in Figure 4, shows that quantum yield will increase with decreasing  $x_0$  in the short wavelength regime. This dependence is in harmony with the measured spectral response of silicon p-i-n photodiodes reported by William.<sup>10</sup>

Two points deserve emphasis. First our study reveals that over the whole optical spectrum the quantum yield of a silicon p-i-n photodiode can be improved by simultaneously increasing depletion layer width  $W$  and decreasing the junction depth  $x_0$ . This is consistent with experimental observations of the quantum yield of silicon p-i-n photodiodes. Second, we have shown quantitatively how the drop in quantum yield occurring on the short wavelength side of the spectrum depends upon the diffusion layer thickness.

## Appendix

### Spectral Response in p-type Surface Region: General treatment

The continuity equation for the p-region in the steady state is

$$\frac{1}{e} \frac{dJ_n}{dx} + \frac{\Delta n}{\tau_n} = \alpha \phi_o (1-R) e^{-\alpha x} \quad (\text{A.1})$$

where  $\Delta n = n - n_p$  with  $n_p$  denoting the electron density in thermal equilibrium.  
The electron current density is

$$J_n = eD_n \frac{dn}{dx} + e\mu_n n \epsilon \quad (\text{A.2})$$

where  $\mu_n$  is the electron mobility which is related to the diffusion coefficient by  $\mu_n = (\frac{e}{kT})D_n$ ;  $\epsilon$  is the built-in electric field in the p-type region. Substituting  $J_n$  given by (A.2) into (A.1) and approximating  $\epsilon$  by a suitable constant, we obtain

$$\frac{d^2 \Delta n}{dx^2} - \left(\frac{\epsilon}{\epsilon_c}\right) \frac{1}{L_n} \frac{d\Delta n}{dx} - \frac{\Delta n}{L_n^2} = \frac{-\alpha \phi_o (1-R) e^{-\alpha x}}{D_n} \quad (\text{A.3})$$

where  $\epsilon_c = \left(\frac{kT}{e}\right) \frac{1}{L_n}$  is defined as the critical field.

The general solution of Eq. (A.3) has the form:

$$\Delta n = A_1 e^{-x/L_1} + A_2 e^{-x/L_2} + C e^{-\alpha x} \quad (\text{A.4})$$

where  $C = -\frac{\alpha \phi_o (1-R) \tau_n}{(\alpha^2 L_n^2 + \alpha L_n |\frac{\epsilon}{\epsilon_c}| - 1)}$ , as determined from the particular solution of Eq. (A.3), (A.5)

$A_1$  and  $A_2$  are constants to be determined from the boundary conditions at  $x = 0$  and  $x = x_o$ .

$$\frac{1}{L_{1,2}} = \frac{1}{2L_n} \left[ \left| \frac{\epsilon}{\epsilon_c} \right| \pm \sqrt{\left| \frac{\epsilon}{\epsilon_c} \right|^2 + 4} \right] \quad (\text{A.6})$$

The boundary conditions at  $x = 0$ , the surface, is given by

$$D_n (d\Delta n/dx) = \Delta n (\mu_n \epsilon + s) \quad (A.7)$$

and, at  $x = x_0$ , the junction,

$$n = n_p \approx 0 \quad (A.8)$$

where  $s$  is the surface recombination velocity.

Before applying boundary conditions (A.7) and (A.8) in determining constants  $A_1$  and  $A_2$  from (A.4) it is noted that for practical diffused p-n junction silicon diodes, the electric field in the p-region,  $|\epsilon|$ , is usually quite high (i.e.  $\epsilon \gtrsim 2000 \text{ V/cm}$ )<sup>2</sup>, and  $|\epsilon_c|$  at room temperature is less than a few V/cm. Thus  $\left| \frac{\epsilon}{\epsilon_c} \right| \gg 1$ , and (A.6) reduces to  $\frac{1}{L_1} = \frac{1}{L_n} \left| \frac{\epsilon}{\epsilon_c} \right|$  and  $\frac{1}{L_2} = 0$ .

Combining Eqs. (A.4) through (A.9), we obtain constants  $A_1$  and  $A_2$ :

$$\begin{aligned} A_1 &= C \left[ \left( \frac{1}{L_1} + \frac{s}{D_n} \right) e^{-\alpha x_0} - \left( \alpha + \frac{1}{L_1} + \frac{s}{D_n} \right) \right] / \left[ \left( \frac{2}{L_1} + \frac{s}{D_n} \right) - \left( \frac{1}{L_1} + \frac{s}{D_n} \right) e^{-x_0/L_1} \right] \\ &= C m_1 \end{aligned} \quad (A.10)$$

$$\begin{aligned} A_2 &= C \left[ \left( \frac{2}{L_1} + \frac{s}{D_n} \right) e^{-\alpha x_0} - \left( \alpha + \frac{1}{L_1} + \frac{s}{D_n} \right) e^{-x_0/L_1} \right] / \left[ \left( \frac{1}{L_1} + \frac{s}{D_n} \right) e^{-x_0/L_1} \right. \\ &\quad \left. - \left( \frac{2}{L_1} + \frac{s}{D_n} \right) \right] \\ &= C m_2 \end{aligned} \quad (A.11)$$

where  $C$  is given by Eq. (A.5), and  $m_1$  and  $m_2$  are constants representing bracket in (A.10) and (A.11).

To obtain the short-circuit photocurrent in the p-region, we use Eqs. (A.2) and A.8) and evaluate  $J_n$  at  $x = x_0$  which gives

$$\begin{aligned} J_n(x) &= q D_n \left. \frac{dn}{dx} \right|_{x_0} \\ &= -q D_n C \left[ \frac{m_1}{L_1} e^{-x_0/L_1} + \alpha e^{-\alpha x_0} \right] \end{aligned} \quad (A.12)$$

The quantum yield in the p-region is thus given by



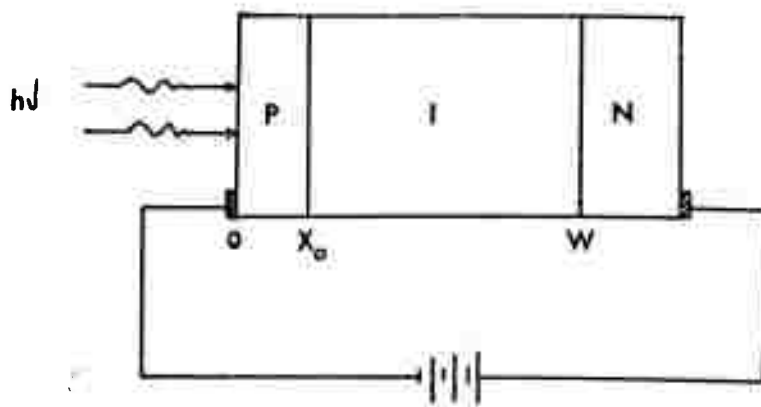
$$\eta_n = \left| \frac{J_n(x_o)}{q\phi_o} \right|$$

$$= \frac{\alpha^2 L_n^2 (1-R)}{[\alpha^2 L_n^2 + L_n \left| \frac{\epsilon}{\epsilon_c} \right| - 1]} \left[ \frac{m_1}{\alpha L_1} e^{-x_o/L_1} + e^{-\alpha x_o} \right] \quad (A.13)$$

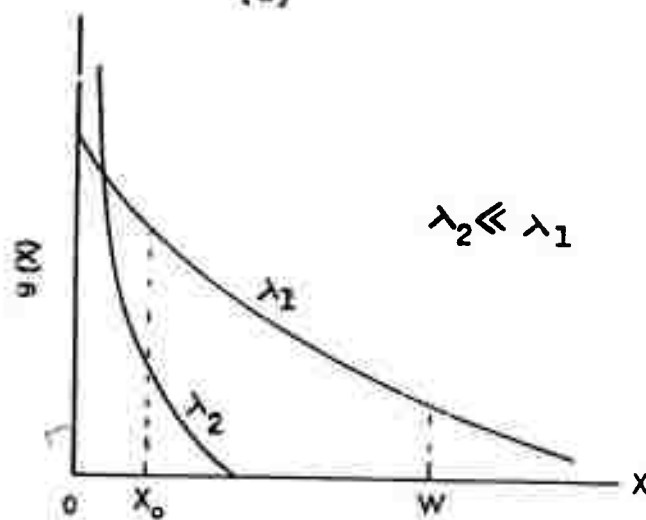
Eq. (A.13) is the general expression for the quantum yield in the p-region taking into account the effect of the surface recombination and the built-in electric field in this region.

## References

1. J. J. Loferski and J. J. Wysocki, RCA Review, p. 38-56, March (1961).
2. B. Dale and F. P. Smith, J. Appl. Phys., Vol. 32, 1377-1381 (1961).
3. M. Wolf, Proc. IEEE, p. 674-693, May (1963).
4. W. W. Gartner, Phys. Rev., Vol. 116, p. 84 (1959).
5. A. G. Jordan and A. G. Milnes, IRE Trans. Elect. Devices, p. 242-251, Oct. (1960).
6. E. S. Rittner, "Electron Processes in Photoconductors," Photoconductivity Conference, edited by R. G. Breckenridge (John Wiley and Sons, Inc.,) New York, 1956), p. 245.
7. McIntyre et al., Conf. on Preparation and Control of Electron Mat., Boston (1966).
8. Sprigings et al., Int. Electron Devices Meeting, Wash, Oct. (1968).
9. S. S. Li, F. A. Lindholm and C. T. Wang, J. Appl. Phys., Oct. (1972)
10. R. L. Williams, J. Optical Soc. America, Vol. 52, 1237 (1962).
11. See, for example, R. A. Smith, "Semiconductors," p. 304, Cambridge Press (1960).
12. W. C. Dash and R. Newman, "Absorption Data in Silicon and Germanium," Phys. Rev., Vol. 99, p. 1151 (1955).
13. B. Ross and J. R. Madigan, "Carrier Lifetime in Silicons," Phys. Rev., Vol. 108, p. 1428 (1957).
14. H. Melchior, M. B. Fisher and F. R. Arams, "Photodetectors for Optical Communication Systems," Proc. IEEE, Vol. 58, p. 1466 (1971).
15. See reference 3, p. 191.



(a)



(b)

- Fig. 1(a) Schematic representation of a p-i-n photodiode under reverse biased condition. Light is impinging upon the p-type region of the diode.
- (b) Spatial dependence of the photocarrier generation rate;  $\lambda_1$  denotes long wavelength photons and  $\lambda_2$  short wavelength photons.

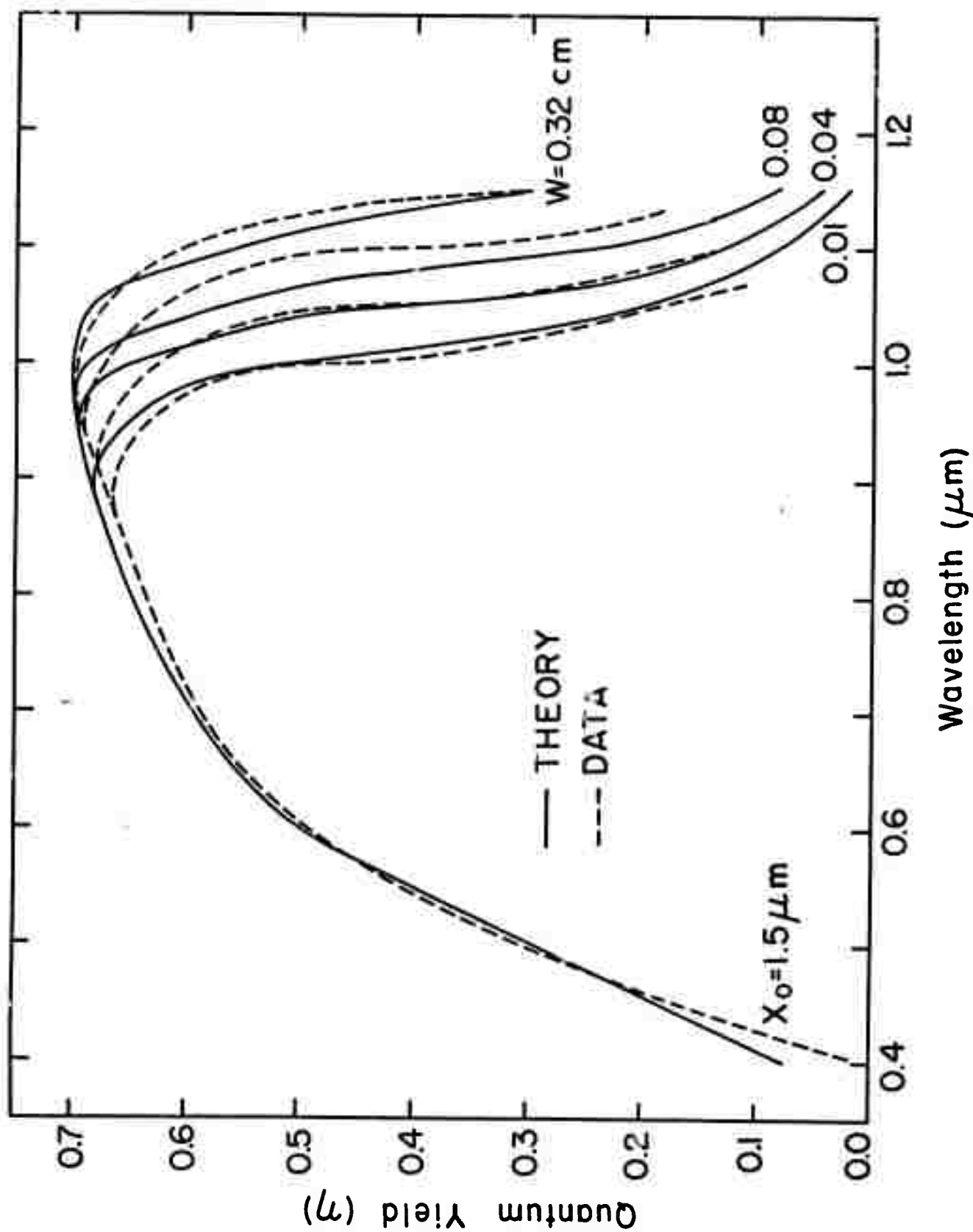


Fig. 2 The quantum yield versus photon wavelength for different depletion layer widths. The solid lines are computed from (14) and the dashed lines are from reference 6 for silicon p-i-n photodiodes. We have assumed the reflection coefficient  $R = 0.3$ .

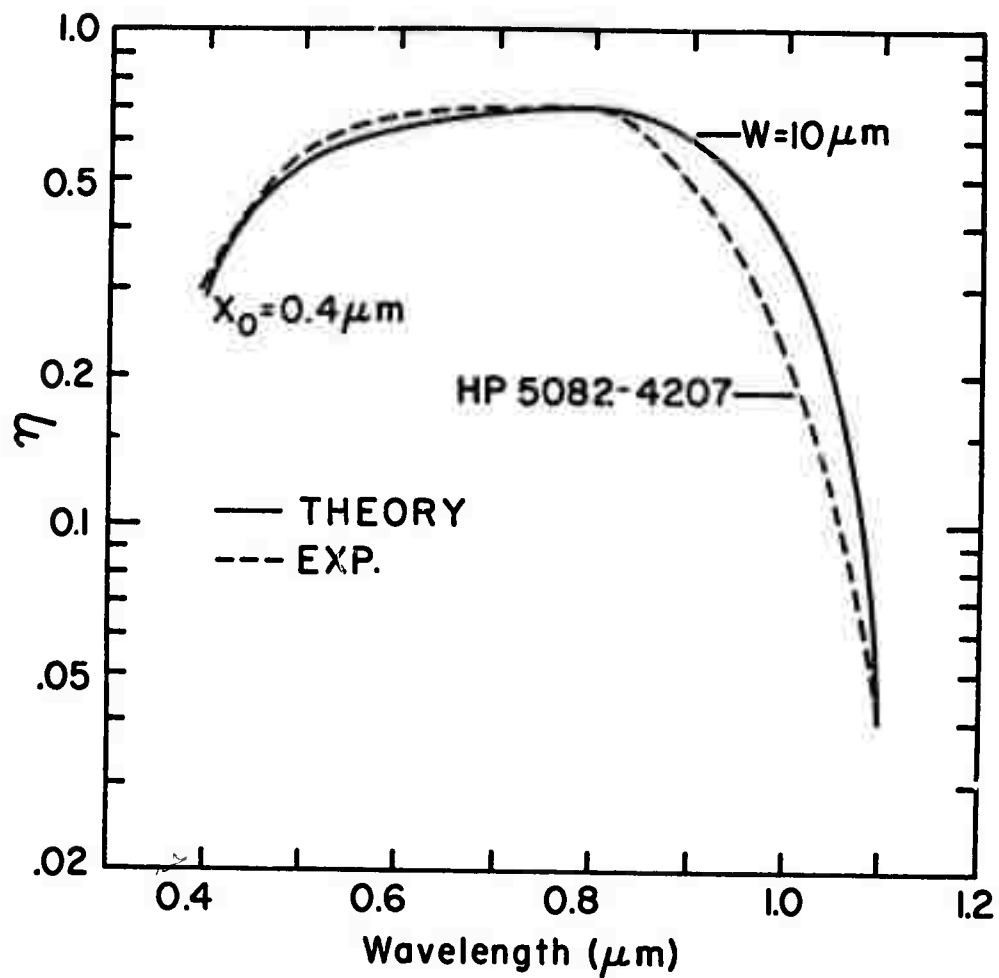


Fig. 3 The quantum yield versus photon wavelength for  $x_0 = 0.4 \mu\text{m}$  and for  $W = 10 \mu\text{m}$ . The solid line was calculated from Eq. (14) and the dashed line displays measured values for an HP 5082-4207 silicon p-i-n photodiode.

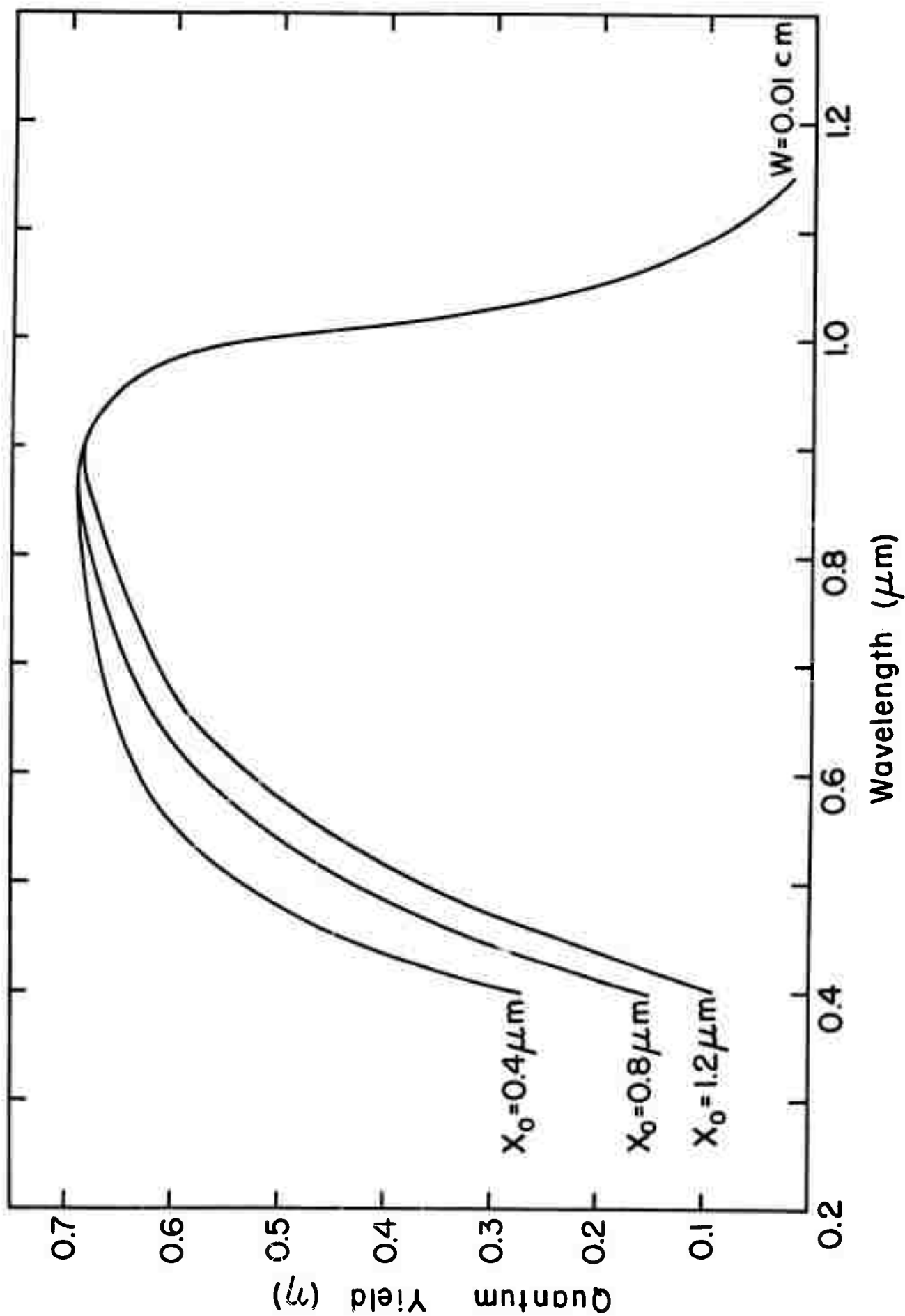


Fig. 4 The quantum yield versus photon wavelength for different values of  $x_0$  and for  $W = 0.01 \text{ cm}$  for silicon p-i-n photodiodes.

## V. Cluster Model Calculations of Silicon Defects (H. F. Schaake and L. L. Hench)

### Introduction

That the properties of a material are determined by the positions and types of the atoms in it has been known virtually since atomic theory was first enunciated. In two areas, the problem of a periodic solid and the problem of a molecule, substantial progress has been made in recent years in developing tractable theories from which all the properties of the material may be calculated. These theories have had a profound influence on progress in these areas; for example, the entire semiconductor technology has been built upon band theory.

A large number of problems do not fall into either of these two areas; these problems are collectively known as the defect solid state. Some of these problems have been successfully treated using perturbation techniques and the band theory of periodic solids. However, when the basic solid deviates greatly from a periodic structure, such as in an amorphous solid, or when the defect cannot be treated as a perturbation, such as a vacancy, calculational methods have not been available.

A logical starting point for the solution of defect solid state problems is from either of the two existing frameworks;

i.e., band theory or molecular theory. In a band theoretic approach, a suitably small number of atoms encompassing the defect and its surroundings would be taken as the unit cell of a solid; periodic boundary conditions would repeat this cell throughout all space. In the molecular approach, a suitably small number of atoms encompassing the defect is treated as a large molecule.

In this work, we report on the development of a molecular approach to the determination of the properties of defect solids. In the first section the basic method is developed (a modification to the semi-empirical CNDO/2 method)<sup>(1-4)</sup> and justified using crystalline defect-free clusters. In the second section, the method is applied to defects in silicon which result from radiation damage; i.e., impurity-vacancy complexes. In the third section, the method is applied to a study of amorphous SiO<sub>2</sub> clusters.

### Molecular Cluster Method

The Schrodinger equation for a system of  $n$  electrons in the potential field of  $n'$  nuclei is

$$H\Psi = E\Psi \quad (1)$$

where the Hamiltonian  $H$  is given by (in atomic units\*)

$$H = \sum_{i=1}^n -\frac{\nabla_i^2}{2} - \sum_{A=1}^{n'} \sum_{i=1}^n \frac{Z_A}{r_{iA}} + \sum_{j>i}^n \sum_{i=1}^n \frac{1}{r_{ij}} ;$$

$$r_{ij} = |\vec{r}_i - \vec{r}_j| \quad (2)$$

---

\*Note: Atomic units are generally used in atomic calculations. This system is defined by  $\hbar = h/2\pi = m = e = 1$ . Distances are measured in Bohr radii (i.e., the radius of the hydrogen atom): 1 Bohr radii = 0.529 Å. Energies are measured in Hartrees: 1 Hartree = 27.21 eV = 2 Rydbergs.



The first term of the Hamiltonian is the kinetic energy of the electrons, the second the potential energy of the electrons in the field of the nuclei, and the third term the potential energy of the interaction of the electrons with each other. The wavefunctions  $\Psi$  have the following restrictions placed on them.

Normality -

$$\int \Psi^* \Psi d^3\vec{r}_1 d^3\vec{r}_2 \dots d^3\vec{r}_n = 1 \quad (3a)$$

and antisymmetry -

$$\Psi(\dots \vec{r}_j, \vec{r}_{j+1} \dots) = -\Psi(\dots \vec{r}_{j+1}, \vec{r}_j \dots) \quad (3b)$$

In the following, no attempt will be made to derive the equations used in the calculations. These derivations are abundantly available in the literature. Particularly clear discussions are given in references 4 and 5.

#### A. Closed-shell Systems

In general, the form of  $\Psi$  is extremely complex. However, an adequate approximation for many problems is to consider the simplest analytic form satisfying equations (3a) and (3b) above, i.e., a single determinant of one-electron wavefunctions:

$$\Psi = \frac{1}{\sqrt{N!}} \begin{vmatrix} \psi_1(\vec{r}_1) & \psi_1(\vec{r}_2) & \psi_1(\vec{r}_3) & \dots \\ \psi_2(\vec{r}_1) & \psi_2(\vec{r}_2) & \psi_2(\vec{r}_3) & \dots \\ \psi_3(\vec{r}_1) & \psi_3(\vec{r}_2) & \psi_3(\vec{r}_3) & \dots \\ \vdots & \vdots & \vdots & \ddots \end{vmatrix} \quad (4)$$

The one-electron functions which best fit equations (1) and (2) (i.e., which give the lowest energy  $E$ ), provided that there are an equal number of electrons of opposite spins, are the solutions to the Hartree-Fock equations:

$$F\psi_i = \epsilon_i \psi_i \quad i = 1, \dots, n \quad (5)$$

where the Fock operator  $F$  is defined as

$$F = [H^{\text{core}} + \sum_j^n (2J_j - K_j)] \quad (5a)$$

with the core Hamiltonian

$$H^{\text{core}} = \sum_{\rho} - \frac{1}{2} \nabla_{\rho}^2 - \sum_A^{n'} \frac{Z_A}{r_{\rho A}} \quad (5b)$$

being the energy of an electron in the bare nucleus; the Coulomb operator

$$J_j(\vec{r}_1) = \int \psi_j^*(\vec{r}_2) \frac{1}{r_{12}} \psi_j(\vec{r}_2) d^3\vec{r}_2 \quad (5c)$$

is the repulsion energy between an electron at  $\vec{r}_1$  and an electron in the state  $\psi_j$ , while the exchange operator is defined as

$$K_j(\vec{r}_1)\psi_i(\vec{r}_1) = [\int \psi_j^*(\vec{r}_2) \frac{1}{r_{12}} \psi_i(\vec{r}_2) d^3\vec{r}_2] \psi_j(\vec{r}_1) \quad (5d)$$

and arises from the Pauli exclusion principle requiring the wavefunction  $\Psi$  to be antisymmetric under interchange of coordinates (3b).

The solution to these equations is also very complex, and they have been treated only for extremely simple molecules. An alternative formulation of the problem is to expand the one-electron wavefunctions in a convenient set of basis functions, the most convenient being atomic orbitals,  $\phi_{\mu}$

$$\psi_i(\vec{r}_1) = \sum_{k=1}^{n'} c_{\mu i} \phi_{\mu}(\vec{r}_1 - \vec{R}_k)$$

Since the AO's are fully specified, only the coefficients  $c_{\mu i}$  need be determined. For the lowest energy  $E$  in equation (1), the  $c_{\mu i}$  are the solutions to the Hartree-Fock-Roothaan<sup>(7)</sup> equations:

$$\sum_{\nu} (F_{\mu\nu} - \epsilon_i S_{\mu\nu}) c_{\nu i} = 0 \quad i = 1, \dots, n \quad (6)$$

where the Fock matrix is given by

$$F_{\mu\nu} = H_{\mu\nu}^{\text{core}} + \sum_{\lambda\sigma} P_{\lambda\sigma} (\mu\nu|\lambda\sigma) - \frac{1}{2}(\mu\lambda|\nu\sigma) \quad (6a)$$

with the core Hamiltonian matrix

$$H_{\mu\nu}^{\text{core}} = \int \phi_{\mu}(\vec{r}_1) \left( -\frac{1}{2} \nabla_1^2 - \sum_A \frac{Z_A}{r_{1A}} \right) \phi_{\nu}(\vec{r}_1) d^3\vec{r}_1 \quad (6b)$$

the density matrix

$$P_{\lambda\sigma} = 2 \sum_i^n c_{\lambda i} c_{\sigma i} \quad (6c)$$

the AO two-electron integrals

$$(\mu\nu|\lambda\sigma) = \iint \phi_{\mu}(\vec{r}_1) \phi_{\nu}(\vec{r}_2) \frac{1}{r_{12}} \phi_{\lambda}(\vec{r}_1) \phi_{\sigma}(\vec{r}_2) d^3\vec{r}_1 d^3\vec{r}_2 \quad (6d)$$

and the overlap integral matrix

$$S_{\mu\nu} = \int \phi_{\mu}(\vec{r}_1) \phi_{\nu}(\vec{r}_1) d^3\vec{r}_1 \quad (6e)$$

These equations are algebraic equations of the third order in  $c_{\mu i}$  and are completely equivalent to the Hartree-Fock equations provided the basis set  $\phi_{\mu}$  is complete. They may be solved by the following iterative procedure: assume a set of  $c_{\mu i}$ ; find  $P_{\lambda\sigma}$  and thus  $F_{\mu\nu}$ ; solve equations (6) for a new set of  $c_{\mu i}$ ; etc., until the new set of  $c_{\mu i}$  differs little from the old set. Such a solution is called a self-consistent field solution. It is most usual to iterate until the total electronic energy  $E$  changes by a small amount. The total electronic energy is given by

$$\begin{aligned} E &= 2 \sum_i^n H_{ii}^{\text{core}} + \sum_i^n \sum_j^n (2J_{ij} - K_{ij}) \\ &= \sum_{\mu\lambda} P_{\mu\lambda} H_{\mu\nu} + \frac{1}{2} \sum_{\mu\nu\lambda\sigma} P_{\mu\nu} P_{\lambda\sigma} [(\mu\nu|\lambda\sigma) - \frac{1}{2} (\mu\lambda|\nu\sigma)] \quad (7) \end{aligned}$$

with the Coulomb exchange and are Hamiltonian integrals

$$J_{ij} = \sum_{\mu\lambda\nu\sigma} c_{\mu i} c_{\lambda j} c_{\nu i} c_{\sigma j} (\mu\nu|\lambda\sigma)$$

$$K_{ij} = \sum_{\mu\lambda\nu\sigma} c_{\mu i} c_{\lambda j} c_{\nu i} c_{\sigma j} (\mu\lambda | \nu\sigma) \quad (9)$$

$$H_{ii}^{\text{core}} = \sum_{\mu\nu} c_{\mu i} c_{\nu i} H_{\mu\nu}^{\text{core}} \quad (10)$$

The total energy of the system relative to the ion cores and free valence electrons is given by

$$E_{\text{Total}} = E + \sum_{A>B} \sum Z_A Z_B R_{AB}^{-1} \quad (11)$$

i.e., the electronic energy plus the core repulsion potential energy.

The resulting one-electron wavefunctions  $\psi_i$  are known as molecular orbitals. (Note that in these equations Greek subscripts refer to AO's, while the Arabic subscripts always refer to MO's!)

The one-electron eigenvalues  $\epsilon_i$  correspond roughly to the energy required to remove an electron in the state  $i$  from the molecule (Koopman's theorem).<sup>(8)</sup> They are given by

$$\epsilon_i = H_{ii}^{\text{core}} + \sum_j^n (2J_{ij} - K_{ij}) \quad i = 1, \dots, n \quad (12)$$

If the basis set contains  $m > n$  orbitals, then, in addition to the  $n$  occupied orbitals, there will be  $(m-n)$  unoccupied orbitals known as virtual orbitals. These correspond to states in which an additional "test" electron is added to the molecule, and hence not exactly to excited states. The energies of the virtual orbitals may be corrected to yield approximate excitation energies, as follows.

The ground-state electronic configuration is given as

$$\psi_1^2 \psi_2^2 \psi_3^2 \dots \psi_n^2$$

i.e., one in which each of the lowest lying orbitals are occupied by one electron with spin  $\alpha$ , and one with spin  $\beta$ . If we look at an excited configuration

$$\psi_1^2 \psi_2^2 \psi_3^2 \dots \psi_n \psi_{n+1}$$

there are four ways of coupling the spins:  $\alpha\alpha$ ,  $\beta\beta$ ,  $\alpha\beta$  and  $\beta\alpha$ . These configurations give rise to magnetic quantum numbers  $M_s = 1, -1, 0$  and  $0$ , respectively. The first two and a combination of the second two belong to a triplet state,  $S = 1$ ,  $M_s = 1, 0, -1$ , while the remaining combination of the second two belong to a singlet state  $S = 0$ ,  $M_s = 0$ . The energy of the triplet state above the ground state may be calculated directly from the excited configuration  $\alpha\alpha$ .

$$\Delta E_T = \epsilon_\ell - \epsilon_n - J_{\ell n} \quad \ell > n \quad (13)$$

The coulomb integral arises since an electron has been removed from molecular orbital  $n$  and therefore  $J_{\ell n}$  should appear only once in equation (12). The exchange integral  $K_{\ell n}$  in equation (12) is correct, since the electron remaining in orbital  $n$  and the electron in orbital  $\ell$  have the same spin, and therefore have an exchange interaction.

The energy of the configurations  $\alpha\beta$  or  $\beta\alpha$  above the ground state will be given by

$$\Delta E_C = \epsilon_\ell - \epsilon_n - J_{\ell n} + K_{\ell n} \quad \ell > n \quad (14)$$

The coulomb integral arises as before since an electron has been removed from state  $n$ . The exchange term  $K_{\ell n}$  should not appear in equation (12) for this configuration, since the electrons in states  $\ell$  and  $n$  have opposite spin and hence no exchange interaction. This term is removed by adding  $K_{\ell n}$  in equation (14). The sum of the configurational energies for  $\alpha\beta$  and  $\beta\alpha$  will be equal to the sum of the singlet and triplet energies; hence for the singlet state

$$\begin{aligned} \Delta E_S &= 2\Delta E_C - \Delta E_T \\ &= \epsilon_\ell - \epsilon_n - J_{\ell n} + 2K_{\ell n} \quad \ell > n \end{aligned} \quad (15)$$

Note that since both  $J$  and  $K$  are positive, the singlet state has a higher energy than the triplet state, in accordance with Hund's rule. (9)

### 1. Open Shell Systems

In the foregoing it was assumed that in the ground state each orbital is occupied by two electrons of opposite spin. In a large number of problems, such as impurity states in semiconductors, dangling bonds in amorphous semiconductors, and magnetically ordered materials, this is not the case. In these cases, since the number of electrons with  $\alpha$  spin is not equal to the number of electrons with  $\beta$  spin (we shall consider  $n_\alpha > n_\beta$ ), the wavefunctions for  $\alpha$  states will differ from the wavefunctions for  $\beta$  states.

For the ground state, the Hartree-Fock Roothan equations become

$$\sum_{\nu} (F_{\mu\nu}^{\alpha} - \epsilon_i^{\alpha} S_{\mu\nu}) c_{\nu i}^{\alpha} = 0 \quad (16a)$$

$$\sum_{\nu} (F_{\mu\nu}^{\beta} - \epsilon_i^{\beta} S_{\mu\nu}) c_{\nu i}^{\beta} = 0 \quad (16b)$$

where the Fock matrices are given by

$$F_{\mu\nu}^{\alpha} = H_{\mu\nu}^{\text{core}} + \sum_{\lambda\sigma} [P_{\lambda\sigma}(\mu\nu|\lambda\sigma) - P_{\lambda\sigma}^{\alpha}(\mu\sigma|\lambda\nu)] \quad (17)$$

and a similar matrix for  $\beta$ . These equations are solved in a manner similar to the closed shell system: An initial guess is made for  $F_{\mu\nu}^{\alpha}$  and  $F_{\mu\nu}^{\beta}$ ; equations (16) are solved for new coefficients  $c_{\nu i}^{\alpha}$  and  $c_{\nu i}^{\beta}$ , and so on until self-consistency is obtained.

The eigenvalues are given by

$$\epsilon_i^{\alpha} = H_{ii}^{\alpha} + \sum_{\alpha}^{n_{\alpha}} (J_{ij}^{\alpha} - K_{ij}^{\alpha}) + \sum_{\beta}^{n_{\beta}} J_{ij}^{\alpha\beta} \quad (18)$$

while the total electronic energy is given by

$$\begin{aligned}
\epsilon = & \sum_i^{n_\alpha} H_{ii}^{\alpha\text{core}} + \sum_j^{n_\beta} H_{ij}^\beta + \frac{1}{2} \left( \sum_i^{n_\alpha} \sum_j^{n_\beta} J_{ij}^{\alpha\alpha} \right. \\
& + \sum_i^{n_\beta} \sum_j^{n_\beta} J_{ij}^{\beta\beta} + \sum_i^{n_\alpha} \sum_j^{n_\beta} J_{ij}^{\alpha\beta} + \sum_i^{n_\beta} \sum_j^{n_\alpha} J_{ij}^{\beta\alpha} \\
& \left. - \sum_i^{n_\alpha} \sum_j^{n_\alpha} K_{ij}^{\alpha\alpha} - \sum_i^{n_\beta} \sum_j^{n_\beta} K_{ij}^{\beta\beta} \right)
\end{aligned} \tag{19}$$

The number of electrons in the system is equal to  $n_\alpha + n_\beta$ . The difference between these two occupation numbers may be specified in terms of the multiplicity:

$$\text{Multiplicity} = 2S+1 \tag{20a}$$

$$n_\alpha - n_\beta = \text{Multiplicity} - 1 \tag{20b}$$

Excited states for the open shell calculations will be given by

$$\Delta E_{\ell n} = \epsilon_\ell - \epsilon_n + J_{\ell n} - K_{\ell n} \quad \ell > n \tag{21}$$

if the initial orbital  $n$  and final orbital  $\ell$  have the same spin, and

$$\Delta E_{\ell n} = \epsilon_\ell - \epsilon_n + J_{\ell n} \quad \ell > n \tag{22}$$

if they have different spins.

## 2. Further Comments on Excited States

The way in which we treat excited states is approximate. This problem may be illustrated most strongly by considering a closed shell system to be calculated by the open shell method. In such a calculation, the multiplicity=1, and therefore  $n_\alpha = n_\beta$ . Under these circumstances, the two Fock matrices will be identical at self-consistency,  $\epsilon_i^\alpha = \epsilon_i^\beta$ , and the two sets of eigenvectors  $c_{vi}$  will be identical. Yet we will not get the singlet

and triplet excitations as derived in the closed shell section. The problem lies in treating the molecular orbitals as the states of the systems rather than configurations. Thus, in the problem under consideration there will be two identical excited configurations,  $\alpha\beta$  and  $\beta\alpha$ . These configurations interact (i.e.,  $\langle\psi^{\alpha\beta}|H|\psi^{\beta\alpha}\rangle \neq 0$ ), resulting in a splitting of the levels into a singlet state and a component of the triplet state. The mathematical process is known as a configuration interaction and a simple form of it was used to derive the singlet and triplet levels in the closed shell section.

The use of configuration interaction changes the Hartree-Fock approximation. The single determinantal approximation to the many electron state function ignores correlation which results from the fact that the charge on the electrons cause them to repel each other, and hence the probability of finding two electrons close together is less than finding them far apart. Letting the electrons correlate their motion reduces the energy. Correlations may be introduced into the many body wavefunctions by adding other single-determinant wavefunctions in an amount to minimize the total electronic energy.

A convenient way of generating these additional determinants is to consider excited configurations having the proper multiplicity. Thus, each additional determinant has one row replaced. Both the ground state and the excited state levels are improved. In fact, since the excited wavefunctions correspond to the cluster with an extra electron and hence are too diffuse, the excited energy levels will be improved more by a configuration interaction than by the ground state.

### 3. Semiempirical Approximations

The above framework is a theory in which calculations at the ab initio level can and have been carried out. The disadvantage of such a procedure is the large number of integrals which must be evaluated, many numerically, and the size of the basis set which must be used, as all electrons are considered



in the calculation. Such a procedure is time consuming, and even for small clusters makes extensive demands on computer storage. Since during the course of study of a defect problem, many defect clusters must be considered, the cost of ab initio calculations makes them unattractive.

A potential way around this quandry is to adopt semi-empirical techniques. That is, rather than attempt to evaluate every integral and use a large basis set, many of the integrals which are difficult to evaluate and which are known to be small are discarded, others are evaluated from empirical data, and the basis set is generally limited to the valence atomic orbitals. Such an approach definitely has its shortcomings; to name two: 1) a particular set of assumptions may work well on one cluster, but fail miserably on another, and 2) a set of assumptions may be adjusted to give good properties of one type and strongly mispredict another. On the other hand, the very nature of the way in which defect solid state problems must be studied, that is, calculations must be made on a large number of similar clusters, each one differing only slightly from another, suggests that a semiempirical technique which basically follows the framework of an ab initio calculation may successfully predict differences between clusters once the parameterization has been adjusted to put the property of interest in the right ball park. This is the approach taken in this work, and the remainder of this section, as well as other sections indicates that this is a not unreasonable assumption.

A wide variety of semiempirical techniques have been developed in the past thirty years. However, one that fits our requirements for a theory which follows the framework of an ab initio calculation and which has been successfully applied to a large range of molecular problems is the CNDO/2 method of Pople, Senter and Segal,<sup>(1-4)</sup> and is the theory which we have adopted. For a full account of the development of the approximations and the parameterization, the reader is referred to

the references cited above; here, we shall merely enumerate the approximations made in the CNDO/2 method.

(1) Complete Neglect of Differential Overlap (CNDO). All two-electron atomic orbital integrals are set equal to zero except for those of the type  $(\mu\mu|\lambda\lambda)$ . These integrals are further reduced to one per pair of atoms (or per atom):  $(\mu\mu|\lambda\lambda) = \gamma_{AB}\phi_\mu$  on A,  $\phi_\lambda$  on B.

(2) Replacing the overlap matrix with the identity in the Hartree-Fock-Roothaan equations, and neglecting overlap in normalizing the molecular orbitals.

(3) The diagonal elements of the core Hamiltonians are approximated as

$$H_{\mu\mu}^{\text{core}} = -\frac{1}{2} (I_\mu + A_\mu) + \sum_B Z_B \gamma_{AB} \quad \phi_\mu \text{ on A.}$$

$I_\mu$  is the ionization potential for orbital  $\mu$  on atom A.

$A_\mu$  is the electron affinity for orbital  $\mu$  on atom A.

$Z_B$  is the core charge (atom-valence electrons) of atom B.

(4) Off diagonal elements of the core Hamiltonian are set equal to

$$H_{\mu\nu}^{\text{core}} = \beta_{AB} S_{\mu\nu} \quad \phi_\mu \text{ on A, } \phi_\nu \text{ on B.}$$

where  $\beta_{AB} = \frac{1}{2} (\beta_A^\circ + \beta_B^\circ)$

unless either A or B (or both) are second row elements, whence

$$\beta_{AB} = \frac{3}{8} (\beta_A^\circ + \beta_B^\circ)$$

$\beta_A^\circ$  and  $\beta_B^\circ$  are empirical parameters adjusted to give good results.

(5)  $\gamma_{AB} = \langle nS_A nS_A | r_{12}^{-1} | nS_B nS_B \rangle$ , where  $nS_A$  is the valence S orbital of atom A, and  $nS_B$  the valence S orbital of atom B.

For hydrogen, the valence basis set consists of one S orbital; for first-row elements one S and three p orbitals, and for second-row elements one S, three p and five d orbitals. All orbitals are Slater-type orbitals (STO) for calculation simplicity.

Using these approximations, the Fock matrix may be written as

$$F_{\mu\mu} = -\frac{1}{2} (I_{\mu} + A_{\mu}) + (P_{AA} - \frac{1}{2} P_{\mu\mu}) \gamma_{AA} + \sum_{B \neq A} (P_{BB} \gamma_{AB} - Z_B \gamma_{AB}) \quad (23a)$$

$$F_{\mu\nu} = \frac{1}{2} K_{AB} (\beta_A^{\circ} + \beta_B^{\circ}) S_{\mu\nu} - \frac{1}{2} P_{\mu\nu} \gamma_{AB} \quad \mu \neq \nu \quad (23b)$$

$K_{AB} = 1$  or  $3/4$  as explained in (4);  $\phi_{\mu}$  is on atom A,  $\phi_{\nu}$  on atom B;  $P_{AA} = \sum_{\lambda \text{ on A}} P_{\lambda\lambda}$ .

The self-consistency is started by an initial Huckel-type approximation by placing  $\gamma_{AA} = \gamma_{AB} = 0$  for all atoms. This initial Fock matrix is diagonalized, a density matrix constructed, the total electronic energy found, a new Fock matrix generated (from now on  $\gamma_{AB}, \gamma_{AA}$  have their calculated values), etc., until the energy changes by less than a predetermined amount. This procedure may be executed by the program listed in the Appendix.\* The extension to open shells is straightforward and will not be considered here. The program in the Appendix will also perform open shell calculations.

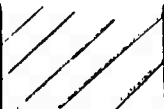
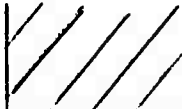


#### 4. Cluster Boundary Conditions

Early in this investigation it was found that a cluster of 17 carbon atoms in a crystalline arrangement did not have a well-defined energy gap -- levels were spread throughout a rather wide range. This problem resulted from the fact that the coordination was improper; instead of a coordination of four, the surface atoms had a coordination of one. The result is an extremely large concentration of "dangling bonds" -- a

\*Available upon request from the Dept. of Materials Science and Engineering, University of Florida, Gainesville, Florida 32601, c/o L. L. Hench.

feature not typical of the solid. This problem has apparently been recognized by several other workers<sup>(10-13)</sup> who have derived several ways around them: saturating the surface with hydrogen, imposing periodic boundary conditions or partial periodic boundary conditions, or immersing the cluster in a potential well. These boundary conditions have various weaknesses. The surface hydrogen atoms, while resulting in a physically plausible molecule, introduce a new chemical species into the system, and under certain circumstances, the surface requires two hydrogen atoms to be separated by about 1 Angstrom, a much smaller distance than found in any molecule. Additionally, the 17 atom carbon cluster requires 36 surface hydrogens for saturation, resulting in the C-H and H-H interactions assuming an extremely important role in determining the electronic structure. Periodic boundary conditions are perhaps the best conditions since the cluster is then surrounded by an array of atoms similar to that which is found in the solid. However, the geometrical constraints placed on the cluster in order to have translational periodicity are rather severe, and generally require a large number of atoms.

An alternative approach may be formulated by considering the problem of the surface in terms of the Fock matrix. Consider first the cluster embedded in the solid surrounded by all of the other atoms in the solid. The Fock matrix will contain off diagonal elements between all orbitals. If a transformation can be found which minimizes off-diagonal elements between orbitals on atoms designated as surface atoms of the cluster, and orbitals on atoms outside the cluster, then the Fock matrix can be reduced to the following form:

	0	
0	$F_{\text{cluster}}$	0
	0	

Under these circumstances, the cluster Fock matrix is separated from the remainder of the total Fock matrix and may be diagonalized by itself to yield the behavior of the wavefunctions within the cluster. Such a transformation is in general impossible in ionic and covalent materials; however, a transformation to hybridized surface orbitals comes surprisingly close.

First of all, it should be realized that, in typical solids, the magnitude of off-diagonal density matrix elements,  $P_{\mu\nu}$ , are one to two orders of magnitude smaller for orbitals on second neighbor atoms than for orbitals on nearest neighbor atoms. Furthermore, the magnitude of these elements decreases very rapidly as the atoms to which the orbitals are attached increase further. If the basis is transformed to a hybridized basis, the overlap integrals are substantially larger for nearest neighbor atoms than for more distant neighbors. In diamond, for example, with an  $sp^3$  hybrid basis, the overlap integral with the nearest neighbor atom to which the hybrid is oriented is 0.94, to other nearest neighbor atoms, 0.01, and to second neighbor atoms, 0.15. This means that in a hybridized basis there is one large off-diagonal element, and the rest are fairly small.

This transformation to a hybrid basis then approximately satisfies the requirements set forth previously, and we can anticipate fairly good results if we terminate the Fock matrix, keeping orbitals with large off-diagonal elements; i.e., the hybridized orbitals on the surface atoms which are oriented toward the interior atoms of the cluster.

The use of surface hybrids has a firm intuitive base. Chemical saturation of the system is maintained by placing an atom with one (or more) hybrids on the surface. The hybrid forms a bond with an interior atom, but since there are no hybrids oriented to the exterior of the cluster, there are no "dangling bonds." This approach requires that we add an electron for every hybrid, and that in order to maintain charge

neutrality (i.e., in a purely covalent structure, the charge on an ion is 0) the core charge must also be set equal to the number of hybrids. This approach will work with Column IV elements of the periodic table, C and Si, which normally have tetrahedral coordination and  $sp^3$  hybridization. Only these elements have been used for surface hybrids in this work.

The program in the Appendix is capable of performing calculations as described above. Only surface atoms are hybridized, leading to a mixed basis set. The diagonal portion of the core Hamiltonian must be entered externally -- for an  $sp^3$  hybrid it has the value  $(\frac{1}{4}H_{ss}^{core} + \frac{3}{4}H_{pp}^{core})$ .

## 5. Parameterization for Energy Level Diagrams

While the CNDO/2 method leads to good values for bond lengths and charge distributions in molecules, it is known to predict a value for the optical absorption energy that is too large. For example, the molecule neo-pentane ( $C_5H_{12}$ , central C atom plus 4 methyl groups in tetrahedral coordination) is calculated to have a lowest excitation energy of about 15 eV in comparison with the experimental value of 7.5 eV. This problem has been examined by a number of investigators, most notably Jaffé and DelBene,<sup>(14-16)</sup> and Salahub and Sandorfy.<sup>(17-20)</sup> They have introduced modifications, the chief ones being to reduce the electron-electron interactions by reducing  $\gamma_{AB}$  and to alter the values of  $\beta^\circ$ . In the calculation of Energy Level Diagrams we have used an extension of the method which Sandorfy and Salahub used for saturated hydrocarbons, with the value of  $\beta^\circ$  adjusted to give reasonable energy gaps. The electron-electron interaction integrals  $\gamma_{AB}$  are evaluated by the method of Pariser and Parr<sup>(21-22)</sup> rather than by the CNDO/2 method.

Furthermore, configuration interactions are not performed; this is a rather time-consuming procedure. The excitation energy is taken as the configurational energy, equation (14). This leads to uncertainties in the calculated energy gaps of about  $K_{ij} \times \frac{1}{2}$  or about 0.05-0.2 eV, depending on the size of

the cluster (as the cluster increases in size,  $K_{ij}$  decreases). Considering the approximate nature of the calculation, this is considered to be an acceptable uncertainty.

## 6. Population Analysis

Having cast the problem in a Linear Combination of Atomic Orbital (LCAO) framework, it is extremely easy to get extensive information on the chemical bonding in the cluster. This information is most easily obtained from a population analysis, introduced by Mulliken.<sup>(23)</sup> Consider the LCAO approach to the hydrogen atom. The ground state MO will be

$$\psi_0 = (c_1\phi_1 + c_2\phi_2)$$

The electron density as a function of position for a single electron will be given by

$$|\psi_0|^2 = c_1^2\phi_1^2 + (c_1c_2+c_2c_1)\phi_1\phi_2 + c_2^2\phi_2^2$$

This distribution may be given the following interpretation:  $c_1^2\phi_1^2$  is the charge distribution arising from atom 1,  $c_2^2\phi_2^2$  from atom 2, and  $(c_1c_2+c_2c_1)\phi_1\phi_2$  the charge distribution arising from the covalent bond. Note that if the two atoms are separated by an infinite distance,  $\phi_1\phi_2=0$ ; i.e., there is no bond, as expected. Integrating each of these terms, we come to the following interpretation, since  $\int \psi_0^2 dt = 1$ , and remembering that two electrons occupy the orbital:

$2c_1^2S_{11}$  is the charge on atom 1,

$2c_2^2S_{22}$  is the charge on atom 2, and

$4c_1c_2S_{12}$  is the charge in the bond.

We can therefore define the orbital population matrix as

$$B_{\mu\nu}^c = P_{\mu\nu} S_{\mu\nu} \quad (24)$$

and the atom bond population as

$$B_{AB} = \sum_{\mu \text{ on } A} \sum_{\nu \text{ on } B} P_{\mu\nu} S_{\mu\nu} \quad (25)$$

$B_{AA}$  represents the charge on atom A and  $2B_{AB}$  the charge in the bond between atoms A and B. If  $B_{AB}$  is negative, then the bond is anti-bonding.

For open shell calculations

$$P_{\mu\nu} = P_{\mu\nu}^{\alpha} + P_{\mu\nu}^{\beta} \quad (26)$$

We can also define a Spin Population matrix

$$B_{\mu\nu}^s = \sum_{\mu \text{ on } A} \sum_{\nu \text{ on } B} (P_{\mu\nu}^{\alpha} - P_{\mu\nu}^{\beta}) S_{\mu\nu} \quad (27)$$

which tells where the electrons contributing to the excess spin are distributed.

In the CNDO method the molecular orbitals are not normalized. Therefore, the populations do not correspond exactly to charges. Nevertheless, they do qualitatively indicate the distribution of charge.

## 7. Results on Crystalline Clusters

We are now in a position to discuss the results of calculations on crystalline clusters. The purpose of this section is to demonstrate that the modified CNDO method as outlined above does in fact yield reasonable results for solids. Later sections will treat specific defect problems.

### a. Diamond and carbon structures

A large amount of work has been done on carbon-based molecules; this work forms a convenient starting point.

Consider first the molecule ethane (Figure 1). Using the Sandorfy and Salahub hydrocarbon parameterization (Table 1),<sup>(17-20)</sup>



the singlet excitation energy is found to be 9.01 eV, versus an experimental value of 9.4 eV. If we remove one hydrogen atom and the associated  $sp^3$  hybrid on the carbon atom, the singlet excitation increases slightly to 9.19 eV. Going even further and plucking off three hydrogen atoms surrounding a single carbon atom and removing the three associated  $sp^3$  hybrids yields a singlet excitation energy of 10.48 eV (the singlet excitation energy of methane  $CH_4$  by comparison is 9.7 eV).

Table 1  
Sandorfy and Salahub Parameterization  
for Saturated Hydrocarbons

$\epsilon_{H-H}$	=	-9.5 eV
$\beta_{C-H}$	=	-11.0
$\beta_{C-C}$	=	-15.0
$\gamma_C$	=	11.1

This trend of increasing excitation energy with decreasing cluster size is well known as a chemical shift. The bond populations for these three clusters is illustrated in Table 2. (In this table and in all remaining tables, atoms having less than the full complement of orbitals are designated by a prime.) It will be noticed that removing atoms has little effect on the bonds formed with other atoms. The charge distributions are also little affected.

The effect of surface hybridized orbitals can be compared to surface saturation by hydrogen by considering the molecule neo-pentane and the cluster  $C_5-C'_{12}$ . These clusters consist of a central carbon atom and four carbon atoms in tetrahedral coordination. The second neighbor coordination shell consists of 12 hydrogen atoms for neo-pentane or 12  $C'$  atoms (in <220>

type locations), each containing a single hybrid (Figure 2). The energy gap is found to be 8.35 eV for neo-pentane and 8.99 eV for  $C_5C'_{12}$  (Figure 3). Nearest neighbor bond populations are shown in Table 4. It will be noticed that there is very little difference between the two clusters. This is an indication that for diamond, surface saturation with hydrogen is not a particularly bad approximation. There are additional small differences; reflecting primarily the shorter hydrogen carbon distance; the second neighbor C-H and H-H bond populations are of the order of 30-100 times greater than the corresponding C-C' and C'-C' bond populations. The parameterization used in this report is summarized in Table 3.

Table 2  
Ethane Bond Populations and Charge Distribution

Bond Population	$C_2H_6$	$CC'H_5$	$CC'H_3$
C-C	0.7204	--	--
C-C'	--	0.6877	0.6496
C-H	0.6733	0.6751	0.6805
C'-H	--	0.6674	--
<u>Charge</u>			
C	4.01	4.00	4.05
C'	--	3.09	1.00
$H_C$	0.997	1.00	0.98
$H'_C$	--	0.961	--

Table 3  
CNDO Parameterization for Electronic Structure

Element	$\beta$ (eV)	$\gamma_{ii}$ (eV)
C	-15.0	11.1
B	-17.0	--
O	-45.0	--
Si	-7.0	8.0
P	-10.0	--

Table 4  
Bond Populations and Charge Distribution,  
Neo-Pentane and  $C_5C'_{12}$  Cluster

Bond Population	$C_5H_{12}$	$C_5C'_{12}$
C-C	0.694	0.686
C-H	0.672	--
C-C'	--	0.641
<u>Charge</u>		
$C_1$	3.910	3.902
$C_2$	4.023	4.007
H	1.000	--
$C'$	--	1.006

Note:  $C_1$  is the central atom,  $C_2$  one of four carbon atoms in tetrahedral coordination about  $C_1$ .

Adding additional shells of carbon atoms causes the energy gap to reduce as is illustrated in Figure 4. The  $CC'_4$  cluster is a methane-like arrangement of atoms;  $C_{17}C'_{24}$  consists of a central carbon, its full complement of four nearest neighbor and 12 second neighbor carbon atoms, 12 third neighbor  $C'$  atoms occupying  $\langle 311 \rangle$  positions and having two hybrids oriented towards  $\langle 220 \rangle$  type carbon atoms, and 12  $C'$  atoms in fifth neighbor  $\langle 331 \rangle$  positions, each having a single hybrid. The energy gap is seen to decrease from 13.23 to 8.99 to 7.33 eV as the cluster size increases. The experimental indirect band gap in diamond is 5.33 eV. Additional comparison with crystal-line diamond can be made with the valence band width. Band structure calculations indicate that this is from 20-25 eV. The cluster calculations show an increase from 15.24 to 28.78 to 38.19 eV as the cluster size increases. These last two large values arise from a few states lying abnormally low. All but the lowest four states in the large cluster, for example, lie in a range of 24 eV. Some indications as to why

this occurs can be seen by considering the electron distribution in these lowest orbitals. The lowest orbital is an A orbital (totally symmetric), and in the large cluster, an electron in this orbital is distributed as follows:  $C_0 = 0.14$ ,  $C_1 = 0.08$ ,  $C_2 = 0.03$ ,  $C_3^1 = 0.013$ , and  $C_5^1 = 0.002$ . Thus, this orbital is localized toward the interior of the cluster, a feature introduced by the finite size of the cluster, since this state in the infinite solid would be uniformly distributed across all atoms. Since the total charge distribution is what would be expected for this agglomeration of atoms (Table 5), this means that there are orbitals which are somewhat localized on the surface -- again an artifact of the finite size of the cluster.

The nearest neighbor bond populations and the atomic charge distribution of these clusters are shown in Table 5. Again, it will be noted that these are fairly consistent for all clusters, although some small variations are observed.

Table 5  
Bond Populations and Charge Distributions  
in Diamond Clusters

Bond Population	$CC'_4$	$C_5C'_{12}$	$C_{17}C'_{41}$
$C_0-C_1$	--	0.686	0.674
$C_1-C_2$	--	--	0.684
$C-C'$	*	0.641	0.648 (<311>C')
			0.635 (<331>C')
<u>Charge</u>			
$C_0$	4.010	3.902	4.005
$C_1$	--	4.007	3.934
$C_2$	--	--	3.985
$C'$	0.998	1.006	2.023 (<311>C')
			1.014 (<331>C')

\*Not calculated.

b. Silicon

The electronic structure of large and small clusters of silicon are illustrated in Figure 5. These clusters,  $\text{Si}_5\text{Si}'_{12}$  and  $\text{Si}_{17}\text{Si}'_{41}$  are analogues of the diamond clusters  $\text{C}_5\text{C}'_{12}$  and  $\text{C}_{17}\text{C}'_{41}$ . The parameterization used in these calculations is shown in Table 3; the value of  $\beta$  was adjusted to yield a reasonable energy gap. The energy gap is seen to decrease from 3.08 to 2.41 eV as the cluster size is increased, compared to an experimental indirect band gap of 1.17 eV at 0°K. The width of the valence states is 11.42 eV in the small cluster and 15.12 eV in the large cluster. This compared favorably with a value of 17 eV from band structure calculations. The nearest neighbor bond populations and charge distributions, listed in Table 6, are again consistent with a covalent structure.

Table 6  
Bond Populations and Charge Distribution  
of Silicon Clusters

Bond Population	$\text{Si}_5\text{Si}'_{12}$	$\text{Si}_{17}\text{Si}'_{24}$
$\text{Si}_0\text{-Si}_1$	0.752	0.732
$\text{Si}_1\text{-Si}_2$	--	0.749
$\text{Si-Si}'$	0.710	0.718 (<311>Si')
		0.705 (<331>Si')
<u>Charge</u>		
$\text{Si}_0$	3.939	4.102
$\text{Si}_1$	3.983	4.010
$\text{Si}_2$	--	3.958
$\text{Si}'$	1.011	2.027 (<311>Si')
		1.004 (<331>Si')

### c. $\beta$ -Silicon Carbide

An acid test of the semiempirical approach, and especially the use of surface hybrids is in  $\beta$ -silicon carbide (sphalerite structure), a solid which contains two types of atoms. Two small clusters were used, one containing a central carbon atom surrounded by four silicon atoms and twelve C' surface hybrids; the other containing a central silicon atom surrounded by four carbon atoms and twelve Si' surface hybrids. The electronic structure of these two clusters is illustrated in Figure 6; the energy gap of the cluster with carbon at its center is 3.63 eV, that of the cluster with Si at its center, 3.30 eV, while the experimental indirect band gap is 2.68 eV at 0°K.

Even more remarkable is the agreement in bond populations and atom charges (Table 7), indicating that the surface hybrids actually appear to the interior of the cluster as the atoms they represent.

Table 7  
Bond Populations and Charge Distribution  
of  $\beta$ -SiC Clusters

C at Origin		Si at Origin	
<u>Bond</u>	<u>Population</u>	<u>Bond</u>	<u>Population</u>
Si-C	0.663	Si-C	0.667
Si-C'	0.618	C-Si'	0.612
<u>Charge</u>		<u>Charge</u>	
C	4.508	C	4.416
Si	3.421	Si	3.210
C'	1.151	Si'	0.927

### d. SiO<sub>2</sub> Clusters

The electronic structures of the silica clusters SiO<sub>4</sub>Si<sub>5</sub>' and Si<sub>5</sub>O<sub>12</sub>Si<sub>12</sub>' are shown in Figure 7. The small cluster consists of a central silicon atom surrounded by four oxygen atoms

in tetrahedral coordination and four silicon surface hybrids such that the Si-O-Si' bond angle is  $180^\circ$ . The large cluster contains a central silicon atom, four oxygen atoms in tetrahedral arrangement, four silicon atoms, twelve oxygen atoms--three each attached to the four silicon atoms in tetrahedral coordination-- and twelve silicon surface hybrids: all Si-O-Si bond angles are  $180^\circ$ . These configurations correspond to the high cristoballite configuration of silica. The energy gap of the small cluster is 10.02 eV, while that of the large cluster is 10.25 eV. This compares favorably with the experimental value of 10 eV. The nearest-neighbor bond populations and atomic charge distributions are shown in Table 8. Again, the results are good. The charge distribution indicates that the structure is about 63% covalent--not far from the value of 50% predicted by Pauling's formula.<sup>(24)</sup>

Table 8  
Bond Populations and Charge Distributions  
for Silica (High Cristoballite) Clusters

<u>Bond</u>	<u>SiO<sub>4</sub>Si'<sub>4</sub></u>	<u>Si<sub>5</sub>O<sub>12</sub>Si'<sub>12</sub></u>
Si <sub>0</sub> -O <sub>1</sub>	0.596	0.591
Si <sub>1</sub> -O <sub>1</sub>	--	0.590
Si <sub>1</sub> -O <sub>2</sub>	--	0.596
Si'-O	0.545	0.545
<u>Charge</u>		
Si <sub>0</sub>	2.489	2.610
Si <sub>1</sub>	--	2.515
O <sub>1</sub>	6.678	6.707
O <sub>2</sub>	--	6.674
Si'	0.700	0.702

#### e. Summary

The preponderance of evidence presented in the foregoing sections is that the CNDO method in conjunction with surface hybrids does reasonably describe the electronic structure of a variety of solids. Furthermore, deviations are predictable with the given parameterization; for example, the energy gaps are consistently too large. Charge distributions undergo a small fluctuation from atom to atom; however, results are consistent to within about 3%. It thus appears that the method is ready to be applied to defect clusters.

#### B. Impurity and Vacancy Complexes

In this section we shall consider the electronic structure of clusters containing impurity atoms and vacancies. Of particular interest in understanding the effects of radiation damage in crystalline semiconductors is impurity clustering and impurity-vacancy complexing. It is of interest to determine the structure of these defects in order to better understand the resulting properties of radiation-damaged devices. We shall therefore first consider single boron and phosphorus impurities in silicon. While these are shallow acceptors and donors, respectively, and can therefore be treated by perturbation methods, a preliminary study is necessary by CNDO techniques.

The electronic structure of the small silicon cluster with a boron atom replacing the central silicon atom is shown in Figure 7. Boron is seen to give rise to a shallow acceptor state 0.21 eV above the valence state; the energy gap of the cluster is 4.46 eV (the energy gap of the pure silicon cluster is 3.08 eV, and the experimental band gap 1.17 eV). If the energies scale linearly, this would correspond to an acceptor state 0.055 eV above the valence band in the crystal--the experimental value being 0.05 eV.



The electron distribution is shown in Figure 8. The charge deficiency (or excess) is defined as the difference between the charge on the defect cluster and the charge on the pure silicon cluster. Because of the CNDO approximations, there is an error of the order of  $\pm 0.04$  electrons per atom (or bond) relative to each other in these calculations. This discrepancy arises from termination of the self-consistency iterative procedure. Since the convergence is slower in the open shell calculation than in the closed shell computation, termination after a specified increment in energy results in the open shell calculation being further from self-consistency than the closed shell calculation. A second source of error is the normalization of the molecular orbitals. Since the orbitals are normalized assuming zero overlap, the charges derived have only a semiquantitative meaning. For this reason, all charge deficiencies (or excesses) should be considered as qualitative results.

The excess spin distribution is sensitive to the self-consistency of the cluster, and therefore differences of  $\pm 0.04$  electrons should be considered insignificant. One puzzling result is the rather large deficiency on one surface hybrid (Figure 8c) of  $-0.296$  and a surplus of  $0.266$  on a neighboring silicon. This will probably not result in any great error, since this results in only about  $1/4 K_{ij}$  or  $0.025$  eV change in the interaction energy. This unusual situation was noted in several of the open shell calculations. Note that this is a shift in spin density only; the overall charge distribution (Figure 8a) remains uniform.

The results of open shell calculations for the large cluster with the boron atom in both a central and noncentral (111) position are shown in Figures 9-12. The position of the acceptor level is seen to be relatively insensitive to atom position; with the boron in the central position, the acceptor state is  $0.40$  eV above the valence states, with an energy gap of  $3.20$  eV (Figure 9), while with the boron off-center, the

acceptor state is 0.54 eV above the valence states, with an energy gap of 2.45 eV. The total energies of these two clusters differ by 1.5 eV.

Concerning the electron distribution in the clusters the following generalizations can be made: (1) The atoms remain fairly neutral; that is, the boron "soaks up" few electrons from the silicon (Figures 8a, 10a, 12a). Since the acceptor state is not strongly peaked on the boron atom (Figures 8d, 10c, 12c), this means that lower-lying occupied orbitals have smaller occupancies on the boron than on the silicon atoms. (2) The acceptor state (Figures 8d, 10c, 12c) is fairly spread out. The peaking which does occur appears to be more a result of the finite size of the cluster than of the impurity itself (compare Figures 10c and 12c, in particular). (3) The Si-B bond is considerably weaker than the Si-Si bond (Figure 8b). The charge deficiency in this bond is not completely unexpected, since the boron atom is electron deficient. (4) The excess spin distribution roughly corresponds to the charge distribution in the acceptor state (Figures 8c,d, 10b,c, 12b,c) This is not totally unexpected, for if we can speak of a hole in silicon, then it must have spin. The spin must be opposite in sign to and have the distribution of the electron which is missing. (5) There is an indication that the cluster would like to undergo a Jahn-Teller distortion. The clusters with the atom at its center have  $T_d$  symmetry, yet the electron distributions deviate from this. No attempt was made to introduce these distortions into the calculation. (6) Considering the magnitude of the energy gaps in comparison with those of the pure silicon cluster, it appears that there should be a tendency for the band gap to widen in the vicinity of a boron impurity in the crystal.

The results on clusters containing a single phosphorus impurity are shown in Figures 13-16. During the self-consistency iteration on the large cluster with the phosphorus at the center of the cluster, the energy diverged (i.e., initially decreased, then increased by progressively larger amounts). The reason

for this divergence is not understood; consequently, the results on this cluster are not presented.

The phosphorus atom is seen to give rise to a donor state lying 0.39 eV below the conduction states, with an energy gap of 3.51 eV in the small cluster (Figure 13), and a donor state lying 0.50 eV below the conduction states with an energy gap of 2.20 eV in the large cluster (Figure 15). It should be remembered that the energy gap is defined as an excitation from the top of the valence states into the conduction states, and consequently the J and K integrals in equation (21) are computed between the impurity state and conduction states for the depth of the donor level, and the top of the valence states and the conduction state to determine the energy gap. This somewhat roundabout method is partially a result of considering a finite cluster, and partially a result of the use of a Hartree-Fock procedure, as discussed in the first section.

The discussion for the boron impurity is also applicable to the phosphorus impurity. The only surprising result is that the bonding between phosphorus and silicon is weaker than between silicon atoms (Figure 14b). On an intuitive basis, the opposite would have been expected, since the phosphorus atom has an excess of electrons. In fact, the phosphorus-silicon bonds are charge deficient, as are the neighboring silicon-silicon bonds. This is probably the explanation for the limited solid-solubility of P in Si.

It is interesting to compare the results of the hydrogenic perturbation treatment of an impurity state with the CNDO treatment. In the hydrogenic model, a point charge is placed on a lattice site. The surrounding medium is polarized by the charge, reducing the effective charge of the impurity center from unity to  $1/K$  where  $K$  is the dielectric constant. The effective charge then acts as the nucleus of a hydrogen atom with an electron having effective mass  $m^*$  in orbit about the center. The hydrogenic model makes no attempt to explain what is happening close to the impurity center; in fact, the perturbation technique breaks down close in to the center. It will

be a good description provided that (1) the close-in effects are short range, and (2) that the impurity state is spread out, so as to experience little of the short range effects of the impurity center.

In the CNDO method, we start from scratch to calculate the effect of an impurity. Since this means that we are redistributing all electrons, in order to obtain accurate information on an impurity state far from the defect, we must have (1) a large cluster, preferably with periodic boundary conditions, and (2) a high degree of self-consistency, since electron differences are small. On the other hand, we can obtain accurate information close in to the defect without either of the above. Confining the carrier to a small volume makes it become strongly influenced by the structure close to the center, and gives rise to something closer to an impurity bound excitonic state. The impurity states should therefore lie somewhat deeper than in reality, as is in fact found.

In the hydrogenic model, the charge of the impurity center is reduced by the appearance of a virtual charge caused by polarization of the medium. In the CNDO model, the charge of the impurity center is reduced by a real charge shift caused by alteration of the populated molecular orbitals.

The CNDO model should therefore be best when considering localized defects. A particular example of this is in the chemical bonding between the impurity atom and the lattice. The detailed structure of the impurity state far from the center will be largely masked by the finite size of the cluster, and the limited degree of self-consistency in the calculation. However, semiquantitative results can still be obtained, as has been demonstrated.

#### 1. Vacancy in Silicon

The problem of a vacancy is one which is beyond the scope of perturbational treatments. The vacancy in diamond has been studied by Swenson using the Extended Huckel Theory (a non-

self-consistent field method) and surface saturation with hydrogen.<sup>(13)</sup> In the present work, we will use a similar procedure with the CNDO method.

A vacancy was created in the large silicon cluster by removing the central atom. The remaining atoms maintained the  $T_d$  symmetry of the initial cluster. The atoms surrounding the vacancy are shown in Figure 17a. When the central atom is removed, these four atoms will each have one unsaturated  $sp^3$  hybrid oriented toward the center. This configuration is not stable; we expect the cluster to distort so that covalent bonds between the atoms can form. Experimentally, this distortion is known to have  $D_{2d}$  symmetry.<sup>(25)</sup> A coordinate system describing all possible distortions from  $T_d$  symmetry to  $D_{2d}$  symmetry may be constructed as in Figure 17b. The positions of the other three central atoms will be related to the one shown through the symmetry operations of the group  $D_{2d}$ . Only the four central atoms were moved.

To determine the equilibrium (lowest energy) position of these atoms a potential surface is constructed showing the energy of the cluster as a function of  $R$  and  $\theta$ . Such a project is rather formidable even in the semiempirical CNDO. (Typically, 10 minutes 360/65 computer time or 15-20 minutes 370-155 time with a 368K partition are required for each point.) Therefore, limited sections through the potential surface were made, based on the assumption that the vacancy is qualitatively similar to that in diamond. These sections are shown in Figure 18. An additional section was attempted with  $\theta = 145^\circ$ ; however, the initial Huckel approximation mispredicted the ordering of the levels, and self-consistency still had not been achieved after nine iterations.

In accordance with general practice, the CNDO/2 parameterization of Pople, Santry and Segal<sup>(1-4)</sup> was used to determine the potential surface, since this parameterization is known to give good equilibrium bond lengths. Some difficulty was encountered with the points for  $R = 0.5$ ; the electronic energy

initially decreased, then increased. The energy is therefore not at self-consistency; these points may consequently lie somewhat higher or lower. The minimum energy in Figure 18 is found to occur at approximately  $R = 0.35$ ,  $\theta = 110^\circ$ . Because of the limited nature of the potential surface constructed, this value should be considered as approximate.

It is interesting to note that the electronic structure in the vicinity of the energy gap was relatively insensitive to the tetrahedral distortion. For example, using the Pople, Santry and Segal parameterization, the energy from the highest populated state to the lowest unpopulated state is 0.23 eV, and the energy from the highest populated state to the conduction states is 2.8 eV for the cluster with  $R = 0.08$ ,  $\theta = 70^\circ$ . For the cluster with  $R = 0.35$ ,  $\theta = 110^\circ$ , these values are 0.42 eV and 3.06 eV, respectively.

The energy structure of the cluster using the parameterization of Table 3 is illustrated in Figure 19. It will be noticed that a vacancy acts as an acceptor state. Comparing this structure with that from the pure Si cluster (Figure 5), it will be seen that the vacancy splits off an occupied level from the valence states and introduces two acceptor states slightly above this level. The details of how this structure fits into the overall band structure cannot be determined; the calculation indicates the acceptor states lie 0.27 eV above the populated states. Additionally, the overall structure appears to indicate that the occupied state split off from the valence states lies fairly deeply in the band gap. If simple energy scaling is valid, the structure would appear as in Figure 20. Further calculations with impurities added to the vacancy cluster, which will be discussed later, indicate that this is a not unreasonable model.

The electron distribution for the vacancy cluster is shown in Figure 21. There is seen to be some depletion of charge from the atoms surrounding the vacancy (Figure 21a). The charge piles up on surface hybrids (not shown). This may be a result of the surface boundary conditions.

The bond populations (Figure 21b) show the formation of a bond between pairs of silicon atoms surrounding the vacancy. With the formation of these bonds, there is a slight weakening of bonds with neighboring silicon atoms. The equilibrium positions of the atoms are those in which the various bonds are maximized.

The charge distribution in various orbitals in the vicinity of the energy gap are illustrated in Figures 21c-f. Figure 21c shows that the highest populated orbital is fairly peaked on the four atoms surrounding the vacancy (60% on these atoms); we are thus justified in speaking of this orbital as arising from the vacancy. Figure 21d shows one of the pair of doubly degenerate acceptor states lying in the energy gap. This state is also rather peaked on a pair of central silicon atoms (50% on a pair -- the other molecular orbital of this set is peaked on the other pair of silicon atoms), and may also be definitely attributed to the vacancy. On the other hand, states higher or lower in energy than the above states are spread out throughout the cluster (Figures 21e,f) and may therefore be spoken of as conduction and valence states.

The rather large degree of localization of the states within the energy gap is a fairly good indication that they lie rather deep within the energy gap. This observation lends support to the energy diagram sketched in Figure 20.

## 2. Vacancy-Impurity Complexes

Having considered the pure vacancy, the next step is to add impurities to the silicon cluster to see how impurities and vacancies interact.

The first problem we shall consider is a single boron impurity added to a vacancy cluster. Two such problems were considered; in the first the boron atom was placed on one of the four positions surrounding the vacancy (nearest neighbor model); in the second, the boron atom was placed on one of the neighboring silicon atoms (next nearest neighbor model). No

additional distortions were considered, although considering the change of charge in the vicinity of the vacancy, a small additional distortion does seem likely.

The energy structure of the nearest neighbor boron model is shown in Figure 22. It will be noted that the boron atom behaves as we intuitively might have expected. Since it is a shallow acceptor in silicon, and since the vacancy has split off a pair of electrons from the valence band fairly deeply into the energy gap, then it would appear that on adding a boron atom, the boron atom will be ionized, accepting an electron from the vacancy complex. This is in fact observed.

The boron has an additional effect, and that is to cause the doubly degenerate pair of acceptor levels arising from the vacancy to split apart. This "chemical splitting," as we shall see, is dependent upon the separation of the vacancy and the boron atom. Again assuming that we can scale the energies, the resulting energy level diagram is shown in Figure 23.

The charge distribution for this cluster is shown in Figure 24. The cluster is seen to be close to being neutral (Figure 24a), as in the impurity clusters. The bond populations, however, have been altered (Figure 24b). In particular, the bond which formed between atoms 2 and 4 during distortion of the vacancy is seriously weakened (bond population from 0.30 to 0.12) while that between atoms 1 and 3 is weakened slightly. The weakening of these bonds is most likely due to the charge deficiency on the boron atom, which allows one less electron to take part in the bonding process.

The distribution of the excess spin (Figure 24c) is rather interesting in that it lends support to our previous argument that the ionized boron acceptor is spread out, while the occupied vacancy levels are localized. In fact, the molecular orbital of the highest populated state (the unionized vacancy state) is found to have a distribution close to that of the excess spin.



Moving the boron to the next nearest neighbor position results in the energy structure shown in Figure 25. Again, the boron acceptor is ionized by an electron from one of the vacancy states. The chemical splitting of the vacancy acceptor states is seen to be substantially less. A scaled energy level diagram is shown in Figure 26. We can anticipate that as the boron atom is moved further from the vacancy, the chemical splitting will become less and less, even though the boron acceptor state remains ionized.

The charge distribution with the boron atom in the next neighbor position is illustrated in Figure 27a. Charge neutrality is still nearly maintained. The weakening of the vacancy bonds is still observed (Figure 27b), although not to as marked degree as when the boron was a nearest neighbor atom.

The excess spin distribution (Figure 27c) is similar to that which was found in the nearest neighbor boron cluster, and is indicative of a localized orbital in the energy gap. It is interesting to note that the atom with most excess spin remains the same; that is, the silicon atom which is paired with the atom closest to the impurity atom through the vacancy bond.

The properties of a phosphorus -vacancy complex have also been determined. An attempt to calculate the structure of such a complex when the phosphorus atom was one of the four atoms surrounding the vacancy (nearest neighbor model) was unsuccessful; the energy was found to diverge during the self-consistency procedure. This divergence resulted from a large amount of charge moving on to the atoms surrounding the vacancy.

A calculation of a cluster in which the phosphorus atom was a next nearest neighbor was successful, however. The energy structure of this complex is shown in Figure 28. This combination too behaves as one would intuitively expect. The phosphorus atom, being a shallow donor, becomes ionized, yielding its electron to one of the vacancy acceptor states. A scaled energy level diagram is shown in Figure 29.

The charge distribution (Figure 30a) again shows that the cluster approximately maintains neutrality. The bonding is similar to that which was observed with boron; that is, a weakening of the vacancy bonds. Interestingly, the populations of the vacancy bonds are smaller in the phosphorus cluster than they were in the boron cluster; this even though the phosphorus atom has an excess of electrons.

The excess spin distribution (Figure 30c) is most interesting, in that it shows signs of spin ordering. The reason for this behavior can be seen by considering the three populated orbitals with levels in the energy gap. Two of these have  $\alpha$  spin; one of these is peaked sharply on atom 3 and more weakly on atom 1; the other is peaked sharply on atom 4 and more weakly on atom 1. The other orbital has  $\beta$  spin; it is peaked sharply on atoms 1 and 2. Consequently, the spins on atom 1 cancel, leaving a net  $\beta$  spin on atom 2 and  $\alpha$  spins on atoms 3 and 4, as the excess spin populations show. That this occurs can be attributed to a high degree of localization of the states. For several electrons confined to a few atoms, the Coulomb integral  $J_{ij}$  is rather large. The magnitude of this integral may be reduced if the states of the system, rather than being spread out over all atoms, are confined to just a few. This phenomenon is known variously as a Mott transition<sup>(26)</sup> or Wigner crystallization.<sup>(27)</sup>

### 3. Multi-Impurity Clusters

Let us now turn our attention to clusters in which there are two or more impurities present. These clusters will be representative of regions in the crystalline semiconductor where impurity clustering occurs due to heavy doping, diffusion, or radiation damage.

The energy structure of a cluster containing two boron atoms which are nearest neighbors is shown in Figure 31. A cluster in which two boron atoms are separated by a second neighbor distance is presented in Figure 32. In both of these

clusters, a shallow acceptor state capable of holding two electrons is formed. The charge distribution in this acceptor state is depicted in Figure 33c for the nearest neighbor borons, and in Figure 34c for the next nearest neighbor boron cluster. In both these cases there appears to be a tendency for the electron in the acceptor state to avoid the boron atom itself, as was the case for a single boron atom (Figures 10 and 12).

Two important questions are: (1) which of the two arrangements of boron atoms is the most stable, and (2) is a pairing of the boron atoms stable with respect to completely isolated atoms in the silicon crystal? Replacing a silicon atom with a boron in the central position results in an increase in the total cluster energy of 0.9407 Hartrees, while replacing it in the off-center position results in an increase of 0.8865 Hartrees. Thus, if there were no interactions between boron atoms, the energy of the nearest neighbor complex should be 1.8272 Hartrees above the pure silicon cluster, while that of the second neighbor arrangement should be 1.7729 Hartrees above. In actuality, the nearest neighbor arrangement has an energy 1.6525 Hartrees above the pure silicon energy, while the second neighbor arrangement of boron atoms has an energy 1.6706 Hartrees above. This means that the interaction energy between two boron atoms in the nearest neighbor configuration is -0.1747 Hartrees, while that of the next nearest neighbor arrangement is -0.1023 Hartrees. Thus, the nearest neighbor arrangement of boron atoms is about 4.75 eV more stable than having them separated an infinite distance, and about 2.0 eV more stable than the next nearest neighbor arrangement. It appears that pair clustering of boron impurities in silicon is favored over a random distribution, at least in the present model. It should be noted that here we are treating only a chemical effect, since no elastic distortions have been added. Distortions may alter this chemical effect and, in addition, will introduce an elastic interaction energy which will probably be repulsive at all distances (the boron atom is smaller than

the silicon, hence it should introduce a dilatational center of strain).

The energy structure of a silicon cluster containing two phosphorus atoms separated by a second neighbor distance is shown in Figure 35. There is a rather deep donor state (doubly occupied). The distribution of charge in both the highest occupied orbital and the lowest unoccupied orbital is somewhat localized (Figure 36c,d), but a good portion of this localization is probably due to cluster boundary conditions (compare with Figure 14). This seems to argue for the two phosphorus atoms compensating each other; that is, the occupied donor levels lie not far from the top of the valence band, while the unoccupied levels lie not far from the bottom of the conduction band. This is in contrast to the case of the two boron impurities where there was little interaction between the two impurity atoms.

The two phosphorus atom complex is found to be more stable than the isolated atoms by approximately 2.2 eV. An attempt was made to perform a calculation on a complex with the phosphorus atoms separated by a nearest neighbor distance, but the energy was found to diverge. Thus, it is not known if the nearest neighbor arrangement would be more stable than the next nearest arrangement.

The electronic structures of silicon clusters having both single boron and single phosphorus impurity atoms separated by a nearest neighbor distance and a next nearest neighbor distance are shown in Figures 39 and 40. In both clusters compensation is evident, the phosphorus impurity state having been ionized into the boron acceptor level. Comparing these figures with the energy structures of the two single boron impurity clusters in the center and off-center position (Figures 9 and 11), it will be noticed that the differences are mainly due to the cluster surface conditions.

The relative stability of these two clusters can be determined as follows. On replacing an off-center silicon atom with

a phosphorus atom the total energy of the cluster decreases by 2.5125 Hartrees. Using the values previously given for the boron atoms, with no interaction energy between the phosphorus and boron, the nearest neighbor cluster total energy will be 1.5718 Hartrees below that of a pure silicon cluster, while that of the next nearest neighbor cluster will be 1.6261 Hartrees lower. In fact, these clusters are 1.7204 and 1.7904 Hartrees lower. This means that the second neighbor cluster is about 4.5 eV more stable than isolated impurities, and about 0.5 eV more stable than the nearest neighbor cluster. Hence, the chemical interaction between boron and phosphorus impurities is attractive at large distances and repulsive at close distances.

The question as to why the boron-phosphorus interaction is repulsive at close distances, while that of the boron-boron is attractive, may be seen in the following. In both types of clusters, the covalent portion of the bonding decreases as the impurities are separated (the sum of the bond orders decreases by about 0.1, see Figures 33b, 34b, 39b and 40b). The ionic portion of the bonding of both types of clusters improves as the impurities are separated. A simple calculation of the nearest neighbor contribution to the ionic bonding (in units of products of the charges) shows that in the two boron atom cluster the ionic bonding increases from 0.16 to 0.26 while that of the boron-phosphorus cluster increases from 0.02 to 0.18. Thus, in the boron-phosphorus cluster, the increase in ionic bonding offsets the decrease in covalent bonding as the atoms are separated. The rather low value of ionic energy for the nearest neighbor BP cluster, and the reason for the sharper increase of the ionic energy in the BP clusters as the impurities are separated is a chemical interaction of these atoms at close distances.

It is also interesting that boron-phosphorus complexing is predicted to be more stable when both species are present, at least considering the present models. Two boron-phosphorus

complexes would be about 2 eV more stable than one phosphorus-phosphorus and one boron-boron complex. It should be emphasized, however, that the only consideration made at arriving at these conclusions is a chemical interaction. Consideration of distortions and elastic interactions may alter these results.

A final impurity cluster which was considered was one containing two phosphorus impurities and one boron. The energy structure of this cluster is shown in Figure 41, and a Scaled Energy Level Diagram in Figure 42. The charge distributions for this cluster are shown in Figure 43. It will be noted that there is a highly localized state about one of the phosphorus atoms (Figure 43c,d). This is consistent with assigning the unionized donor state to a level deep in the energy gap. It also supports the previous argument that there is a substantial phosphorus-phosphorus interaction which strongly alters the donor levels.

## References

1. J. A. Pople, D. P. Santry and G. A. Segal, J. Chem. Phys., 43, 5129 (1965).
2. J. A. Pople and G. A. Segal, J. Chem. Phys., 43, 5136 (1965).
3. J. A. Pople and G. A. Segal, J. Chem. Phys., 44, 3289 (1966).
4. J. A. Pople and D. L. Beveridge, Approximate Molecular Orbital Theory, McGraw-Hill, New York, 1970.
5. J. C. Slater, Quantum Theory of Matter, 2nd ed., McGraw-Hill, New York, 1968, Chapters 16-21.
6. J. C. Slater, *ibid.*, Chapter 16.
7. C. C. J. Roothaan, Rev. Mod. Phys., 23, 68 (1951).
8. T. C. Koopmans, Physica, 1, 104 (1933).
9. J. C. Slater, *ibid.*, Chapter 10.
10. R. P. Messmer and G. D. Watkins, Phys. Rev. Letters, 25, 656 (1970).
11. J. Keller, J. Phys. Chem., 4, 3143 (1971).
12. A. J. Bennett and L. M. Roth, J. Phys. Chem. Solids (GB), 32, 1251 (1971).
13. J. Swenson, Ph.D. Thesis, Cornell University, 1971.
14. J. Del Bene and H. H. Jaffé, J. Chem. Phys., 48, 1807 (1968).
15. J. Del Bene and H. H. Jaffé, J. Chem. Phys., 48, 4050 (1968).
16. J. Del Bene and H. H. Jaffé, J. Chem. Phys., 49, 1221 (1968).
17. D. R. Salahub and C. Sandorfy, Theoret. Chem. Acta (Berlin), 20, 227 (1971).
18. D. R. Salahub and C. Sandorfy, Chem. Phys. Letters, 8, 71 (1971).
19. D. R. Salahub, Theoret. Chim. Acta (Berlin), 22, 325 (1971).
20. D. R. Salahub, Theoret. Chim. Acta (Berlin), 22, 330 (1971).

21. R. G. Parr, J. Chem. Phys., 20, 1499 (1952).
22. R. Pariser, J. Chem. Phys., 21, 568 (1953).
23. R. Mulliken, J. Chem. Phys., 23, 1833 (1955); *ibid.*, p. 2343.
24. L. Pauling, Nature of the Chemical Bond, 3rd ed., Cornell University Press, 1960, pp. 93-98.
25. G. D. Watkins, J. Phys. Soc. Japan, 18, Suppl. 2, 22 (1962).
26. E. P. Wigner, Phys. Rev., 46, 1002 (1934).
27. N. F. Mott, Proc. Phys. Soc. (London), A62, 416 (1949).



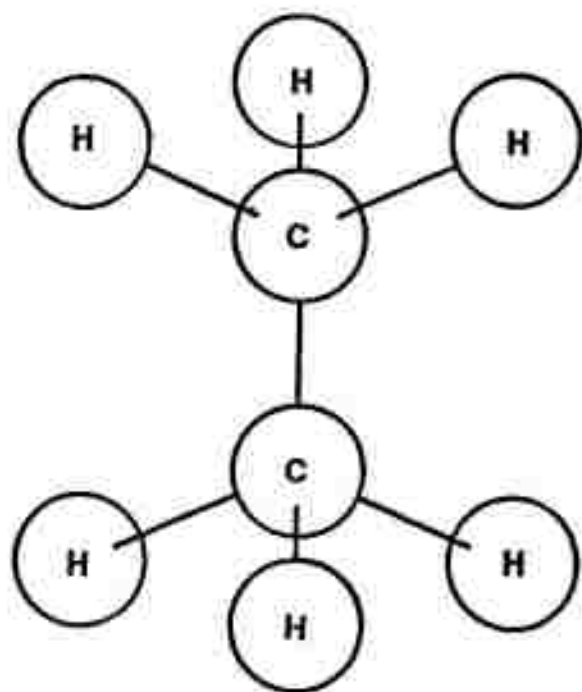


**Figure 1      Ethane Molecule.**

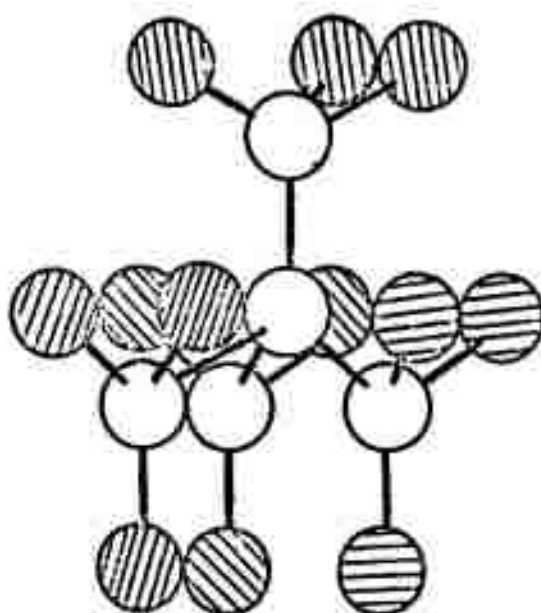


Figure 2 Neo-pentane Molecule and  $C_5C_{12}$  Cluster. Shaded atoms are  $^5C_{12}H_{12}$  in neo-pentane.

Fig. 3a. Energy structure  
of C<sub>5</sub>H<sub>12</sub>.

*****	( 3 )	0.76,	0.47,	C.43.
*****	( 3 )	-0.41,	-0.49,	-0.50.
*****	( 5 )	-1.03,	-1.18,	-1.26,
*****		-2.19		-1.04.
*****	( 3 )	-2.98,	-3.09,	-2.99.
*****		-3.83		

-8.00 | F L F L F L F L

*****	( 3 )	-12.19,	-12.19,	-12.19.
*****	( 3 )	-13.97,	-13.97,	-13.97.
*****	( 2 )	-15.91,	-15.91,	

*****	( 3 )	-18.84,	-18.84,	-18.84.
-------	-------	---------	---------	---------

\*\*\*\*\* -20.92

*****	( 3 )	-28.56,	-28.56,	-28.56.
-------	-------	---------	---------	---------

-32.00 |

\*\*\*\*\* -39.06

FERMI LEVEL = -8.01 BAND GAP = 6.35

Fig. 3b. Energy structure of  $C_5C_{12}$ .

[illegible]

**Fig. 4. Energy structure of  $C_{17}C'_{24}$ .**

[illegible]

[illegible]

[illegible][illegible]

**Fig. 6a. Energy structure of  $\text{SiC}_4\text{Si}_{11}\text{I}_2$ .**

[illegible]

**-9.00IFLFLFLFL**

\*\*\*\*\* (3) -11.06, -11.06, -11.06.

*****	( 3 )	-13.46.	-13.46.
-------	-------	---------	---------

\*\*\*\*\* (2) -14.81. -14.81.

\*\*\*\*\* ( 3 ) -16.20. -16.20. -16.20.

\*\*\*\*\*  
-18.06

\*\*\*\*\* (3) -20.34, -20.34, -20.34.

**-24.00%**

-29.001

FERMI LEVEL = -9.24 RAND GAP = 3.63



FIG. 50. ENERGY STRUCTURE  
of  $CS_4Cl_2$ .

[illegible]

EXCITATION FROM LEVEL 16A

[illegible]

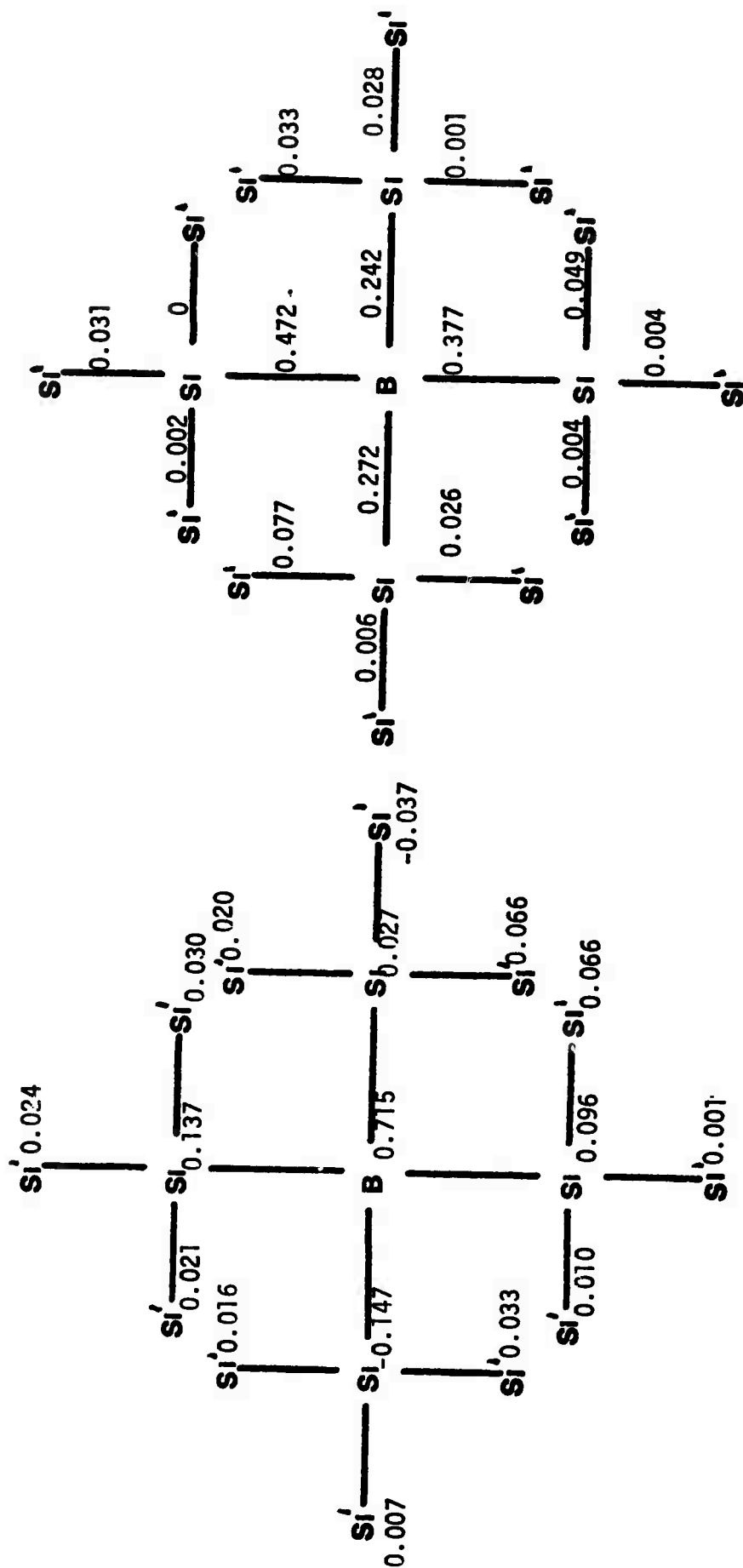


Figure 8A

Total Charge Deficiency  
on Atoms in Small Cluster;  
B Impurity.

Figure 8B

Total Charge Deficiency  
in Bonds, Small Cluster;  
B Impurity.



EXCITATION FROM LEVEL 51B

of BS116Si24  
boron in central  
position.

0.0	***** ( 3 )	-1.49 102B	-1.45 103R	-1.24 104H	-2.39 90H	-2.37 92A	( 1 )
	***** ( 4 )	-1.65 100A	-1.64 103A	-1.64 102A	-2.43 89A	-2.95 73B	( 2 )
	***** (28)	-2.46 86B	-2.45 92R	-2.45 89B	-2.96 75B	-3.10 70B	( 3 )
	***** (30)	-3.00 74A	-3.00 75A	-2.98 74B	-3.16 69B	-3.58 67B	( 4 )
	***** ( 7 )	-3.35 68A	-3.17 71A	-3.16 70A	-3.62 66B	-4.36 62A	( 5 )
	***** ( 8 )	-3.81 65A	-3.77 65B	-3.63 66A	-4.39 59B		
	***** (12)	-4.45 61B	-4.43 59A	-4.39 61A	-4.64 58B		
-5.00	***** ( 4 )	-4.79 57A	-4.76 57B	-4.65 58A	-5.28 54B	-5.25 54A	( 6 )
	***** ( 7 )	-5.48 53B	-5.41 55A	-5.33 55B			
	*****	-5.59 53A					

10.00	IFLFLFLFLFL***** ( 5 )	-8.39 52B	-8.89 51A	-8.83 52A	-8.79 51B		
	***** ( 4 )	-8.95 50A	-9.47 49A	-9.45 48A			
	***** ( 9 )	-9.49 48A	-9.98 43B	-9.92 44B	-9.85 46A	-9.84 45B	( 7 )
	***** ( 7 )	-10.27 40A	-10.26 40B	-10.14 41A	-10.05 42A	-10.03 43A	( 8 )
	***** ( 7 )	-10.94 36B	-10.83 37A	-10.40 38A	-10.79 37B	-10.72 38B	( 9 )
	***** ( 8 )	-11.48 32B	-11.18 33A	-11.16 34A	-11.12 35A	-11.12 34B	(10)
	***** ( 7 )	-11.70 29A	-11.65 29B	-11.63 30A	-11.54 31A	-11.51 31B	(11)
	***** ( 6 )	-12.26 26A	-12.16 26A	-12.09 27A	-12.04 28A	-12.02 28B	
	***** ( 6 )	-12.68 23B	-12.66 23A	-12.60 24A	-12.55 25A	-12.55 25B	
	***** (10)	-13.45 19A	-13.41 19B	-13.41 19A	-13.30 20A	-13.25 20B	(12)
15.00	***** ( 8 )	-14.94 14A	-14.86 14B	-14.86 15A	-14.77 16B	-14.76 16A	(13)

	***** ( 6 )	-16.82 11B	-16.80 11A	-16.73 12B	-16.69 13B	-16.68 13A	
	***** ( 4 )	-17.32 9B	-17.30 9A	-17.25 10B			
	***** ( 2 )	-18.24 8A	-18.19 8B				
	***** ( 6 )	-18.64 5A	-18.62 5B	-18.59 6B	-18.56 7B	-18.53 7A	

-20.00	***** ( 3 )	-21.00 3A	-20.93 4B	-20.93 4A			
	***** ( 3 )	-21.07 2A	-21.06 2B	-21.04 3B			

-25.00	***** ( 2 )	-24.96 1A	-24.95 1B				
--------	-------------	-----------	-----------	--	--	--	--

FERMI LEVEL = -8.59 ENERGY GAP = 0.40

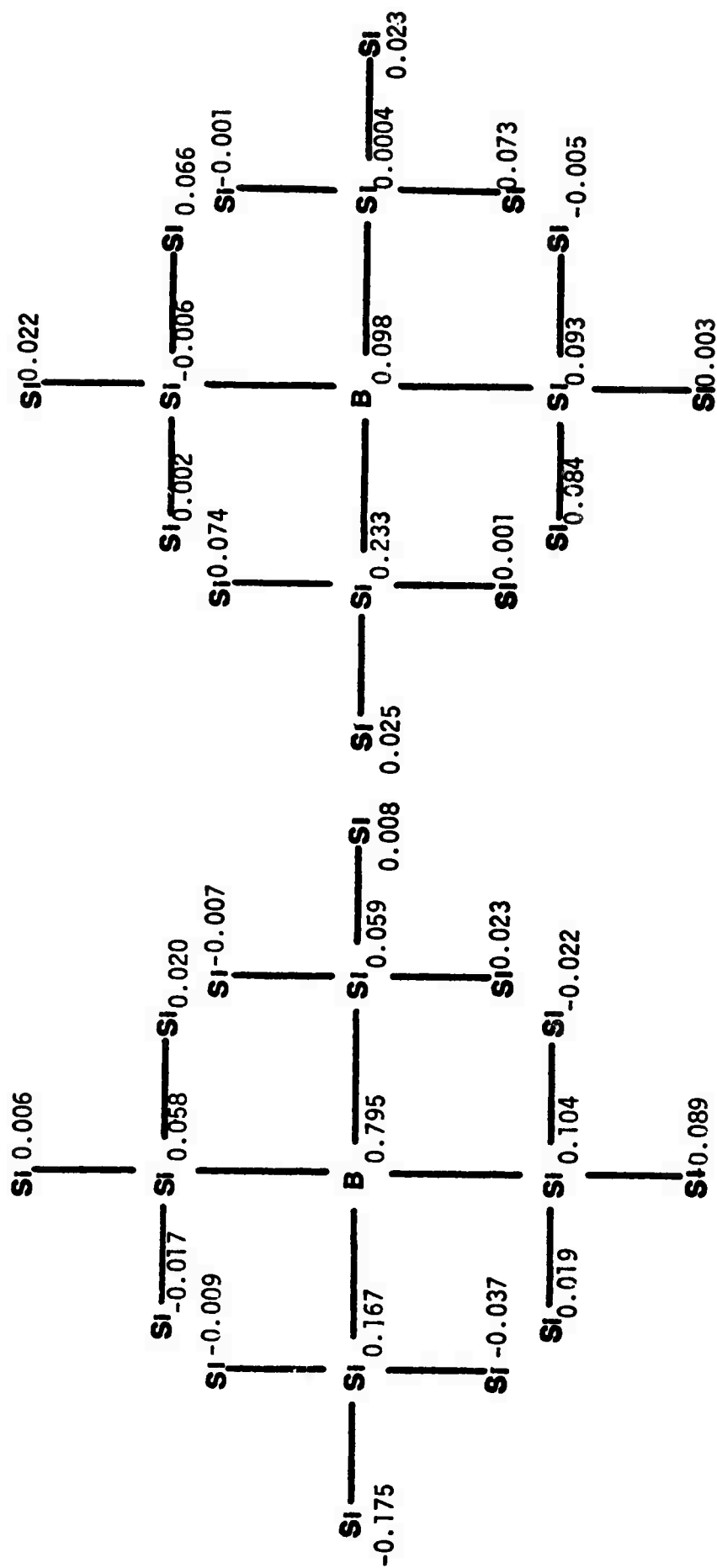


Figure 10A Total Charge Deficiency on Atoms; Large Cluster, B Impurity in Center.

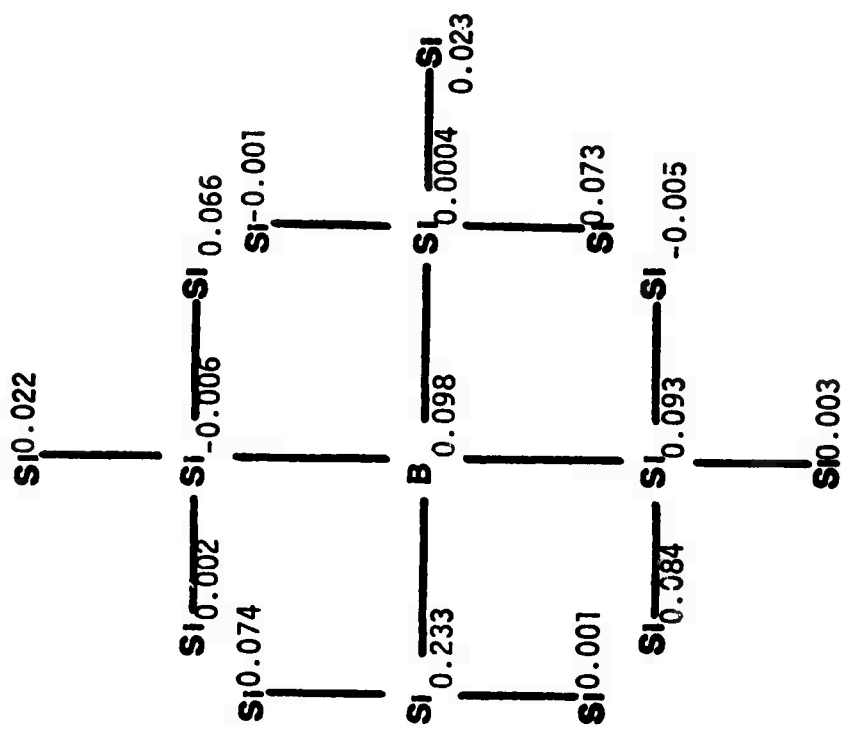


Figure 10B Excess Spin Distribution on Atoms; Large Cluster, B Impurity in Center.

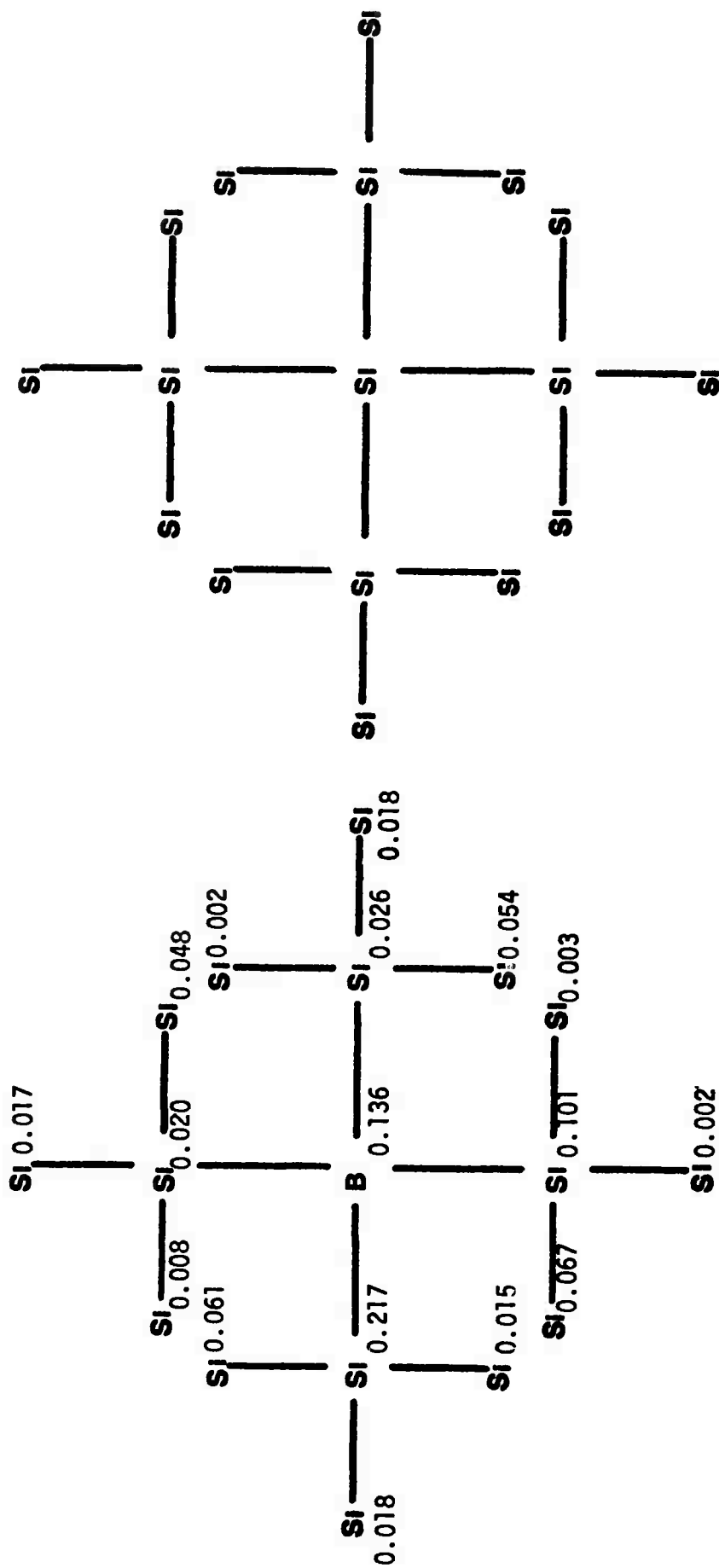


Figure 10C Charge Distribution of Impurity Acceptor State; Large Cluster, B Impurity in Center.





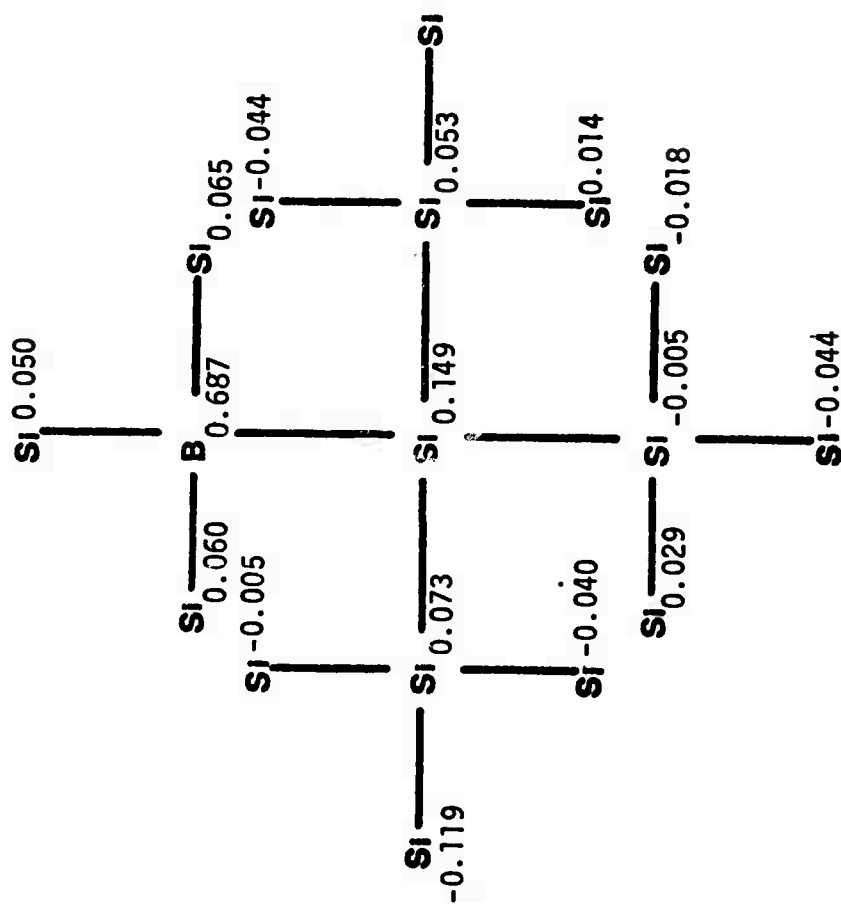


Figure 12A

Total Charge Deficiency on Atoms; Large Cluster, B Impurity Off-Center.

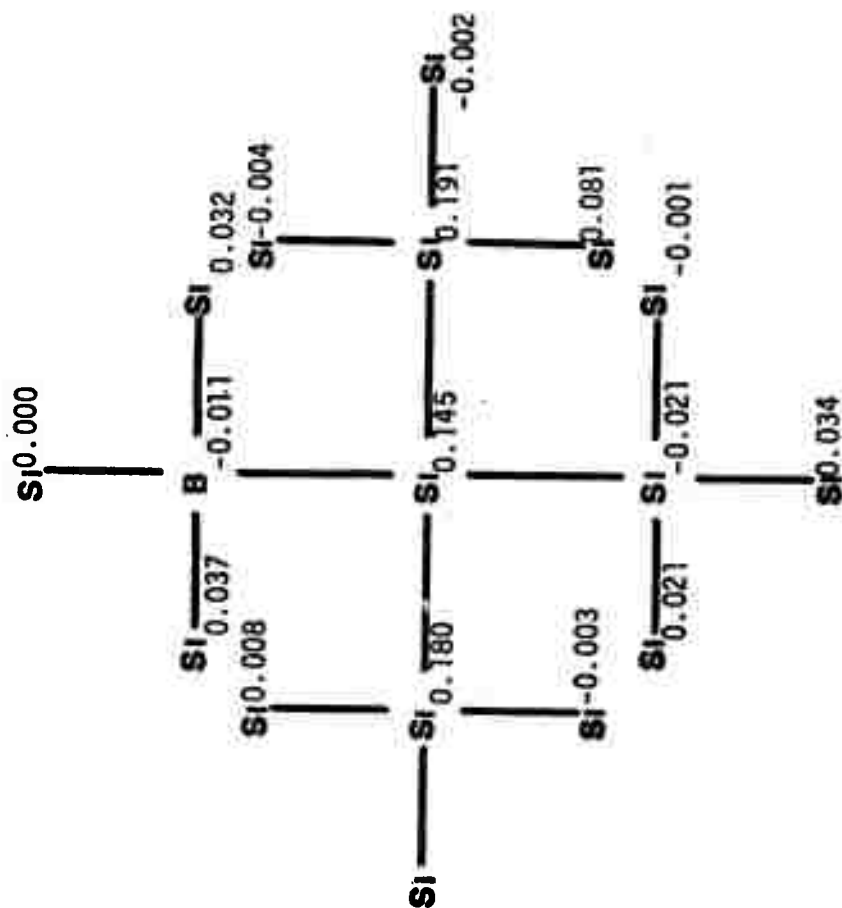


Figure 12B

Excess Spin Distribution on Atoms; Large Cluster, B Impurity Off-Center.







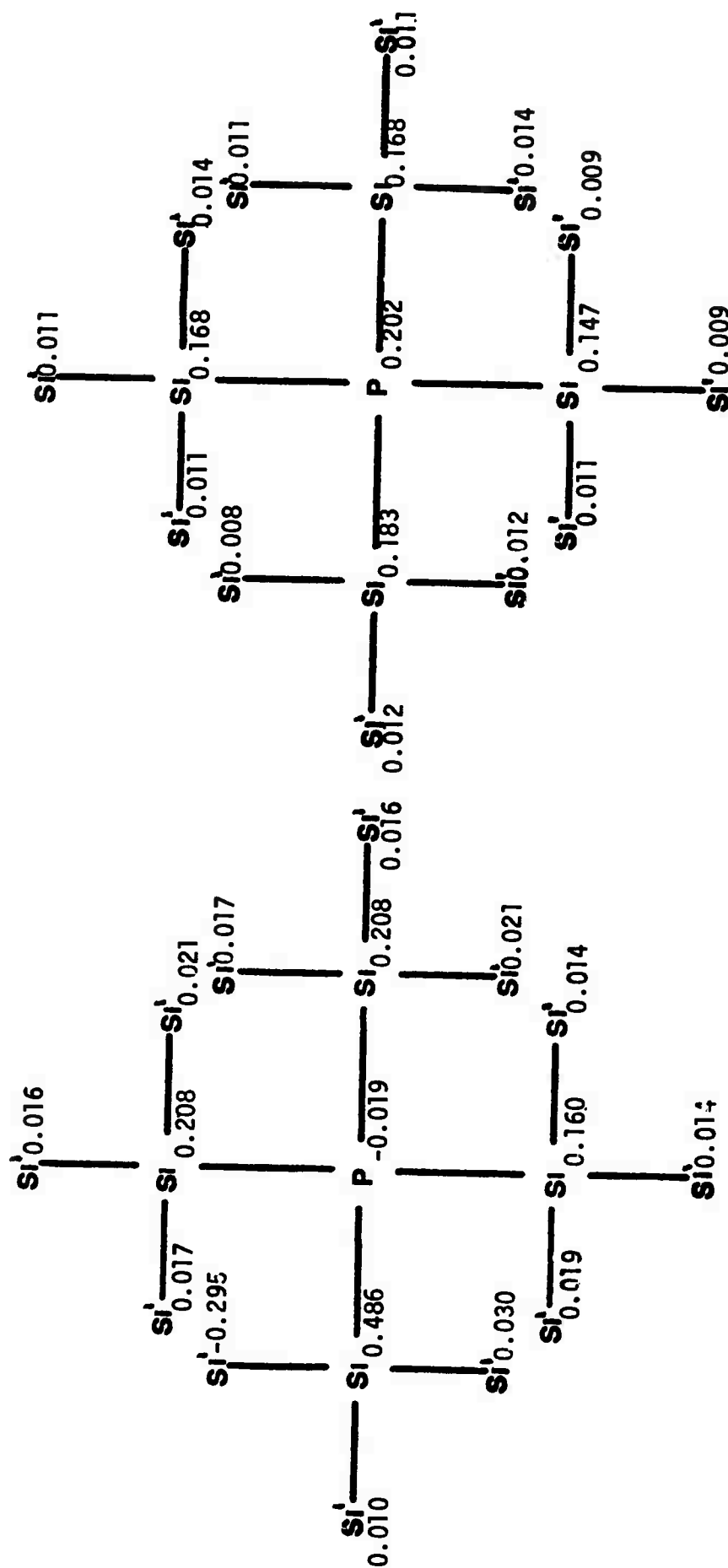


**Figure 14C**

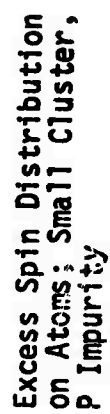


**Figure 14D**

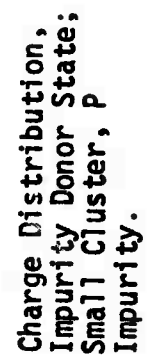
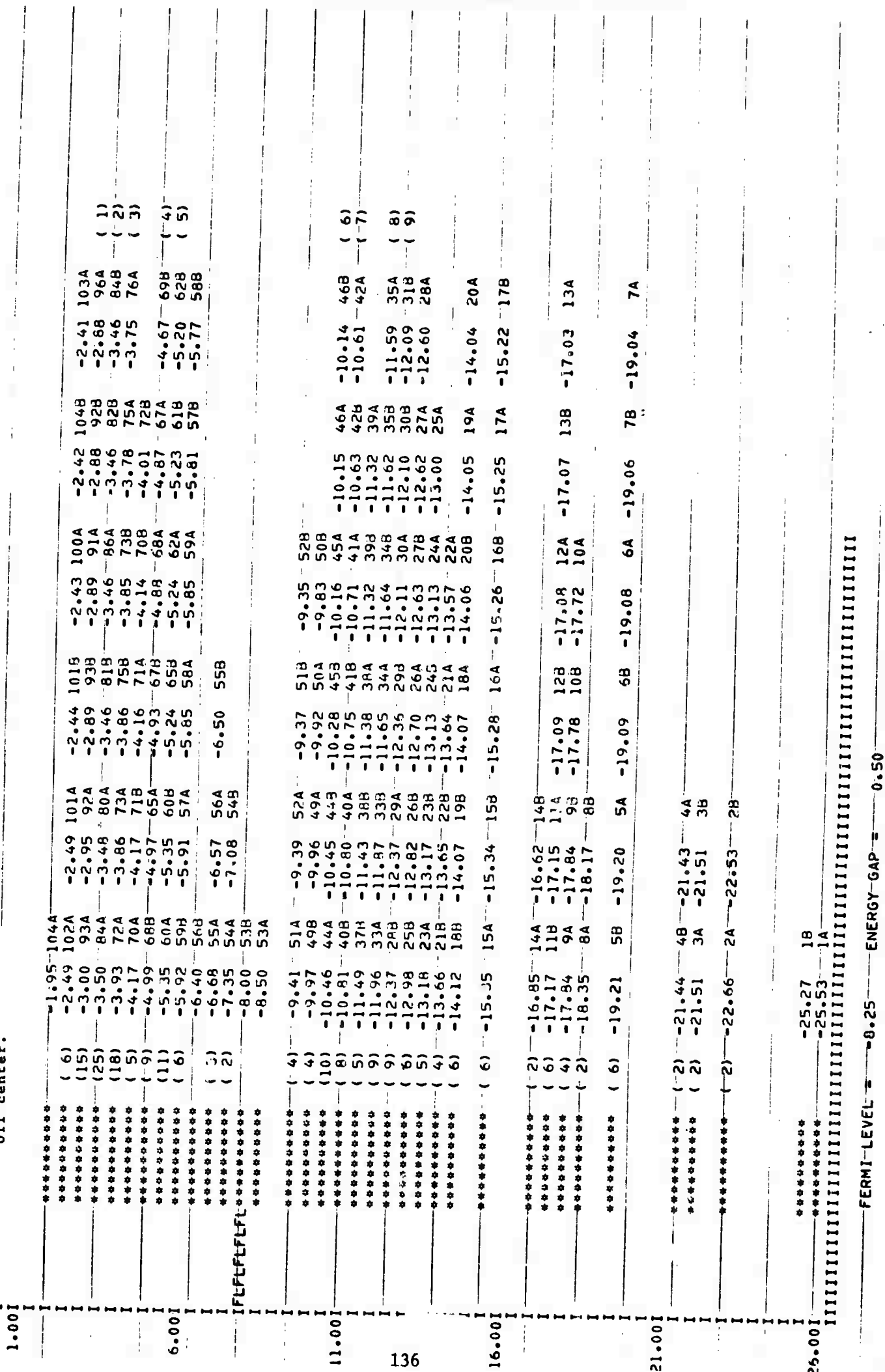


Fig. 15. Energy structure of  $\text{PSi}_{16}\text{Si}_{124}$  phosphorus off center. — EXCITATION FROM LEVEL 53A



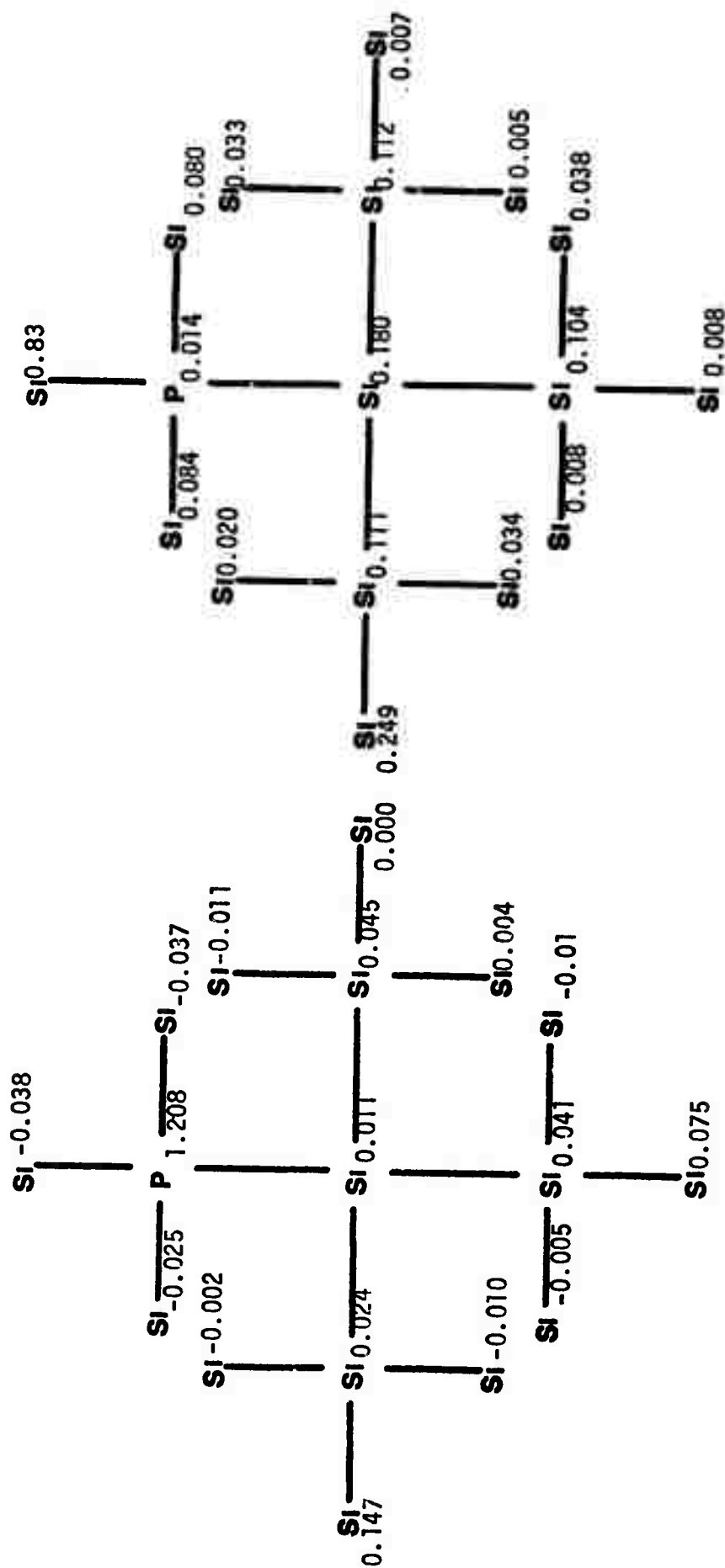


Figure 16A

Total Charge Excess  
on Atoms; Large Cluster,  
P Impurity Off-Center.

Figure 16B

Excess Spin Distribution  
on Atoms; Large Cluster  
P Impurity Off-Center.

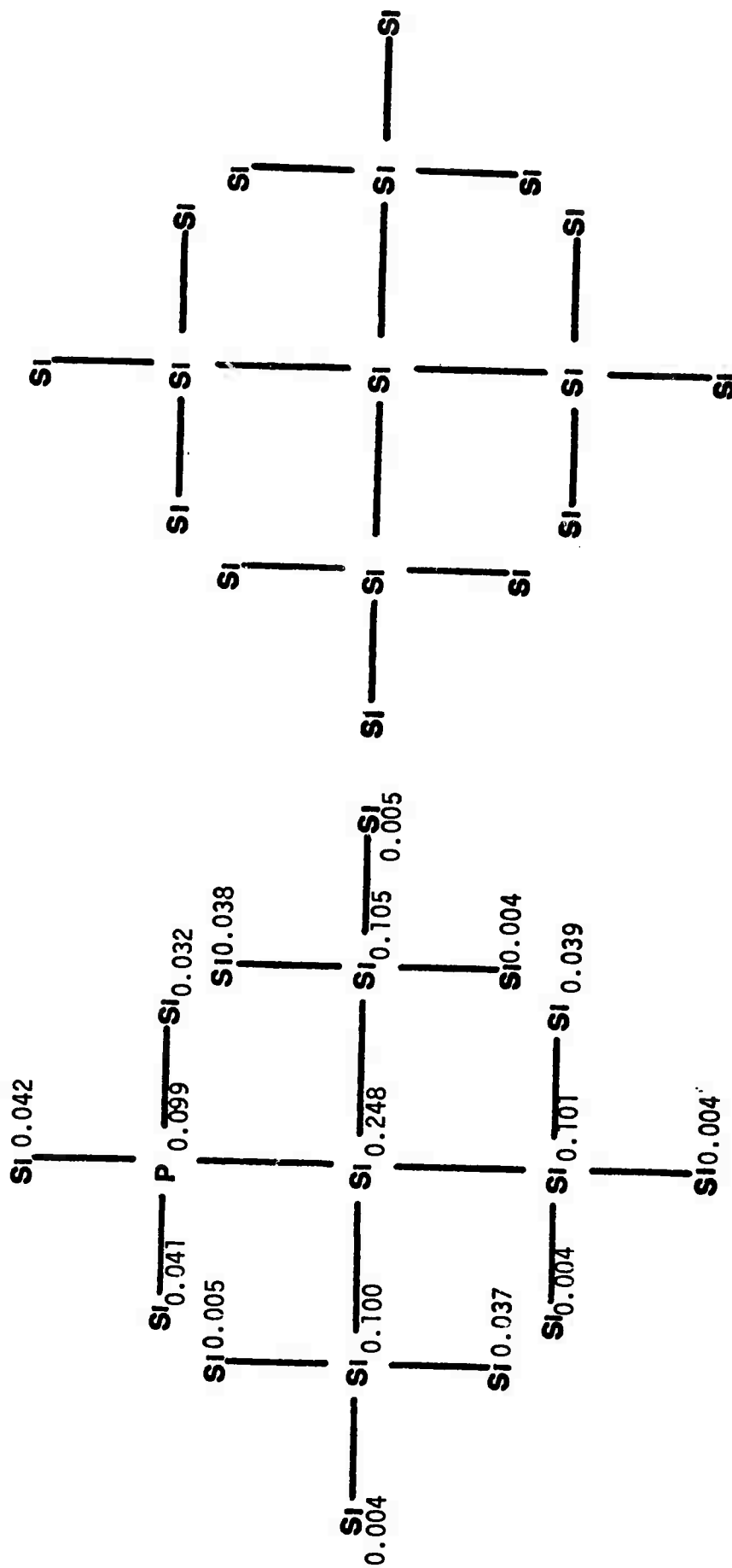


Figure 16C Charge Distribution,  
Impurity Donor State,  
Large Cluster, P Impurity  
Off-Center.



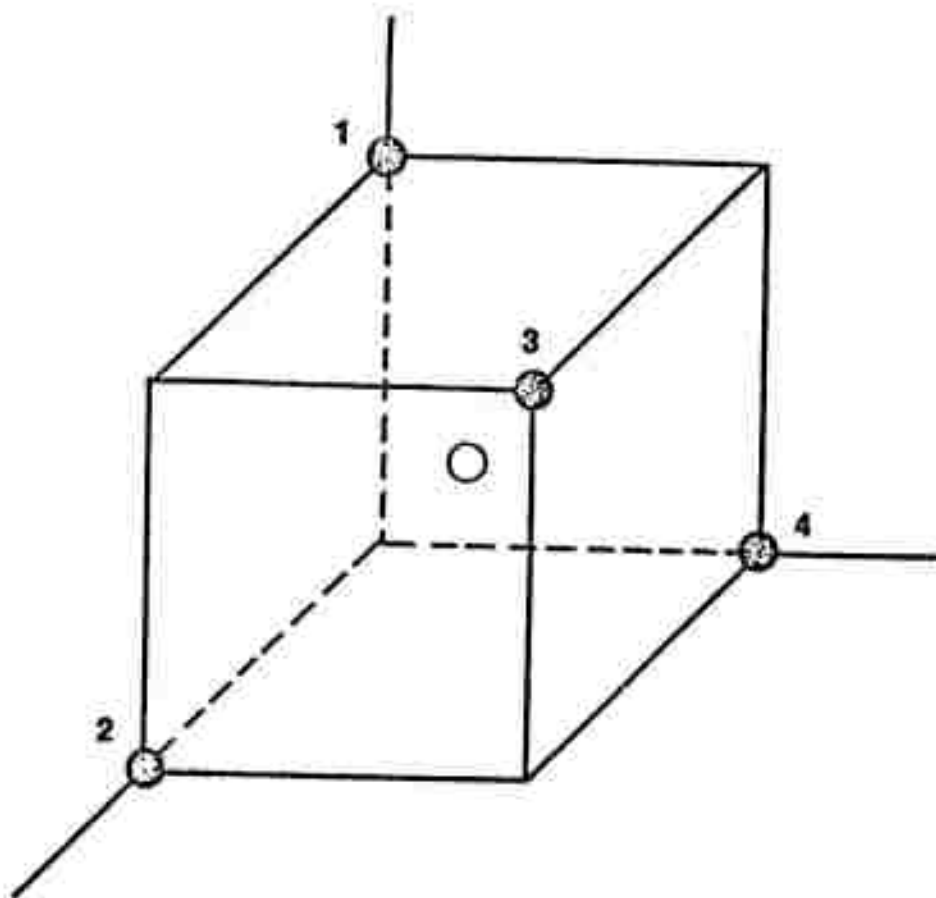


Figure 17A Atoms Surrounding a Vacancy.

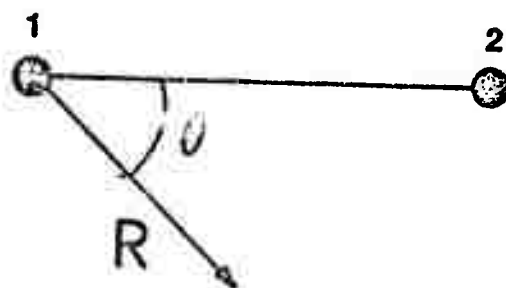


Figure 17B Coordinate System for Tetragonal Distortion of Atoms Surrounding Vacancy.

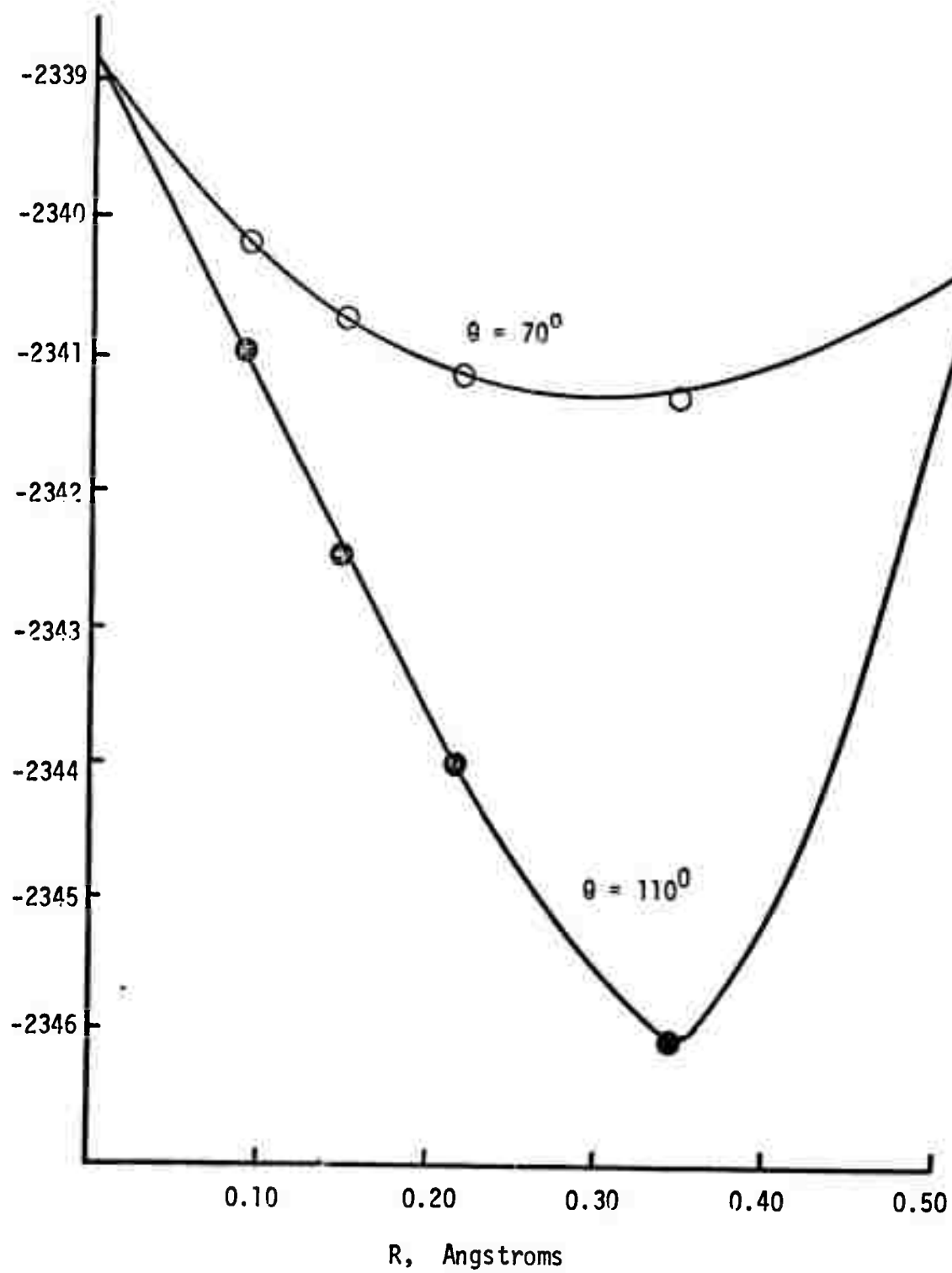
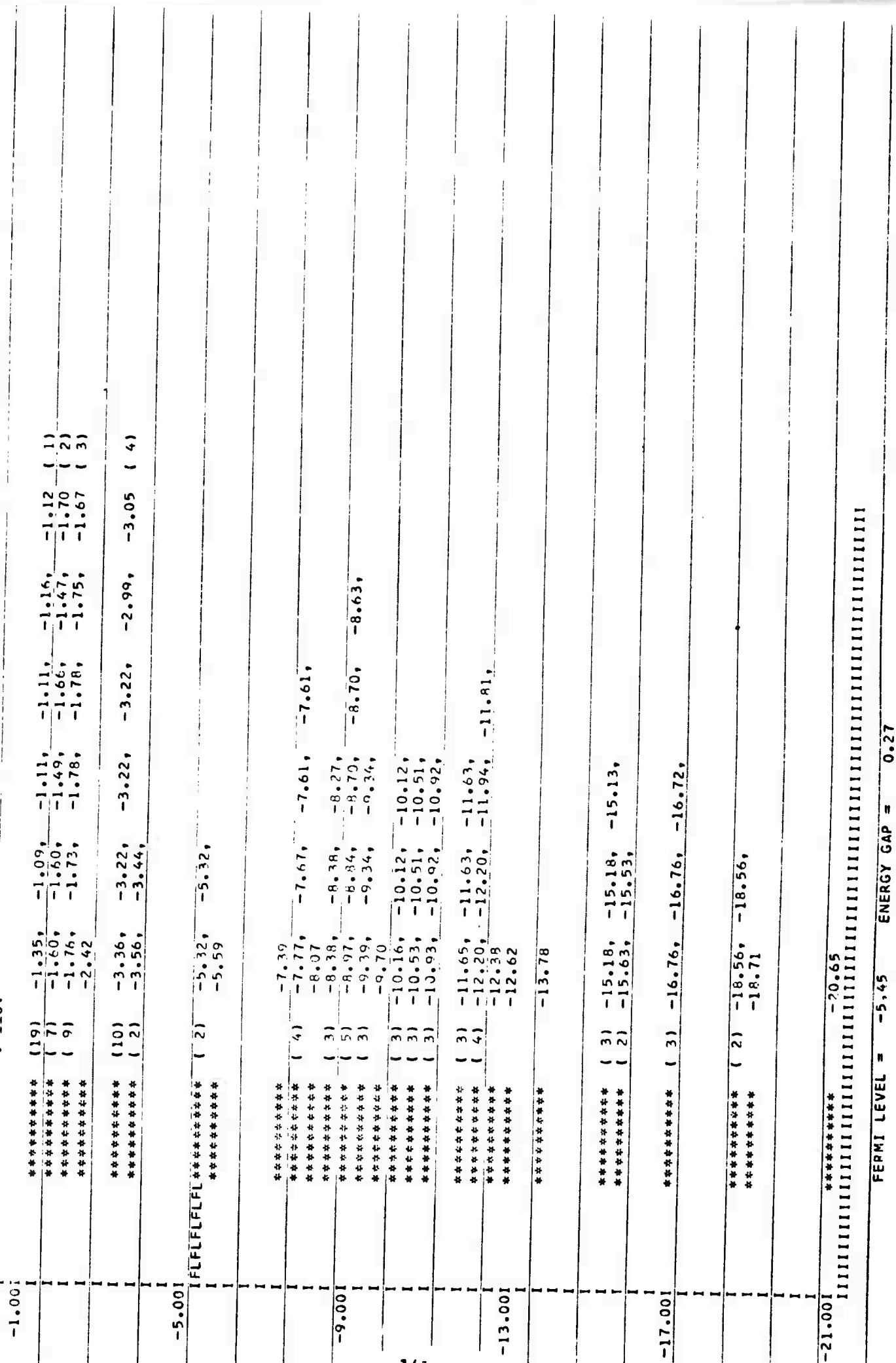


Figure 18 Potential Surface for Vacancy in Silicon.

Fig. 19. Energy structure  
of silicon vacancy  
cluster; R=0.35,  
 $\theta=110^\circ$ .



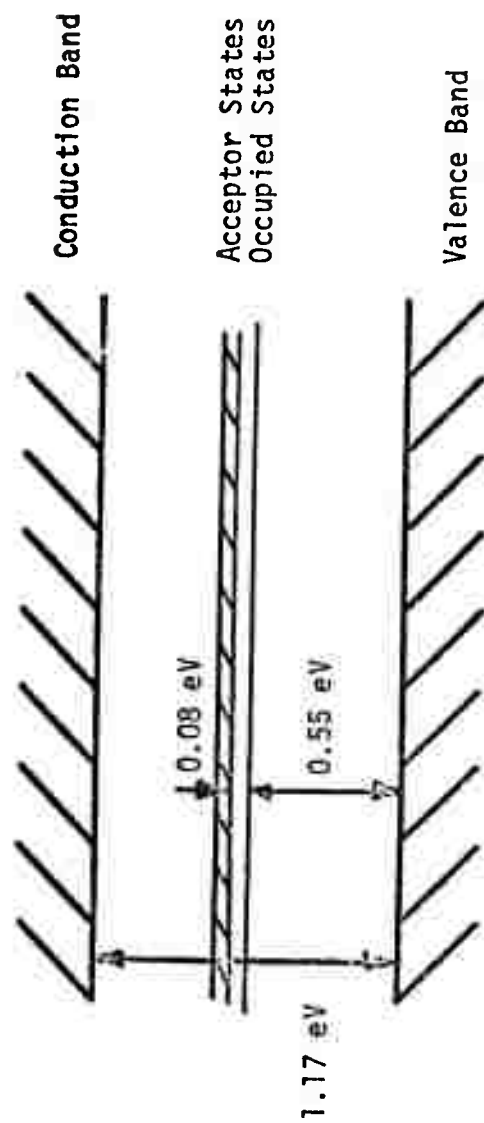


Figure 20 Scaled Energy Level Diagram of Vacancy.

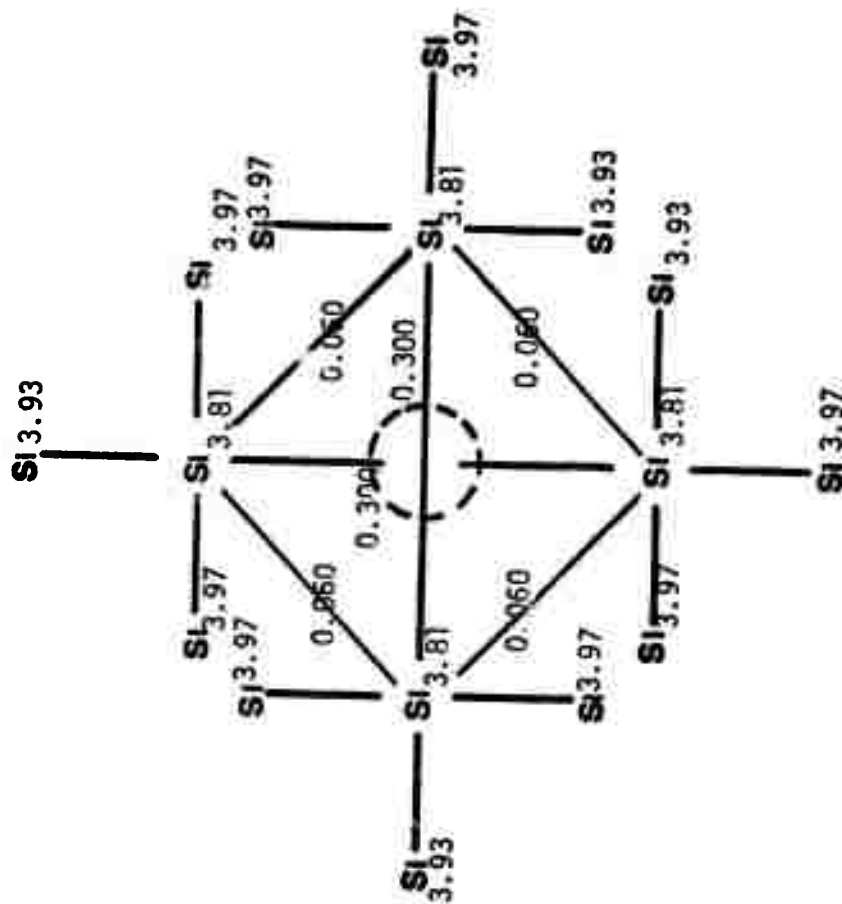


Figure 21A Charge Distribution on Atoms in Vacancy Cluster.

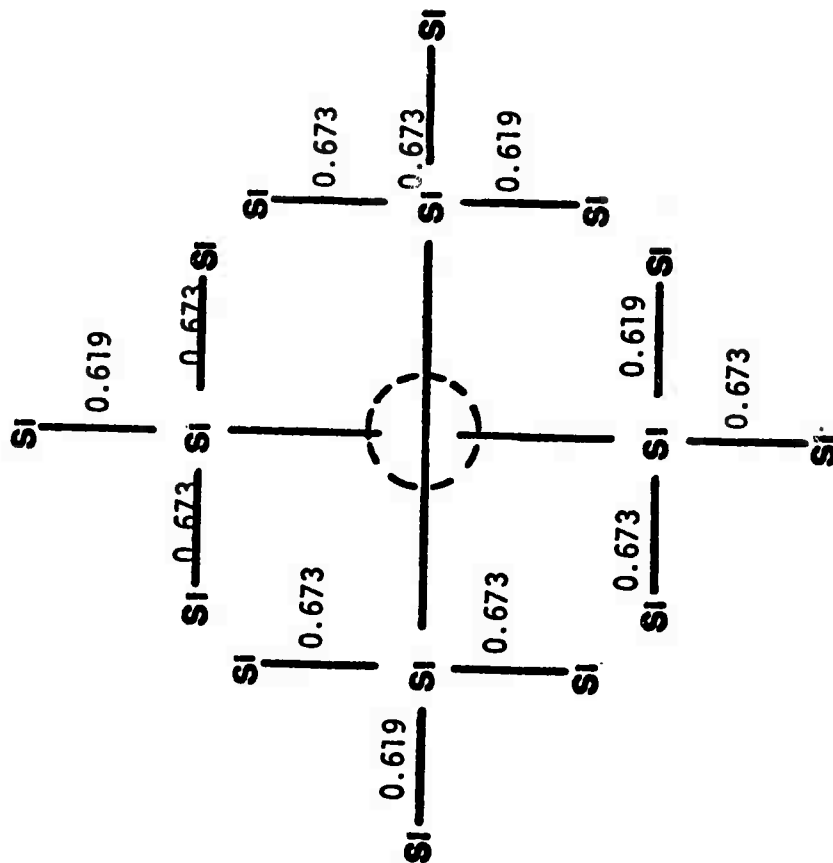


Figure 21B Bond Populations in Vacancy Cluster.

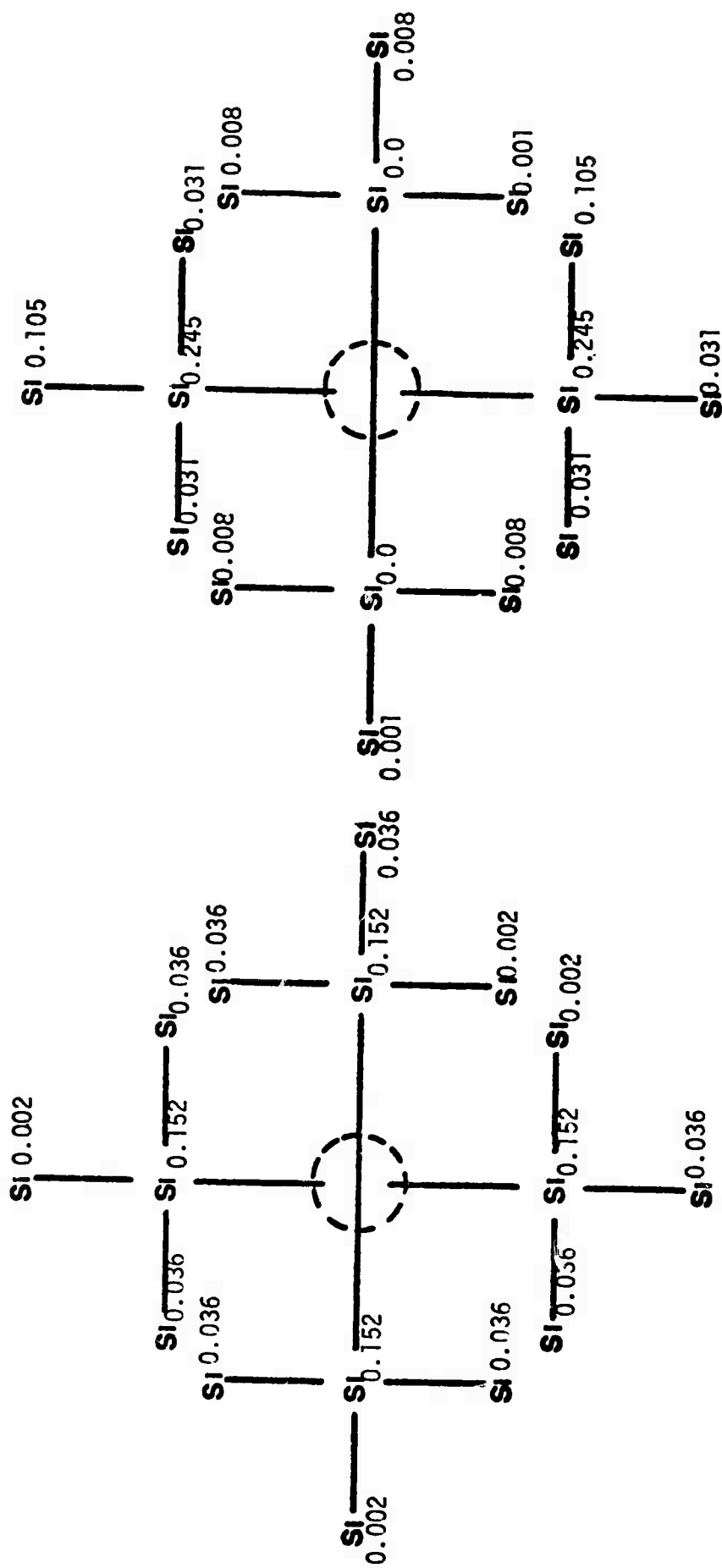


Figure 21C

Distribution of Charge  
in Highest Populated  
MO: Vacancy Cluster

Figure 21D

Distribution of Charge  
on Acceptor State Orbital:  
Vacancy Cluster.

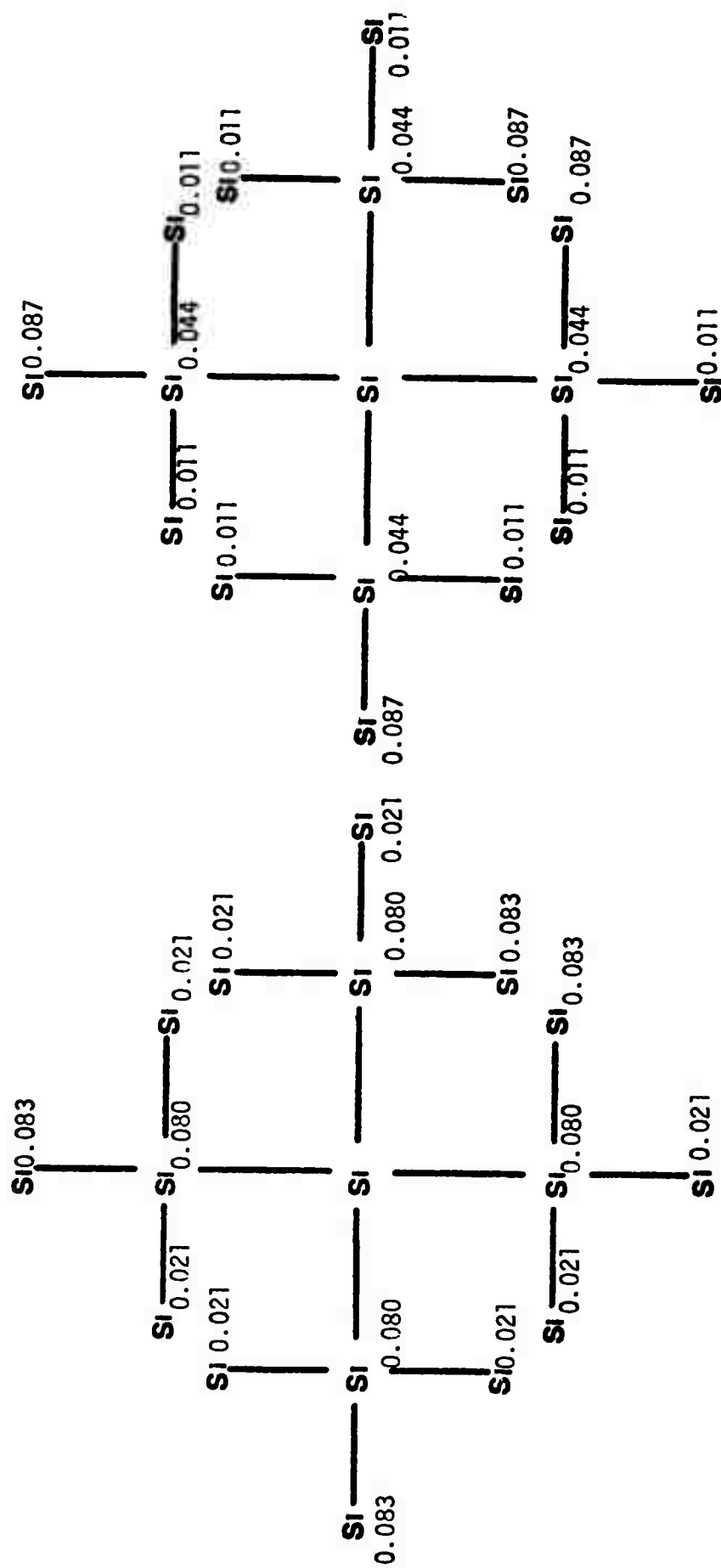


Figure 21E

Distribution of Charge  
in Highest Valence State:  
Vacancy Cluster.

Figure 21F

Distribution of Charge  
in Lowest Conduction State:  
Vacancy Cluster.





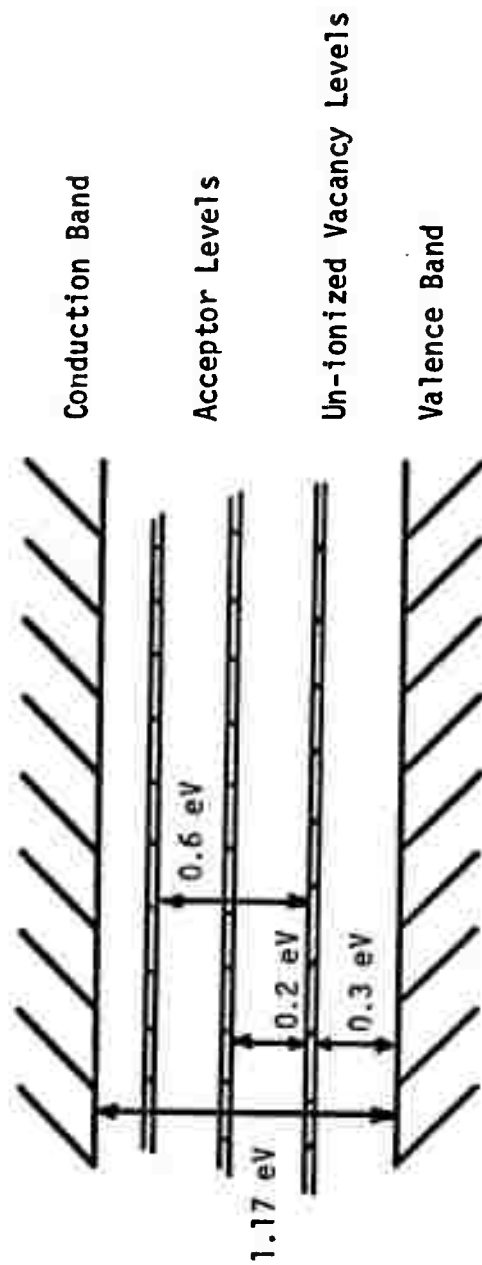


Figure 23 Scaled Energy Level Diagram: Vacancy Plus Boron Impurity: Nearest Neighbors.

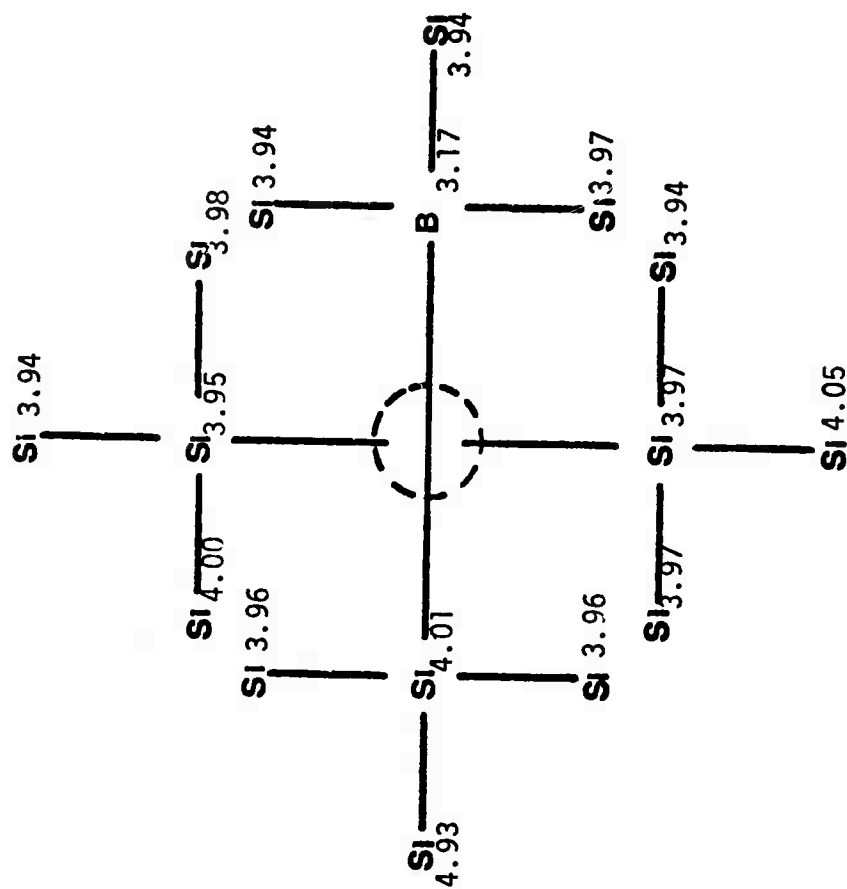


Figure 24A

Charge Distribution  
on Atoms: Vacancy +  
B Impurity: Nearest  
Neighbors.

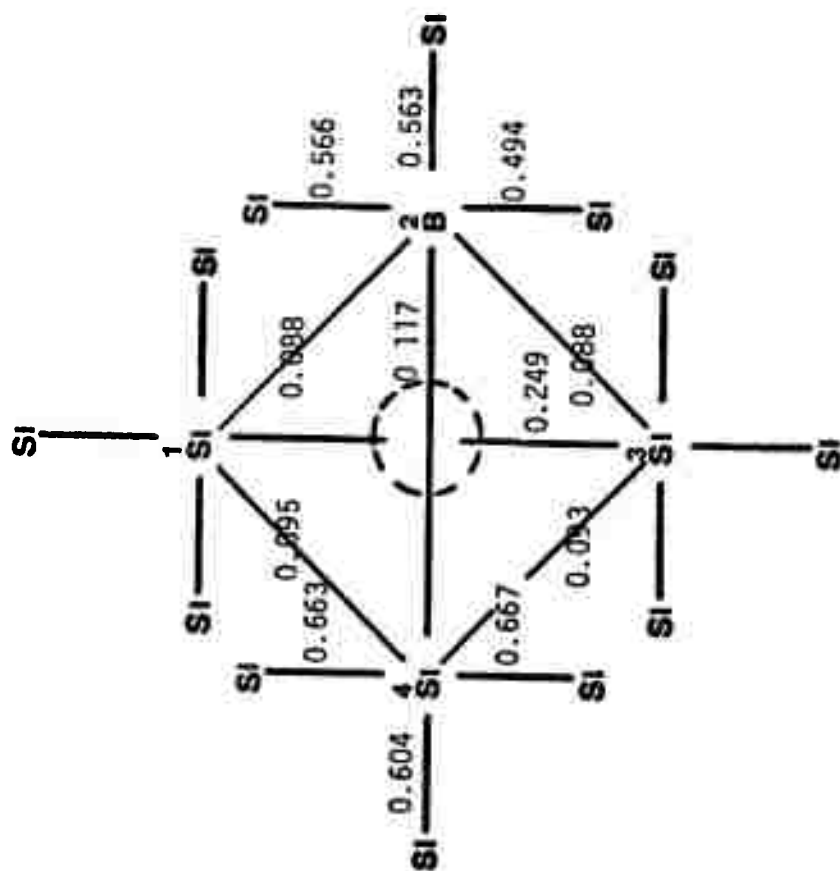


Figure 24B

Bond Populations:  
Vacancy + B Impurity  
Nearest Neighbors.

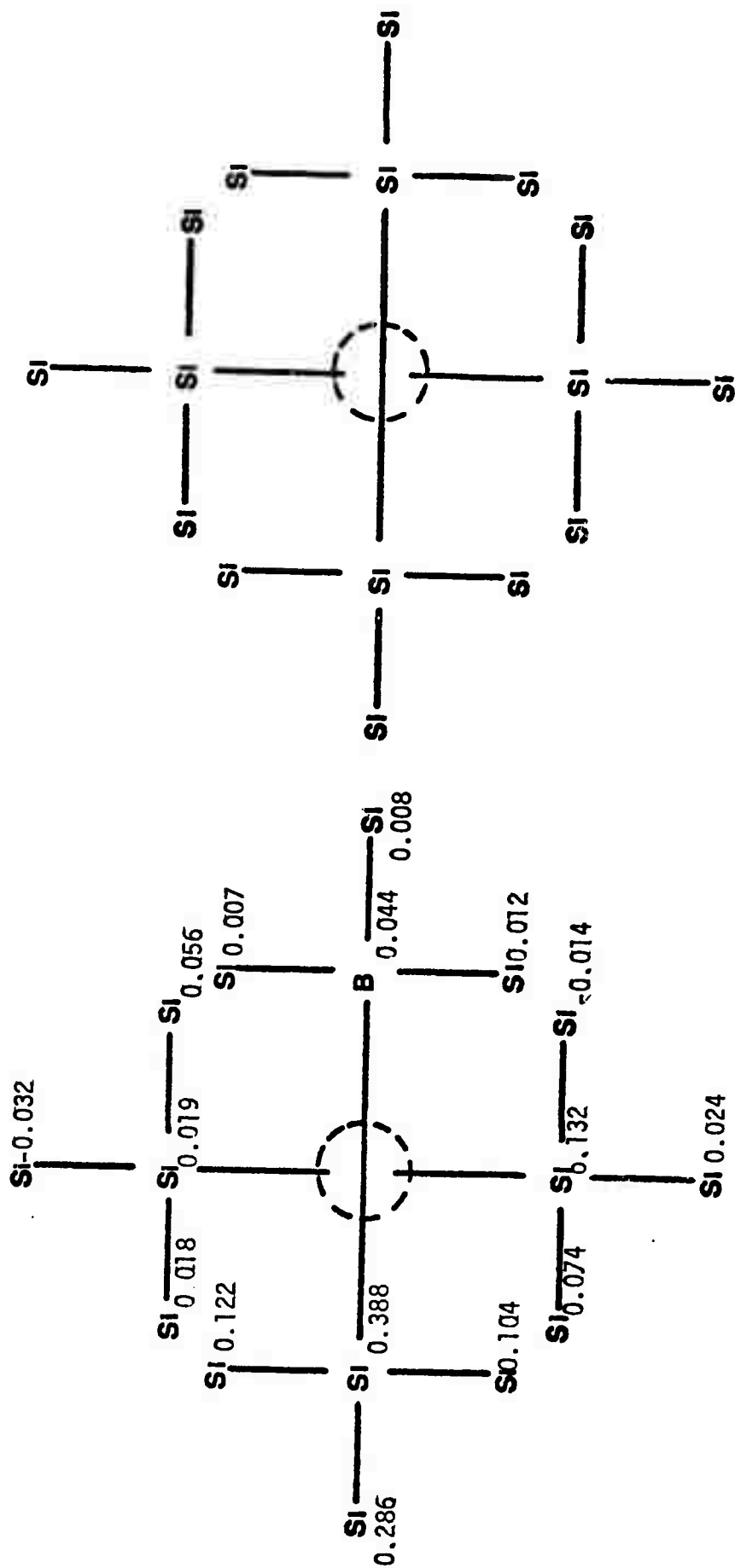


Figure 24C      Excess Spin on Atoms:  
 Vacancy + B Impurity;  
 Nearest Neighbors.



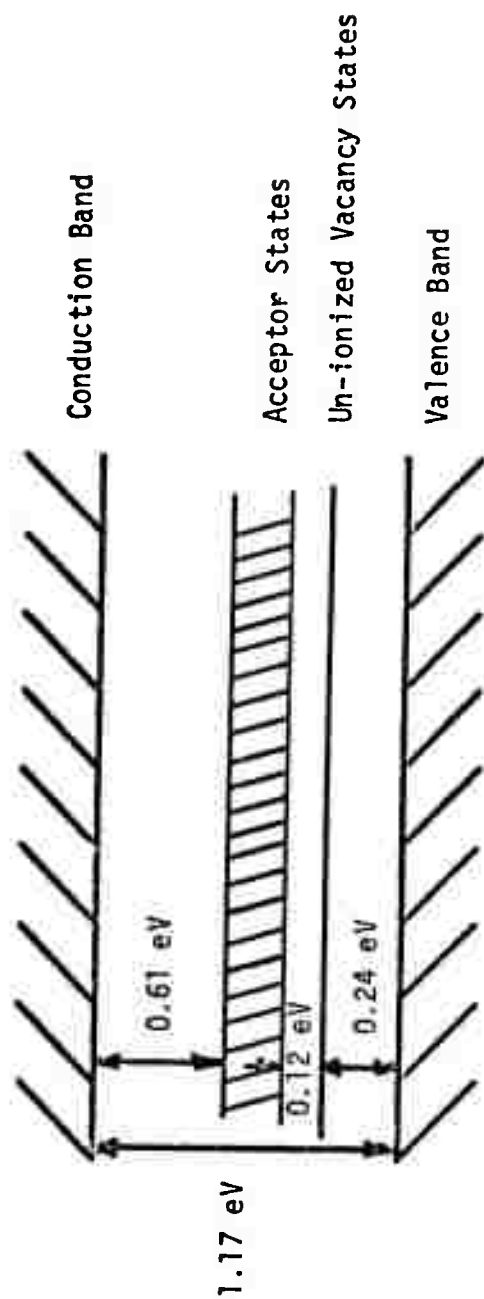


Figure 26 Scaled Energy Diagram for Vacancy Plus Boron Impurity: Next Nearest Neighbors.

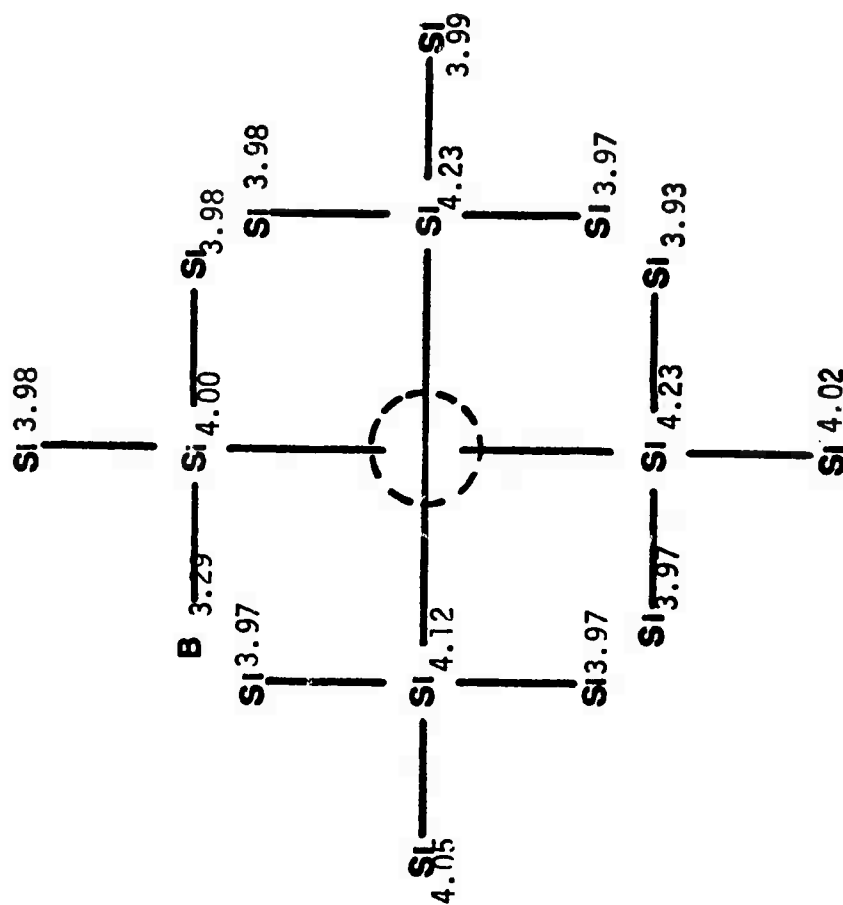


Figure 27A Charge Distribution on Atoms: Vacancy + B Impurity: Next Nearest Neighbors.

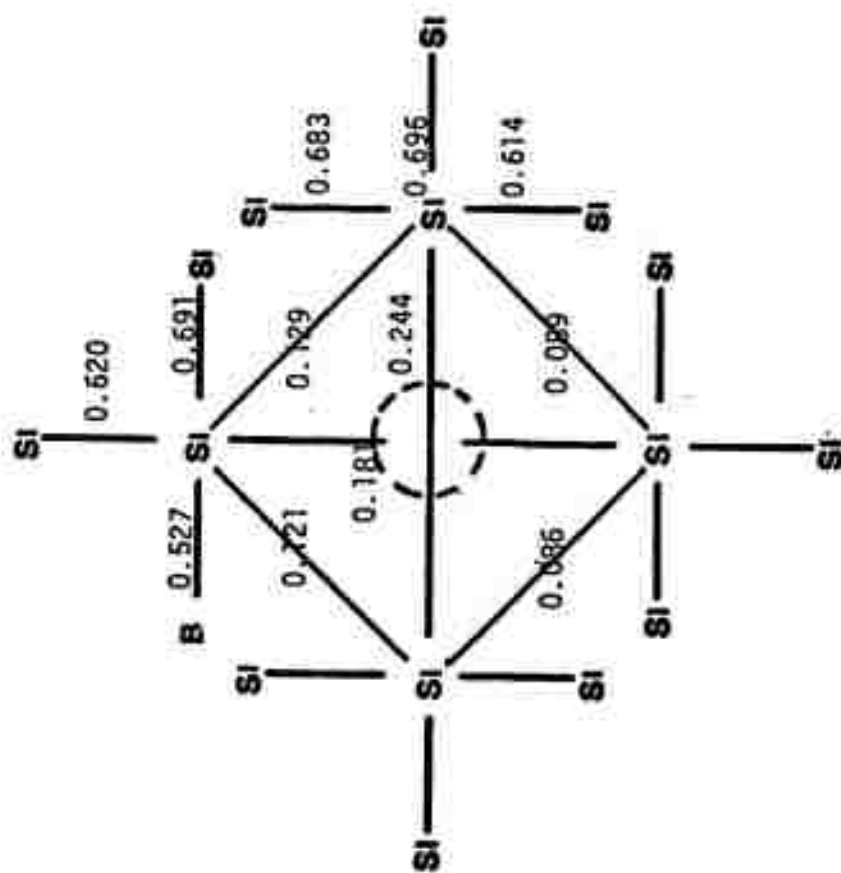


Figure 27B Bond Populations: Vacancy + B Impurity: Next Nearest Neighbors.

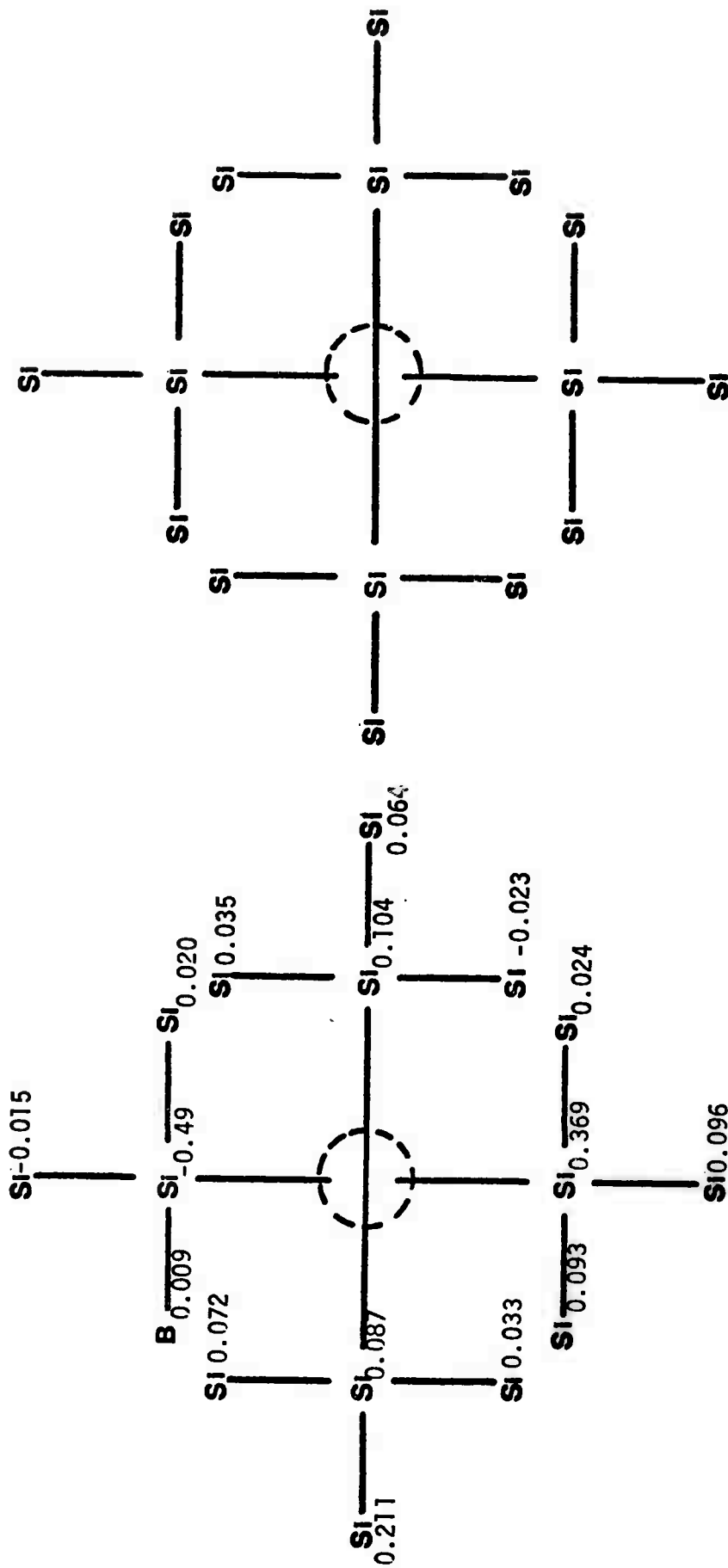


Figure 27C Excess Spin on Atoms:  
Vacancy + B Impurity:  
Next Nearest Neighbors.

# ENERGY LEVEL DIAGRAM - EXCITATION FROM LEVEL 51A

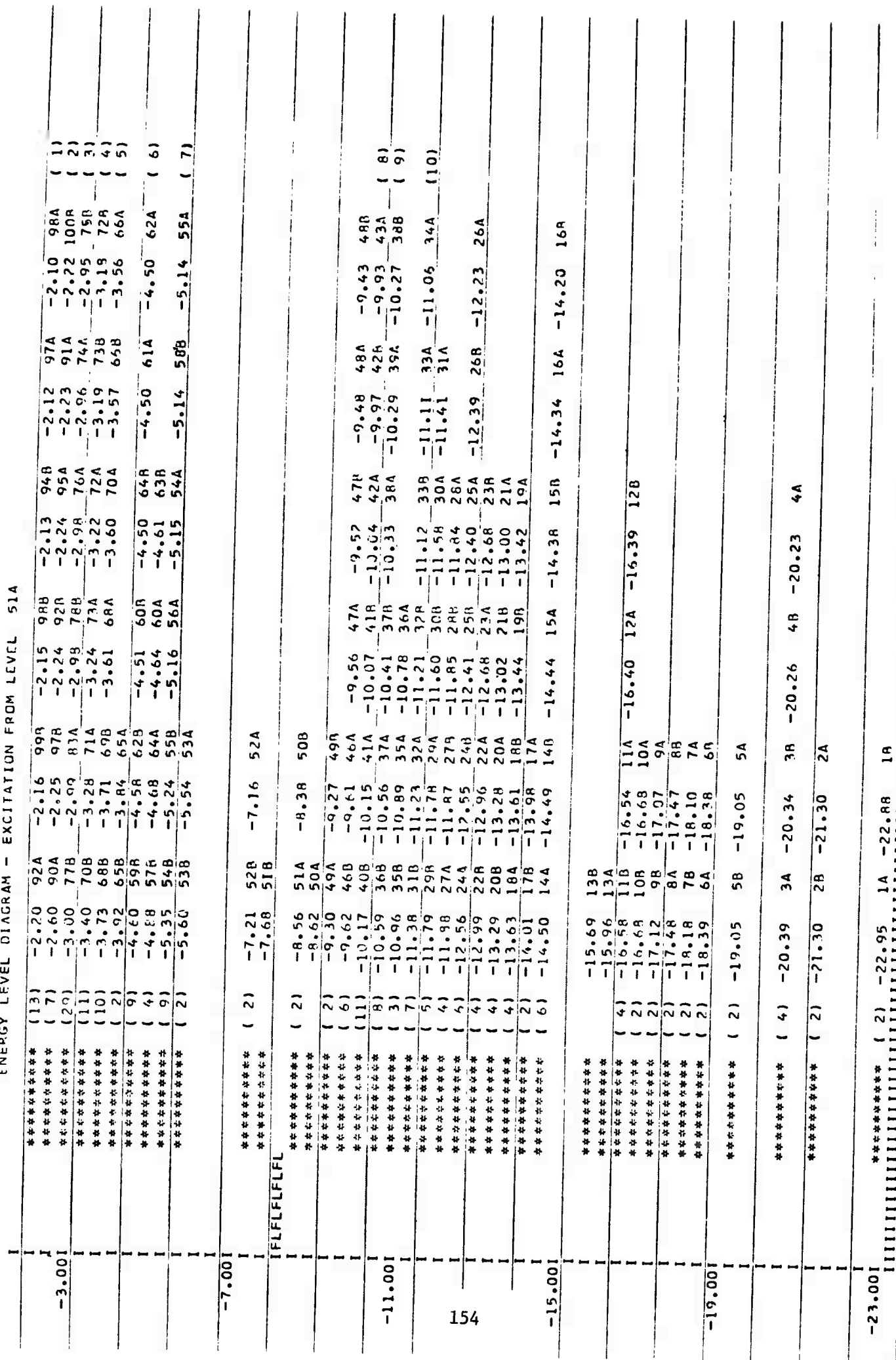


Fig. 28. Energy structure of silicon vacancy cluster with phosphorus in next nearest neighbor

FERMI LEVEL = -8.03 ENERGY GAP = 0.70



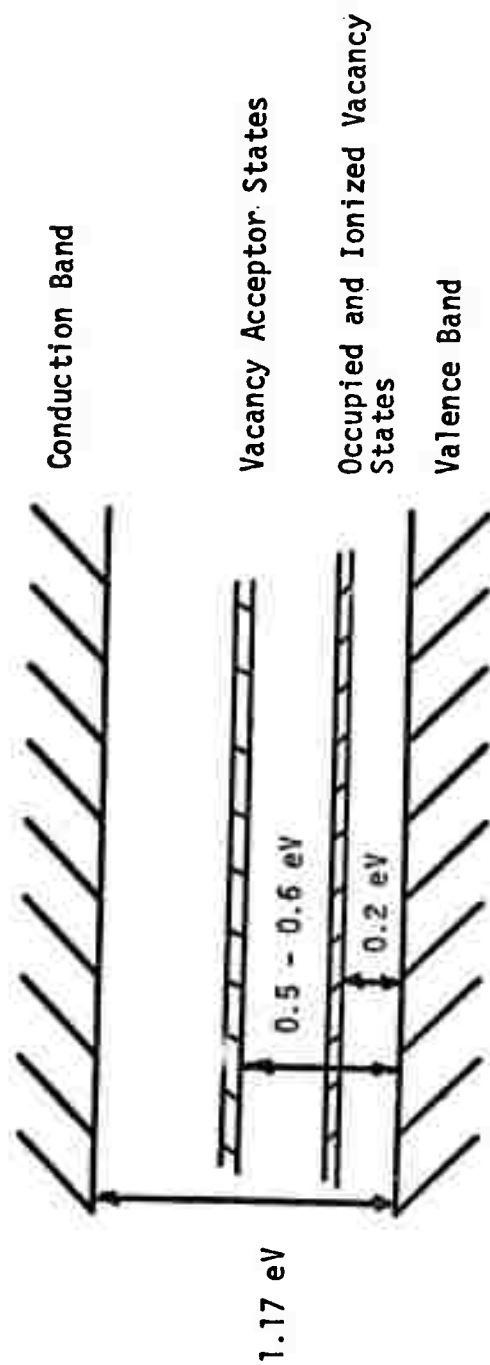


Figure 29 Scaled Energy Level Diagram: Vacancy Plus Phosphorus Impurity: Next Nearest Neighbors.

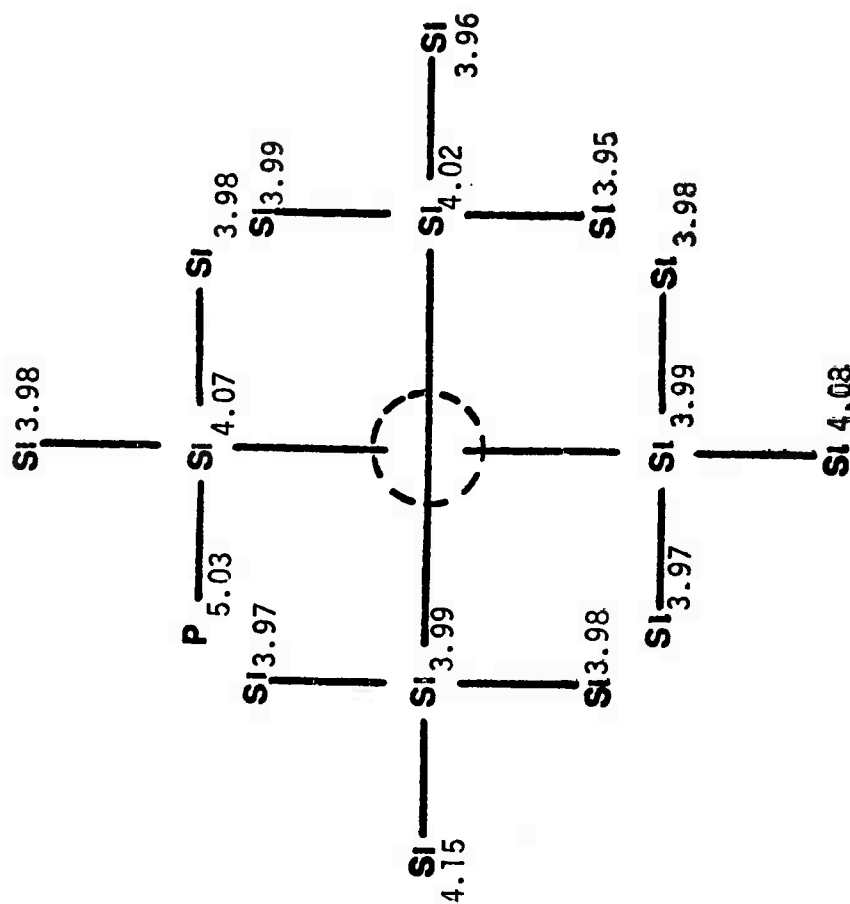


Figure 30A Charge Distribution on Atoms: Vacancy + P Impurity: Next Nearest Neighbors.

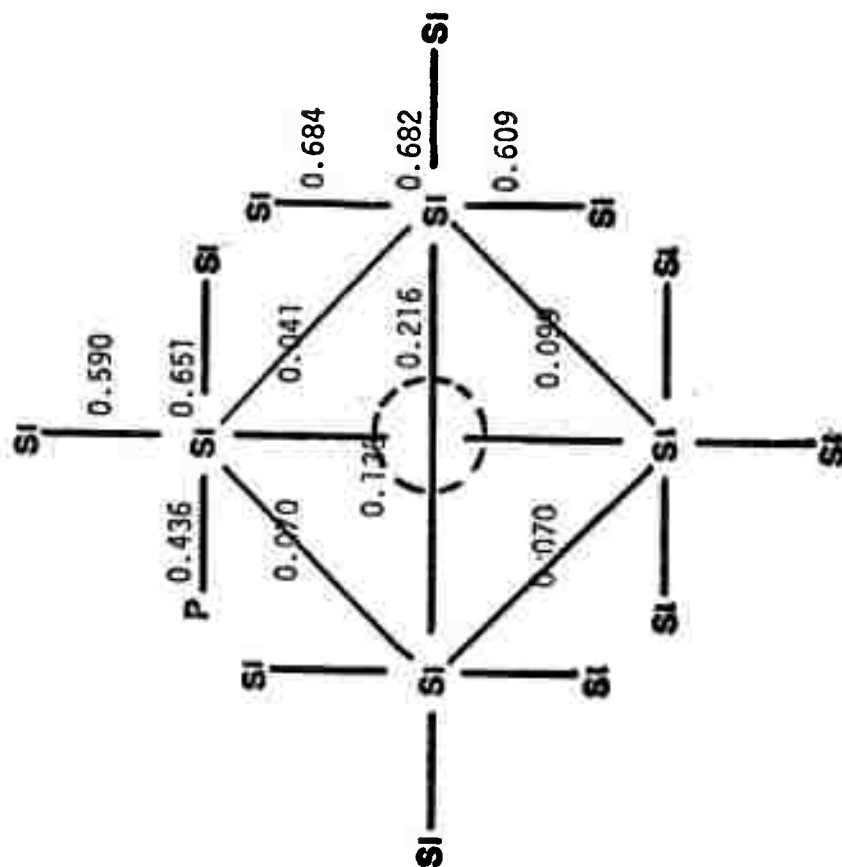


Figure 30B Bond Populations: Vacancy + P Impurity: Next Nearest Neighbors.

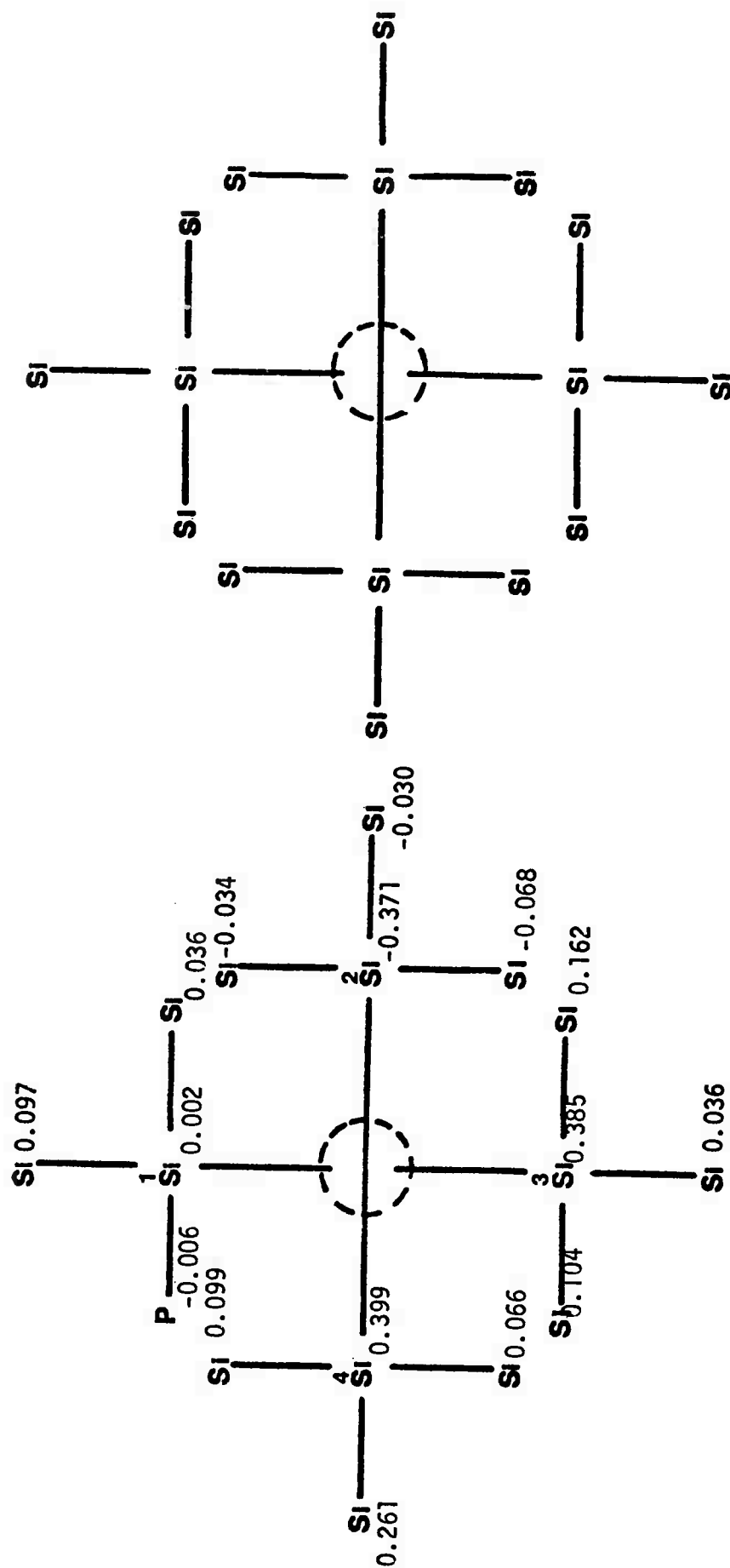


Figure 30C Excess Spin Population:  
Vacancy + P Impurity:  
Next Nearest Neighbors.

1

																																																																																																																																																																																																																																																																																																																																																																																																																																																																																																																																																																																																																																																																																																																																																																																																																																																																																																																																																																																																																																																																																																																																																																																																																																																																																																																																																																																																																																																			</
--	--	--	--	--	--	--	--	--	--	--	--	--	--	--	--	--	--	--	--	--	--	--	--	--	--	--	--	--	--	--	--	--	--	--	--	--	--	--	--	--	--	--	--	--	--	--	--	--	--	--	--	--	--	--	--	--	--	--	--	--	--	--	--	--	--	--	--	--	--	--	--	--	--	--	--	--	--	--	--	--	--	--	--	--	--	--	--	--	--	--	--	--	--	--	--	--	--	--	--	--	--	--	--	--	--	--	--	--	--	--	--	--	--	--	--	--	--	--	--	--	--	--	--	--	--	--	--	--	--	--	--	--	--	--	--	--	--	--	--	--	--	--	--	--	--	--	--	--	--	--	--	--	--	--	--	--	--	--	--	--	--	--	--	--	--	--	--	--	--	--	--	--	--	--	--	--	--	--	--	--	--	--	--	--	--	--	--	--	--	--	--	--	--	--	--	--	--	--	--	--	--	--	--	--	--	--	--	--	--	--	--	--	--	--	--	--	--	--	--	--	--	--	--	--	--	--	--	--	--	--	--	--	--	--	--	--	--	--	--	--	--	--	--	--	--	--	--	--	--	--	--	--	--	--	--	--	--	--	--	--	--	--	--	--	--	--	--	--	--	--	--	--	--	--	--	--	--	--	--	--	--	--	--	--	--	--	--	--	--	--	--	--	--	--	--	--	--	--	--	--	--	--	--	--	--	--	--	--	--	--	--	--	--	--	--	--	--	--	--	--	--	--	--	--	--	--	--	--	--	--	--	--	--	--	--	--	--	--	--	--	--	--	--	--	--	--	--	--	--	--	--	--	--	--	--	--	--	--	--	--	--	--	--	--	--	--	--	--	--	--	--	--	--	--	--	--	--	--	--	--	--	--	--	--	--	--	--	--	--	--	--	--	--	--	--	--	--	--	--	--	--	--	--	--	--	--	--	--	--	--	--	--	--	--	--	--	--	--	--	--	--	--	--	--	--	--	--	--	--	--	--	--	--	--	--	--	--	--	--	--	--	--	--	--	--	--	--	--	--	--	--	--	--	--	--	--	--	--	--	--	--	--	--	--	--	--	--	--	--	--	--	--	--	--	--	--	--	--	--	--	--	--	--	--	--	--	--	--	--	--	--	--	--	--	--	--	--	--	--	--	--	--	--	--	--	--	--	--	--	--	--	--	--	--	--	--	--	--	--	--	--	--	--	--	--	--	--	--	--	--	--	--	--	--	--	--	--	--	--	--	--	--	--	--	--	--	--	--	--	--	--	--	--	--	--	--	--	--	--	--	--	--	--	--	--	--	--	--	--	--	--	--	--	--	--	--	--	--	--	--	--	--	--	--	--	--	--	--	--	--	--	--	--	--	--	--	--	--	--	--	--	--	--	--	--	--	--	--	--	--	--	--	--	--	--	--	--	--	--	--	--	--	--	--	--	--	--	--	--	--	--	--	--	--	--	--	--	--	--	--	--	--	--	--	--	--	--	--	--	--	--	--	--	--	--	--	--	--	--	--	--	--	--	--	--	--	--	--	--	--	--	--	--	--	--	--	--	--	--	--	--	--	--	--	--	--	--	--	--	--	--	--	--	--	--	--	--	--	--	--	--	--	--	--	--	--	--	--	--	--	--	--	--	--	--	--	--	--	--	--	--	--	--	--	--	--	--	--	--	--	--	--	--	--	--	--	--	--	--	--	--	--	--	--	--	--	--	--	--	--	--	--	--	--	--	--	--	--	--	--	--	--	--	--	--	--	--	--	--	--	--	--	--	--	--	--	--	--	--	--	--	--	--	--	--	--	--	--	--	--	--	--	--	--	--	--	--	--	--	--	--	--	--	--	--	--	--	--	--	--	--	--	--	--	--	--	--	--	--	--	--	--	--	--	--	--	--	--	--	--	--	--	--	--	--	--	--	--	--	--	--	--	--	--	--	--	--	--	--	--	--	--	--	--	--	--	--	--	--	--	--	--	--	--	--	--	--	--	--	--	--	--	--	--	--	--	--	--	--	--	--	--	--	--	--	--	--	--	--	--	--	--	--	--	--	--	--	--	--	--	--	--	--	--	--	--	--	--	--	--	--	--	--	--	--	--	--	--	--	--	--	--	--	--	--	--	--	--	--	--	--	--	--	--	--	--	--	--	--	--	--	--	--	--	--	--	--	--	--	--	--	--	--	--	--	--	--	--	--	--	--	--	--	--	--	--	--	--	--	--	--	--	--	--	--	--	--	--	--	--	--	--	--	--	--	--	--	--	--	--	--	--	--	--	--	--	--	--	--	--	--	--	--	--	--	--	--	--	--	--	--	--	--	--	--	--	--	--	--	--	--	--	--	--	--	--	--	--	--	--	--	--	--	--	--	--	--	--	--	--	--	--	--	--	--	--	--	--	--	--	--	--	--	--	--	--	--	--	--	--	--	--	--	--	--	--	--	--	--	--	--	--	--	--	--	--	--	--	--	--	--	--	--	--	--	--	--	--	--	--	--	--	--	--	--	--	--	--	--	--	--	--	--	--	--	--	--	--	--	--	--	--	--	--	--	--	--	--	--	--	--	--	--	--	--	--	--	--	--	--	--	--	--	--	--	--	--	--	--	--	--	--	--	--	--	--	--	--	--	--	--	--	--	--	--	--	--	--	--	--	--	--	--	--	--	--	--	--	--	--	--	--	--	--	--	--	--	--	--	--	--	--	--	--	--	--	--	--	--	--	--	--	--	--	--	--	--	--	--	--	--	--	--	--	--	--	--	--	--	--	--	--	--	--	--	--	--	--	--	--	--	--	--	--	--	--	--	--	--	--	--	--	--	--	--	--	--	--	--	--	--	--	--	--	--	--	--	--	--	--	--	--	--	--	--	--	--	--	--	--	--	--	--	--	--	--	--	--	--	--	--	--	--	--	--	--	--	--	--	--	--	--	--	--	--	--	--	--	--	--	--	--	--	--	--	--	--	--	--	--	--	--	--	--	--	--	--	--	--	--	--	--	--	--	--	--	--	--	--	--	--	--	--	--	--	--	--	--	--	--	--	--	--	--	--	--	--	--	--	--	--	--	--	--	--	--	--	--	--	--	--	--	--	--	--	--	--	--	--	--	--	--	--	--	--	--	--	--	--	--	--	--	--	--	--	--	--	--	--	--	--	--	--	--	--	--	--	--	--	--	--	--	--	--	----

of silicon cluster  
with 2 boron  
impurities next  
nearest neighbors.

0.0	*****	( 5)	-0.40,	-0.20,	-0.14,	-0.10,	-0.11,
	*****		-0.60				
	*****	( 6)	-1.36,	-1.47,	-1.36,	-1.46,	-1.21,
	*****	( 7)	-1.80,	-1.69,	-1.84,	-1.80,	-1.81,
	*****	(12)	-2.36,	-2.24,	-2.16,	-2.29,	-2.27
	*****	( 6)	-2.80,	-2.78,	-2.73,	-2.47,	-2.58,
	*****	( 6)	-3.35,	-3.25,	-3.29,	-3.34,	-3.35,
	*****	( 2)	-3.69,	-3.67,			-3.04
	*****	( 5)	-4.34,	-4.27,	-4.03,	-4.13,	-4.36,
-5.00	*****		-5.29				
	*****		-5.54				

	IFLFLFLFL	*****	-7.99
	*****	( 2)	-8.34,
	*****	( 7)	-8.98,
	*****	( 3)	-9.30,
	*****	( 5)	-9.82,
	*****	( 5)	-10.47,
	*****	( 3)	-10.84,
	*****	( 4)	-11.48,
	*****	( 2)	-11.68,
	*****	( 3)	-12.35,
	*****	( 4)	-13.00,
	*****		-13.10

	*****	( 3)	-14.44
	*****	( 3)	-14.60,
	*****	( 3)	-16.39,
	*****	( 7)	-16.99,
	*****		-17.03
	*****	( 3)	-18.39,
	*****	( 3)	-18.32,
	*****		-18.16,

	*****		-20.86
	*****		-21.19
	*****		-21.62

	*****		-24.58
--	-------	--	--------

FERMI LEVEL = -8.17 ENERGY GAP = 0.35

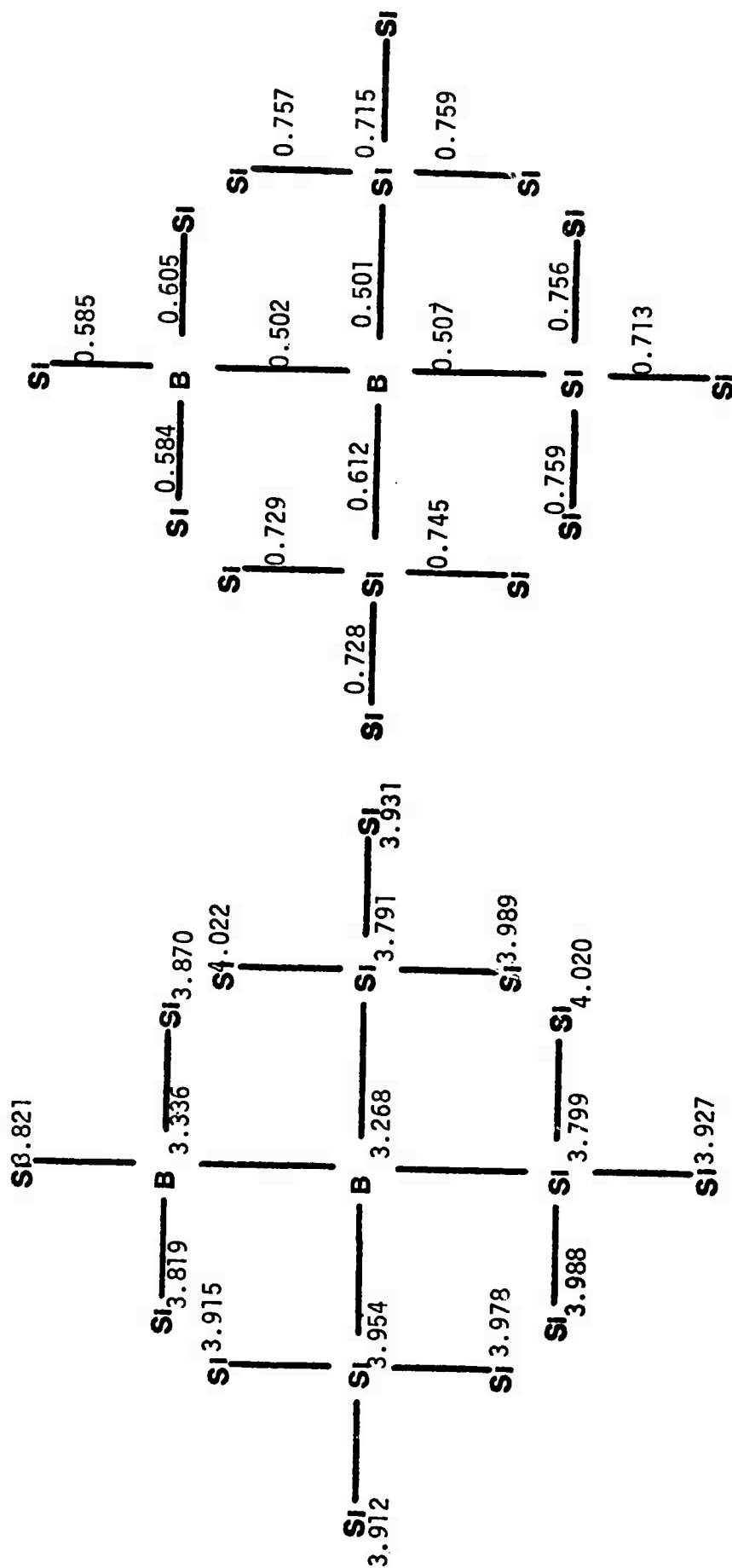


Figure 33A Charge Distribution on Atoms: Silicon Cluster with 2 Boron Nearest Neighbor Impurities.

Figure 33B Bond Populations: Silicon Cluster with 2 Boron Nearest Neighbor Impurities.

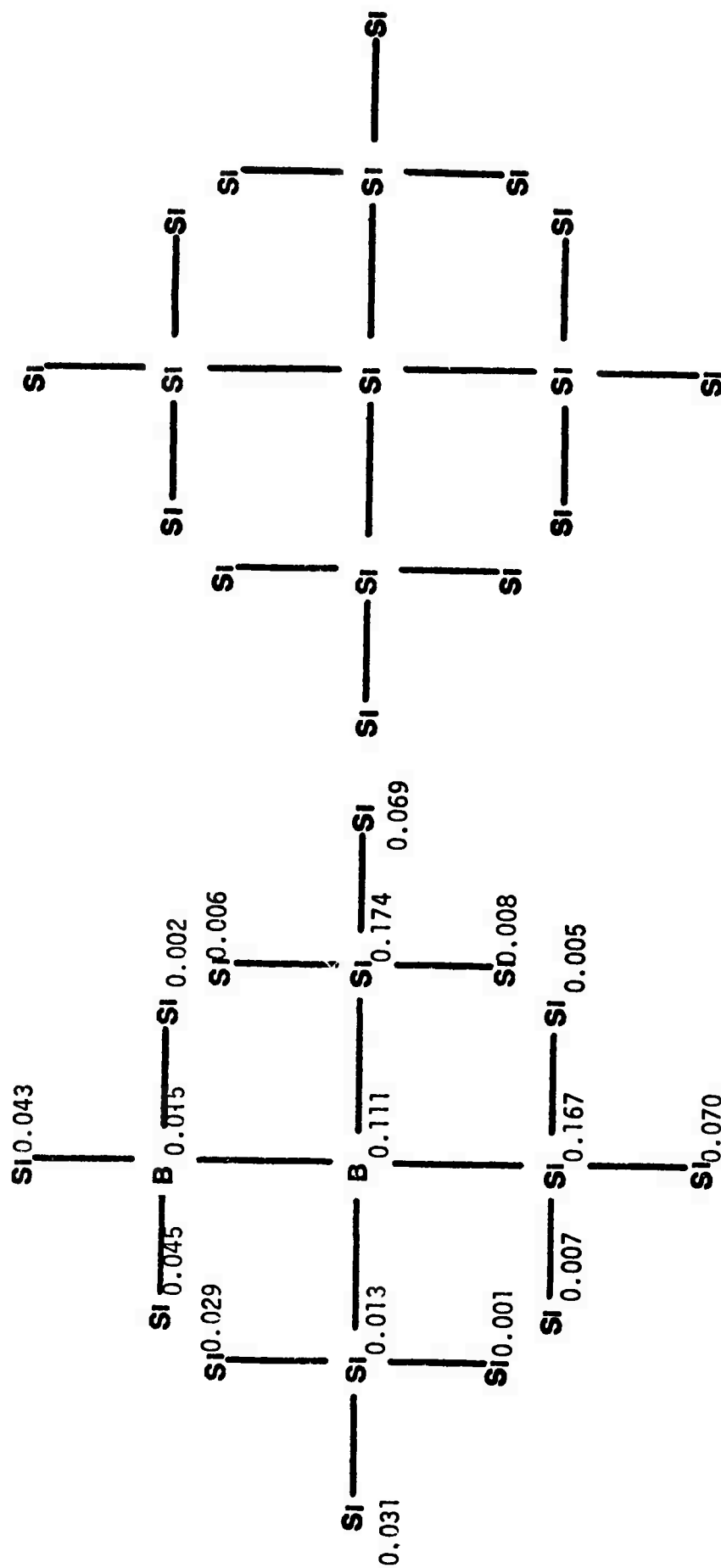


Figure 33C Charge Distribution:  
Acceptor State, Silicon  
Cluster with 2 Boron  
Nearest Neighbor Impurities.

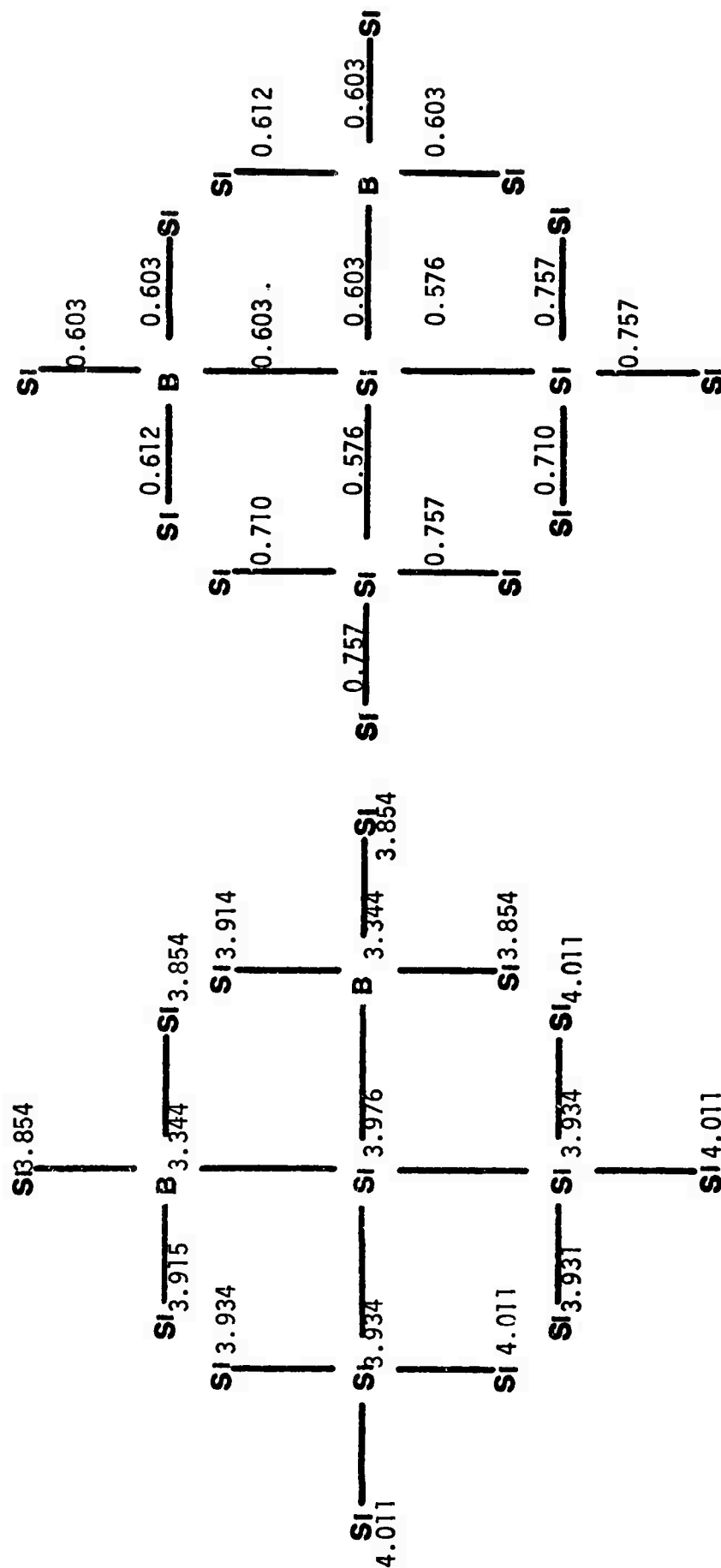


Figure 34A Charge Distribution on Atoms: Silicon Cluster with 2 Boron Impurities: Next Nearest Neighbors.

Figure 34B Bond Populations: Silicon Cluster with 2 Boron Impurities: Next Nearest Neighbors.





**Fig. 35. Energy structure**

FERMI LEVEL =	-7.92	ENERGY GAP =	0.96
---------------	-------	--------------	------



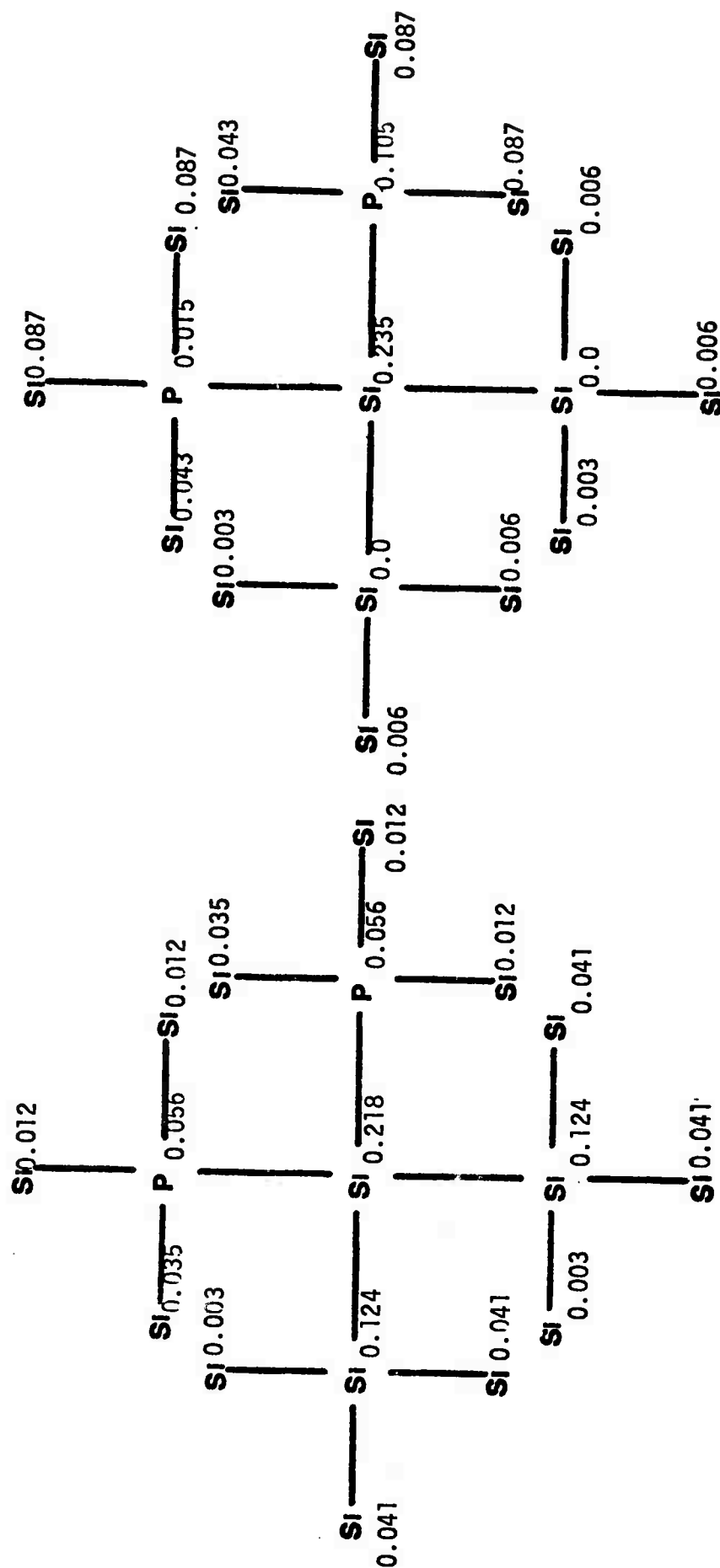


Figure 36C

Charge Distribution in Highest Populated Orbital: Silicon Cluster with 2 P Impurities: Next Nearest Neighbors.

Figure 36D

Charge Distribution in Lowest Unoccupied Orbital: Silicon Cluster with 2 P Impurities: Next Nearest Neighbors.

silicon cluster with  
boron and phosphorus  
impurities nearest  
neighbors.

1000

[illegible]

```

-5.001
-----
-4.30.
*****
( 5)
-4.28.
*****
-4.27

```

**IFLFLFLFL**

I	*****	( 2 )	-8.24,	-8.24,	
I	*****	( 3 )	-8.86,	-8.86,	-8.78,
I	*****	( 4 )	-9.37,	-9.19,	-9.19,
-10.00	*****	( 4 )	-9.69,	-9.61,	-9.12,
I	*****	( 2 )	-10.43,	-9.69,	-9.61,
I	*****	( 5 )	-10.87,	-10.28,	
I	*****	( 5 )	-11.38,	-10.62,	-10.51,
I	*****	( 3 )	-11.89,	-11.32,	-10.51,
I	*****	( 2 )	-12.15,	-11.64,	-11.07,
I	*****	( 2 )	-12.59,	-12.15,	
I	*****	( 3 )	-13.07,	-12.59,	
I	*****	( 3 )	-13.06,	-13.06,	-13.06,

```

167 ***** ( 3) -13.07, -13.06, -13.06,
1 *****

```

131 - 140319 - 140249 - 140249

I	*****	-15.73	
I	*****	( 3 ) -16.09	-16.09, -16.03,
I	*****	( 2 ) -16.78	-16.78,

I	*****	-17.75
I	*****	( 3) -18.17, -18.03, -18.03,
I	*****	

1	*****	( 2 )	-20.35,	-20.35,
1	*****			

\*\*\*\*\*  
-21.52

*****	-25.001
*****	-24.87

FERMI LEVEL =	-6.70	ENERGY GAP =	3.09
---------------	-------	--------------	------

**Fig. 38.** Energy structure of silicon cluster with boron and phosphorus impurities next nearest neighbors.

[illegible]

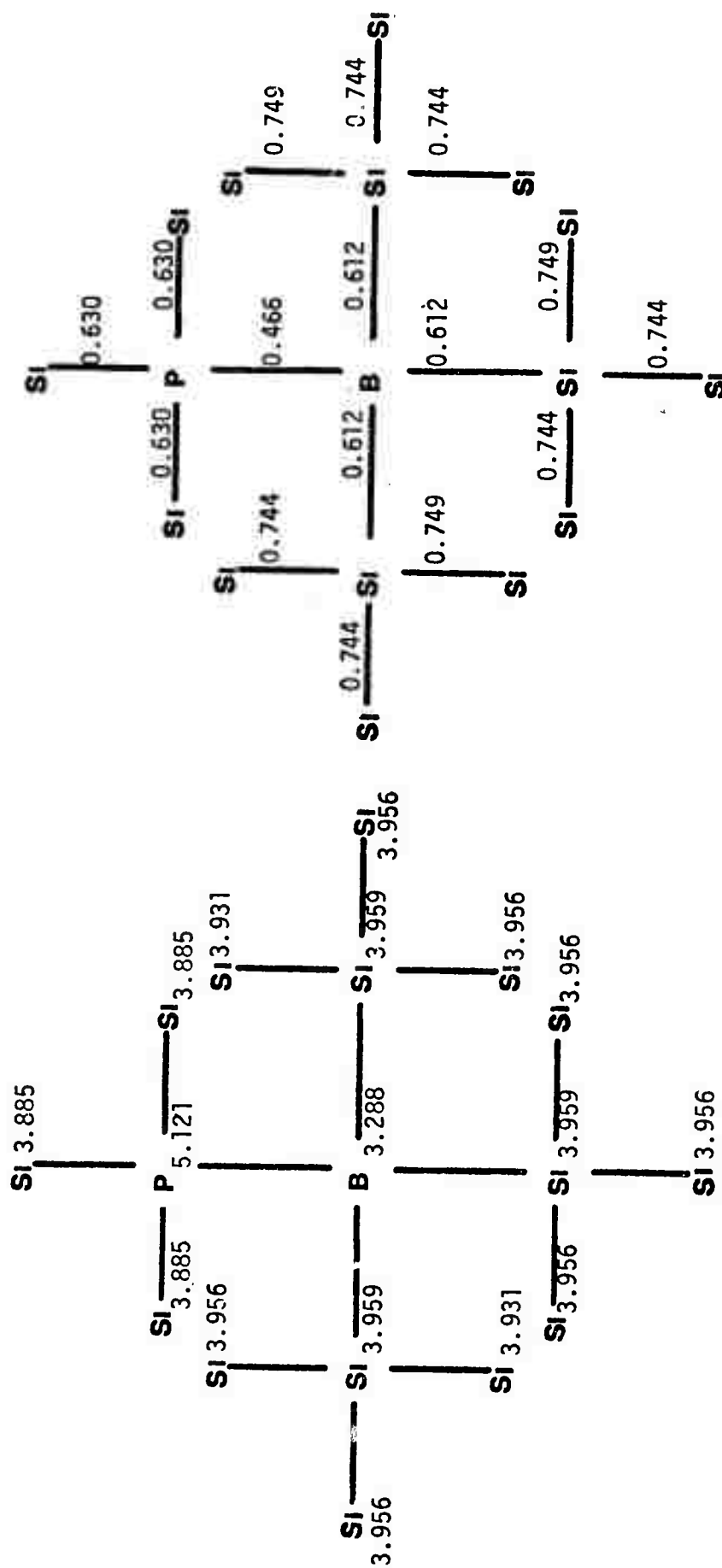
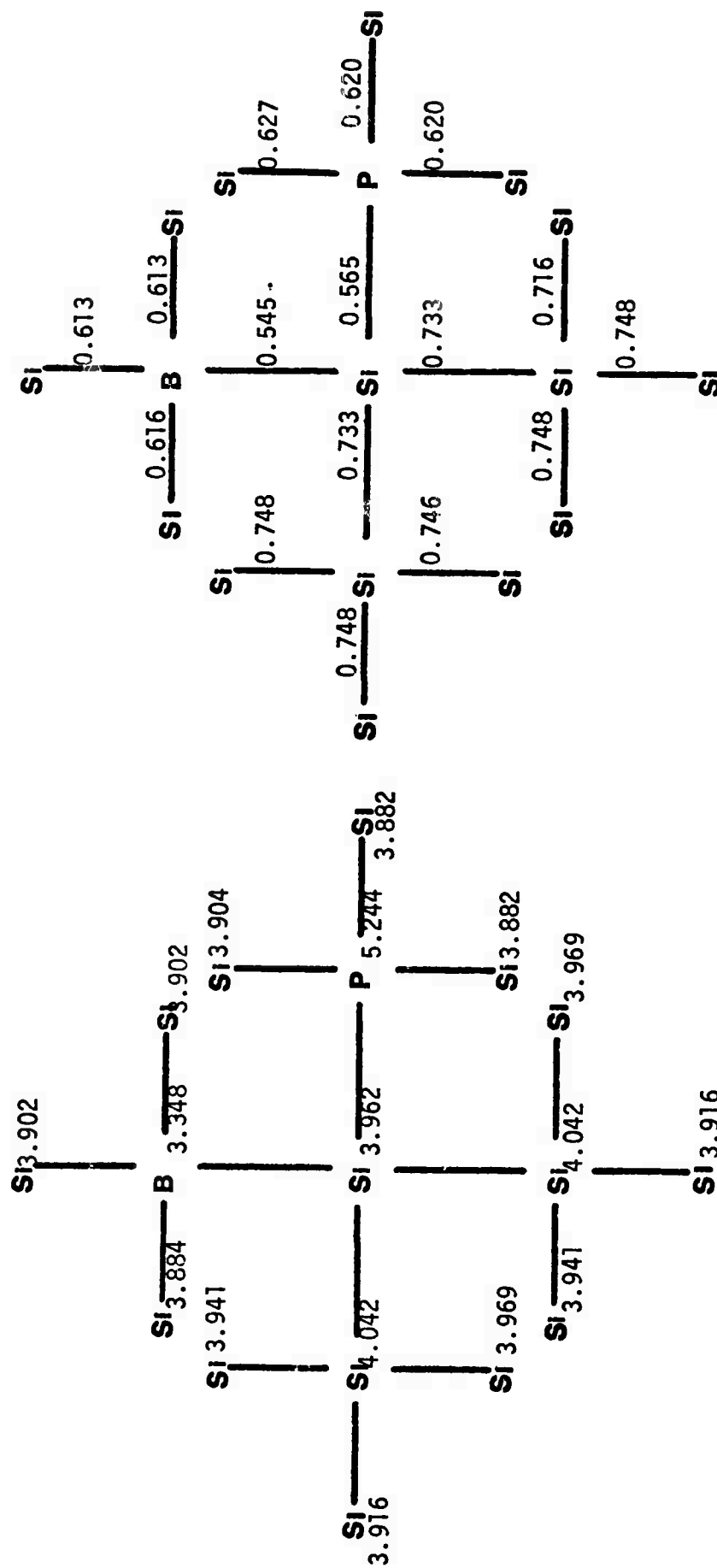


Figure 39A

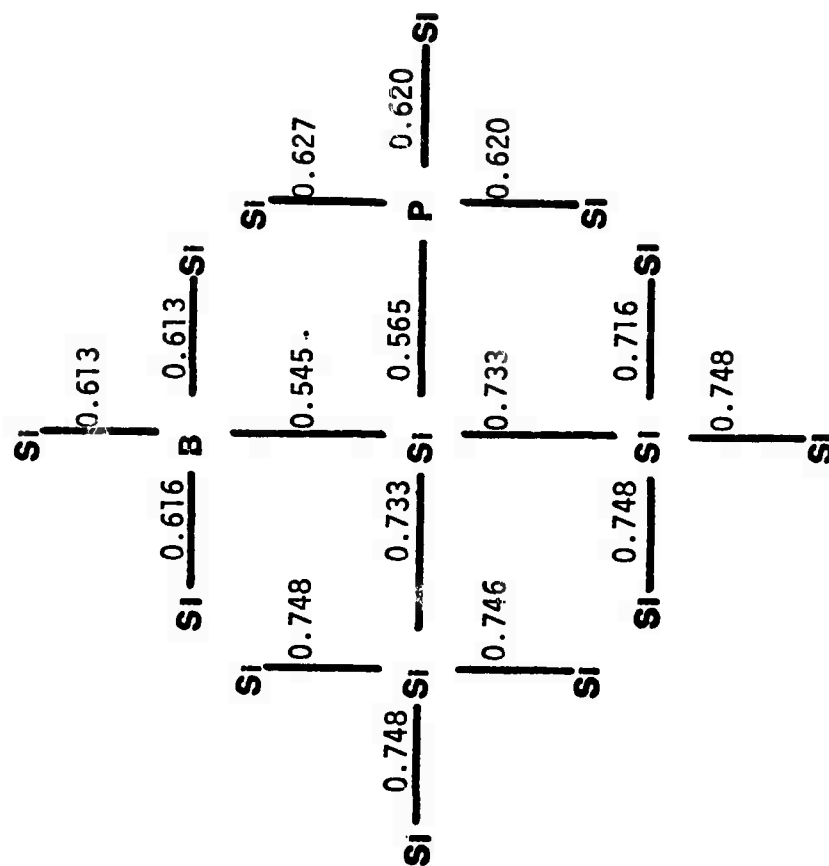
Charge Distribution on  
Atoms: Silicon Cluster with  
B and P Impurities:  
Nearest Neighbors.

Figure 39B

Silicon Cluster with  
B and P Impurities:  
Nearest Neighbors.



**Figure 40A** Charge Distribution on Atoms: Silicon Cluster with B and P Impurities: Next Nearest Neighbors.



**Figure 40B**  
**Bond Populations:**  
**Silicon Cluster with**  
**B and P Impurities:**  
**Next Nearest Neighbors.**



- - EXCITATION FROM LEVEL 53A

FERMI LEVEL = -6.70      ENERGY GAP = 0.86

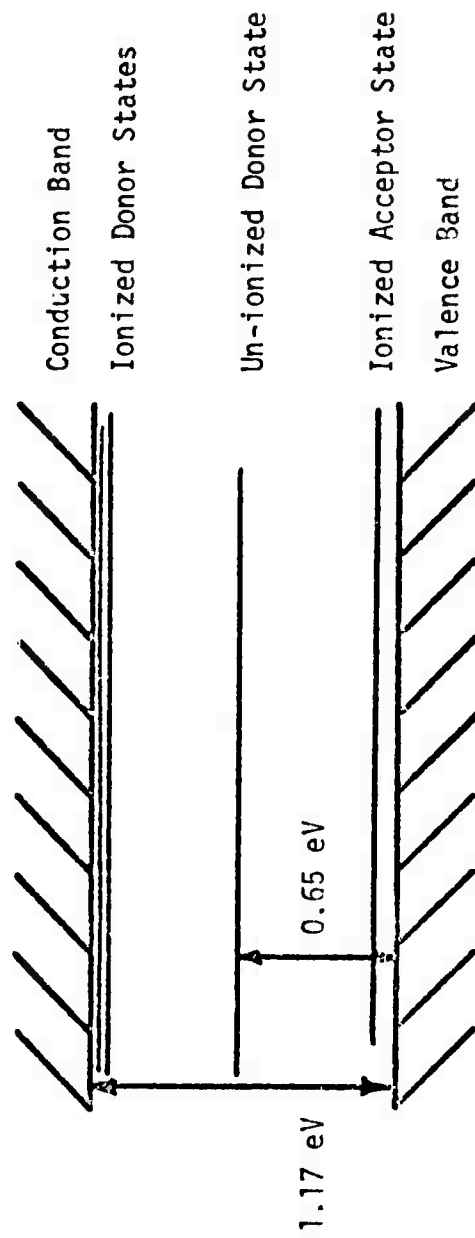


Figure 42 Scaled Energy Level Diagram: Silicon Cluster with 2 Phosphorus and 1 Boron Impurities.

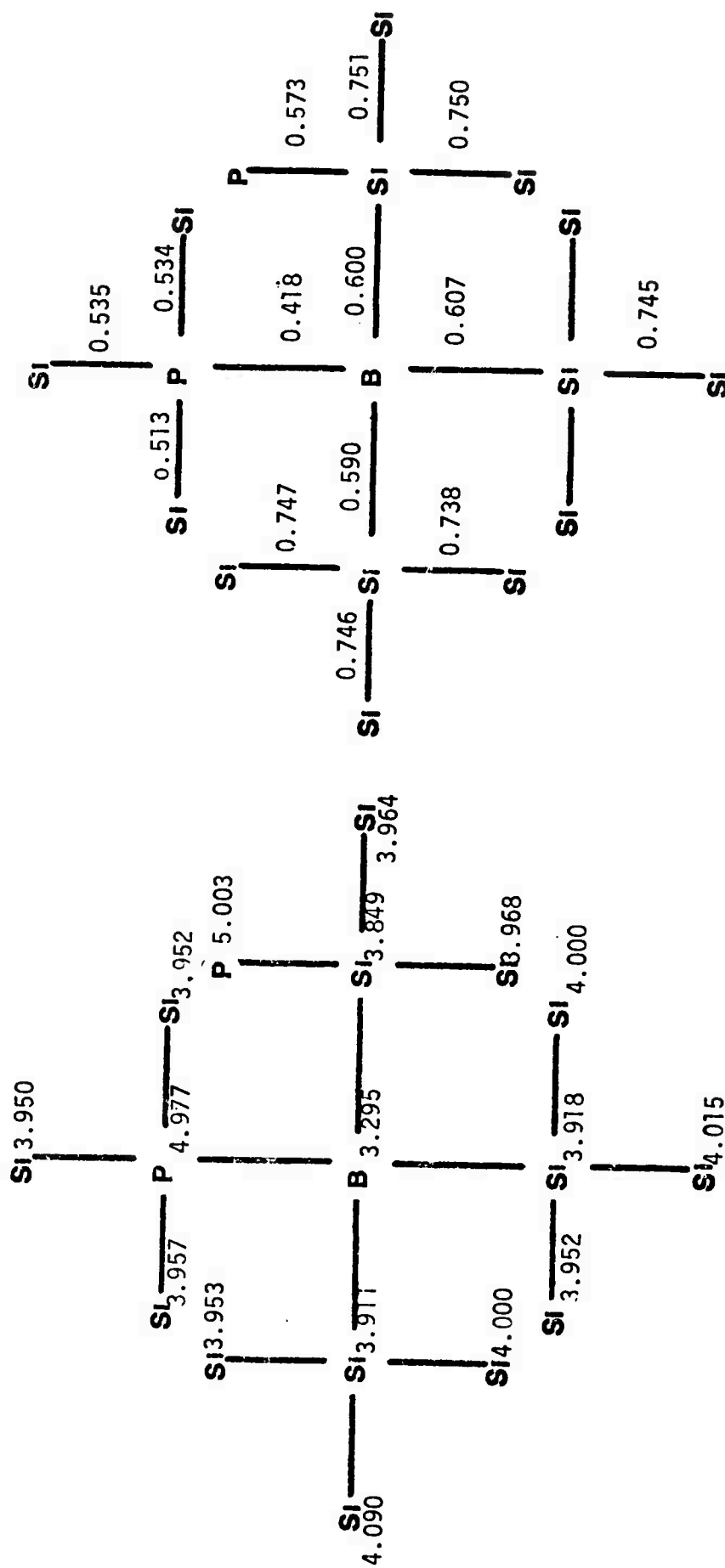


Figure 43A

Charge Distribution on  
Atoms: Silicon Cluster  
with 2 P and 1 B  
Impurities.

Figure 43B

Bond Populations:  
Silicon Cluster with  
2 P and 1 B Impurities.

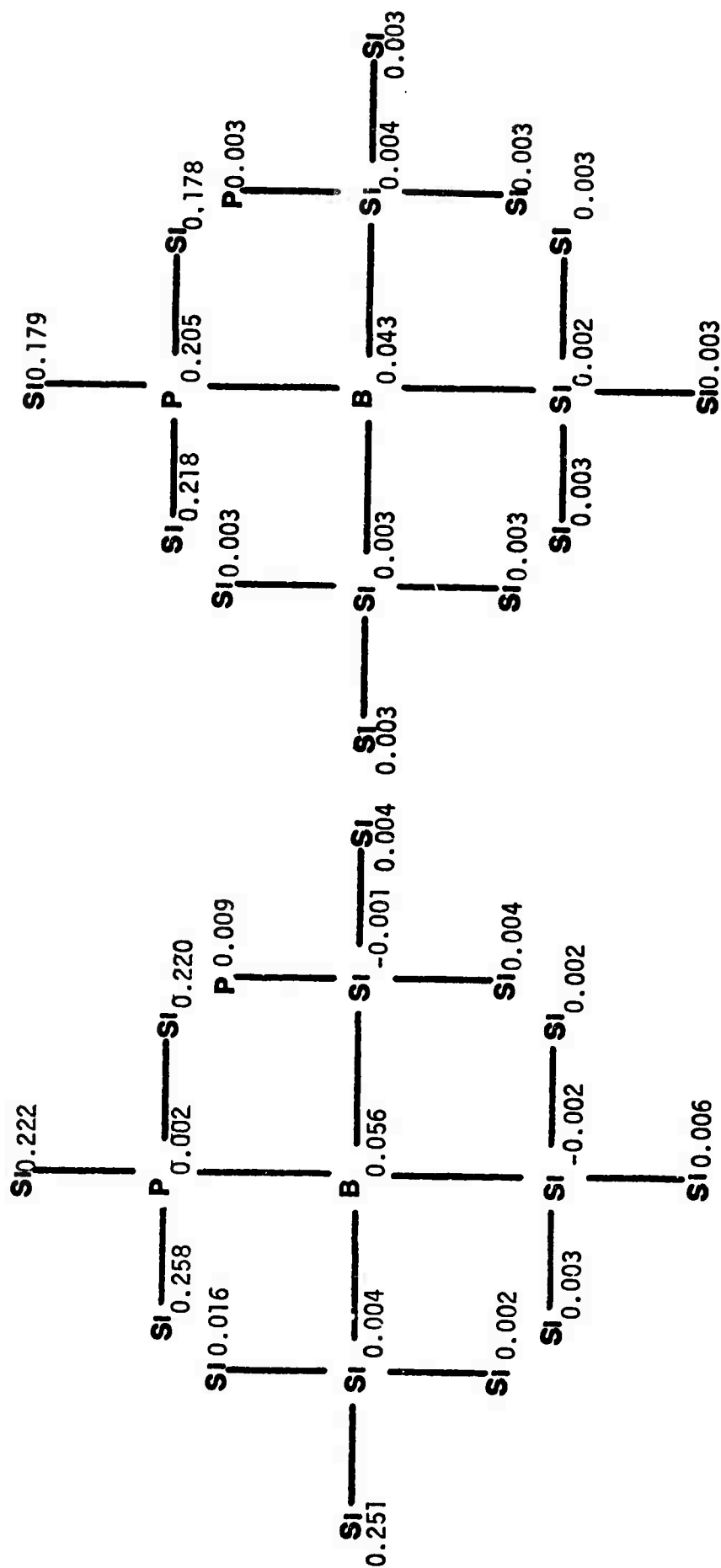


Figure 43C

Excess Spin Distributions:  
Silicon Cluster with  
2 P and 1 B Impurities.

Figure 43D

Charge Distribution in  
Highest Occupied Orbital:  
Silicon Cluster with  
2 P and 1 B Impurities.

VI. Investigation of Recombination and Trapping Processes in  $3\text{As}_2\text{Se}_3$ - $2\text{Sb}_2\text{Se}_3$  Amorphous Films by Photoconductivity Method (By S. S. Li and P. K. Chaudhari)

1. INTRODUCTION

The electrical and optical properties of  $3\text{As}_2\text{Se}_3$ - $2\text{Sb}_2\text{Se}_3$  amorphous films have recently been studied by Chaudhari et.al.<sup>1-2)</sup> Possible band structures were proposed by them and detailed information on the basic parameters such as mobility gap, electron mobility, absorption coefficient, optical gap and index of refraction for these films have been reported in their papers.<sup>1-2)</sup>

Weiser et.al.<sup>3-4)</sup> have recently reported the experimental results on the transport and photoconductivity in the  $2\text{As}_2\text{Te}_3$ - $\text{As}_2\text{Se}_3$  amorphous system, and analyzed their photoconductivity data in terms of "recombination edges" in the CFO model for amorphous chalcogenides.<sup>5)</sup>

In this paper we report the results of our photoconductivity experiment on  $3\text{As}_2\text{Se}_3$ - $2\text{Sb}_2\text{Se}_3$  amorphous films in the temperature range from 278°K to 308°K. Experimental results on these films suggest to us that their photoconductivity behavior is analogous to high resistivity semiconductors in which the recombination and trapping processes can be considered as taking place through an effective trap center. A simple model is established to account for the recombination and trapping processes of the photo-injected carriers in these films.

2. THEORY

Results of the photoconductivity experiments on the specimens of  $3\text{As}_2\text{Se}_3$ - $2\text{Sb}_2\text{Se}_3$  amorphous films indicate that high injection conditions prevail over the light intensity ranges used in the present experiment. This means that the light intensity is strong enough so that the condition  $\Delta n \gg n_0$  and  $\Delta p \gg p_0$  is satisfied. The observed dependence of the photo-current on light intensity,  $I_0$ , could be well interpreted by using a recombination and trapping model which takes into account the trapping of carriers through an effective trap center and the dependence of the carrier lifetime on the injection.

A generalized expression for the photoconductivity in these films may be derived under the assumptions that:

- (1) The effect of trapping through an effective single trap center can be expressed by

$$\Delta p = \Gamma \Delta n \quad (1)$$

where  $\Gamma = \frac{\tau_p}{\tau_n} > 1$  for electron trapping, and

$$\Gamma = \frac{\tau_p}{\tau_n} < 1 \text{ for hole trapping}$$

- (2) The dependence of excess carrier lifetime on injected carrier density (or light intensity) may be expressed in the form:

$$\tau_n = \kappa \Delta n^\beta \quad (2)$$

where  $\kappa$  is a constant, independent of  $\Delta n$ , and  $\Delta n$  is the photoinjected excess electron density;  $\beta$  is a parameter which may vary between -1 and 0, depending upon the injection range. The photocurrent per unit electric field is given by :<sup>6)</sup>

$$\begin{aligned} i_{p.c.} &= q \int_0^d W (\mu_n \Delta n + \mu_p \Delta p) dy \\ &= q \mu_n \int_0^{\Delta n_0} W \left( \Delta n + \frac{\Delta p}{b} \right) \frac{D d \Delta n}{\left[ 2 \int_0^{\Delta n} D R d \Delta n \right]^{1/2}} \end{aligned} \quad (3)$$

where  $D = D_n (p + n \frac{dp}{dn}) / (p + bn)$  is the generalized diffusion coefficient (3-a) and,

$$R = \frac{\Delta n}{\tau_n} \text{ is the rate of recombination} \quad (3-b)$$

Here  $\Delta n_0$  is the excess electron density at the illumination surface and  $d$  is the film thickness;  $W$  is the width of the specimen,  $b = \mu_n / \mu_p$ . Note that for large injection,  $p = \Delta p$  and  $n = \Delta n$  in (3-a).

With the help of Eqs. (1) and (2), Eqs. (3-a) and (3-b) reduce to:

$$D = \frac{2D_n \Gamma}{(1+b)} \quad (4-a)$$

and

$$R = \frac{1/n}{\kappa \Delta n^\beta} = \kappa^{-1} \Delta n^{1-\beta} \quad (4-b)$$

Substituting (4-a), (4-b) and (1) into Eq. (3), we obtain:

$$i_{pc} = \left( \frac{2q\mu_n}{2+b} \right) \left[ \frac{D_n \kappa \Gamma (b+\Gamma) (2-\beta)}{b^2} \right]^{1/2} W \Delta n_o^{(2+\beta)/2} \quad (5)$$

Eq. (5) is valid for different injection ranges, so long as the assumptions made in Eqs. (1) and (2) are valid. The values of  $\beta$  may vary from one injection range to another and may be determined from the slope of  $i_{pc}$  versus  $I_o$  (light intensity) plot. For example,  $\beta = 0$ , if the carrier lifetime is constant and independent of light intensity; this is indeed the case in the low and high injection regions. Furthermore, if the effect of trapping is negligible, then  $\Gamma$  in Eq. (5) is equal to unity.

The injected electron density,  $\Delta n_o$ , at the illuminated surface is directly related to the incident photon flux density,  $Q_o$ , and may be determined from the boundary condition. The result for the present case is given by<sup>7)</sup>

$$Q_o = s_o \Delta n_o + 2 \left[ \frac{D}{\kappa (2-\beta)} \right]^{1/2} \Delta n_o^{2-\beta} \quad (6)$$

where  $s_o$  is the surface recombination velocity at the illuminated surface.  $Q_o$  is the photon flux density which is related to the light intensity  $I_o$  (watt/cm<sup>2</sup>) by  $Q_o = \frac{I_o}{h\nu}$ .  $D$  is the effective diffusion constant, and is given by Eq. (4-a)/

In general, we found that the dependence of the photocurrent on the light intensity in semi-insulating materials (e.g., Cr-doped GaAs) could be analyzed by means of Eqs. (5) and (6), using a monochromatic light source.<sup>6)</sup>

### 3. EXPERIMENTAL DETAILS

Samples on Corning 0211 glass were employed for photoconductivity measurements. An Aminco Grating monochromator, model #4-8400, was used with a 650 watt Tungsten movie projector lamp focused on the entrance of the monochromator. The sample was mounted inside the monochromator housing to avoid any background illumination. Light was

focused on the back of the semitransparent substrate in order to eliminate any contact effect (e.g. photovoltaic effect). Ohmic contacts were made on these films by evaporating a small gold dot on top of the film. I-V measurements on these films indicate that good ohmic contact is obtained for the test specimens. The d.c. photoconductivity was measured by using an HP 413A micro-micro ammeter and a Harrison 6112A digital power supply. One volt bias was used for most of the data. The photo-response was measured by using a constant slit width. The films showed considerable photoresponse covering the whole visible spectral range (Fig. 1). The relative spectral output of the light source, monochromator mirror, and lens combination was measured by an Optics Technology model #615 power meter.

Other measurements such as conductivity, absorption coefficients in these films were reported in references 1 and 2, and will not be repeated here.

#### 4. RESULTS AND DISCUSSIONS

The specimens used in the present photoconductivity experiment were identical to those used in the electrical conductivity measurements reported by Chaudhari et al.<sup>2)</sup> The film has a dark resistivity of about  $10^9 \Omega\text{-cm}$  and the electron mobility estimated from optical measurements,<sup>1-2)</sup> is less than  $5 \text{ cm}^2/\text{V-sec.}$ , at  $300^\circ\text{K}$ . The present photoconductivity experiment is performed under the condition that the photoinjected excess electron density is much greater than the dark electron density (i.e.  $\Delta n \gg n_0$ ). To investigate the recombination and trapping processes of the photoinjected carriers in these films, we first measure the spectral response of the photoconductivity. The result is shown in Fig. 1 for a  $2.23 \mu$  thick  $3\text{As}_2\text{Se}_3\text{-}2\text{Sb}_2\text{Se}_3$  film. Here the photocurrent is normalized to the per unit incident power as measured with the optical power meter. There is no evidence for a wavelength at which the response vanishes completely. In such a case the band gap is defined as the energy at which the response has fallen to half of its peak value. This yields  $E_{ph} = 1.70 (+0.02) \text{ eV}$ , as the photoconductivity gap, which is referred to as an intrinsic gap for the following reasons: (1) the absorption due to localized states would not give rise to photoconductivity; and (2) the recombination time for transitions from the tail of the valence band to the nonlocalized states in the conduction band might be considerably



less than that for the intrinsic process. It is clear from Fig. 1 that thin films of  $3\text{As}_2\text{Se}_3-2\text{Sb}_2\text{Se}_3$  are sensitive photoconductors over the range of visible light. The fall-off in the photoconductivity response at higher energy is due to the recombination of excess carriers at the surface. Optical absorption data reported in reference 1 reveals that intrinsic absorption coefficient is in excess of  $10^4 \text{ cm}^{-1}$  for photon energy greater than 1.67eV (or  $\lambda < 0.73 \mu\text{m}$ ).<sup>1)</sup>

In investigating the recombination mechanism, we measure the photocurrent versus light intensity,  $I_0$ , by choosing monochromatic light with  $\lambda = 5850\text{\AA}$  for several  $3\text{As}_2\text{Se}_3-2\text{Sb}_2\text{Se}_3$  amorphous films. The result for a  $1.35\mu$  thick film is displayed in Fig. 2 for different temperatures. Two distinct injection regions were observed. At the intermediate light levels,  $i_{pc}$  is directly proportional to  $I_0$ . This result may be interpreted in terms of the theoretical expression given in the previous section.

(a) Intermediate light level:

In this injection range, we assume that the effect of electron trapping in the trap centers is important and thus the relation between  $\Delta n$  and  $\Delta p$  is described by Eq. (1), and the electron lifetime depends on the light intensity in the form that

$$\tau_n \propto I_0^{-1/3} \quad (\text{i.e. with } \beta = -1/3 \text{ in Eq. (2)})$$

(7)

The dependence of the carrier lifetime on the injection is due to the fact that in the intermediate injection level charge fluctuation in the trap centers plays an important role in controlling the carrier recombination lifetimes. The carrier lifetime is normally decreased with increasing light intensity. If the injection is very high (strong light intensity), the trap centers are saturated by the excess carriers, and in this case the carrier lifetime reaches a constant value at high injection level.

If the incident radiation is uniformly absorbed in the films, and thus the bulk term in Eq.(6) is the dominant term that contributes to the photocurrent, then the result for photocurrent in the intermediate injection range can be deduced from Eqs. (5-6).

$$i_{pc} = \left(\frac{6q}{5}\right) \mu_p W(b+1) \left(\frac{7D_n}{3}\right)^{1/2} \left\{ \frac{Q_0}{2\left(\frac{3n}{7k}\right)^{1/2}} \right\}^{5/7} \quad (8)$$

which shows that  $i_{pc}$  varies in proportion with  $Q_0^{5/7}$  in this injection range. Since the photon flux density  $Q_0$  is linearly related to the light intensity  $I_0$ , we conclude that  $i_{pc}$  in this range is directly proportional to  $I_0^{0.71}$ , which is in excellent agreement with the observed result shown in Fig. 2.

(b) The high light levels:

If the light intensity is further increased, we see that the slope of  $i_{pc}$  versus  $I_0$  approaches unity (see Fig. 2). This means that at high light levels the lifetime of excess carriers becomes independent of light intensity and the effect of trapping is negligible. The expression of the photocurrent per unit electric field for this case is deduced from Eqs. (5-6) by setting  $\Gamma = 1$  and  $\beta = 0$ , which yields:

$$i_{pc} = q \mu_p (1+b) (D_a \tau_n)^{1/2} W Q_0 / [s_0 + (D_a / \tau_n)^{1/2}] \quad (9)$$

where  $D_a = \frac{2D_n}{1+b}$  is the high injection ambipolar diffusion constant.

Eq. (9) predicts that at high light levels, the photocurrent is directly proportional to  $Q_0$  (or  $I_0$ ), which agrees well with the observed data shown in Fig. 2.

Summing up the above analysis, we come to the conclusion that the effect of trapping is obvious in the intermediate light levels, and the carrier lifetime is a function of light intensity. However, at high light levels, the trap levels are saturated by the excess electrons, and therefore the carrier lifetime reaches a constant value, which is consistent with our observation. The present results on the recombination and trapping processes of the photoinjected carriers in these high resistivity amorphous films are similar to that observed in the high resistivity semiconductors such as Cr-doped GaAs.<sup>7)</sup>

To determine the trap levels in these films, we investigate the temperature dependence of the photocurrent at a constant light intensity. Fig. 3 shows  $i_{pc}$  versus  $1/T$ ; the slope of this semi-log plot yields an

effective trap level at 0.3eV below the band edge. The trap-depth may correspond to a maximum in the statistical distribution of discrete levels. These levels may be due to structural defects, short range disorder fluctuations.<sup>8)</sup> Results of Kolomiets et al.<sup>9-10)</sup> for  $\text{Tl}_2\text{Se}_3\text{-As}_2\text{Te}_3$  and  $\text{As}_2\text{Se}_3$  glasses also show evidence of trap levels. In the presence of such a distribution Rose<sup>11)</sup> has shown that the photocurrent varies as a fraction power ( $i_{pc}$  is proportional to  $I_o^n$ , with  $0.5 < n < 1$ ) of the light intensity. This conclusion supports our theoretical model and the experimental findings reported here.

## REFERENCES

- 1) P. K. Chaudhari, E. R. Chenette, and A. van der Ziel, Paper I, J. Appl. Phys., to be published July (1972).
- 2) P. K. Chaudhari, E. R. Chenette, and A. van der Ziel, Paper II, J. Appl. Phys., to be published July (1972).
- 3) K. Weiser, Electrochem. Soc., Fall Meeting (1970).
- 4) K. Weiser, R. Fisher, and M. H. Brodsky, Proc. 10th Intern. Conf. on the Physics of Semiconductors, Cambridge, England, 667-671 (1970).
- 5) M.H. Cohen, H. Fritzsche, and S. R. Ovshinsky, Phys. Rev. Letters 22, 1065 (1969).
- 6) J. Agraz-G and S. S. Li, Phys. Rev. 2, 1847 (1970).
- 7) S.S. Li and C. I. Huang, J. Appl. Phys. 43, 1757 (1972).
- 8) A.I. Gubanov, Sov. Phys. Solid State 4, 2104 (1963).
- 9) B. T. Kolomietz, T. N. Mamontova, and G. I. Stepanov, Sov. Phys. Solid State 9, 19 (1967).
- 10) B. T. Kolomietz, E. A. Lebedev, F. T. Mazec, T. N. Manontova, and G. I. Stepanov, Proc. of the Seventh Intern. Conc, Paris, 1283 (1964).
- 11) A. Rose, Phys. Rev. 97 No. 2, 322-33 (1955).

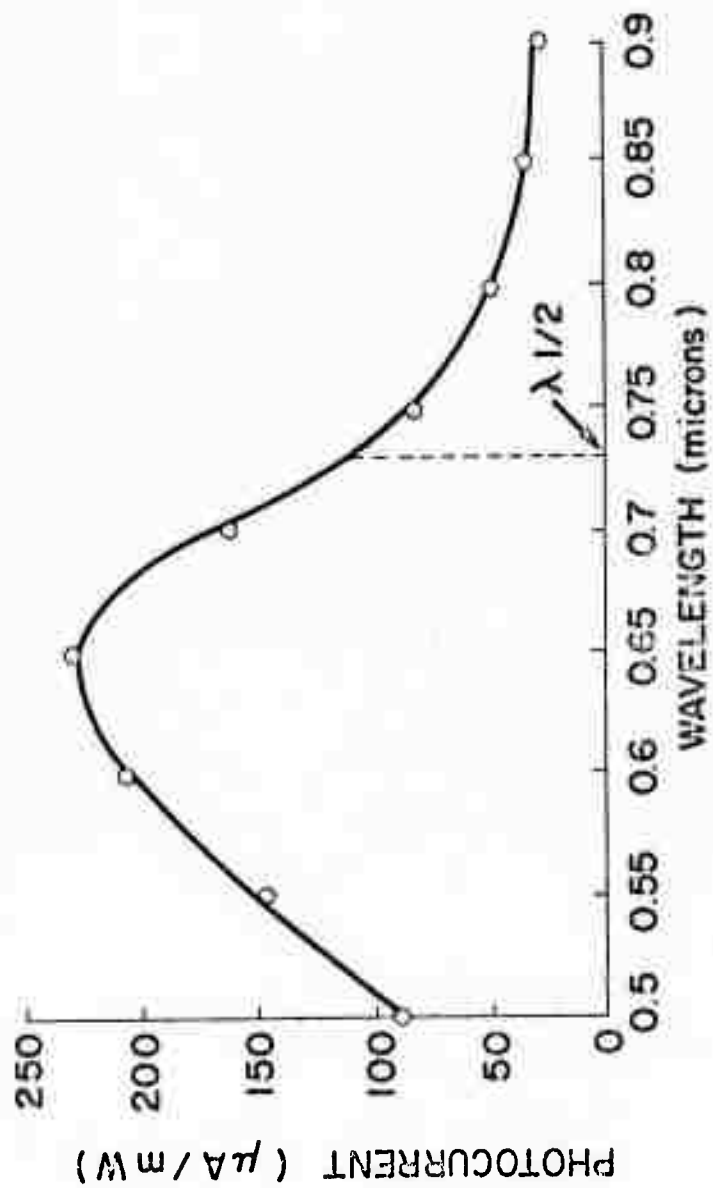


Fig. 1 Photoconductor response in  $\mu\text{A}/\text{mW}$  versus wavelength for sample  $P_4$ .  $\lambda_{1/2}$  denotes the cutoff wavelength for photoconductivity gap. ( $\lambda_{1/2} \approx 0.73 \mu\text{m}$ ).

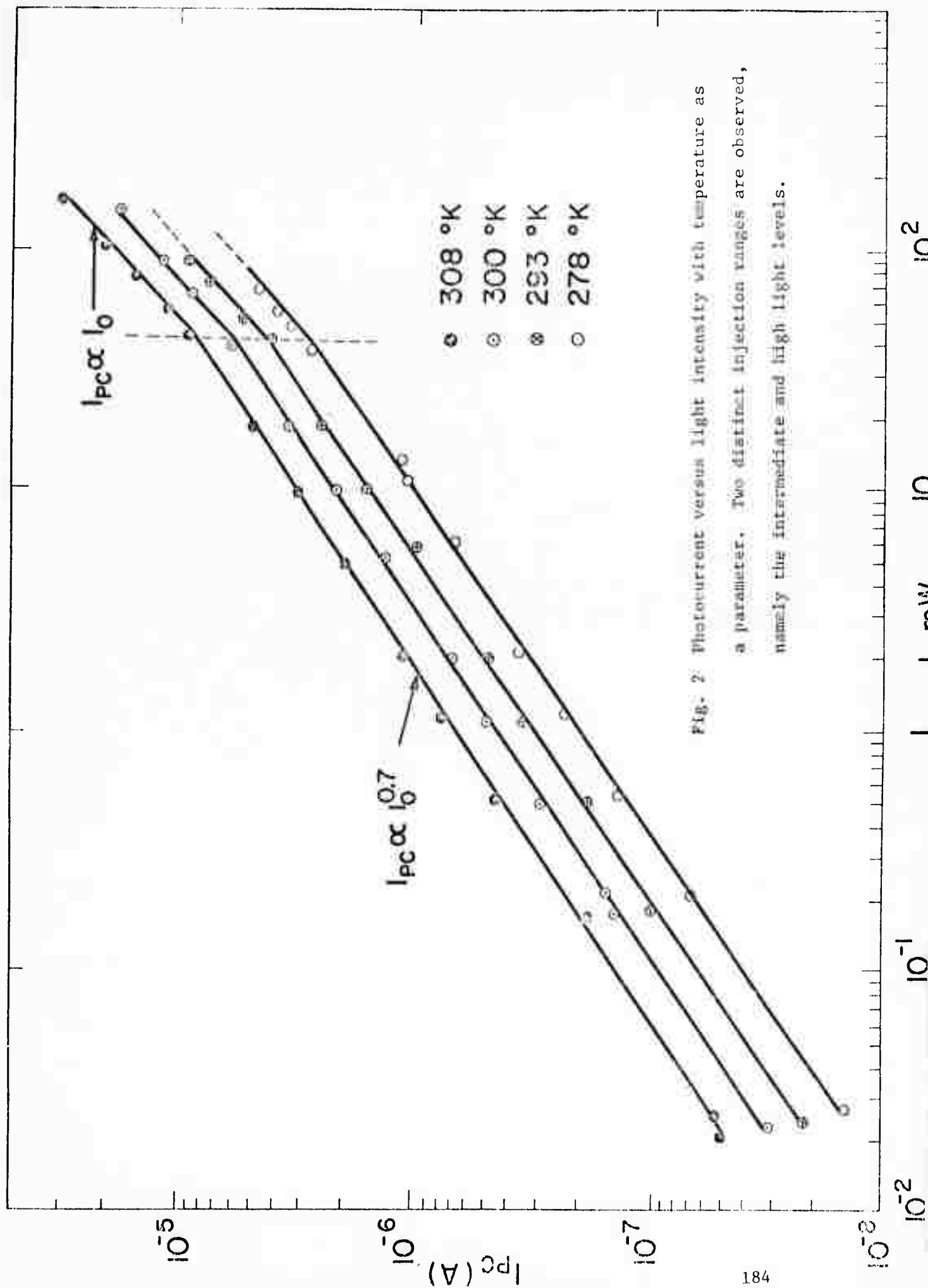


FIG. 2: Photocurrent versus light intensity with temperature as a parameter. Two distinct injection ranges are observed, namely the intermediate and high light levels.

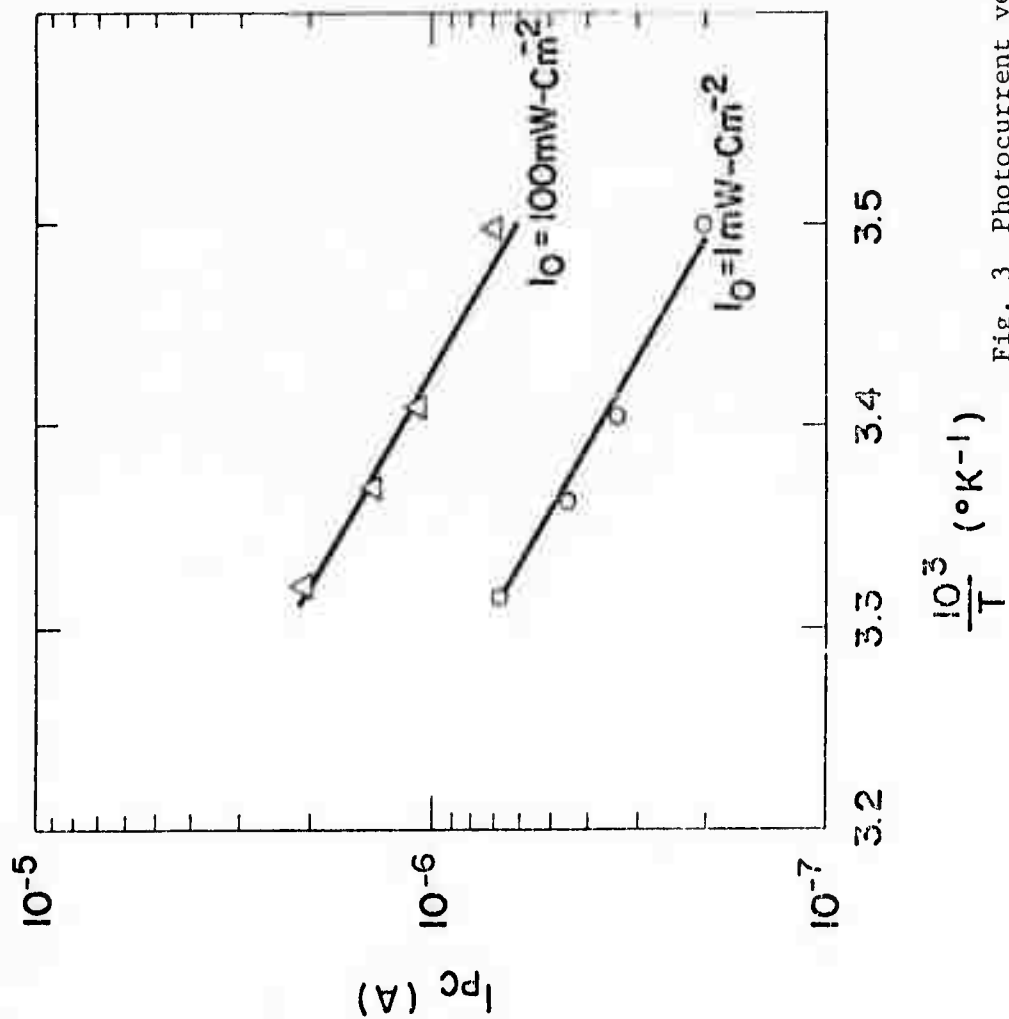


Fig. 3 Photocurrent versus temperature with constant light intensity. The slope of this plot yields  $E_t = 0.3\text{eV}$ , the effective trap level, below the band edge.

DIELECTRIC PROPERTIES OF  
LITHIUM-DISILICATE GLASS-CERAMICS

By

W. D. Tuohig and L. L. Hench

Introduction

The importance of microstructure as a variable for determining dielectric properties of solids has been recognized for many years. Maxwell<sup>(1)</sup> derived an expression for the dielectric properties of a layered body consisting of material having two different dielectric constants. Wagner<sup>(2)</sup> extended this approach to materials containing dispersed spheres of material A having a dielectric constant  $K'_A$  in a continuum matrix B with a dielectric constant  $K'_B$ . Sillars<sup>(3)</sup> extended the model to include dispersed spheroids and, more recently, Fricke<sup>(4)</sup> derived a relationship for ellipsoids. All of these expressions contain the conductivity, dielectric constant and volume fraction of both phases in describing the dielectric properties of a two-phase composite material.

Most commercial ceramic dielectrics contain a vitreous phase which plays a key role in determining the performance of the material, both from an electrical and a mechanical standpoint. The presence of a glassy matrix in porcelain insulators renders them both strong and impervious to moisture. Because



of high dielectric losses usually associated with glasses, the extent of vitreous phase must be minimized for high temperature dielectrics. Therefore, both the composition and the amount of glassy phase are of the utmost importance in determining the suitability of a ceramic material for electronic applications. A general review<sup>(5)</sup> of microstructural effects in ceramic dielectrics also points out that porosity, grain boundary structures and other microstructural features are important parameters for ceramic dielectrics. This study also points out that little systematic information is available for characterized microstructures.

Experimental determination of the dielectric properties of heterogeneous materials was reported by Buchner<sup>(6)</sup> for  $\text{TiO}_2$  in various matrices. The effects of porosity on dielectric properties has been studied by Economos.<sup>(7)</sup>

The dielectric properties of glasses has been the subject of study by a number of workers. Both Owen<sup>(8)</sup> and Isand<sup>(9)</sup> explained their results in terms of a type of heterogeneous dielectric model. Charles'<sup>(10)</sup> study of dielectric properties of lithia-silica glasses indicated the importance of phase separated microstructures upon the interpretation of dielectric properties. More recently, Kinser and Hench<sup>(11)</sup> have shown the importance of thermal history and resulting crystalline microstructure upon the dielectric properties of glasses. Their study further indicated that the metastable crystalline phase precipitated as the result of isothermal heat treatment. It was established that this metastable phase was a precursor to equilibrium phases during controlled devitrification in the lithia-silica system.

Recent studies have shown that a controlled volume fraction of  $\text{Li}_2\text{Si}_2\text{O}_5$  crystals can be grown in a glass of the same composition with appropriate nucleation and crystallization treatments.<sup>(12)</sup>

It is the objective of the present study to establish the dielectric behavior of the 33 mole%  $\text{Li}_2\text{O}$ -67 mole%  $\text{SiO}_2$  glass as a function of the volume fraction of  $\text{Li}_2\text{Si}_2\text{O}_5$  present.

## Experimental Procedure

Specimens for this study were prepared by melting at 1350°C in a covered Pt crucible 5µm Min-U-Sil (Pennsylvania Glass Sand Corporation) and  $\text{Li}_2\text{CO}_3$  in amounts to yield a 33 mole%  $\text{Li}_2\text{O-SiO}_2$  glass composition. Initial melting was for a period of 18 hours; the material was then cast, crushed and remelted for 4 hours at 1350°C prior to casting disc-shaped specimens 1.8 cm in diameter by approximately 0.5 cm thick. Specimens were immediately transferred to an annealing oven at 300°C to relieve quenching stresses.

Vapor deposited gold electrodes in double guard ring configuration were employed. A sample chamber allowed measurements to be made under a 1µ vacuum at controlled temperatures. The apparatus, which includes Wayne Kerr B-221 and B-601 bridges, has been described by Kinser and Hench.<sup>(11)</sup>

Thermal treatments consisted of nucleation at 475°C for 24 hours with subsequent crystallization at 575°C for times of 25 to 85 minutes. The respective volume fractions of  $\text{Li}_2\text{Si}_2\text{O}_5$  were 10, 25, 50 and 70%  $\pm$  5% as inferred from the data of Freiman and Hench.<sup>(12)</sup>

Scanning microscopy was undertaken on fracture surfaces etched with dilute HF. The specimens were thoroughly rinsed and dried and plated with gold-palladium by vacuum deposition.

## Results

Figure 1 shows the frequency dependence of the measured ac conductivity.  $\sigma$  is almost independent of frequency over the audio range for the samples with 10% and 25% crystals present. However, the dependence becomes more pronounced with increasing crystallinity.

Figure 2 shows the dependence of conductivity, AC and DC on volume fraction of  $\text{Li}_2\text{Si}_2\text{O}_5$  crystals. A major change in dependence occurs when  $V_v \approx .25$  due to alkali depletion of the glass.

Figure 3 is a plot of conductivity at 10,000 Hz vs.  $1/T$ . Data for the as-cast, 10%, 25% and 50% samples exhibit

identical slopes, implying that there is no change in activation energy. The 70% specimen exhibits a somewhat lower activation energy.  $\sigma$  decreases continuously with  $V_v$  as expected.

Figure 4 shows dielectric constant  $K'$  vs. frequency for the few volume fractions of crystalline phase at 100°C.  $K'$  decreases as  $V_v$  increases and, for  $V_v = 0.70$ , there is almost no change in  $K'$  with frequency over the range.

Figure 5 shows the dielectric constant vs.  $V_v$  crystalline phase at 500 and 20,000 Hz measured at 100°C.

Figure 6 is a plot of  $\sigma_{DC}$  vs.  $1/T$ . Slopes of as-cast 10%, 25% and 50% specimens are identical, implying no change in activation energy. A continuous decrease in  $\sigma$  occurs as the concentration of free carriers (alkali ions in vitreous network) decreases. The 70% specimen exhibits higher activation energy for DC conduction.

Figure 7 shows the loss tangent vs. frequency at a measuring temperature of 100°C. As-cast specimens show usual low frequency dispersion. The loss peak observed after 24 hours at 475°C implies the presence of  $Li_2O-SiO_2$  as reported by Kinser and Hench. With the onset of equilibrium crystallization, loss peaks are no longer present, and the loss factor decreases markedly with increasing volume fraction of crystalline phase.

## Discussion

Scanning electron micrographs of etched fracture surfaces are shown in Figure 8. The formation of rod-like crystals reported by Freiman and Hench is evident. The  $V_v = 0.50$  indicates that crystal growth occurs to impingement. It appears that residual matrices apparently crystallize in a dendritic fashion. This secondary crystallization apparently produces smaller crystallites within the interstices of the impinged spherulites. This microstructure is no longer evident in the  $V_v = 0.70$  specimen, which has an appearance of an intergranular fracture.

The dielectric properties appear to reflect the continuous or matrix phase. The AC and DC conductivity of specimens in which the major phase is vitreous are similar in terms of magnitude and activation energy. As  $\text{Li}_2\text{Si}_2\text{O}_5$  becomes the dominant constituent, the activation energy is clearly altered. The dielectric constant decreases as the volume fraction of crystalline phase increases, as does the loss factor. The appearance of the relaxation peaks at 2,000 Hz after nucleation and its subsequent disappearance is in agreement with the findings of Kinser, and with unpublished work of the present authors.

Fig. 1

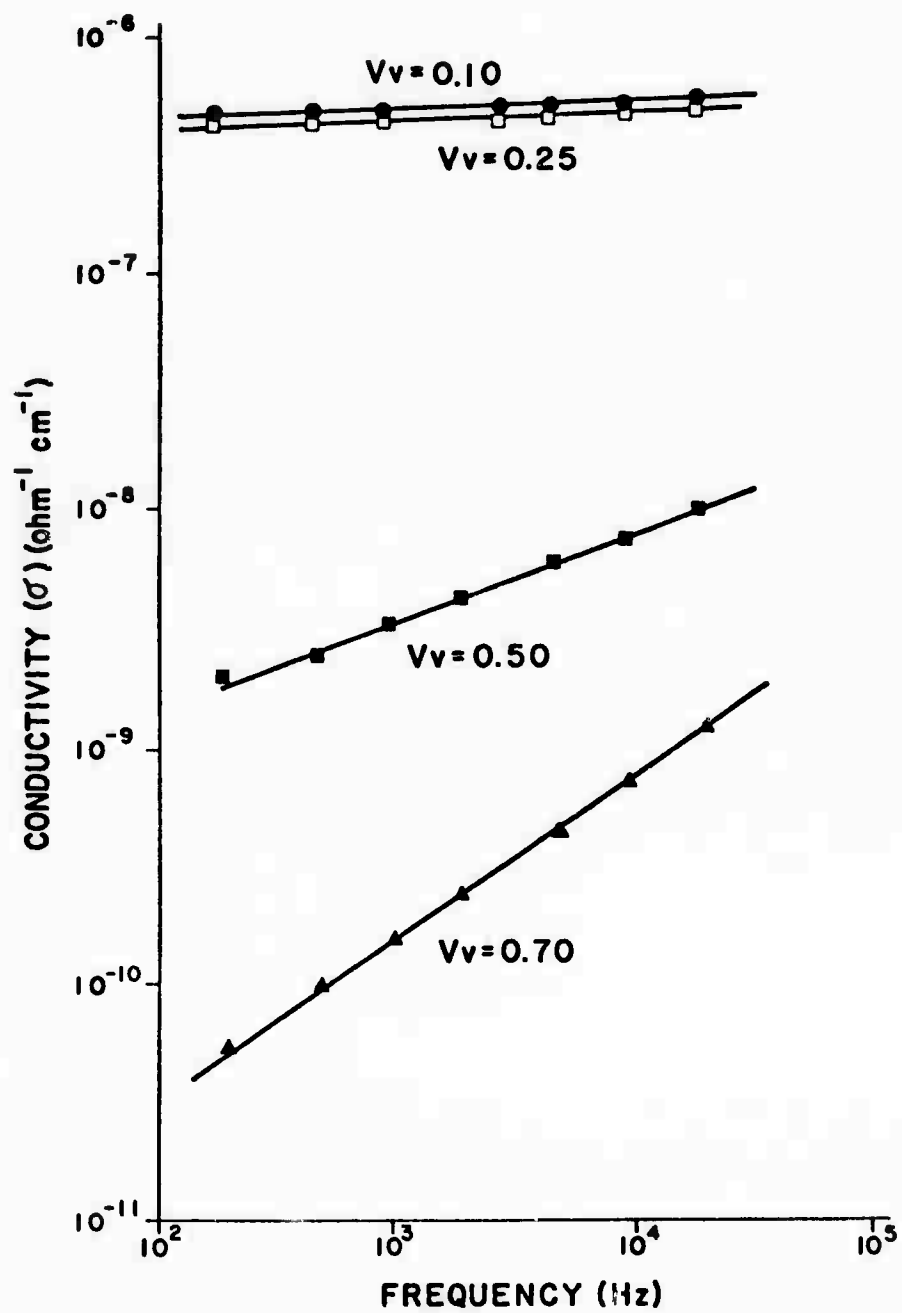


Fig. 2

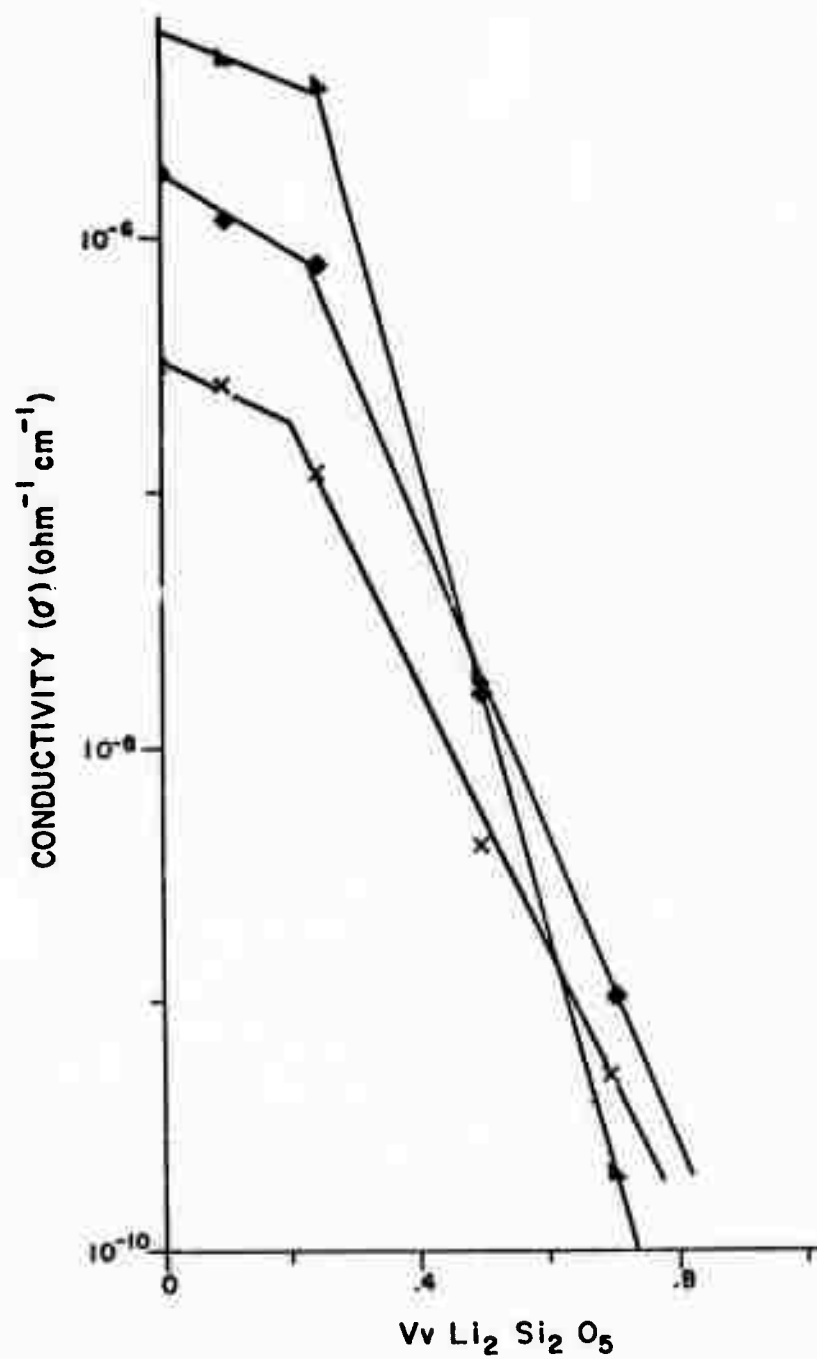


Fig. 3

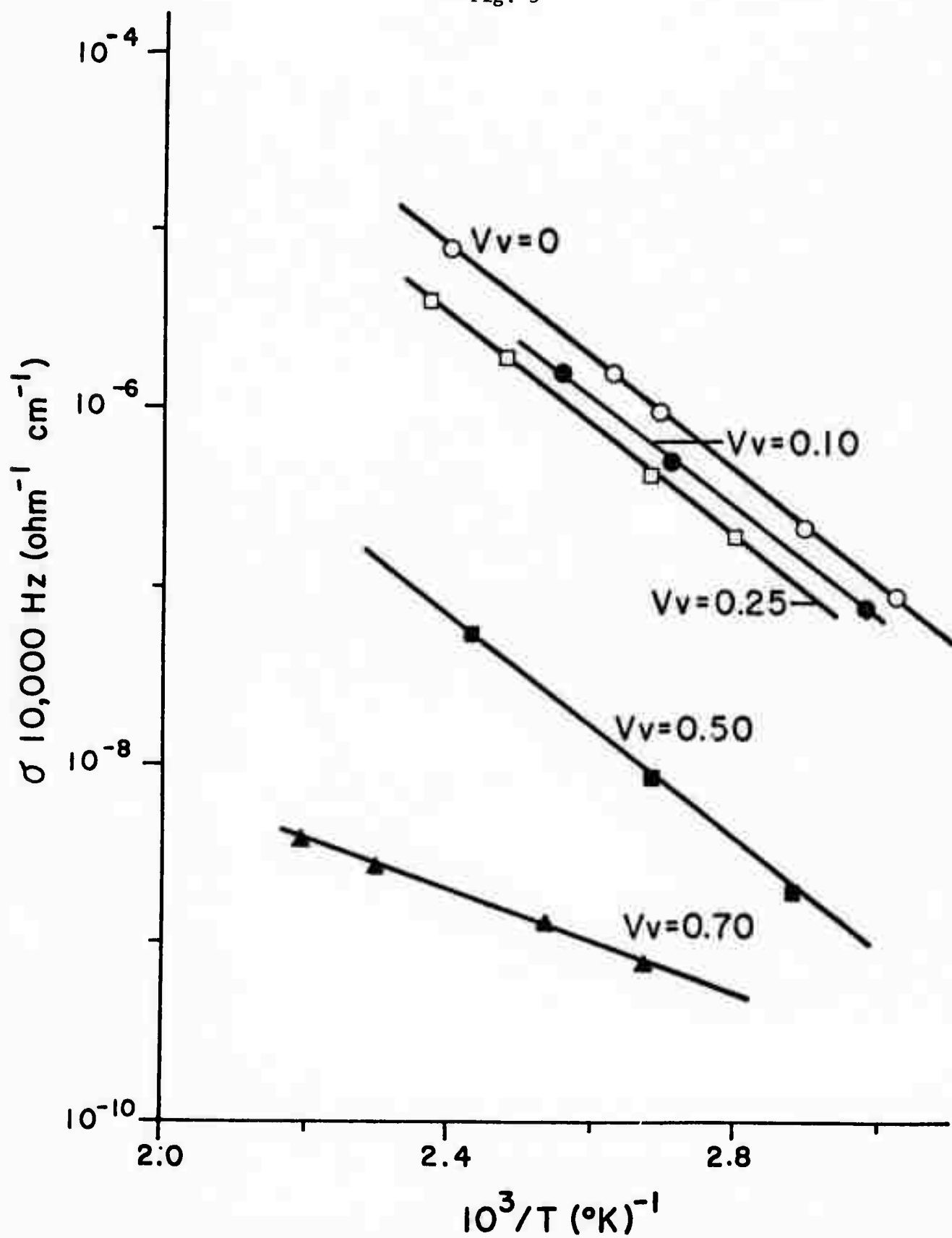


Fig. 4

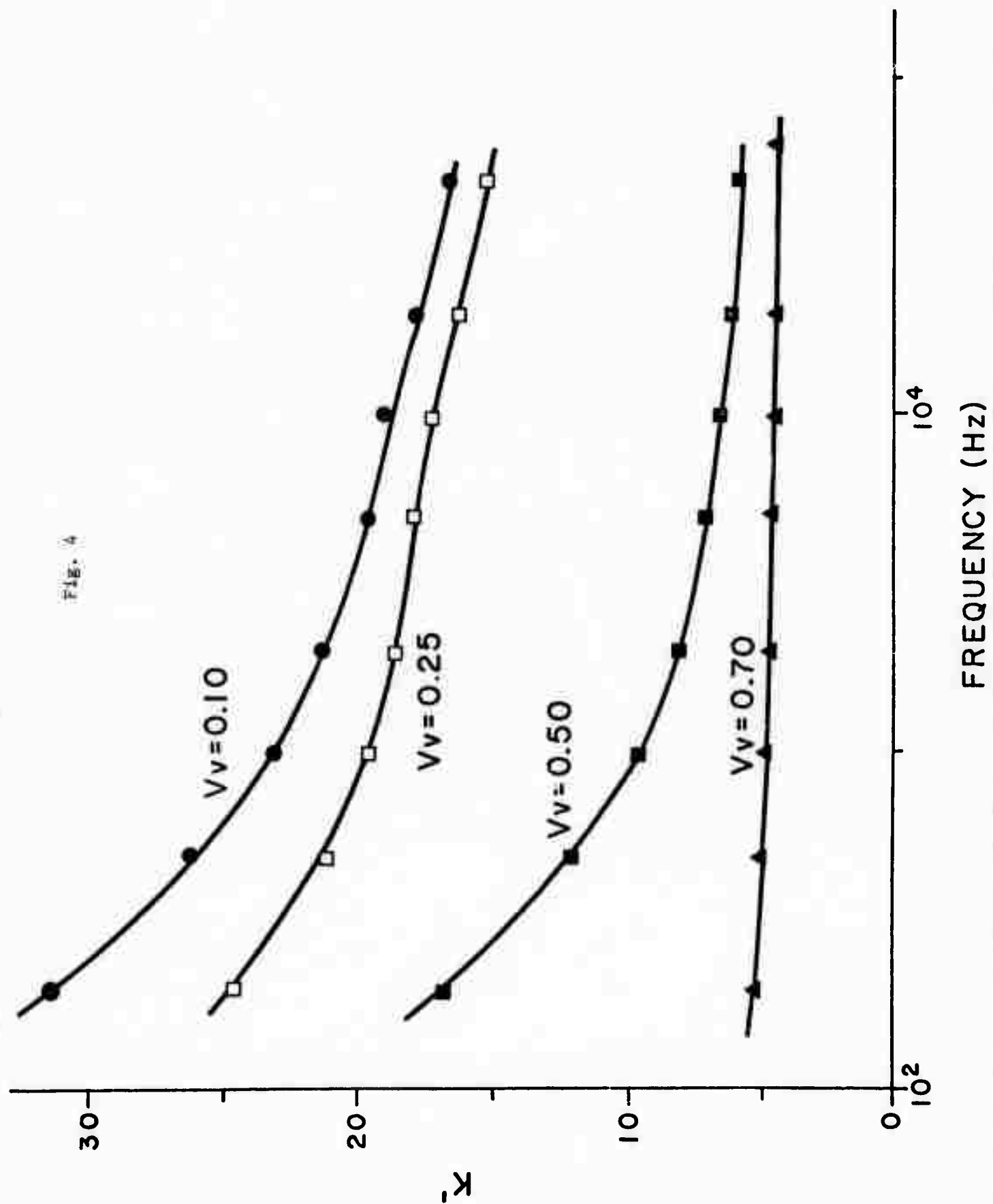




Fig. 3

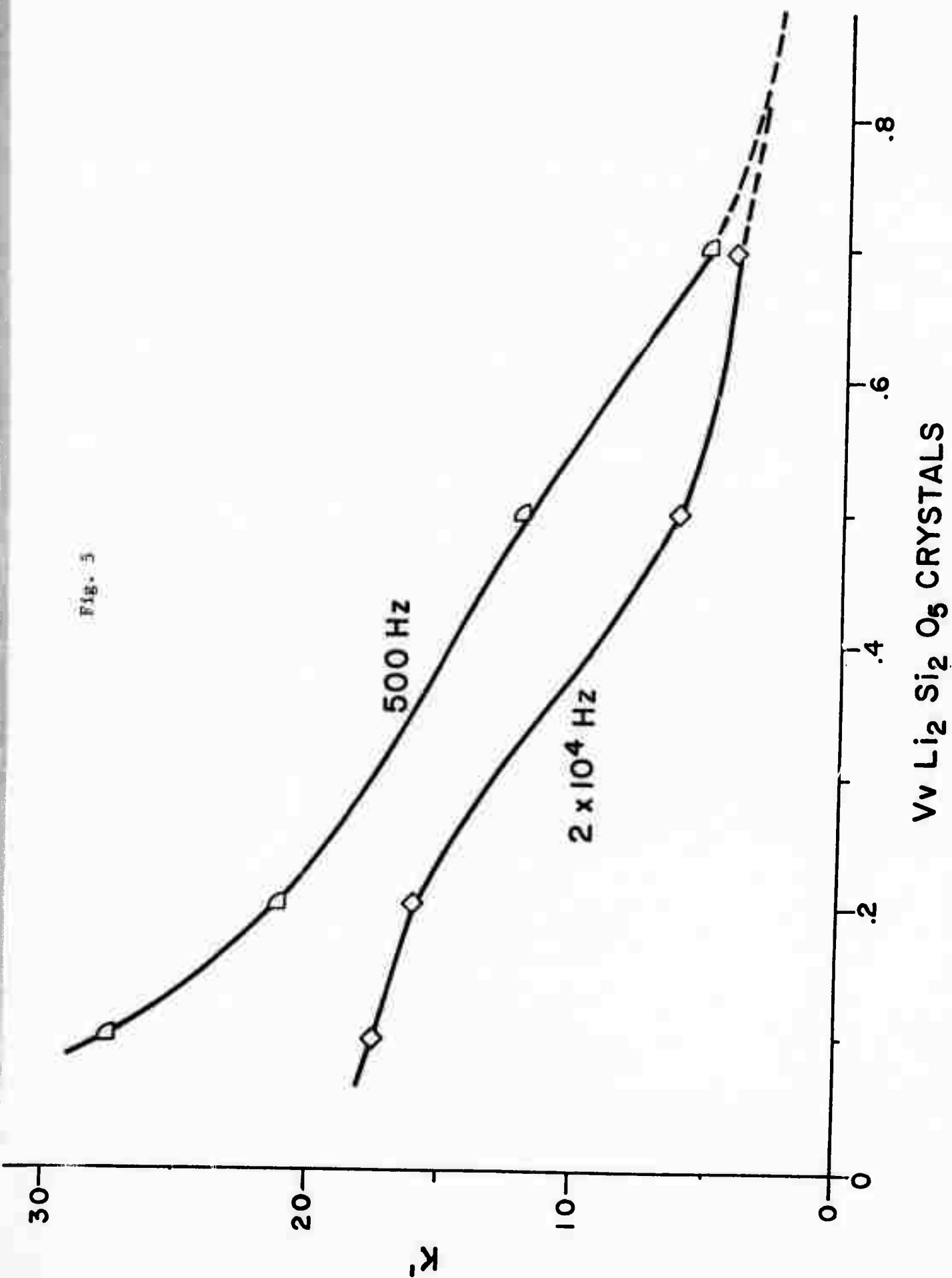


Fig. 6

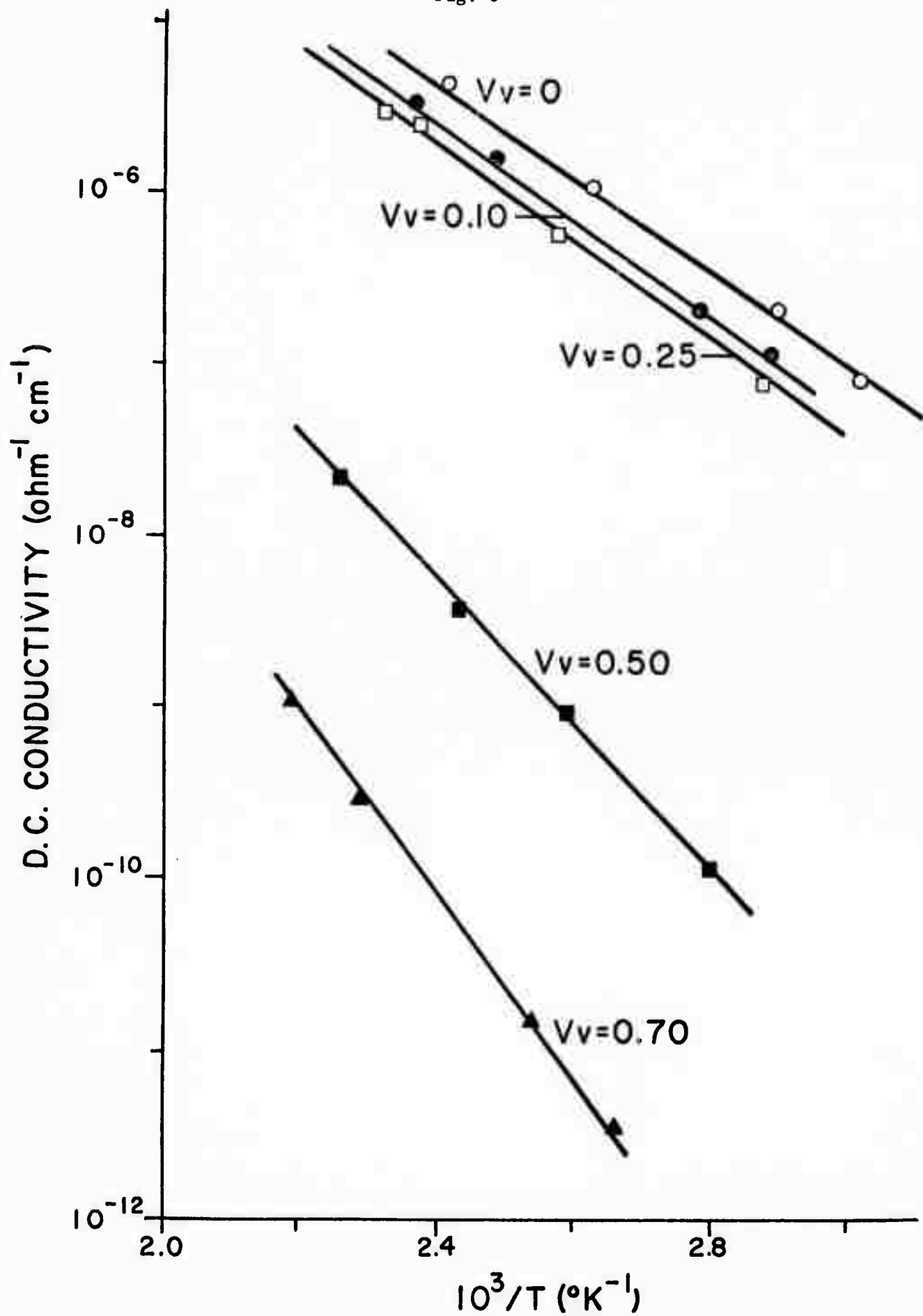


Fig. 7

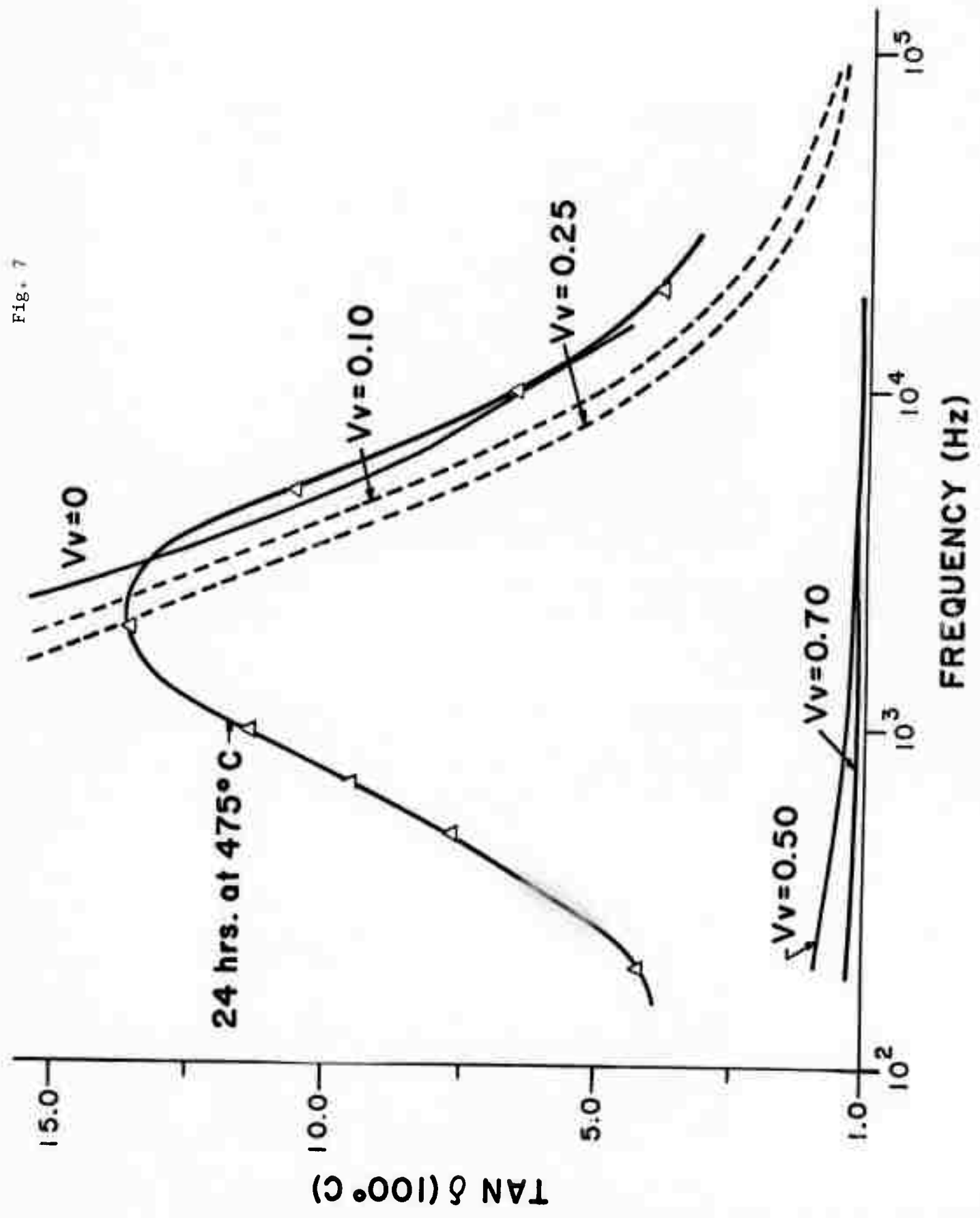
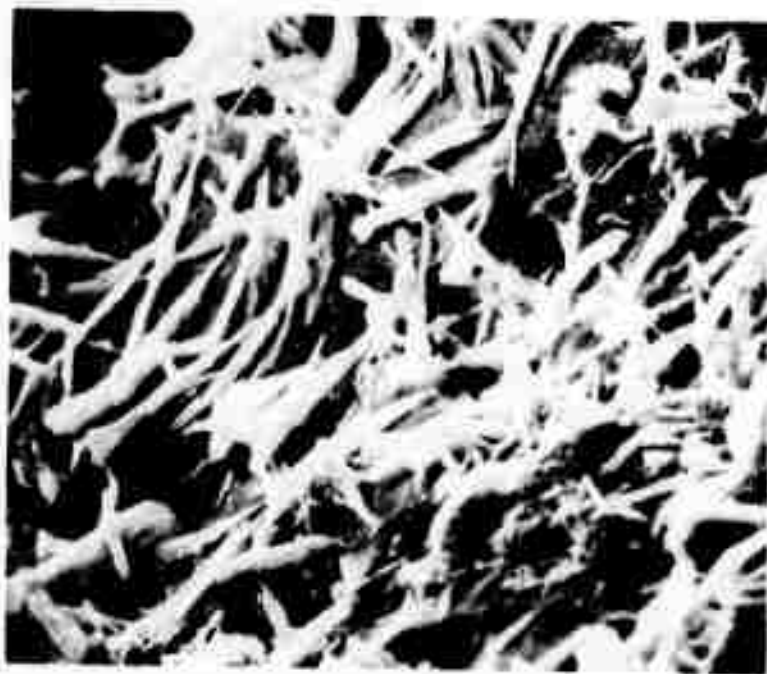


Fig. 8

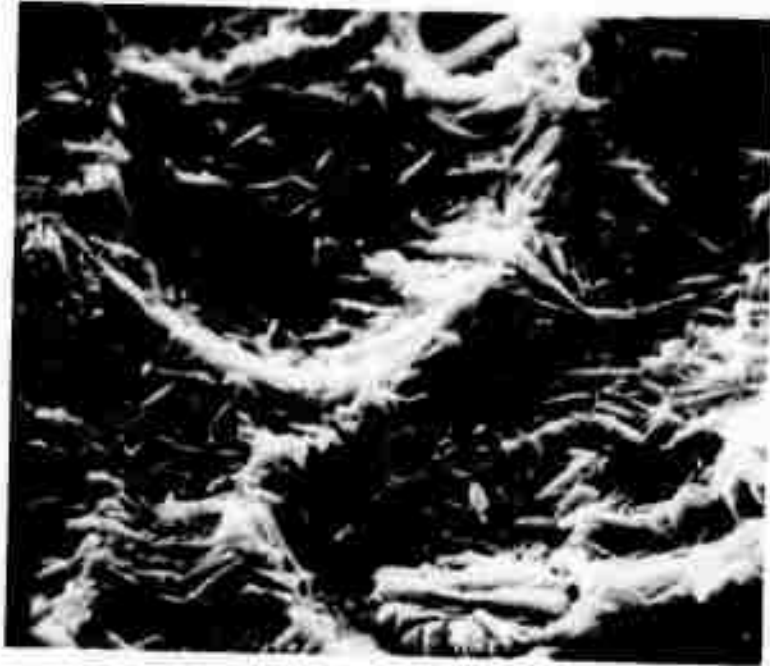


8A:  $V_V = 0.10$ , (1000x)



8B:  $V_V = 0.25$ , (1000x)

Fig. 9



8C:  $v_v = 0.50$ , (1000x)



8D:  $v_v = 0.70$ , (1000x)

### VIII. Discussion

The research of this tenth semiannual period has provided technical findings that bear on problems of interest to the Department of Defense.

The performance of transistors plays a central role in determining the operation of many electronic systems used in military applications. For such applications as detection and amplification, for example, the gain and the cutoff frequency are especially important parameters. In Section III of this report we demonstrate that the bias voltage at the collector terminals can control both gain and cutoff frequency and determine the device behavior at high currents. The study reported here furnishes an understanding that may enable improved design of devices and aid in the computer-aided design of transistor circuits.

Section IV extends the present understanding of the quantum yield of p-i-n photodiodes. Such devices find use as photodetectors in applications of interest to the D.O.D.

In Section V a method is described for the computer calculation of the properties of silicon containing certain types of defects. Among these defects is the impurity-vacancy complex which can commonly result from radiation damage. Thus the study pertains to the design of radiation hardened systems.

The last two sections describe properties of amorphous semiconductors and glass-ceramics potentially critical in the application of these materials to devices and military systems. Because of the hardness they exhibit to irradiation, amorphous semiconductors are of special interest.

This is the final report in the series describing research supported by ARPA Contract F 19628-68-C-0058. A major part of the research program will continue under the support of ARPA Contract F 19628-72-C-0368.